Eduardo Moscatelli de Souza

Topology optimization to design labyrinth seals considering turbulent flow and fluid-structure interaction with discrete and continuous design variables

São Paulo
2024

Eduardo Moscatelli de Souza

Topology optimization to design labyrinth seals considering turbulent flow and fluid-structure interaction with discrete and continuous design variables

Revised Version

Ph. D. Thesis submitted to the Escola Politécnica, University of São Paulo, in partial fulfilment of the requirements for the degree of Doctor of Science.

Concentration area:
Control and Mechanical Automation Engineering (3152)

Advisor:
Prof. Dr. Emílio Carlos Nelli Silva

São Paulo
2024

Este exemplar foi revisado e corrigido em relação à versão original, sob responsabilidade única do autor e com a anuência de seu orientador.

São Paulo, _____ de _____ de _____

Assinatura do autor: _____

Assinatura do orientador: _____

Catalogação-na-publicação

Souza, Eduardo Moscatelli de
Topology optimization to design labyrinth seals considering turbulent flow and fluid-structure interaction with discrete and continuous design variables / E. M. Souza -- versão corr. -- São Paulo, 2024.
169 p.

Tese (Doutorado) - Escola Politécnica da Universidade de São Paulo. Departamento de Engenharia Mecatrônica e de Sistemas Mecânicos.

1.Método de Otimização Topológica 2.Método dos Elementos Finitos 3.Selos Labirinto 4.Selos Infláveis 5.Escoamento Incompressível I.Universidade de São Paulo. Escola Politécnica. Departamento de Engenharia Mecatrônica e de Sistemas Mecânicos II.t.

Souza, Eduardo Moscatelli de. **Topology optimization to design labyrinth seals considering turbulent flow and fluid-structure interaction with discrete and continuous design variables**. 2024. 169 p. Ph. D. Thesis (Doctor of Science) - Escola Politécnica, University of São Paulo, São Paulo, 2024.

Approved in:

Examination Committee

Prof. Dr. _____

Institution: _____

Judgement: _____

Prof. Dr. _____

Institution: _____

Judgement: _____

Prof. Dr. _____

Institution: _____

Judgement: _____

Prof. Dr. _____

Institution: _____

Judgement: _____

Prof. Dr. _____

Institution: _____

Judgement: _____

AGRADECIMENTOS

Aos meus pais, Luiza e Valdivino, pelo amor, carinho, suporte, dedicação e exemplo em todos os momentos. Sem vocês eu não teria conseguido concluir este trabalho. Obrigado por todo sacrifício para me oferecerem a melhor educação possível. Eu precisaria de muitas páginas para agradecer vocês de forma adequada.

À minha esposa, Ariane, pelo amor, companhia, compreensão, conselhos e incentivo aos meus estudos. Com você minha vida é mais feliz e juntos conseguimos ir mais longe. Obrigado por me ensinar a sonhar.

Aos meus familiares e amigos, em especial ao meu irmão Marcel, pelo companheirismo e pelos momentos de descontração que são indispensáveis para recarregar as energias.

Ao meu orientador, Prof. Dr. Emílio Silva, pelos conselhos, incentivo e dedicação enquanto me guiava no desenvolvimento deste trabalho. Aos professores Dr. Renato Picelli, Dr. Luís Sá, Dr. Hélio Emmendoerfer Junior, Dr. Niels Aage e Dr. Casper Andreasen pelas colaborações indispensáveis para este trabalho.

Aos colegas do *Multiphysics Systems Optimization Laboratory* (MSOL) e do *Offshore Technology and Topology Optimization Laboratory* (OTTO) pelas valiosas discussões, com menção especial para André Silva, Lucas Siqueira, Rômulo Cortez, Anderson Azevêdo, Felipe Maffei e Ruben Sallas.

Eu agradeço o apoio do RCGI – Centro de Pesquisa para Inovação em Gases de Efeito Estufa (23.1.8493.1.9), sediado na Universidade de São Paulo (USP) e patrocinado pela FAPESP – Fundação de Amparo à Pesquisa do Estado de São Paulo (2020/15230-5) e Shell Brasil , assim como à importância estratégica do apoio da ANP (Agência Nacional do Petróleo, Gás Natural e Biocombustíveis) por meio da regulamentação da taxa de P&DI. Também agradeço a FAPESP pelo apoio financeiro através do processo 2021/02340-0.

RESUMO

Selos labirinto são dispositivos mecânicos utilizados para selar máquinas rotativas em aplicações envolvendo compressão de metano (CH_4) e gás carbônico (CO_2). Portanto, a otimização de selos labirintos é crucial para controlar o aumento da temperatura atmosférica, uma vez que o CH_4 e o CO_2 são gases de efeito estufa. Neste contexto, o objetivo deste trabalho é desenvolver algoritmos de otimização topológica considerando escoamento turbulento e interação fluido-estrutura e aplicar estes algoritmos para projetar selos labirinto eficientes, reduzindo a emissão de CH_4 e CO_2. Os principais desafios da otimização topológica de selos labirinto são evitar o fechamento do canal, atribuir velocidades diferentes ao rotor e ao estator e evitar ilhas de sólido desconectadas das paredes. Este trabalho propõe duas abordagens que atendem a esses três requisitos e compara as duas. A primeira abordagem envolve variáveis de projeto binárias e uma extensão do método TOBS (*Topology Optimization of Binary Structures*) que evita distribuições de material indesejadas. A segunda abordagem é baseada em variáveis de projeto contínuas e um método que considera o canal como a interface entre o rotor e o estator. Esta última abordagem exige restrições de conectividade para evitar ilhas de sólido. Duas restrições de conectividade são exploradas, uma baseada em interação fluido-estrutura e outra em um problema virtual de transferência de calor. As abordagens binária e contínua são comparadas para escoamento laminar e turbulento. Como alguns projetos apresentam distribuições de material que não podem ser montadas diretamente devido à interferência entre o rotor e estator, este trabalho também investiga a combinação dos conceitos de selos labirinto e selos infláveis, que são selos que se deformam quando pressurizados. Esta característica pode ser utilizada, por exemplo, para ajustar o vão entre o rotor e o estator após a montagem e atingir configurações de montagem complexas. A modelagem do selo labirinto considera escoamento turbulento, que afeta o desempenho de selo labirinto. O escoamento na cavidade do selo labirinto é modelado pelas equações de Navier-Stokes médias (RANS) acopladas com o modelo de Spalart-Allmaras. Já o projeto dos selos infláveis considera o equilíbrio estático de estruturas sujeitas a carregamentos de pressão e grandes deformações. O método dos elementos finitos (FEM) é utilizado para resolver as equações de equilíbrio. A análise de sensibilidades é feita com diferenciação automática. O problema de otimização é resolvido com as bibliotecas CPLEX® e MMA (*Method of Moving Asymptotes*). Três arranjos de selos labirinto são otimizados: eixo liso, eixo escalonado e eixo escalonado com entrada e saída não alinhadas. Os selos infláveis são projetados por otimização topológica com carregamento de pressão e grandes deslocamentos.

Palavras-chave: otimização topológica, selo labirinto, escoamento turbulento, escoamento incompressível, interação fluido-estrutura, grandes deformações, método dos elementos finitos

ABSTRACT

Labyrinth seals are mechanical devices used for sealing turbomachinery equipment in applications such as methane (CH_4) and carbon dioxide (CO_2) compression. Therefore, the optimization of labyrinth seals is crucial for controlling the increase in temperature of the atmosphere because CH_4 and CO_2 are greenhouse gases (GHGs). In this context, this work aims to develop topology optimization formulations by considering turbulent flow and fluid-structure interaction (FSI) and to apply these formulations to the design of efficient labyrinth seals, reducing GHGs emissions. The main challenges of labyrinth seal topology optimization are avoiding the channel closure, assigning different velocities for the rotor and stator, and avoiding solid islands disconnected from the walls. This work proposes two topology optimization algorithms that attend to these requirements and compare them. The first algorithm is based on binary design variables and one extension of the TOBS method (Topology Optimization of Binary Structures) that avoids undesired material distributions. The second algorithm is based on continuous design variables and one method that considers the fluid channel as the interface between the rotor and stator. This last algorithm requires the use of connectivity constraints to avoid solid islands. Two connectivity constraints are investigated, one based on fluid-structure interaction and the other on a virtual heat transfer problem. The binary and continuous approaches are compared for laminar and turbulent flows. As some designs present material distributions that cannot be assembled directly due to interference between the rotor and stator, this work also investigates the combination of the concepts of labyrinth seals and inflatable seals, which are seals that deform when pressurized. This characteristic may be used to adjust the clearance between the assembled parts and to reach complex assemblies, for example. The labyrinth seal model considers turbulence, which influences labyrinth seal performance. The Reynolds Averaged Navier-Stokes (RANS) equations closed with the Spalart-Allmaras turbulence model are used to model the flow in the labyrinth seal cavity. The inflatable seal design considers the static equilibrium of structures subjected to pressure loads and large deformations. The finite element method (FEM) is used to solve the equilibrium equations. The sensitivity analysis is carried out with automatic differentiation. The optimization problem is solved with the CPLEX® and MMA (Method of Moving Asymptotes) optimizers. Three labyrinth seal configurations are optimized: straight-through, staggered and stepped. The inflatable seals are designed by topology optimization with pressure loads and large deformations.

Keywords: topology optimization, labyrinth seal, turbulent flow, incompressible flow, fluid-structure interaction, large deformations, finite element method

LIST OF FIGURES

LIST OF TABLES

ACRONYMS

CH_4	Methane
CO_2	Carbon dioxide
DOF	Degree of Freedom
FEM	Finite Element Method
FVM	Finite Volume Method
PDE	Partial Differential Equation
SIMP	Solid Isotropic Material with Penalization
VFSI	Virtual Fluid-Structure Interaction
VTM	Virtual Temperature Method

NOTATION

a_u	Bilinear form of the weak linear elasticity equation
A	Arbitrary functional
$\boldsymbol{b}$	Body forces
$\boldsymbol{b}_\mathrm{f}$	PDE filter "load" vector (FEM)
c_b1	Spalart-Allmaras model constant
c_b2	Spalart-Allmaras model constant
c_v1	Spalart-Allmaras model constant
c_w1	Spalart-Allmaras model constant
c_w2	Spalart-Allmaras model constant
c_w3	Spalart-Allmaras model constant
C	Objective function
C_D	Drag coefficient
C_f	VFSI virtual compliance
$\overline{C}_f$	VFSI maximum virtual compliance
C_L	Lift coefficient
C_s	Structural compliance
d	Distance
$\mathrm{d}\Omega$	Infinitesimal of volume
$\mathrm{d}\Gamma$	Infinitesimal of area
D	Shaft diameter
Di	Diodicity
e_H	Inlet/outlet size
e_L	Inlet/outlet channel length
$\boldsymbol{e}$	Deviatoric strain tensor
$\boldsymbol{e}_r$	Radial direction
$\boldsymbol{e}_z$	Axial direction
$\boldsymbol{e}_\theta$	Tangential direction
E_d	Viscous energy dissipation
E_t	Total energy dissipation
f_v1	Spalart-Allmaras model additional variable
f_v2	Spalart-Allmaras model additional variable
f_w	Spalart-Allmaras model additional variable
f_Ω	Spalart-Allmaras model constant
F	Weak form
F_ns	Weak form of Navier-Stokes equations

F_{rans}	Weak form of RANS equations
F_{sa}	Weak form of Spalart-Allmaras equation
$F_{\text{rans}}^{\text{sa}}$	Weak form of RANS equations with Spalart-Allmaras model
$\boldsymbol{F}$	Deformation gradient
F_{Di}	Objective function to design fluidic diodes
g	Gravity acceleration
g_{min}	Minimum gap
$g_{\tilde{\nu}}$	Spalart-Allmaras model additional variable
G	Generic constraint
G_f	VFSI constraint
G_{t}	VTM constraint
G_V	Volume constraint
G_{shear}	Shear modulus
G_{max}	Maximum value of shear modulus
G_{min}	Minimum value of shear modulus
$\mathcal{G}$	Reciprocal wall distance
$\mathcal{G}_0$	Reciprocal wall distance reference value
$\overline{G}$	Maximum value of a generic constraint
$\overline{V}$	Maximum volume fraction
h	Element size
$\boldsymbol{h}_{\text{s}}$	Discrete density filter weights vector
H	Design domain height
$\boldsymbol{H}_{\text{m}}$	Discrete density filter matrix
$\boldsymbol{I}$	Identity matrix
I_{C}	First invariant of the right Cauchy-Green tensor
J	Head loss
J_{F}	Determinant of the deformation gradient
k	Turbulent kinetic energy
k_{t}	VTM thermal conductivity
k_0	VTM reference thermal conductivity
K	Arbitrary mesh element
K_{L}	Loss coefficient
K_{S}	Simplified loss coefficient
K_{bulk}	Bulk modulus
K_{max}	Maximum value of bulk modulus
K_{min}	Minimum value of bulk modulus
$\boldsymbol{K}_{\text{f}}$	PDE filter “stiffness” matrix (FEM)
$\boldsymbol{K}_{\text{t}}$	VTM “stiffness” matrix (FEM)
l_{w}	Wall distance

$\boldsymbol{l}_\mathrm{D}$	Drag direction
$\boldsymbol{l}_\mathrm{L}$	Lift direction
$\boldsymbol{l}_\mathrm{O}$	Output port movement direction
ℓ_1	taxicab norm
L	Design domain length
L_C	Characteristic length
L_u	Linear form of the weak linear elasticity equation
$\boldsymbol{L}_\mathrm{f}$	PDE filter "load" matrix (FEM)
m	Design variable field
m_b	Blurred variable field
${m_\mathrm{b}}^*$	Blurred variable boundary condition
m_d	Dilated variable field
m_e	Eroded variable field
m_f	Filtered variable field
${m_\mathrm{f}}^*$	Filtered variable boundary condition
m_p	Projected variable field
m_r	Rotor variable field
m_s	Stator variable field
m_t	VTM variable
$\boldsymbol{m}$	Design variable DOFs vector
$\boldsymbol{m}_\mathrm{f}$	Filtered variable DOFs vector
M_i	Design variable DOF
$M_{f,i}$	Filtered variable DOF
$\mathcal{M}$	Design space
$\mathcal{M}_0$	Homogeneous design space
n_d	Number of spatial dimensions
$\boldsymbol{n}$	Outward normal vector
$\boldsymbol{n}_\mathrm{s}$	Solid outward normal vector
$\boldsymbol{n}_\mathrm{f}$	Fluid outward normal vector
N_m	Number of DOFs in design variable discretization
N_t	Number of DOFs in VTM discretization
$\mathbb{N}_\mathrm{e}$	Set of neighbors elements
$\mathcal{N}$	Function space for auxiliary turbulent viscosity
O	Output port displacement
p	Kinematic pressure field
p_in	Mean pressure at inlet
p_out	Mean pressure at outlet
P	Pressure
P_o	Dissipation in porous material

P_{simp}	SIMP penalization exponent
q_{c}	Inverse permeability convexity for momentum equation
q_{q}	VTM heat source convexity
q_{t}	VTM thermal conductivity convexity
$\boldsymbol{q}_{\text{t}}$	VTM "load" vector (FEM)
Q	VTM heat source
Q_0	VTM reference heat source
Q_{v}	Volumetric leakage
$\mathcal{Q}$	Pressure function space
r	Radial coordinate
r_{b}	Blur filter physical size
r_{i}	Spalart-Allmaras model additional variable
r_{min}	Filter physical size
R_{b}	Blur filter length parameter
R_{f}	PDE filter length parameter
$\boldsymbol{s}$	State variable vector
$\mathcal{S}$	Set of allowed changes for rotor-stator algorithm
$\boldsymbol{t}^*$	Traction loads
T_c	VTM calibration temperature
T_{v}	Virtual temperature
$\overline{T}_{\text{v}}$	VTM maximum temperature
$T_{\text{v},\,i}$	Virtual temperature DOF
$\boldsymbol{T}_{\text{v}}$	Virtual temperature DOFs vector
$\mathcal{T}$	Virtual temperature function space
$\boldsymbol{u}$	Displacement field vector
$\boldsymbol{u}^*$	Displacement boundary condition
$\boldsymbol{u}_f$	VFSI displacement field vector
$\mathcal{U}$	Displacement function space
v_{avg}	Average inlet velocity
v_{in}	Maximum inlet velocity
$\boldsymbol{v}$	Velocity field vector
$\boldsymbol{v}^*$	Velocity boundary condition
$\boldsymbol{v}_{\text{in}}$	Inlet velocity profile vector
$\boldsymbol{v}_{\text{s}}$	Velocity at solid surface
$\boldsymbol{v}_{\text{f}}$	Velocity at fluid surface
$\boldsymbol{v}_{\text{fwd}}$	Velocity in the forward direction (fluidic diode problem)
$\boldsymbol{v}_{\text{rev}}$	Velocity in the forward direction (fluidic diode problem)
V	Neighborhood in rotor-stator algorithm
V_{C}	Characteristic velocity

V	Volume
$\mathcal{V}$	Volumetric function
$\mathcal{V}_{\mathrm{d}}$	Volumetric function of the deviatoric component
$\mathcal{V}_{\mathrm{SC}}$	Simo-Ciarlet volumetric function
$\mathcal{V}_{\mathrm{BW}}$	Bonet-Wood volumetric function
$\mathcal{V}$	Velocity function space
w_{e}	Weight of neighbor for discrete filter
w_m	Design variable test function
w_p	Pressure test function
w_t	Virtual temperature test function
$\boldsymbol{w}_u$	Displacement test function
$\boldsymbol{w}_v$	Velocity test function
$w_{\tilde{\nu}}$	Auxiliary turbulent viscosity test function
w_{rev}	Penalization factor of reverse direction (fluidic diode problem)
W_{m}	Mean spin tensor magnitude
$\tilde{W}$	Adjusted mean spin tensor magnitude
$\tilde{W}_{\mathrm{r}}$	Lower-bounded mean spin tensor magnitude
$\boldsymbol{W}$	Mean spin tensor
x_c	Normalized coordinate for turbulent inlet velocity
x_0	Inlet lower edge coordinate
$\boldsymbol{x}$	Cartesian coordinates vector
z	Axial coordinate
α	Arbitrary design variable or stator design variable
β	Rotor design variable
β_{fl}	TOBS flip limits factor
β_{th}	Smooth Heaviside projection slope
β_γ	Slope of the indicator function projection
γ	Indicator function
${}^{t}\Gamma_{\mathrm{fsi}}$	FSI surface
${}^{0}\Gamma_{\mathrm{i}}$	Mesh internal edges
${}^{0}\Gamma_{\mathrm{n}}$	Surface of traction boundary conditions
${}^{t}\Gamma_{\mathrm{n}}$	Surface of traction boundary conditions in deformed configuration
${}^{0}\Gamma_{\mathrm{v}}$	Surface of velocity boundary conditions
${}^{t}\Gamma_{\mathrm{u}}$	Surface of displacement boundary conditions in deformed configuration
${}^{0}\Gamma_{\mathrm{inlet}}$	Inlet surface
${}^{0}\Gamma_{\mathrm{outlet}}$	Outlet surface
${}^{0}\Gamma_{\mathrm{rotor}}$	Rotor surface
${}^{0}\Gamma_{\mathrm{stator}}$	Stator surface

${}^{0}\Gamma_{\text{output}}$	Output port surface (for inflatable seal only)
Γ^{m}	Design domain boundary
$\Gamma^{\text{m}}_{\text{d}}$	Design domain boundary with Dirichlet condition
$\Gamma^{\text{m}}_{\text{n}}$	Design domain boundary with Neumann condition
γ_{ip}	Interior penalization constant
Δp	Pressure difference
$\Delta\eta$	Parameter to define dilation and erode thresholds
ϵ	TOBS constraint relaxation factor
ε	Rate of dissipation of turbulent kinetic energy
ϵ_m	MMA tolerance (minimum change of design variable)
ζ	Yoon's function
η_{th}	Smooth Heaviside projection threshold
η_γ	Threshold of the indicator function projection
η_{l}	Threshold for dilation operation
η_{h}	Threshold for erode operation
θ	Tangential coordinate
κ	Inverse permeability of momentum equation
κ_{max}	Maximum inverse permeability
κ_{min}	Minimum inverse permeability
κ_1	Normalized inverse permeability
κ_{vk}	Von Kármán constant
$\kappa_{\mathcal{G}}$	Inverse permeability of Eikonal equation
$\kappa_{\tilde{\nu}}$	Inverse permeability of Spalart-Allmaras equation
λ_{1st}	Lamé's first parameter
$\lambda_{\tilde{\nu}}$	Relaxation for Spalart-Allmaras absorption term
μ_{2nd}	Lamé's second parameter
ν	Molecular kinematic viscosity
ν_{eff}	Effective kinematic viscosity
ν_{T}	Turbulent kinematic viscosity
$\tilde{\nu}$	Auxiliary turbulent viscosity of Spalart-Allmaras model
$\tilde{\nu}_{\text{in}}$	Spalart-Allmaras model inlet boundary condition
ξ	Shape function
$\boldsymbol{\xi}$	Shape function vector
Π	Total potential energy
σ_{w}	Eikonal relaxation factor
$\sigma_{\tilde{\nu}}$	Spalart-Allmaras model constant
$\boldsymbol{\sigma}_{\text{f}}$	Fluid Cauchy stress tensor
$\boldsymbol{\sigma}_{\text{s}}$	Solid Cauchy stress tensor
ϕ	Arbitrary field

Ψ	Strain energy density function
Ψ_{d}	Deviatoric component of the strain energy density function
$\Psi_{\mathrm{d,e}}$	Element-wise deviatoric strain energy density function
$\overline{\Psi}_{\mathrm{d}}^{\mathrm{L}}$	Deviatoric component of the linear strain energy density function
$\overline{\Psi}_{\mathrm{d}}^{\mathrm{N}}$	Deviatoric component of the nonlinear strain energy density function
Ψ_{e}	Element-wise strain energy density function
Ψ_{h}	Hydrostatic component of the strain energy density function
$\Psi_{\mathrm{h,e}}$	Element-wise hydrostatic strain energy density function
$\overline{\Psi}_{\mathrm{h}}^{\mathrm{L}}$	Hydrostatic component of the linear strain energy density function
$\overline{\Psi}_{\mathrm{h}}^{\mathrm{N}}$	Hydrostatic component of the nonlinear strain energy density function
$\overline{\Psi}^{\mathrm{L}}$	Linear strain energy density function
$\overline{\Psi}^{\mathrm{N}}$	Nonlinear strain energy density function
χ	Spalart-Allmaras model additional variable
ω	Turbulence frequency
ω_{r}	Shaft angular velocity
Ω_{f}	Fluid domain
Ω_{s}	Solid domain
$\Omega_{\mathrm{s}}^{\mathrm{r}}$	Rotor domain
$\Omega_{\mathrm{s}}^{\mathrm{s}}$	Stator domain
Ω^{m}	Design domain

CONTENTS

1 INTRODUCTION

Labyrinth seals are commonly used for sealing turbomachinery equipment in applications involving greenhouse gases (GHGs) such as methane (CH_4) and carbon dioxide (CO_2). As the number of turbines and compressors used in the industry worldwide is large, optimizing labyrinth seals is important for controlling the increase in atmospheric temperature. For example, the primary source of GHGs emissions during natural gas processing is fugitive CH_4 from compressors, accounting for about 8% of total CH_4 emissions in natural gas systems according to EPA (2011) page 3-44, with natural gas systems representing around 32% of total CH_4 emissions according to Table ES-2 from EPA (2011). However, improving the performance of labyrinth seals is not trivial because many geometric parameters are involved, and it is hard to select a group to analyze. Thus, the topology optimization method is a promising approach to enhance labyrinth seal performance due to its independence on predefined parameters.

This chapter introduces the concepts of labyrinth seals, inflatable seals, and topology optimization for turbulent flow, fluid-structure interaction, and large deformations. Then, the motivation, objectives, and scientific contributions are presented. Finally, the outline of other chapters is described.

1.1 Labyrinth Seals

Centrifugal compressors are actuated by motors or turbines, and seals are applied between the actuating axis and the compressor housing to avoid leakage. Seals are mechanical components designed to help join system parts while reducing leakage, containing pressure, avoiding a mixture of sealing liquid and process gas, and preventing environmental contamination. One of the leading technologies used for centrifugal compressors is the labyrinth seal, as illustrated in Fig. 1.1.

Labyrinth seals are non-contacting seals that impose a contorted path to inhibit the leakage (FLITNEY, 2014). Therefore, these seals do not provide a complete barrier to leakage. They are used because they provide low wear, especially when used with high-speed gas. There are two main applications for labyrinth seals: bearing protection and pressure sealing in turbomachinery. As this work concerns GHGs compressors, the interest is in pressure sealing seals.

According to Sneck (1974), the development of labyrinth seals started at the beginning of the twentieth century to reduce the leakage in steam turbines. Since then, the development of analytical models and experiments to understand the flow inside a labyrinth seal has

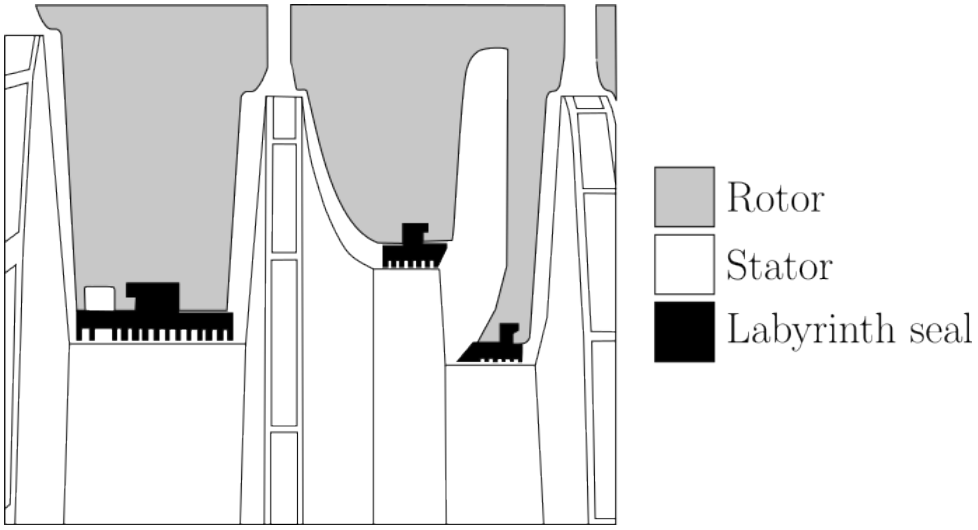

Figure 1.1 – Illustration of labyrinth seals applied to a multi-stage centrifugal compressor.

been of scientific and industrial interest. For example, Egli (1935) provided a theoretical treatment of the fluid flow inside labyrinth seals with sharp-edged orifices. The author introduces an analytical expression for the mass leakage by applying the Saint-Venant's equation with adiabatic assumption. Ehrich (1968) studies the aeroelastic instability in labyrinth seals through a model that relates pressure perturbations to vibrations of the rotor or stator. The model also relate these vibrations to pressure perturbations. As the pressure perturbations and vibrations excite each other, there is a potential positive feedback leading to instability. The author also proposes a stability parameter in terms of the supply pressures, seal geometry, and elastic properties of the rotor and stator. Stocker (1975) design, fabricate, and test unique labyrinth seal concepts to reduce leakage in gas turbines. First, the author tested several seal configurations in a water tunnel capable of providing flow visualizations. Then, he fabricated the most promising configurations and tested them in a static air rig. The labyrinth seals that presented higher leakage reductions with respect to a baseline configuration were tested with rotation. Nowadays, the trend shifted to the development of numerical methods and computer simulations to support the analysis and optimization of labyrinth seals. In this context, Schramm et al. (2004) apply the simulated annealing method to perform parametric optimization of stepped labyrinth seals. The design variables are the position and height of trapezoidal labyrinth steps, and the objective function is the discharge coefficient based on an isentropic expansion mass flow rate. The fluid flow analysis runs in 2D without rotation. Hirano, Guo and Kirk (2005) compare the rotordynamic force of a labyrinth seal calculated by Computational Fluid Dynamics (CFD) with results from simplified models that were used by machinery manufacturers. The authors conclude that the simplified models give a pessimistic prediction of the destabilizing forces. Bellaouar, Kopey and Abdelbaki (2013) optimized a labyrinth seal operating on CH_4 by applying parametric optimization. The goal is to minimize the average pressure in the last gap of a labyrinth seal. Yoon et al. (2013) optimized the labyrinth seal of block-type VHTR (Very-High-Temperature Reactor)

through response surface approximation (RSA), which is a shape optimization technique. The flow resistance coefficient in the bypass gapis the objective function. Wein et al. (2020) applied particle image velocimetry to validate RANS turbulence models for labyrinth seals. The authors show that the choice of turbulence model has great impact in the performance parameters. They identified that all models are not accurate to predict the size of separations and the swirl imposed by viscous effects at the rotor surface. Tyacke et al. (2021) combine genetic algorithms and Large Eddy Simulation (LES) to reduce the leakage in labyrinth seals. Although LES is an expensive analysis method, it enables more accurate modelling than RANS. The authors use parallel programming to obtain results in a reasonable time. Zhao and Wang (2021) runned parametric optimization for a straight-through labyrinth by considering a chaotic optimization algorithm with the seal clearance, fin width, fin height, fin pitch, fin backward, and forward expansion angle as design variables. The work of Souza (2020) is the first to apply topology optimization to design labyrinth seals. The author models labyrinth seals as a fluidic diodes by using the diodicity as objective function, which avoids the channel closure during optimization. Later, Sá et al. (2021b) extends the idea of modeling labyrinth seal as fluidic diodes by introducing a continuous boundary propagation method capable of assigning different velocities for the rotor and stator.

In turbomachinery applications, labyrinth seals typically comprise a series of teeth that provide a small gap between the rotor and the stator, according to Figure 1.2. At each tooth, the pressure head is converted into kinetic energy to be dissipated in the next chamber (SNECK, 1974). The labyrinth seal may be arranged in a straight-through configuration (Fig. 1.2a), in a staggered configuration (Fig. 1.2b), or in a stepped configuration (Fig. 1.2c). The pressure reduction for the staggered and stepped configurations is superior because the grooves on the shaft prevent the fluid from bypassing the expansion volumes between the teeth, i.e., there are no straight flow lines. For equivalent dimensions, the leakage on a straight-through seal is 20-30% higher than on a stepped seal (FLITNEY, 2014). However, stepped designs are harder to manufacture and assemble. One of the ideas of this work to tackle this problem is to facilitate the manufacturing of stepped labyrinth seals by deforming the teeth after the assemblage.

For the last 20 years, researchers and engineers have been studying and applying polymeric materials to design labyrinth seals (WHALEN et al., 2013). The motivation is to reduce the clearance in order to improve efficiency, which is possible because polymeric seals can rub against the rotor without damaging it. Also, polymeric seals return to their original form after rubs, which can occur during start-up and at critical speeds. This work is interested in another opportunity open by the use of polymeric materials: to use seal deformation to reduce leakage.

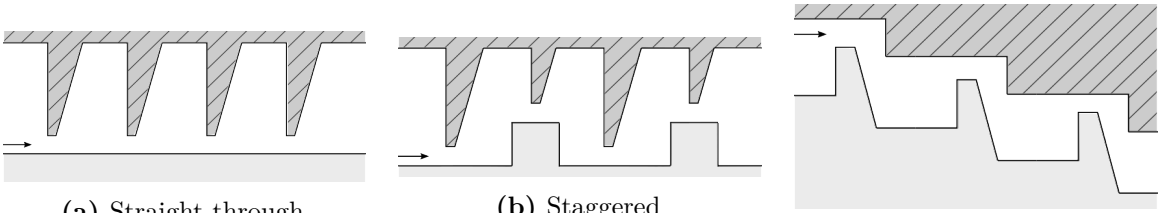

(a) Straight-through **(b)** Staggered **(c)** Stepped

Figure 1.2 – Schematic representation of labyrinth seals with the stator in dashed dark gray and the rotor in solid light gray.

1.1.1 Inflatable Seals

Inflatable seals consist of hyperelastic chambers that expand when pressurized to reduce the clearance size or to close it. Figure 1.3 presents an example of an inflatable seal cross-section in undeformed and deformed configurations. This work studies the application of inflatable seals to CH_4 and CO_2 compressors. The idea is to combine the principle of inflatable seals with labyrinth seals for an adapting seal behavior. One of the advantages of designing inflatable labyrinth seals is to create a seal that can be assembled in the undeformed state and that can obtain minimum leakage in the deformed state according to the concept presented in Fig. 1.4, which could help contain fluid at low velocities. Another possibility would be to use lower gaps during steady-state operation of the rotating machine than during transient conditions, such as start-up.

(a) Undeformed **(b)** Deformed

Figure 1.3 – Example of an inflatable seal cross-section in undeformed and deformed configurations.

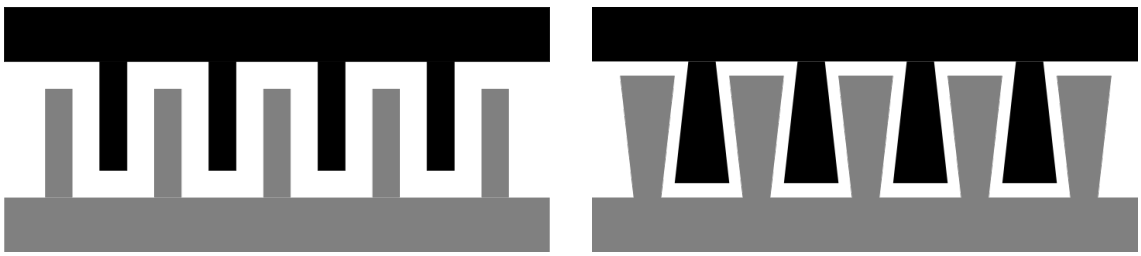

(a) Undeformed **(b)** Deformed

Figure 1.4 – Concept of an inflatable labyrinth seal. The undeformed state can be assembled and the deformed state offers higher leakage reduction.

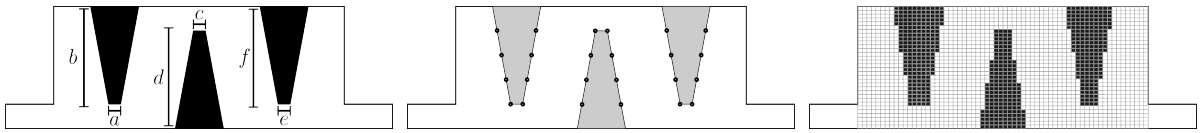

(a) Parametric optimization **(b)** Shape optimization **(c)** Topology optimization

Figure 1.5 – Illustration of optimization approaches for the design of labyrinth seals.

1.1.2 Labyrinth Seal Optimization

Labyrinth seals are applied to turbomachines operating on high pressures and velocities. Therefore, the fluid flow inside these machines presents turbulent effects that must be accounted for when designing labyrinth seals. Also, as the pressure drop within the labyrinth seal is high, it is important to evaluate the mechanical response of the seal in the presence of the flow by considering fluid-structure interaction (FSI). In order to obtain actuated labyrinth seals inspired by inflatable seals, the present work also investigates the possibilities of teeth deformation during assemblage and operation, which could be modeled by considering finite deformation and static pressure loads.

Another characteristic of labyrinth seals is the high number of geometric parameters involved in their design, such as the width and height of each tooth, the number of teeth, the maximum gap between rotor and stator, the angle of each tooth, and others. Therefore, topology optimization is indicated as it is independent of predefined parameters (SOUZA, 2020). Also, it is the most general optimization approach because it does not specify predefined parameters and can potentially obtain the most efficient results. Thus, topology optimization, turbulent flow, finite deformation, and FSI are the main subjects of this research to improve labyrinth seal performance.

1.2 Topology Optimization

The optimization of an engineering component is the process of searching for a design that maximizes its performance given a set of operating conditions. There are different approaches to the optimization process, and they are grouped according to their capabilities of changing the initial design of the component. Figure 1.5 illustrates the approaches for optimizing a labyrinth seal.

The less general approach is parametric optimization, which consists of defining a small set of parameters (such as dimensions or rate of dimensions) as design variables for the optimization algorithm. For example, it is possible to optimize the geometry of the teeth of a labyrinth seal by using each tooth's height and thickness as design variables according to what is presented in Fig. 1.5a.

Shape optimization is a more general approach in which curves or surfaces explicitly parameterize the shape of the component and the coefficients of the parameterization are

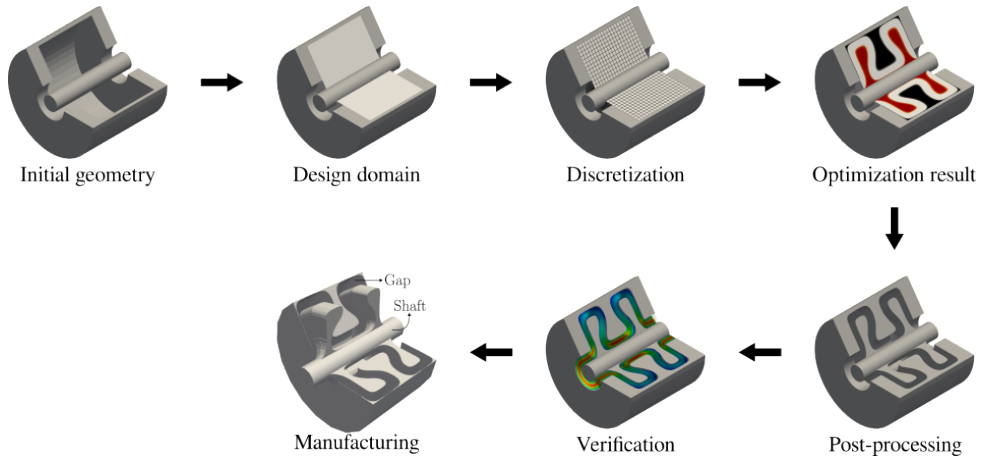

Figure 1.6 – Illustration of the topology optimization process from design to fabrication

used as design variables for the optimization algorithm. For the labyrinth seal example, the teeth can be parameterized by splines and the control points position can be used as design variables according to what is presented in Fig. 1.5b.

The most general approach is topology optimization, which consists of choosing a design domain, dividing it into elements (pixels in 2D and voxels in 3D), and calculating the material of each element. Topology optimization does not impose a predefined topology so that holes can be added or removed during the process. Only the design domain is predefined. The seminal paper of Bendsøe and Kikuchi (1988) introduces the technique and Fig. 1.5c illustrates the approach for the labyrinth seal problem.

The complete topology optimization design cycle involves selecting a design domain in an initial geometry, discretizing the design domain, running the topology optimization algorithm, post-processing the result, verifying the post-processed design, and manufacturing it, as shown in Fig. 1.6. The post-processing step is the translation of the topology optimization result into a physical representation, such as a CAD file. The verification step evaluates the physical representation without the additional topology optimization models. The manufacturing step consists of devising a process to fabricate the design. Additive manufacturing (AM) is commonly used to manufacture topology optimization results because it can achieve complex material distributions.

There are multiple approaches to solving topology optimization problems. The work of Bendsøe and Kikuchi (1988) employed homogenization techniques to model the constitutive behavior of the material (macroscopic properties) in terms of the design variables (microscopic properties). Then, Bendsøe (1989) presented the density-based approach, which consists of assigning a pseudo-density design variable to each element of the discretized design domain and calculating constitutive parameters based on these pseudo-densities. Wang, Wang and Guo (2003) proposed using level-set methods (LSM) in topology optimization. A level set is a set of points where a function has a constant value. Level sets are used to perform computations on curves without having to parameterize them. In Bourdin and

Chambolle (2003), a phase-field approach is introduced to solve design-dependent loads problems. In Xie and Steven (1993), authors propose an evolutionary approach for the topology optimization of structures.

Recently, Sivapuram and Picelli (2018) proposed a new binary approach for topology optimization named "Topology Optimization of Binary Structures" (TOBS). The technique solves a sequence of linearized optimization subproblems based on Taylor's first-order approximation of the objective function and constraints. The key idea of TOBS is using the pseudo-density change as the design variable of the subproblems. The TOBS approach has been chosen for this project's initial approach because it is well-suited for fluid problems (SOUZA et al., 2021), as binary design variables make the interface between solid and fluid well-defined. Also, a well-defined interface helps model the boundary layer in turbulent flows. Then, the continuous design variable approach was also investigated for comparison purposes.

1.2.1 Fluid Flow and Turbulence

Topology optimization applied to fluid flow problems has received considerable attention from the research community and an extensive review on fluid flow and fluid-based problems is provided by Alexandersen and Andreasen (2020). The contributions have considered steady laminar flow, unsteady flow, turbulent flow, and porous media.

Steven, Li and Xie (2000) published the first work addressing fluid flow topology optimization, in which they solve the pipe bend problem by using the Evolutionary Structural Optimization (ESO) approach for an inviscid incompressible flow. Then, in the seminal paper of Borrvall and Petersson (2003), authors introduce an additional term in the momentum equation to account for solid elements, and they minimize the power dissipation in Stokes flow. The material properties parameterization considers two parallel plates and their frictional resistance according to the distance between them. In this model, solid elements are approximated by elements with vanishing distances between plates. Later, Gersborg-Hansen, Sigmund and Haber (2005) extend the work of Borrvall and Petersson (2003) by considering low-to-moderate Reynolds numbers, i.e., the Navier-Stokes equations. The authors investigate the whole of inertia in channel flow optimization. Both Borrvall and Petersson (2003) and Gersborg-Hansen, Sigmund and Haber (2005) recognize the similarities between the obtained equations and the Brinkman-type model of Darcy's law. Also, Guest and Prévost (2006) propose a new formulation that models solid as a porous medium governed by Darcy's flow and fluid with Stokes flow. Authors argue that Darcy's flow can effectively simulate the no-slip condition while the formulation proposed by Borrvall and Petersson (2003) only simulates the no-slip condition.

The work of Othmer (2008) is the first in topology optimization of turbulent flows. The

author derives the continuous adjoint of Navier-Stokes equations and does not consider the influence of turbulence in the sensitivity analysis by invoking the "frozen turbulence" assumption. However, as shown by Zymaris et al. (2009), neglecting the influence of the turbulence variables during the adjoint analysis may result in considerable errors, such as sensitivities with the wrong sign. Then, Kontoleontos et al. (2013) are the first to include turbulence in the sensitivity analysis of topology optimization by introducing penalization terms in the turbulence model equations and following the continuous adjoint approach. They consider the density-based topology optimization with the one-equation Spalart-Allmaras model and corroborate that the "frozen turbulence" assumption may result in incorrect sensitivities. Later, Papoutsis-Kiachagias and Giannakoglou (2014) introduce the wall distance dependence in the sensitivity analysis of Spalart-Allmaras turbulence model through the solution of the Eikonal equation. In Yoon (2016), the author also considers the Spalart-Allmaras turbulence model with a discrete adjoint approach to calculate the sensitivities. In Dilgen et al. (2018), authors use the one-equation Spalart-Allmaras model and the two-equation $k-\omega$ model in the density-based topology optimization of 2D and 3D flow problems. A penalization term similar to the Brinkman model is added to the transport equations to penalize solid regions. They use automatic differentiation to compute the exact sensitivities of the model and also show that the "frozen turbulence" assumption produces inexact sensitivities. In Yoon (2020), the author uses the k-ε model in density-based topology optimization to solve 2D problems using commercial software. The transport equations are also penalized with a term similar to the Brinkman-type model added to the momentum equation.

More recently, Sá et al. (2021a) use the Spalart-Allmaras model with rotation/curvature correction to optimize the impeller of flow machines. The authors also propose using a different Eikonal equation to calculate the wall distance. Then, Picelli et al. (2022) propose trimming the design domain to extract the fluid elements and executing the turbulent fluid flow analysis in a smoothed version of the trimmed fluid domain. The method's advantages are a more accurate prediction of the boundary layer using a mesh based on the physical problem and a reduced computational cost as the fluid volume fraction is reduced. In Alonso et al. (2022), the authors explore the Wray-Agarwal turbulence model for topology optimization. The advantages of this model are related to computational efficiency because it uses a single equation to model turbulence and this equation is independent of the wall distance. For other turbulence closure models, the wall distance calculation would require the solution of a partial differential equation in the best case. In Kubo et al. (2021), the authors propose a level-set-based topology optimization algorithm for turbulent flow using the immersed boundary method. The topological derivative is used for sensitivity analysis and a reaction-diffusion equation is used to update the level-set function. Only two-dimensional problems are solved and the "frozen turbulence" assumption is invoked.

This work considers the topology optimization of labyrinth seals operating with CO_2 under turbulent incompressible flow, that is, low Mach numbers (less than 0.3) and small pressure changes. The incompressibility hypothesis is reasonable for many operation conditions of labyrinth seals.

1.2.2 Finite Deformation of Solids

Most works in structural topology optimization consider small displacement and linear constitutive behavior. Nevertheless, considerable progress has been made in using nonlinear kinematics and material models. The first work to address these nonlinearities in topology optimization is presented by Jog (1996), where the author applies the perimeter method to nonlinear thermoelasticity problems. However, the interfaces and holes of his results are not clearly defined. Then, Bruns and Tortorelli (1998) perform topology optimization using nonlinear kinematics and the St. Venant-Kirchhoff constitutive model. Still, their results present intermediate densities and are equivalent to results obtained for small displacements and linear constitutive behavior.

Buhl, Pedersen and Sigmund (2000) are the first to present truly nonlinear results in topology optimization with finite deformation. Although the constitutive behavior is assumed to be linear (small strains), the kinematics is nonlinear, and the authors show that the results are different from pure linear analysis after a certain load magnitude. They describe the instabilities associated with low-density elements and the fragile designs that may be obtained using end-compliance as the objective function. Also, they propose a relaxation to the convergence criterion of the equilibrium iterations in which nodes surrounded by void elements are not considered in the convergence criterion of Newton's method iterations. Then, Pedersen, Buhl and Sigmund (2001) extend the approach to design compliant mechanisms under large displacements and small strains. They introduce two objective functions appropriate for nonlinear analysis. One objective function transfers the motion from the input to the output port, and the other is devised for path generation. Later, Bruns and Tortorelli (2001) present nonlinear topology optimization results using the St.Venant-Kirchhoff constitutive model and introduce the idea of applying the power-law material interpolation to the strain energy density function. The formulation is still limited to small strains because the St.Venant-Kirchhoff material model has little practical use beyond small strains (BONET; WOOD, 2008).

Bruns and Tortorelli (2003) propose a method for removing and reintroducing low-density elements to avoid their instabilities. The idea is to remove and reintroduce elements whose pseudo-density is below or above a predefined threshold. The reintroduction is enabled by the density filter, which allows pseudo-density changes of removed elements by increasing the design variable of other elements in the filter's kernel. Removing the elements reduces the overall computation time, which is interesting when solving 3D problems. Later, the

element removal and reintroduction approach is used by Bruns and Sigmund (2004) to design mechanisms exhibiting snap-through behavior, although topology optimization only partially automates the design process.

Yoon and Kim (2005) propose a new topology optimization approach to avoid the instabilities of low-density elements in finite deformation. All the domain is kept solid during the topology optimization process, and an element connectivity parameterization based on zero-length links is introduced. The design variables control the stiffness of the links, with high stiffness indicating connection and low stiffness indicating disconnection. Only geometrical nonlinearities are addressed.

The work of Kemmler, Lipka and Ramm (2005) highlights that the concept of the stiffest structure loses its uniqueness when considering nonlinear kinematics. Therefore, using different objective functions such as strain energy, end compliance, and end stiffness produces different results.

Klarbring and Strömberg (2012) consider non-zero prescribed displacements during topology optimization for nonlinear stiffness. The authors emphasize the importance of using the potential energy as the objective function for obtaining stiffness when considering geometrical and material nonlinearities and non-zero prescribed displacements. They explore seven hyperelastic strain energy functions and highlight the bad performance of St. Venant-Kirchhoff material model in topology optimization due to its unphysical behavior under compression.

The work of Lahuerta et al. (2013) applies a polyconvex material model to stabilize the low-density elements. The authors also propose a relaxation function to solve the problems associated with excessive distortion of the finite elements. Combining the polyconvex material model and the relaxation function enables topology optimization without removing low-density finite elements and the associated internal forces. A Neo-Hookean material model is used and substantial differences are observed in relation to results obtained with the St.Venant-Kirchhoff model.

Wang et al. (2014) propose a new energy interpolation scheme to stabilize low-density elements. The idea is to interpolate the strain energy function between the desired nonlinear model and the linear strain function. Also, a smooth Heaviside projection with a low threshold and high steepness separates regions modeled by nonlinear and linear analysis. The formulation is applied to minimum compliance and compliant mechanisms problems.

More recently, more complex formulations have been reported in the context of topology optimization with finite deformation. De Leon, Gonçalves and Souza (2020) use a stress constraint in density-based topology optimization considering geometrical and material nonlinearities. The stress constraint successfully avoids the appearance of hinges and the nonlinear material model helps stabilize low-density regions, besides improving the accuracy

of stress calculation. In Silva, Beck and Sigmund (2020), authors consider stress constraint and manufacturing uncertainty in topology optimization involving finite deformation. Two objective functions are studied under this framework: maximum output displacement and path following displacement. Silva et al. (2020) optimize the fiber orientation of composite material by considering geometrical and material nonlinearities. The constitutive behavior is described with a Neo-Hookean model and the Normal Distribution of Fiber Optimization method is applied. Zhang, Chi and Zhao (2021) design hyperelastic structures reinforced by nonlinear-anisotropic fibers under large deformation. A material interpolation scheme is proposed to incorporate the contributions of the matrix and fiber phases into the stored energy density function.

1.2.3 Fluid-Structure Interaction

Fluid-structure interaction is the coupling of fluid and solid equations when there is interdependence between the fluid flow and the structural motion. The coupling occurs at the interface between the fluid and solid domains, and it is classified as weak or strong, depending on the characteristics of the interaction. If the solid deformations and the fluid loads are large, it is necessary to account for both the solid deformations when solving the fluid flow equations and the fluid loads when solving the structural equations. In this case, the FSI is strongly coupled (or two-way coupled). However, if the solid deformations are small and the fluid loads are large, the fluid flow equations may be solved independently of the solid equations and the velocity and pressure are used to calculate the input loads to the structural equations. In this case, the FSI is classified as weak (or one-way) coupling. Also, if there is finite deformation, and the fluid loads are negligible (e.g., low Reynolds flow), the solid equations may be solved without taking into account the fluid loads and the displacements obtained are used as input to solve the fluid equations, which is another example of weak (or one-way) coupling.

There are two strategies for solving the system of fluid and solid equations. The first strategy is to solve the fluid and solid equations sequentially, which is known as the partitioned or staggered approach. The second strategy is to solve the fluid and solid equations simultaneously, which is known as the monolithic or simultaneous approach. The staggered approach enables the use of existing solvers and it is naturally applied to weakly coupled problems. The staggered approach may also be used for strongly coupled problems at the cost of stability. The monolithic approach is more stable and accurate; however, it requires the development of a new solver.

When optimizing multi-physics problems involving FSI, the problem can be classified according to which parts are allowed to change during the optimization (JENKINS; MAUTE, 2015). If only the interface between the solid and the fluid changes, the problem is classified as a “wet” optimization problem. If only the internal part of the structure is

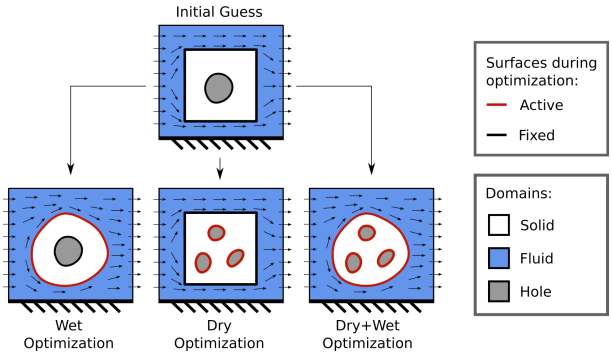

Figure 1.7 – Classification of topology optimization approaches according to Jenkins and Maute (2015).

allowed to change during the optimization, the problem is classified as a "dry" optimization problem. If both the interface and the topology of the structure are allowed to change, the optimization problem is classified as a "dry+wet" problem. Figure 1.7 illustrates and summarizes this classification.

In density-based topology optimization, the interface between solid and fluid is not clearly defined and changes during optimization. To address this problem, Yoon (2010) developed a formulation based on a unified domain for solid and fluid. The solid and fluid equations are written with respect to the reference configuration by using a change of coordinates based on the deformation gradient. The unified approach introduces an extra computational effort because the solid and fluid equations are solved over the whole fixed domain. Later, Yoon (2014) extended his work by considering stress-based topology optimization to minimize the volume. A qp-relaxation is proposed to solve the problem. The final stress constraint used is a global p-norm stress constraint due to instabilities with local constraints.

Kreissl et al. (2010) designed microfluidic devices through an approach that includes topology optimization with FSI and large deformations. The fluid loads on the structure are neglected due to the low velocities, leading to a one-way FSI coupling. The fluid flow equations are solved with the Lattice Boltzmann method (LBM) and the structure equations are solved with nonlinear finite element method (FEM). Other design variables are used to optimize the thickness of the structural layers, the support locations, and the layout of the active material.

One idea explored to avoid unclear interfaces is to employ discrete design variables. In this context, Picelli, Vicente and Pavanello (2015) extended the bi-directional evolutionary structural optimization (BESO) method to handle design-dependent pressure loads by coupling Laplace and Cauchy equations for fluid and solid elements, respectively. The pressure loads are transmitted to the structure surfaces; however, the structure motion does not affect Laplace's equation, leading to a one-way coupling. Later, Picelli, Vicente and Pavanello (2017) extended the work to include the steady-state incompressible Navier-Stokes equations in their BESO formulation.

Jenkins and Maute (2015) use the level-set method (LSM) to address "dry" topology optimization of FSI problems. The authors use a monolithic solver based on the extended finite element method (XFEM) for linear elasticity equations and a stabilized finite element method for incompressible Navier-Stokes equations. Then, in Jenkins and Maute (2016), the authors extend their method to dry and wet topology optimization. They optimize a bio-prosthetic valve and solve the wall example of Yoon (2010).

Lundgaard et al. (2018) revisit the unified density-based topology optimization formulation proposed by Yoon (2010). Their work also introduces two new flow mechanism problems that can be used as benchmark problems in future research on topology optimization of FSI problems.

Silva et al. (2022) extended the TOBS-GT method to FSI problems with large deformations. The Arbitrary Lagrangian Eulerian (ALE) approach is used to couple the fluid and structural equations, which are described by the steady-state incompressible Navier-Stokes and the Cauchy equation. The St.Venant-Kirchhoff constitutive behavior is considered with SIMP interpolation to the Young modulus. A linear interpolation is applied to the stress coupling.

Høghøj et al. (2023) combine shape and topology optimization to design the external shape and the internal topology of wings. The design goal is to minimize drag while constraining the maximum lift and the minimum compliance. The authors use it to calculate the aerodynamic response and linear elastic equations for the structural response in a one-way coupling.

Yoon (2023) reports transient FSI topology optimization results by adding inertial terms to the formulation described in Yoon (2010). The inlet velocity is varied in time.

1.3 Motivation

Improving labyrinth seal performance reduces global warming and improves industrial efficiency by reducing the leakage in compressors operating on GHGs. Although the emission for a single turbomachine is low, studies show that around 8% of CH_4 emission during the processing of natural gas comes from machinery leakage (EPA, 2011). This expressive contribution of turbomachines to GHGs emissions is caused by the large number of compressors and turbines used in the industry. Therefore, optimized labyrinth seals are of great interest, and methodologies to design them must be investigated. As topology optimization is the most general optimization approach, it must be studied for labyrinth seals. However, the topology optimization of labyrinth seals presents additional requirements, such as the simultaneous design of solids with different velocities, the control of the minimum gap size, and the avoidance of free-floating solid islands.

There are also practical motivations for developing this work. According to Flitney (2014), developments in material science and design techniques are extending the performance of seals in most application areas. As this work is inserted in the context of design techniques for labyrinth seals, it can improve the performance of these components. However, this task presents considerable challenges because the optimization of dynamic seals must seek minimum leakage and minimum friction/wear, which are exclusive objectives (FLITNEY, 2014). One of the current approaches to obtain a better compromise between these exclusive objectives is to use polymeric materials, and this work encompasses the study of these materials in topology optimization.

The scientific motivations behind this work are the challenges and open research opportunities presented in the investigated fields. According to Deaton and Grandhi (2013), multiphysics design is one of the trending topics in topology optimization. Also, according to the review of Alexandersen and Andreasen (2020), section 4.9, the works reviewed by authors on wet topology optimization of FSI remain restricted to small deformation despite the high potential of large deformations in contexts such as biomechanical. Even further, few papers on topology optimization consider turbulence according to Alexandersen and Andreasen (2020). Therefore, there is great scientific interest in investigating large deformations in the context of fluid-structure interaction with turbulence in topology optimization. This scientific interest is also justified by the potential application of these models to the optimized design of pumps and fluidic diodes.

1.4 Objectives

The general objective of this thesis is to use topology optimization to design labyrinth seals. The specific objectives of this research are:

- To design labyrinth seals with topology optimization by considering turbulent flow;
- To develop topology optimization algorithms for straight-through, staggered and stepped labyrinth seal configurations. The staggered and stepped arrangements require:
  - the simultaneous design of the stator and rotor parts (i.e., solids with different velocities);
  - the control of the minimum gap size;
  - the avoidance of free-floating solid islands;
- To explore the use of binary design variables in the topology optimization of labyrinth seals through the TOBS approach;
- To include FSI during topology optimization of labyrinth seals;
- To explore the combination of the concepts of labyrinth seals and inflatable seals;
- To develop topology optimization algorithms with large displacement and design-dependent

loads.

1.5 Scientific Contributions

The scientific contributions of this work are:

- The development of topology optimization formulations for the simultaneous design of the stator and rotor of labyrinth seals;
- The development of techniques to control the minimum gap size during the topology optimization of labyrinth seals;
- The investigation of two constraints to avoid free-floating islands of solid elements during the topology optimization of labyrinth seals:
  - Virtual temperature method (VTM);
  - Virtual fluid-structure interaction (VFSI);
- The inclusion of turbulent flow during the topology optimization of labyrinth seals;
- The development of topology optimization formulations with design-dependent pressure loads and large deformations.

Six journal articles have been published:

1. "Topology optimization of turbulent fluid flow via the TOBS method and a geometry trimming procedure" (PICELLI et al., 2022);
2. "Topology optimisation for rotor-stator fluid flow devices" (MOSCATELLI et al., 2022);
3. "Hybrid geometry trimming algorithm based on Integer Linear Programming for fluid flow topology optimization" (MOSCATELLI et al., 2022);
4. "Integer programming topology optimization for subsonic compressible flows with geometry trimming" (MAFFEI et al., 2023);
5. "Pure-displacement formulation and bulk modulus propagation for topology optimization with pressure loads" (MOSCATELLI et al., 2023);
6. "Topology optimization of labyrinth seals using interface identification techniques" (MOSCATELLI et al., 2024).

The first and third publications of the list above are not addressed directly in this thesis. The third publication is briefly presented in Appendix A. Also, this work builds upon previous research developed in our laboratory, and it is important to clarify the novelties presented in this thesis. Alonso et al. (2018) introduced the 2D swirl flow model in topology optimization, which is extended here to the simultaneous optimization of the rotor and stator components. Souza et al. (2021) adapted the TOBS approach to fluid flow problems and designed labyrinth seals using the diodicity objective function (SOUZA, 2020). This work proposes new techniques to impose a minimum gap between rotating

and stationary parts, which allows the use of the head loss objective function instead of the diodicity. Sá et al. (2021b) introduced a continuous boundary propagation model capable of assigning different velocities to rotor and stator elements. Here, the differences in velocity are modeled with two Brinkman penalization terms. These differences are discussed in detail in Chapter 2.

1.6 Document Outline

This thesis is organized as follows: Chapter 2 presents the theory of fluid flow modeling, nonlinear solid modeling, FSI, and topology optimization. First, the Navier-Stokes equations are discussed, and the Reynolds average is applied to obtain the formulation for turbulent flow analysis. The solid modeling encompasses the motion of linear elastic and hyperelastic mediums. Then, the approaches for solving FSI problems are discussed, and a formulation suitable for density-based topology optimization is presented. Finally, the TOBS and continuous approaches for topology optimization are described with the modifications to design labyrinth seals. Chapter 3 describes the algorithms and tools used for the numerical solution of the topology optimization problems. A flowchart illustrates the optimization algorithm, and each optimization step is discussed in detail. The main software components are described, and a rationale for their utilization is provided. Chapter 4 presents the topology optimization results of labyrinth and inflatable seals. The labyrinth seal results are grouped according to the flow regime (laminar or turbulent) and the design variable type (discrete or continuous). All labyrinth seal arrangements (Fig. 1.2) are explored. The inflatable seal section begins with the solution of benchmark problems of structural optimization to verify the consistency of the proposed formulations for pressure loads with finite deformation. Then, the inflatable seals are optimized by prescribing movements to the seal. Chapter 5 summarizes the discussions and conclusions of this work, and presents opportunities for future work.

2 THEORETICAL FORMULATION

The topology optimization of labyrinth seals requires the analysis of the flow in the cavity of the seals, which is generally turbulent. Also, the fluid interacts with walls at different velocities because the labyrinth seal is partly mounted on the stator and rotor, which have different velocities. In addition, the solid walls must resist the fluid forces without large deformations or instabilities during operation. Therefore, the FSI analysis must also be part of the topology optimization of labyrinth seals. Also, the combination of the concepts of labyrinth seals and inflatable seals demands FSI and the analysis of inflatable seals requires modeling solid with finite strain theory as the seal undergoes large deformation from the initial configuration to the actuated configuration.

In this work, two topology optimization approaches are proposed to design labyrinth seals with walls at different velocities (i.e., the stator and rotor of the labyrinth seals are designed simultaneously). These approaches are investigated for laminar and turbulent flows. In the latter case, the Reynolds Averaged Navier-Stokes (RANS) equations are solved with the Spalart-Allmaras closure model. An initial investigation of the topology optimization of labyrinth seals with FSI is presented by defining a connectivity constraint based on structural compliance due to FSI loads. The effectiveness of this constraint is compared to the virtual temperature method (VTM) of Liu et al. (2015). The finite deformation formulation is used to solve topology optimization problems with large deformations and pressure loads, which is an initial step toward designing inflatable labyrinth seals with topology optimization.

Then, this section presents the modeling of incompressible fluid flow in laminar and turbulent regimes with the additional Darcy terms necessary for the topology optimization of labyrinth seals. Then, the solid equations with nonlinear geometric and material behavior are presented, and the coupling between fluid and solid equations is discussed. The topology optimization problem is stated, and the TOBS and continuous approaches are presented. Finally, the proposed topology optimization approaches to design labyrinth seals are presented. Regarding the analysis, the focus is to present the weak form of the equations because they are the starting point for obtaining finite element equations, and they are the input of the FEniCS library, which is used for numerical implementation and described in Section 3.

2.1 Fluid Flow Modeling

2.1.1 Incompressible Navier-Stokes Equations

The fluid flow equations are stated with an Eulerian description in the reference configuration ${}^0\Omega$, assuming that the steady-state flow is incompressible and Newtonian. The solid bodies are modeled as a porous medium through a Darcy term. Then, the complete description of the fluid flow problem is given by

$$\begin{aligned} &(\boldsymbol{v}\cdot\nabla)\,\boldsymbol{v} = \nabla\cdot\boldsymbol{\sigma}_{\mathrm{f}}(\nu,\,\boldsymbol{v},\,p)\underbrace{-\kappa(m)\,\boldsymbol{v}}_{\text{Darcy term}} && \text{in } {}^0\Omega \\ &\nabla\cdot\boldsymbol{v} = 0 && \text{in } {}^0\Omega \\ &\boldsymbol{v} = \boldsymbol{v}^* && \text{on } {}^0\Gamma_{\mathrm{v}} \\ &\boldsymbol{\sigma}_{\mathrm{f}}(\nu,\,\boldsymbol{v},\,p)\,\boldsymbol{n} = \boldsymbol{t}^* && \text{on } {}^0\Gamma_{\mathrm{n}} \end{aligned} \tag{2.1}$$

where $\boldsymbol{v}$ is the velocity, p is the kinematic pressure, ν is the kinematic viscosity, κ is the inverse permeability function of the Darcy term (BORRVALL; PETERSSON, 2003), $\boldsymbol{t}^*$ are the surfaces loads, $\boldsymbol{v}^*$ are the prescribed velocities, and $\boldsymbol{n}$ is the outward normal vector. The Cauchy stress tensor for a Newtonian fluid is given by

$$\boldsymbol{\sigma}_{\mathrm{f}}(\nu,\,\boldsymbol{v},\,p) = \nu\left(\nabla\boldsymbol{v} + \nabla\boldsymbol{v}^T\right) - p\,\boldsymbol{I} \tag{2.2}$$

where $\boldsymbol{I}$ is the identity tensor. The behavior of the fluid flow may be inferred by the Reynolds number (Re), which is a dimensionless quantity calculated as follows

$$\mathrm{Re} = \frac{V_{\mathrm{C}}\,L_{\mathrm{C}}}{\nu} \tag{2.3}$$

with V_{C} and L_{C} denoting the characteristic velocity and length scales of the problem, respectively. In this work, L_{C} is taken as half of the inlet size and V_{C} as the maximum inlet velocity.

The fluid flow problem described by Eq. 2.1 is general and abstract. Therefore, it is convenient to specialize it for the labyrinth seal problem studied in this work. In general, labyrinth seals present axisymmetry to reduce the instabilities associated with high angular velocities. The axisymmetry may be used to model the labyrinth seal in a 2D cylindrical reference frame, as shown in Fig. 2.1a, allowing the representation of three velocity fields (radial, tangential, and axial) in a 2D domain.

The boundaries of the labyrinth seal are divided into inlet, outlet, rotor and stator, with the velocity being known at the inlet, stator and rotor surfaces. Then, the Dirichlet surface ${}^0\Gamma_{\mathrm{v}}$ of Eq. 2.1 is divided in ${}^0\Gamma_{\mathrm{inlet}}$, ${}^0\Gamma_{\mathrm{stator}}$, and ${}^0\Gamma_{\mathrm{rotor}}$. A velocity profile $\boldsymbol{v}_{\mathrm{in}}$ is

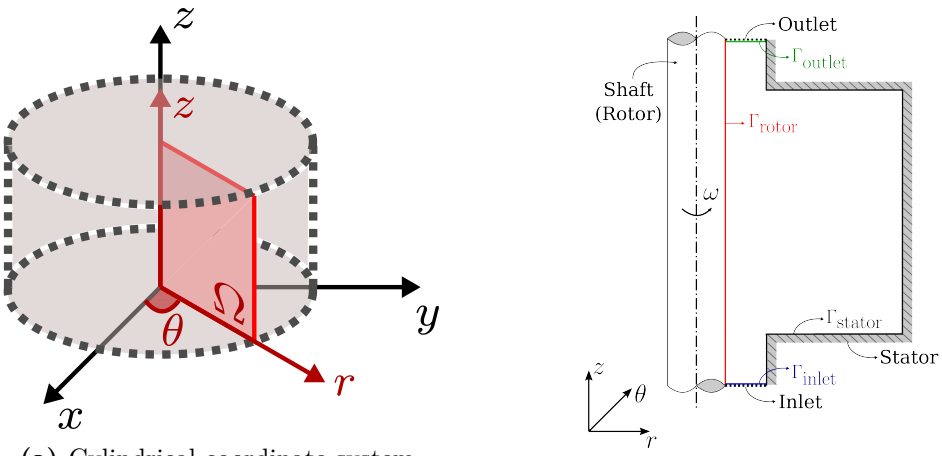

(a) Cylindrical coordinate system

(b) Fluid flow problem

Figure 2.1 – Illustration of the labyrinth seal modeling in a 2D axisymmetric reference frame.

prescribed to the inlet surface ${}^0\Gamma_{\text{inlet}}$, the no-slip condition is imposed to the stator surface ${}^0\Gamma_{\text{stator}}$, and a velocity proportional to the radial coordinate r and to the shaft angular velocity ω_{r} is assigned to the rotor surface ${}^0\Gamma_{\text{rotor}}$. The traction surface ${}^0\Gamma_{\text{n}}$ of Eq. 2.1 comprises only the outlet surface ${}^0\Gamma_{\text{outlet}}$, which is associated with a free stress condition ($\boldsymbol{t}^* = 0$). The Neumann boundary condition involving the normal component of the stress tensor is the correct way of applying pressure boundary conditions according to Gresho and Sani (1987). Therefore, the Navier-Stokes equations for the labyrinth seal are given by

$$
\begin{aligned}
&(\boldsymbol{v}\cdot\nabla)\,\boldsymbol{v} - \nabla\cdot\boldsymbol{\sigma}_{\text{f}} + \underbrace{\kappa(m_{\text{s}})\boldsymbol{v}}_{\text{stator}} + \underbrace{\kappa(m_{\text{r}})(\boldsymbol{v}-\omega_{\text{r}}\,r\,\boldsymbol{e}_\theta)}_{\text{rotor}} = 0 \quad && \text{in } {}^0\Omega \\
&\nabla\cdot\boldsymbol{v} = 0 && \text{in } {}^0\Omega \\
&\boldsymbol{v} = \boldsymbol{v}_{\text{in}} && \text{on } {}^0\Gamma_{\text{inlet}} \\
&\boldsymbol{v} = \boldsymbol{0} && \text{on } {}^0\Gamma_{\text{stator}} \\
&\boldsymbol{v} = \omega_{\text{r}}\,r\,\boldsymbol{e}_\theta && \text{on } {}^0\Gamma_{\text{rotor}} \\
&\boldsymbol{\sigma}_{\text{f}}\boldsymbol{n} = \boldsymbol{0} && \text{on } {}^0\Gamma_{\text{outlet}}
\end{aligned}
\tag{2.4}
$$

where m_{s} and m_{r} describe the stator and rotor material distributions, respectively. Two Darcy terms are necessary because the velocities of the stator and rotor are different (MOSCATELLI et al., 2022). Note that m_{s} and m_{r} must not overlap for the consistency of Eq. 2.4. Therefore, any topology optimization algorithm that uses Eq. 2.4 must satisfy the condition that m_{s} and m_{r} are not overlapping during the optimization.

2.1.2 Reynolds-Averaged Navier-Stokes (RANS) Equations

Turbulent flow is challenging to simulate because it presents unsteady and non-periodic motion, strong dependence on initial and boundary conditions (chaotic behavior), and contains a wide range of scales (size of the eddies) according to Pope (2000). There are

three main approaches to simulate turbulent flow: direct numerical simulation (DNS), large eddy simulation (LES), and Reynolds-Averaged Navier-Stokes (RANS). In many applications, the details provided by DNS or even LES are not required for design purposes, and time-averaged quantities are appropriate for engineering practice. Therefore, this work employs the RANS approach due to its computational cost advantages.

The RANS approach to simulate turbulent fluid flow solves the transport equations to find the time-averaged values of the state variables. The Reynolds average applied to an arbitrary scalar field ϕ is given by

$$\overline{\phi}(\boldsymbol{x}) = \lim_{T\to\infty} \int_0^T \phi(\boldsymbol{x},\, t)\, dt \tag{2.5}$$

The Reynolds average separates flow variables in average $\overline{\phi}$ and fluctuating components ϕ'. This separation is known as Reynolds decomposition, and its application to velocity and pressure fields gives

$$\begin{aligned} \boldsymbol{v}(\boldsymbol{x},\, t) &= \overline{\boldsymbol{v}}(\boldsymbol{x}) + \boldsymbol{v}'(\boldsymbol{x},\, t) \\ p(\boldsymbol{x},\, t) &= \overline{p}(\boldsymbol{x}) + p'(\boldsymbol{x},\, t) \end{aligned} \tag{2.6}$$

By taking the mean of problem 2.1 and substituting the Reynolds decomposition of velocity and pressure, the RANS equations are obtained

$$\begin{aligned} &(\overline{\boldsymbol{v}} \cdot \nabla)\, \overline{\boldsymbol{v}} = \nabla \cdot \left[\boldsymbol{\sigma}_{\mathrm{f}}(\nu,\, \overline{\boldsymbol{v}},\, \overline{p}) - \overline{\boldsymbol{v}' \otimes \boldsymbol{v}'}\right] - \kappa(m)\, \overline{\boldsymbol{v}} && \text{in } {}^0\Omega \\ &\nabla \cdot \overline{\boldsymbol{v}} = 0 && \text{in } {}^0\Omega \\ &\overline{\boldsymbol{v}} = \overline{\boldsymbol{v}^*} && \text{on } {}^0\Gamma_{\mathrm{v}} \\ &\boldsymbol{\sigma}_{\mathrm{f}}(\nu,\, \overline{\boldsymbol{v}},\, \overline{p})\, \boldsymbol{n} = \overline{\boldsymbol{t}^*} && \text{on } {}^0\Gamma_{\mathrm{n}} \end{aligned} \tag{2.7}$$

2.1.3 Turbulence Modeling

The problem 2.7 is open because the tensor $\overline{\boldsymbol{v}' \otimes \boldsymbol{v}'}$, known as the Reynolds stress, depends on the fluctuating components of the velocity. There are multiple ways of closing the problem, such as the Boussinesq hypothesis or Reynolds stress transport models. This work uses the Boussinesq hypothesis because it is less computationally expensive.

The first step to define the Boussinesq hypothesis is to separate the Reynolds stress into isotropic and deviatoric components. In fact, only the deviatoric stress components effectively transport momentum (POPE, 2000). By defining the turbulent kinetic energy k as

$$k = \overline{\boldsymbol{v}' \cdot \boldsymbol{v}'} \tag{2.8}$$

the Reynolds stress may be decomposed into isotropic and deviatoric parts. According to the Boussinesq hypothesis, the deviatoric part may be written as the product of a

turbulent viscosity ν_{T} by the strain rate of the mean velocity. Therefore

$$\overline{\boldsymbol{v}' \otimes \boldsymbol{v}'} = \underbrace{\frac{2}{3} k \boldsymbol{I}}_{\substack{\text{isotropic} \\ \text{part}}} + \underbrace{\nu_{\mathrm{T}} \left(\nabla \overline{\boldsymbol{v}} + \nabla \overline{\boldsymbol{v}}^{T} \right)}_{\substack{\text{deviatoric part with} \\ \text{Boussinesq hypothesis}}} \tag{2.9}$$

By incorporating the isotropic part of the stress tensor in the pressure and by considering an effective viscosity defined as $\nu_{\mathrm{eff}} = \nu + \nu_{\mathrm{T}}$, the RANS equations may be written as

$$\begin{aligned}
&(\overline{\boldsymbol{v}} \cdot \nabla)\, \overline{\boldsymbol{v}} = \nabla \cdot \boldsymbol{\sigma}_{\mathrm{f}}(\nu_{\mathrm{eff}},\, \overline{\boldsymbol{v}},\, \overline{p}) - \kappa(m)\, \overline{\boldsymbol{v}} && \text{in } {}^{0}\Omega \\
&\nabla \cdot \overline{\boldsymbol{v}} = 0 && \text{in } {}^{0}\Omega \\
&\overline{\boldsymbol{v}} = \overline{\boldsymbol{v}^{*}} && \text{on } {}^{0}\Gamma_{\mathrm{v}} \\
&\boldsymbol{\sigma}_{\mathrm{f}}(\nu_{\mathrm{eff}},\, \overline{\boldsymbol{v}},\, \overline{p})\, \boldsymbol{n} = \overline{\boldsymbol{t}^{*}} && \text{on } {}^{0}\Gamma_{\mathrm{n}}
\end{aligned} \tag{2.10}$$

The problem 2.10 is still open because there are three unknowns (the mean velocity, the mean pressure, and the turbulent viscosity) and two equations (the momentum equation and the continuity equation). This issue may be solved with the introduction of turbulence closure models. Also, problem 2.10 may be adapted to the labyrinth seal design following the same procedure to obtain problem 2.4.

2.1.4 Spalart-Allmaras Turbulence Model

The Spalart-Allmaras model is a one-equation turbulence closure model based on empiricism and dimensional analysis (SPALART; ALLMARAS, 1992). The model was designed for aerodynamic flows, such as transonic flow over airfoils with boundary layer separation (POPE, 2000). The model is computationally simpler than two-equation models, presenting cost and ease of use advantages. Also, according to Bardina, Huang and Coakley (1997), the Spalart-Allmaras model is even more accurate than the $k - \omega$ and $k - \varepsilon$ for coarser meshes near the wall, what is attractive for topology optimization when no remeshing is applied.

There are variations of Spalart-Allmaras turbulence model and the version used in this work introduces a transport equation for an auxiliary kinematic turbulent viscosity $\tilde{\nu}$ (YOON, 2016; ALONSO; RODRIGUEZ; SILVA, 2021), which is related to the actual kinematic turbulent viscosity ν_{T} by the following equation

$$\nu_{\mathrm{T}} = f_{\mathrm{v1}} \tilde{\nu} \tag{2.11}$$

in which the damping function f_{v1} is given by

$$f_{\mathrm{v1}} = \frac{\chi^{3}}{\chi^{3} + {c_{\mathrm{v1}}}^{3}}, \quad \chi = \frac{\tilde{\nu}}{\nu}, \quad c_{\mathrm{v1}} = 7.1 \tag{2.12}$$

Then, the steady-state and incompressible transport equation for the Spalart-Allmaras model considered in this work is

$$\underbrace{\overline{\boldsymbol{v}} \cdot \nabla \tilde{\nu}}_{\text{Convection}} = \underbrace{\nabla \cdot \left(\frac{\nu + \tilde{\nu}}{\sigma_{\tilde{\nu}}} \nabla \tilde{\nu} \right)}_{\substack{\text{Conservative} \\ \text{diffusion}}} + \underbrace{\frac{c_{\text{b2}}}{\sigma_{\tilde{\nu}}} \nabla \tilde{\nu} \cdot \nabla \tilde{\nu}}_{\substack{\text{Non-conservative} \\ \text{diffusion}}} + \underbrace{c_{\text{b1}} \tilde{W} \tilde{\nu}}_{\text{Production}} - \underbrace{c_{\text{w1}} f_{\text{w}} \left(\frac{\tilde{\nu}}{l_{\text{w}}} \right)^2}_{\text{Destruction}} - \underbrace{\lambda_{\tilde{\nu}} \kappa_{\tilde{\nu}}(m) \tilde{\nu}}_{\substack{\text{Absorption in} \\ \text{the solid}}} \tag{2.13}$$

in which the parameters are

$$\boldsymbol{W} = \frac{1}{2} \left(\nabla \overline{\boldsymbol{v}} - \nabla \overline{\boldsymbol{v}}^T \right), \quad W_{\text{m}} = \sqrt{\boldsymbol{W} : \boldsymbol{W}}, \quad \tilde{W} = \max \left[W_{\text{m}} + \frac{\tilde{\nu}}{{\kappa_{\text{vk}}}^2 {l_{\text{w}}}^2} f_{\text{v2}},\, f_{\Omega} W_{\text{m}} \right], \tag{2.14}$$

$$f_{\text{v2}} = 1 - \frac{\chi}{1 + \chi f_{\text{v1}}}, \quad f_{\text{w}} = g_{\tilde{\nu}} \left(\frac{1 + {c_{\text{w3}}}^6}{{g_{\tilde{\nu}}}^6 + {c_{\text{w3}}}^6} \right), \quad g_{\tilde{\nu}} = r_{\text{i}} + c_{\text{w2}} \left({r_{\text{i}}}^6 - r_{\text{i}} \right), \tag{2.15}$$

$$r_{\text{i}} = \min \left[\frac{\tilde{\nu}}{\tilde{W}_{\text{r}} {\kappa_{\text{vk}}}^2 {l_{\text{w}}}^2},\, 10 \right], \quad \tilde{W}_{\text{r}} = \max \left[\tilde{W},\, 10^{-6} \right] \tag{2.16}$$

and the turbulence constants are

$$c_{\text{b1}} = 0.1355, \quad c_{\text{b2}} = 0.6220, \quad \sigma_{\tilde{\nu}} = \frac{2}{3}, \quad f_{\Omega} = 0.3, \quad \kappa_{\text{vk}} = 0.41 \tag{2.17}$$

$$c_{\text{w1}} = \frac{c_{\text{b1}}}{{\kappa_{\text{vk}}}^2} + \frac{1 + c_{\text{b2}}}{\sigma_{\tilde{\nu}}}, \quad c_{\text{w2}} = 0.3, \quad c_{\text{w3}} = 2 \tag{2.18}$$

The destruction term of the Spalart-Allmaras model depends on the distance to the wall, which changes during topology optimization as the material distribution is modified. This work calculates the wall distance by solving a modified Eikonal equation including absorption term to model the solid (YOON, 2016). The corresponding boundary value problem is given by

$$\begin{aligned}
&\nabla \mathcal{G} \cdot \nabla \mathcal{G} + \sigma_{\text{w}} \mathcal{G} \left(\nabla^2 \mathcal{G} \right) = (1 + 2\sigma_{\text{w}}) \mathcal{G}^4 + \kappa_{\mathcal{G}}(m)(\mathcal{G} - \mathcal{G}_0) && \text{in } {}^0\Omega \\
&\nabla \mathcal{G} \cdot \boldsymbol{n} = 0 && \text{on } {}^0\Gamma_{\text{inlet}} \cap {}^0\Gamma_{\text{outlet}} \\
&\mathcal{G} = \mathcal{G}_0 && \text{on } {}^0\Gamma_{\text{stator}} \cap {}^0\Gamma_{\text{rotor}}
\end{aligned} \tag{2.19}$$

where $\mathcal{G}$ is the reciprocal wall distance, $\mathcal{G}_0$ is a reference value for the reciprocal wall distance, and σ_{w} is a relaxation factor. In this work, $\mathcal{G}_0$ is the inverse of the maximum mesh element size and $\sigma_{\text{w}} = 0.1$. Then, the wall distance is given by

$$l_{\text{w}} = \frac{1}{\mathcal{G}} - \frac{1}{\mathcal{G}_0} \tag{2.20}$$

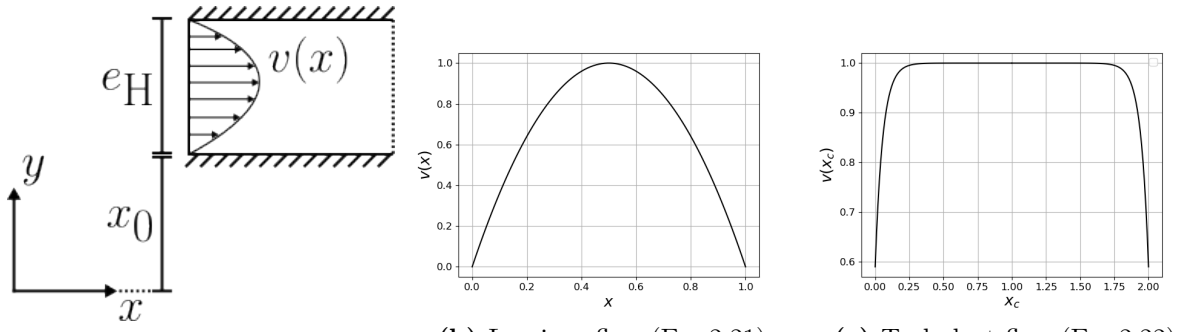

(a) Inlet illustration **(b)** Laminar flow (Eq. 2.21) **(c)** Turbulent flow (Eq. 2.22)

Figure 2.2 – Inlet illustration and velocity profile functions.

2.1.5 Fluid Flow Boundary Conditions

The inlet flow is assumed to have a fully-developed velocity profile, so a parabolic function is used to describe the inlet velocity for laminar flow (Eq. 2.21) and a near-constant profile is imposed for turbulent flow (Eq. 2.22). The definition of the functions from Eqs. 2.21 and 2.22 involves the maximum centerline velocity v_{in}, the inlet length e_{H}, and the coordinate of the inlet lower edge x_0. Also, the turbulent velocity profile definition uses an auxiliary coordinate x_c to simplify the equation. The graphs of Eqs. 2.21 and 2.22 are illustrated in Fig. 2.2.

$$v(x) = \frac{4\,v_{\text{in}}}{e_{\text{H}}^2}(x - x_0)(e_{\text{H}} + x_0 - x) \tag{2.21}$$

$$\begin{aligned} x_c(x) &= \frac{2(x - x_0)}{e_{\text{H}}} \\ v(x_c) &= \begin{cases} v_{\text{in}}\left(1 - e^{-18(x_c + 0.0495)}\right), & 0 \leq x_c \leq 1 \\ v_{\text{in}}\left(1 - e^{-18(2 - x_c + 0.0495)}\right), & 1 < x_c \leq 2 \end{cases} \end{aligned} \tag{2.22}$$

2.2 Solid Modeling

The static equilibrium of an elastic body may be obtained from the linear momentum equations or from variational principles. In this section, the linear elasticity equations are derived from the linear momentum equations, while the nonlinear equations are obtained from the minimization of the total potential energy. In both cases, the objective is to find the displacement field $\boldsymbol{u}$ of the body, which is used to define other quantities of interest. The equations are initially stated in the current configuration ${}^t\Omega$ (Lagrangian approach).

2.2.1 Linear Elasticity

The static equilibrium of a solid body must also satisfy the momentum equations given the boundary conditions. One difference from the fluid flow problem is that the reference

and deformed configurations are different for the solid, with the equilibrium occurring in the deformed configuration ${}^t\Omega$. Then, the static equilibrium problem is given by

$$\begin{aligned} {}^t\nabla \cdot \boldsymbol{\sigma}_{\mathrm{s}}(\boldsymbol{u}) + \boldsymbol{b} &= \boldsymbol{0} \quad \text{in } {}^t\Omega \\ \boldsymbol{u} &= \boldsymbol{u}^* \quad \text{on } {}^t\Gamma_{\mathrm{u}} \\ \boldsymbol{\sigma}_{\mathrm{s}}(\boldsymbol{u})\,\boldsymbol{n} &= \boldsymbol{t}^* \quad \text{on } {}^t\Gamma_{\mathrm{n}} \end{aligned} \tag{2.23}$$

where $\boldsymbol{b}$ are the body forces, $\boldsymbol{u}^*$ are the prescribed displacements, and $\boldsymbol{t}^*$ are the traction loads. For a linearly elastic solid (or Hookean elastic solid), the relation between loading and deformation is linear, and, for an isotropic solid, the material properties are independent of the direction. The Cauchy tensor for a linear and isotropic solid expressed in terms of the Lamé's parameters $\lambda_{1\mathrm{st}}$ and $\mu_{2\mathrm{nd}}$ is

$$\boldsymbol{\sigma}_{\mathrm{s}}(\boldsymbol{u}) = \lambda_{1\mathrm{st}}\,\mathrm{tr}\left(\boldsymbol{\varepsilon}(\boldsymbol{u})\right)\boldsymbol{I} + 2\,\mu_{2\mathrm{nd}}\,\boldsymbol{\varepsilon}(\boldsymbol{u}) \tag{2.24}$$

where $\boldsymbol{\varepsilon}$ is the linear strain tensor

$$\boldsymbol{\varepsilon}(\boldsymbol{u}) = \frac{1}{2}\left(\nabla\boldsymbol{u} + \nabla\boldsymbol{u}^T\right) \tag{2.25}$$

For linear elasticity, the current configuration ${}^t\Omega$ may be approximated by the reference configuration ${}^0\Omega$ because the displacements are small. Also, the gradient operations may be considered equivalent (${}^t\nabla \approx \nabla$). Then, the weak form of problem 2.23 is

$$\int_{{}^0\Omega} \boldsymbol{\sigma}_{\mathrm{s}}(\boldsymbol{u}) : \boldsymbol{\varepsilon}(\boldsymbol{w}_u)\,\mathrm{d}\Omega = \int_{{}^0\Omega} \boldsymbol{b}\cdot\boldsymbol{w}_u\,\mathrm{d}\Omega + \int_{{}^0\Gamma_{\mathrm{n}}} \boldsymbol{t}^*\cdot\boldsymbol{w}_u\,\mathrm{d}\Gamma \tag{2.26}$$

where $\boldsymbol{w}_u$ is the displacement field test function.

2.2.2 Hyperelasticity

The solid is modeled as a hyperelastic material for the nonlinear analysis, so its constitutive behavior is described by a strain energy density function Ψ, which can be used to obtain the total potential energy Π of the body as follows

$$\Pi(\boldsymbol{u}) = \int_{{}^0\Omega} \Psi(\boldsymbol{u})\,\mathrm{d}\Omega - \int_{{}^0\Omega} \boldsymbol{b}\cdot\boldsymbol{u}\,\mathrm{d}\Omega - \int_{{}^0\Gamma_{\mathrm{n}}} \boldsymbol{t}^*\cdot\boldsymbol{u}\,\mathrm{d}\Gamma \tag{2.27}$$

The equilibrium of a continuum body is the configuration in which the total potential energy of the body is minimal. Therefore, the problem of finding the equilibrium configuration can be stated as finding the displacement $\boldsymbol{u}$, which minimizes the total potential energy

according to Equation 2.28.

$$\min_{\boldsymbol{u}\in\mathcal{U}} \quad \Pi(\boldsymbol{u}) \tag{2.28}$$

At a point of minimum, the directional derivative (Fréchet's derivative) of the total potential energy Π with respect to $\boldsymbol{u}$ in an arbitrary direction $\boldsymbol{w}_u$ must be zero for all feasible directions, according to Eq. 2.29.

$$D\,\Pi(\boldsymbol{u})[\boldsymbol{w}_u] = \int_{{}^0\Omega} D\,\Pi(\boldsymbol{u})[\boldsymbol{w}_u]\,\mathrm{d}\Omega - \int_{{}^0\Omega} \boldsymbol{b}\cdot\boldsymbol{w}_u\,\mathrm{d}\Omega - \int_{{}^0\Gamma_{\mathrm{n}}} \boldsymbol{t}^*\cdot\boldsymbol{w}_u\,\mathrm{d}\Gamma = 0 \quad \forall \boldsymbol{w}_u \in \mathcal{U} \tag{2.29}$$

2.2.2.1 Isotropic Linearly Elastic Solid

The strain energy density function for an isotropic linearly elastic solid is given by

$$\Pi\left(\boldsymbol{u}\right) = \Pi\left(\boldsymbol{\varepsilon}\left(\boldsymbol{u}\right)\right) = \frac{\lambda_{1\mathrm{st}}}{2}\,\mathrm{tr}\left(\boldsymbol{\varepsilon}\left(\boldsymbol{u}\right)\right)^2 + \mu_{2\mathrm{nd}}\,\boldsymbol{\varepsilon}\left(\boldsymbol{u}\right) : \boldsymbol{\varepsilon}\left(\boldsymbol{u}\right) \tag{2.30}$$

where it is seen that the strain energy is a function of the linear strain tensor. When the displacement changes by $\boldsymbol{w}_u$, the linear strain changes by $\boldsymbol{\varepsilon}\left(\boldsymbol{w}_u\right)$. Therefore, the directional derivative may be calculated with respect to $\boldsymbol{\varepsilon}\left(\boldsymbol{u}\right)$ in the direction of $\boldsymbol{\varepsilon}\left(\boldsymbol{w}_u\right)$ as follows

$$\begin{aligned} D\,\Pi\left(\boldsymbol{u}\right)\left[\boldsymbol{w}_u\right] &= D\,\Pi(\boldsymbol{\varepsilon}\left(\boldsymbol{u}\right))\left[\boldsymbol{\varepsilon}\left(\boldsymbol{w}_u\right)\right] = \\ &= \frac{\boldsymbol{\partial}\Pi(\boldsymbol{\varepsilon}\left(\boldsymbol{u}\right))}{\boldsymbol{\partial}\boldsymbol{\varepsilon}} : \boldsymbol{\varepsilon}\left(\boldsymbol{w}_u\right) = \lambda_{1\mathrm{st}}\,\mathrm{tr}\left(\boldsymbol{\varepsilon}\left(\boldsymbol{u}\right)\right)\boldsymbol{I} : \boldsymbol{\varepsilon}\left(\boldsymbol{w}_u\right) + 2\mu_{2\mathrm{nd}}\,\boldsymbol{\varepsilon}\left(\boldsymbol{u}\right) : \boldsymbol{\varepsilon}\left(\boldsymbol{w}_u\right) \\ &= \lambda_{1\mathrm{st}}\left(\nabla\cdot\boldsymbol{u}\right)\left(\nabla\cdot\boldsymbol{w}_u\right) + \frac{\mu_{2\mathrm{nd}}}{2}\left(\nabla\boldsymbol{u} + \nabla\boldsymbol{u}^T\right) : \left(\nabla\boldsymbol{w}_u + \nabla{\boldsymbol{w}_u}^T\right) \end{aligned} \tag{2.31}$$

The directional derivative of the strain energy density function is a bilinear form for the isotropic linearly elastic solid. Therefore, the equilibrium may be stated as the solution of the following linear variational problem

$$\begin{aligned} &a_u(\boldsymbol{u},\,\boldsymbol{w}_u) = L_u(\boldsymbol{w}_u) \quad \forall \boldsymbol{w}_u \in \mathcal{U} \\ &a_u(\boldsymbol{u},\,\boldsymbol{w}_u) = \int_{{}^0\Omega} \frac{\mu_{2\mathrm{nd}}}{2}\left(\nabla\boldsymbol{u} + \nabla\boldsymbol{u}^T\right) : \left(\nabla\boldsymbol{w}_u + \nabla{\boldsymbol{w}_u}^T\right)\,\mathrm{d}\Omega + \int_{{}^0\Omega} \lambda_{1\mathrm{st}}\left(\nabla\cdot\boldsymbol{u}\right)\left(\nabla\cdot\boldsymbol{w}_u\right)\,\mathrm{d}\Omega \\ &L_u(\boldsymbol{w}_u) = \int_{{}^0\Omega} \boldsymbol{b}\cdot\boldsymbol{w}_u\,\mathrm{d}\Omega + \int_{{}^0\Gamma_{\mathrm{n}}} \boldsymbol{t}^*\cdot\boldsymbol{w}_u\,\mathrm{d}\Gamma \end{aligned} \tag{2.32}$$

which is equivalent to Eq. 2.29.

2.2.2.2 Neo-Hookean Solid

The strain energy density function of a Neo-Hookean solid can be written according to Eq. 2.33 where $\boldsymbol{F} = \boldsymbol{I} + \nabla\boldsymbol{u}$ is the deformation gradient.

$$\Pi(\boldsymbol{F}) = \frac{\lambda_{1\mathrm{st}}}{2}\left(\ln(\det(\boldsymbol{F}))\right)^2 + \frac{\mu_{2\mathrm{nd}}}{2}\left(\mathrm{tr}(\boldsymbol{F}^T\boldsymbol{F}) - 2 - 2\ln(\det(\boldsymbol{F}))\right) \tag{2.33}$$

The directional derivative of $\Pi(\boldsymbol{F})$ with respect to $\boldsymbol{F}$ in an arbitrary direction $\boldsymbol{G}$ is presented in Equation 2.34.

$$D\,\Pi(\boldsymbol{F})[\boldsymbol{G}] = \frac{\boldsymbol{\partial}\Pi(\boldsymbol{F})}{\boldsymbol{\partial F}} : \boldsymbol{G} = \left(\mu_{2\text{nd}}\boldsymbol{F} - \mu_{2\text{nd}}\boldsymbol{F}^{-T} + \lambda_{1\text{st}} \ln\left(\det\left(\boldsymbol{F}\right)\right) \boldsymbol{F}^{-T}\right) : \boldsymbol{G} \tag{2.34}$$

For a virtual displacement of $\boldsymbol{w}_u$, the deformation gradient changes $\nabla \boldsymbol{w}_u$. Therefore, $\boldsymbol{G} = \nabla \boldsymbol{w}_u$ when writing the residual form of the equilibrium of a Neo-Hookean solid.

2.3 Fluid-Structure Interaction

The basic idea for implementing the coupling in a FSI solver is to use the displacement obtained with the solid solver to define the geometry for the fluid solver and to use the velocity and pressure obtained with the fluid solver to calculate the loads over the solid. The loads over the structure are calculated by the continuity in traction (dynamic condition) in the interface ${}^{t}\Gamma_{\text{fsi}}$ according to

$$\boldsymbol{\sigma}_{\text{s}}\boldsymbol{n}_{\text{s}} = \boldsymbol{\sigma}_{\text{f}}\boldsymbol{n}_{\text{f}} \quad \text{on } {}^{t}\Gamma_{\text{fsi}} \tag{2.35}$$

Also, at the fluid-structure interface ${}^{t}\Gamma_{\text{fsi}}$, the fluid velocity must equal the solid velocity to preserve the velocity continuity (kinematic condition), which is achieved by imposing

$$\boldsymbol{v}_{\text{s}} = \boldsymbol{v}_{\text{f}} \quad \text{on } {}^{t}\Gamma_{\text{fsi}} \tag{2.36}$$

There are two approaches to solving FSI problems: staggered and monolithic. In the staggered approach (Fig 2.3a), the equations of fluid mechanics, solid mechanics, and mesh update are solved sequentially in an uncoupled fashion. The advantage of the staggered approach is the possibility of using existing fluid and solid solvers. However, the staggered approach may present convergence issues in some applications, such as light structures interacting with heavy fluids and incompressible flows enclosed by solids, such as the labyrinth seal problem studied in this work.

In the monolithic approach (Fig. 2.3b), the equations of fluid mechanics, solid mechanics, and mesh moving are solved synchronously. Therefore, there are no independent solvers for the fluid and solid equations, and there is no possibility of using existing solvers. The advantage of solving the equations simultaneously is robustness.

This work applies the FSI formulation proposed by Yoon (2010) for density-based topology optimization, which consists of applying the divergence theorem to obtain a system of equations that approximates the coupling between the solid and the fluid. The

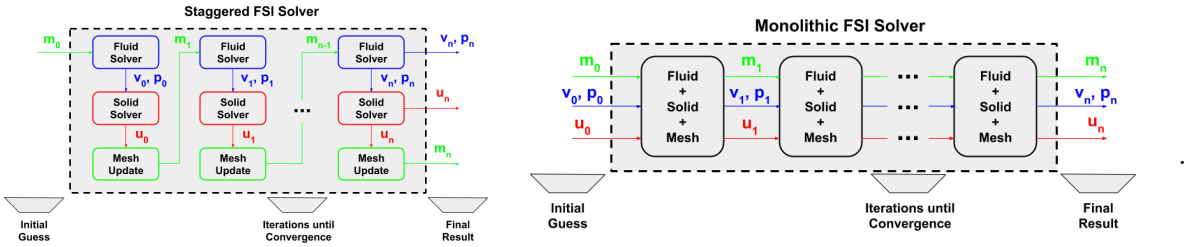

(a) Staggered **(b)** Monolithic

Figure 2.3 – Architecture of staggered and monolithic FSI solvers

formulation is valid for small displacements, and it is given by

$$\begin{aligned}
&\int_{0_\Omega} \left(\boldsymbol{v} \cdot \boldsymbol{F}^{-T} \nabla \boldsymbol{v}\right) \cdot \boldsymbol{w}_v |J_\mathrm{F}| \, \mathrm{d}\Omega + \int_{0_\Omega} \boldsymbol{\sigma}_\mathrm{f} : \boldsymbol{F}^{-T} \nabla \boldsymbol{w}_v |J_\mathrm{F}| \, \mathrm{d}\Omega \\
&\qquad + \int_{0_\Omega} \kappa(m) \boldsymbol{v} \cdot \boldsymbol{w}_v |J_\mathrm{F}| \, \mathrm{d}\Omega = \int_{0_{\Gamma_\mathrm{n}}} \boldsymbol{t}^* \cdot \boldsymbol{w}_v \, \mathrm{d}\Omega \\
&\int_{0_\Omega} (\nabla \cdot \boldsymbol{v}) \, w_p |J_\mathrm{F}| \, \mathrm{d}\Omega = 0 \\
&\int_{0_\Omega} \boldsymbol{\sigma}_\mathrm{s} : \boldsymbol{\varepsilon}\left(\boldsymbol{w}_u\right) \, \mathrm{d}\Omega = \int_{0_\Omega} \zeta \left(\boldsymbol{F}^{-T} \nabla p\right) \boldsymbol{w}_u |J_\mathrm{F}| \, \mathrm{d}\Omega
\end{aligned} \tag{2.37}$$

where ζ is a function that identifies solid and fluid, and $J_\mathrm{F} = \det(\boldsymbol{F})$. Yoon (2010) solves Eq. 2.37 following a monolithic approach, which is costly. As the objective here is to develop a connectivity constraint based on FSI, the accuracy of the displacement field may be sacrificed to reduce the computational time. Therefore, the system of equations is solved in a segregated approach with one-way coupling from fluid to solid. First, the fluid equations are solved without considering the mesh displacement ($\boldsymbol{F} = \boldsymbol{I}$ and $J_\mathrm{F} = 1$) as follows

$$\begin{aligned}
&\int_{0_\Omega} (\boldsymbol{v} \cdot \nabla \boldsymbol{v}) \cdot \boldsymbol{w}_v \, \mathrm{d}\Omega + \int_{0_\Omega} \boldsymbol{\sigma}_\mathrm{f} : \nabla \boldsymbol{w}_v \, \mathrm{d}\Omega + \int_{0_\Omega} \kappa(m) \boldsymbol{v} \cdot \boldsymbol{w}_v \, \mathrm{d}\Omega = \int_{0_{\Gamma_\mathrm{n}}} \boldsymbol{t}^* \cdot \boldsymbol{w}_v \, \mathrm{d}\Omega \\
&\int_{0_\Omega} (\nabla \cdot \boldsymbol{v}) \, w_p \, \mathrm{d}\Omega = 0
\end{aligned} \tag{2.38}$$

which is equivalent to solving the fluid flow problem alone. Then, the structure equilibrium is solved for the pressure of the flow field as follows

$$\int_{0_\Omega} \boldsymbol{\sigma}_\mathrm{s} : \boldsymbol{\varepsilon}\left(\boldsymbol{w}_u\right) \, \mathrm{d}\Omega = \int_{0_\Omega} \zeta \left(\boldsymbol{F}^{-T} \nabla p\right) \boldsymbol{w}_u |J_\mathrm{F}| \, \mathrm{d}\Omega \tag{2.39}$$

2.4 Topology Optimization Method

The mathematical statement of the topology optimization problem is presented in 2.40, in which C is the objective function, F is the weak statement of the physical equations, G_j are the constraints, N_G is the number of constraints, α is the design variable field, and

$\boldsymbol{s}$ are the state variables of the physical equations.

$$\begin{aligned} \min_{\alpha} \quad & C(\alpha,\, \boldsymbol{s}) \\ \text{s.t.} \quad & F(\alpha,\, \boldsymbol{s}) = 0 \\ & G_j(\alpha,\, \boldsymbol{s}) \leq \overline{G}_j, \quad j \in [1,\, N_G] \\ & \alpha \in \{0, 1\} \end{aligned} \tag{2.40}$$

As the objective function and constraints are generally nonlinear, and the discretization of α results in many design variables, the direct solution of problem 2.40 is computationally expensive. There are various alternatives for solving problem 2.40 in the context of fluid flow problems. This work explores the TOBS approach (SIVAPURAM; PICELLI, 2018) and the classical continuous variable approach (BORRVALL; PETERSSON, 2003). Some advantages of the TOBS approach are a clear interface between fluid and solid, and avoiding the continuation of parameters (SOUZA et al., 2021).

2.4.1 Topology Optimization of Binary Structures (TOBS)

The TOBS approach consists of the iterative solution of problem 2.40 by a sequence of linearized versions of the same problem (SIVAPURAM; PICELLI, 2018). At each iteration k, the design variable change $\Delta\alpha^{(k)}$ is calculated and the design variable is updated $\alpha^{(k+1)} = \alpha^{(k)} + \Delta\alpha^{(k)}$. The linear problems are obtained by applying Taylor's series expansions to the objective function and constraints. The expansion about the current design variable $\alpha^{(k)}$ is given by

$$C\left(\alpha^{(k)} + \Delta\alpha^{(k)},\, \boldsymbol{s}^{(k)}\right) = \underbrace{C\left(\alpha^{(k)},\, \boldsymbol{s}^{(k)}\right)}_{\text{constant}} + \underbrace{\frac{\partial C}{\partial \alpha}\left(\alpha^{(k)},\, \boldsymbol{s}^{(k)}\right)\Delta\alpha^{(k)}}_{\text{first-order term}} + \mathcal{O}\left(\left(\Delta\alpha^{(k)}\right)^2\right) \tag{2.41}$$

As the term $C\left(\alpha^{(k)},\, \boldsymbol{s}^{(k)}\right)$ is known (it is a constant in Taylor's series), the minimization of the left-hand side of equation 2.41 is approximately the minimization of the first order term if the step $\Delta\alpha^{(k)}$ is small. The step size $\left\|\Delta\alpha^{(k)}\right\|_1$ may be controlled by a linear constraint that can be obtained by using the fact that α is either 0 or 1.

$$\alpha \in \{0,\, 1\} \quad \Rightarrow \quad \left\|\Delta\alpha^{(k)}\right\|_1 = \sum_{i=1}^{N_\alpha}\left(1 - \alpha_i^{(k)}\right)\Delta\alpha_i^{(k)} \leq \beta_{\text{fl}} N_\alpha \tag{2.42}$$

The linearized constraints impose that the product of the constraint sensitivity $\frac{\partial G_j}{\partial \alpha}$ and the step $\Delta\alpha^{(k)}$ must be lower than the difference $\overline{G}_j - G_j\left(\alpha^{(k)},\, \boldsymbol{s}^{(k)}\right)$. However, the flip limits constraint limits the step size, and the direct use of the linearized constraint may

lead to unfeasible problems. Therefore, the linearized constraints are relaxed as follows

$$\Delta G_j\left(\alpha^{(k)},\, \boldsymbol{s}^{(k)}\right) = \begin{cases} -\epsilon_j G_j\left(\alpha^{(k)},\, \boldsymbol{s}^{(k)}\right), & \overline{G}_j < (1-\epsilon_j)\overline{G}_j \\ \overline{G}_j - G_j\left(\alpha^{(k)},\, \boldsymbol{s}^{(k)}\right), & \overline{G}_j \in [(1-\epsilon_j)\overline{G}_j,\, (1+\epsilon_j)\overline{G}_j] \\ \epsilon_j G_j\left(\alpha^{(k)},\, \boldsymbol{s}^{(k)}\right), & \overline{G}_j > (1+\epsilon_j)\overline{G}_j \end{cases} \tag{2.43}$$

Then, each step of the TOBS algorithm corresponds to the solution of the following integer linear optimization problem

$$\begin{aligned} \min_{\Delta\alpha^{(k)}} \quad & \frac{\partial C}{\partial \alpha}\left(\alpha^{(k)},\, \boldsymbol{s}^{(k)}\right)\Delta\alpha^{(k)} \\ \text{s.t.} \quad & F\left(\alpha^{(k)},\, \boldsymbol{s}^{(k)}\right) = 0 \\ & \frac{\partial G_j}{\partial \alpha}\left(\alpha^{(k)},\, \boldsymbol{s}^{(k)}\right)\Delta\alpha^{(k)} \leq \Delta G_j\left(\alpha^{(k)},\, \boldsymbol{s}^{(k)}\right), \quad j \in [1,\, N_G] \\ & \left\|\Delta\alpha^{(k)}\right\|_1 \leq \beta_{\text{fl}} N_\alpha \\ & \Delta\alpha^{(k)} \in \left\{-\alpha^{(k)}, 1-\alpha^{(k)}\right\} \end{aligned} \tag{2.44}$$

2.4.2 Continuous Variable Approach

The continuous approach relaxes the binary condition of the topology optimization problem ($\alpha \in \{0,\, 1\}$) by allowing the design variables to be continuous ($\alpha \in [0,\, 1]$), as shown in Eq. 2.45. Then, it applies techniques such as penalization and projection to avoid intermediate pseudo-densities in the optimization result. In this work, the continuous design variables are denoted as m.

$$\begin{aligned} \min_{m} \quad & C(m,\, \boldsymbol{s}) \\ \text{s.t.} \quad & F(m,\, \boldsymbol{s}) = 0 \\ & G_j(m,\, \boldsymbol{s}) \leq \overline{G}_j, \quad j \in [1,\, N_G] \\ & m \in [0,\, 1] \end{aligned} \tag{2.45}$$

Directly using the design variable field in the material interpolation functions may render the topology optimization problem mesh-dependent. One way of regularizing the problem is to use density filters (BRUNS; TORTORELLI, 2001; BOURDIN, 2001). In this work, two forms of density filters are investigated. The first is the PDE filter proposed by Lazarov and Sigmund (2010), which consists of solving the following boundary value problem to obtain the filtered field m_{f}

$$-{R_{\text{f}}}^2\nabla^2 m_{\text{f}} + m_{\text{f}} = m \qquad \text{on } \Omega^{\text{m}} \tag{2.46a}$$

$$m_{\text{f}} = {m_{\text{f}}}^* \qquad \text{in } \Gamma^{\text{m}}_{\text{d}} \tag{2.46b}$$

$$\nabla m_{\text{f}} \cdot \boldsymbol{n} = 0 \qquad \text{in } \Gamma^{\text{m}}_{\text{n}} \tag{2.46c}$$

where R_f is a length scale related to the physical radius r_min by the equation $r_\mathrm{min} = 2\sqrt{3}\,R_\mathrm{f}$. The field m_f^* may impose desired values of m_f on the boundary of the design domain. The notation Ω^m is introduced to define the design domain and to highlight that it may not match the physical domain Ω (i.e., there may be non-optimizable regions in the physical domain).

The second density filter has a discrete form and compact support (GUEST; PRÉVOST; BELYTSCHKO, 2004). The filtered value of each element is computed as a weighted sum of the design variables of the neighbors inside the ball $\mathbb{N}_\mathrm{e}$, which is the circle in 2D or the sphere in 3D of radius r_min centered in the element. Therefore, the set $\mathbb{N}_\mathrm{e}$ is defined as follows

$$\mathbb{N}_\mathrm{e} = \{\mathrm{i} : ||\boldsymbol{x}_\mathrm{e} - \boldsymbol{x}_\mathrm{i}||_2 < r_\mathrm{min}\} \tag{2.47}$$

and the filtered degrees of freedom $m_{\mathrm{f},\,e}$ are given by

$$\begin{aligned} m_{\mathrm{f},\,e} &= \frac{\sum\limits_{i\in\mathbb{N}_\mathrm{e}} w_\mathrm{e}\left(\boldsymbol{x}_i\right) V_i m_i}{\sum\limits_{i\in\mathbb{N}_\mathrm{e}} w_\mathrm{e}\left(\boldsymbol{x}_i\right) V_i} \\ w_\mathrm{e}\left(\boldsymbol{x}_i\right) &= r_\mathrm{min} - ||\boldsymbol{x}_e - \boldsymbol{x}_i||_2 \end{aligned} \tag{2.48}$$

where V_i is the volume or area of the element.

The density filters introduce intermediate pseudo-densities which are undesired in the final solution. This problem may be circumvented using smooth Heaviside projection (WANG; LAZAROV; SIGMUND, 2010).

$$m_\mathrm{p} = \frac{\tanh\left(\beta_\mathrm{th}\eta_\mathrm{th}\right) + \tanh\left(\beta_\mathrm{th}(m_\mathrm{f} - \eta_\mathrm{th})\right)}{\tanh\left(\beta_\mathrm{th}\eta_\mathrm{th}\right) + \tanh\left(\beta_\mathrm{th}(1 - \eta_\mathrm{th})\right)} \tag{2.49}$$

where η_th is the projection threshold, i.e., the value of m_f where the transition from 0 to 1. The parameter β_th controls the transition slope, going from an almost linear behavior for $\beta_\mathrm{th} = 1$ and approaching the Heaviside function for $\beta_\mathrm{th} \to \infty$. Figure 2.4 shows the behavior of the smooth Heaviside projection for different values of η_th and β_th. Generally, the threshold η_th is kept constant during the optimization, and β_th is increased (continuation) until a satisfactory reduction of intermediate pseudo-densities is obtained.

2.4.3 Material Model for Fluid Flow Equations

This work considers continuous and binary design variables, with zero indicating fluid elements and one indicating solid elements. The inverse permeability terms are interpolated by the convex function introduced by Borrvall and Petersson (2003) modified to obtain $\kappa(0) = \kappa_\mathrm{min}$ and $\kappa(1) = \kappa_\mathrm{max}$ according to Eq. 2.50. A linear material model is also a valid choice for the TOBS approach for fluid flows (SOUZA et al., 2021). However, the

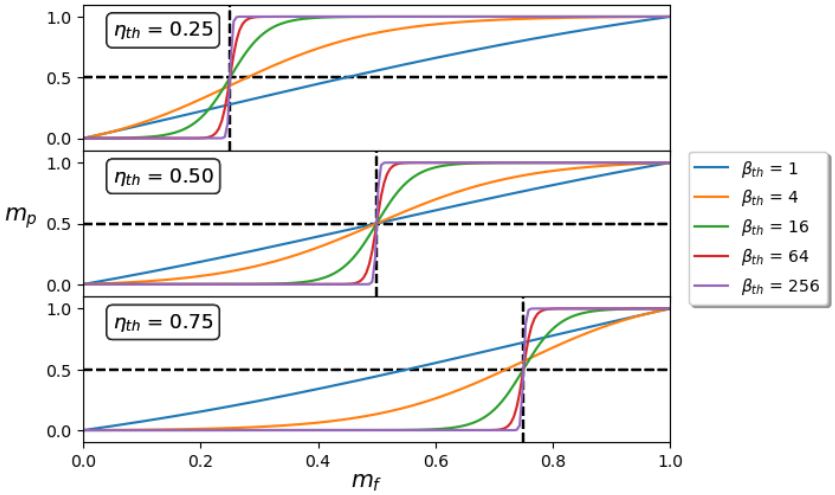

Figure 2.4 – Smooth Heaviside projection (Eq. 2.49) for different values of η and β. The parameter η_{th} is the threshold of the projection and β_{th} controls the slope of the curve.

convex model of Eq. 2.50 is selected because it is more general as it can reproduce an almost linear behavior for $q_c \geq 10$ as illustrated in Fig. 2.5. Also, the minimum inverse permeability is considered zero for all cases: $\kappa_{\min} = 0$.

$$\kappa(\alpha) = \kappa_{\max}\kappa_1(\alpha) = \kappa_{\max}\frac{q_c\alpha}{1-\alpha+q_c} \tag{2.50}$$

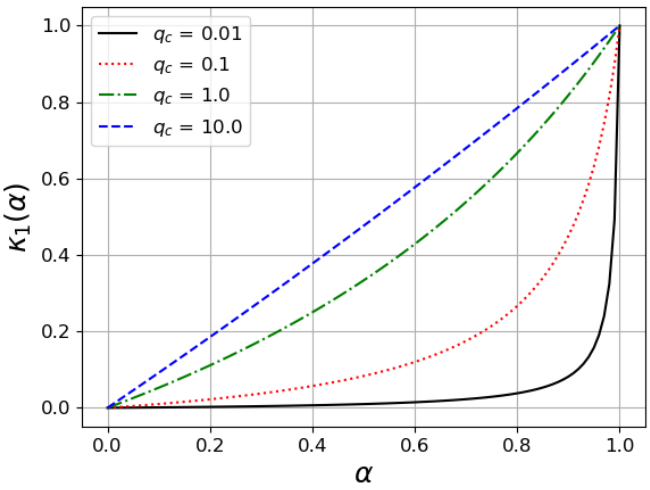

Figure 2.5 – Material model for the normalized inverse permeability κ_1.

2.4.4 Material Model for Solid Equations

This work considers the topology optimization of structures subjected to pressure loads, which are one type of design-dependent load because they are always normal to the structure's surface, changing during the optimization. The topic has received considerable attention from the scientific community, and several approaches are available in the literature to model pressure loads during density-based topology optimization (CHEN;

KIKUCHI, 2001; DU; OLHOFF, 2004; LEE; MARTINS, 2012; KUMAR; FROUWS; LANGELAAR, 2020). This work follows the ideas introduced by Sigmund and Clausen (2007) of transmitting the pressure load through a hydrostatic stress state in the non-solid (fluid or void) phase. However, instead of using a mixed displacement-pressure formulation, a pure displacement formulation is used (MOSCATELLI et al., 2023). For linear elasticity, the Cauchy stress tensor expressed in terms of the shear G_{shear} and bulk K_{bulk} modulus is given by

$$\boldsymbol{\sigma}_{\text{s}}(\alpha,\, \boldsymbol{u}) = \underbrace{2\, G_{\text{shear}}(\alpha)\boldsymbol{e}(\boldsymbol{u})}_{\text{Deviatoric}} + \underbrace{K_{\text{bulk}}(\alpha)\, (\nabla \cdot \boldsymbol{u})\, \boldsymbol{I}}_{\text{Hydrostatic}} \tag{2.51}$$

where $\boldsymbol{e}$ is the deviatoric strain tensor defined as

$$\boldsymbol{e}(\boldsymbol{u}) = \begin{cases} \boldsymbol{\varepsilon}(\boldsymbol{u}) - \dfrac{1}{2}\, (\nabla \cdot \boldsymbol{u})\, \boldsymbol{I}, & \text{for 2D} \\ \boldsymbol{\varepsilon}(\boldsymbol{u}) - \dfrac{1}{3}\, (\nabla \cdot \boldsymbol{u})\, \boldsymbol{I}, & \text{for 3D} \end{cases} \tag{2.52}$$

The shear and bulk modulus are interpolated by the SIMP (Solid Isotropic Material with Penalization) function as follows

$$\begin{aligned} G_{\text{shear}}\,(\alpha) &= G_{\text{min}} + (G_{\text{max}} - G_{\text{min}})\, \alpha^{P_{\text{simp}}} \\ K_{\text{bulk}}\,(\alpha) &= K_{\text{min}} + (K_{\text{max}} - K_{\text{min}})\, \alpha^{P_{\text{simp}}} \end{aligned} \tag{2.53}$$

where P_{simp} is the SIMP penalization exponent.

For nonlinear elasticity, the approach proposed by Wang et al. (2014) of using linear strain energy for low-density elements is adapted to transmit pressure loads through the decomposition of the strain energy density function in deviatoric and hydrostatic parts as follows

$$\Psi\,(\boldsymbol{u}) = \underbrace{\Psi_{\text{d}}\,(\boldsymbol{u})}_{\text{Deviatoric}} + \underbrace{\Psi_{\text{h}}\,(\boldsymbol{u})}_{\text{Hydrostatic}} \tag{2.54}$$

which is an extension of the idea introduced by Sigmund and Clausen (2007) to nonlinear elasticity. The strain energy is evaluated element-wise (through the use of DG0 design variables) to reduce the influence of intermediate values, increasing the stability of the numerical solution of the structural equilibrium. The notation used for the element-wise strain energy functions is given by

$$\Psi_{\text{e}}\,(\boldsymbol{u}) = \Psi_{\text{d,e}}\,(\boldsymbol{u}) + \Psi_{\text{h,e}}\,(\boldsymbol{u}) \tag{2.55}$$

Then, the deviatoric and hydrostatic components of the element strain energy are interpolated in the same way the full strain energy is interpolated in the work of Wang et

al. (2014), which gives

$$\begin{aligned}\Psi_{\mathrm{d,e}} &= \left(\overline{\Psi}_{\mathrm{d}}^{\mathrm{N}}\left(\gamma\boldsymbol{u}_{\mathrm{e}}\right) - \overline{\Psi}_{\mathrm{d}}^{\mathrm{L}}\left(\gamma\boldsymbol{u}_{\mathrm{e}}\right) + \overline{\Psi}_{\mathrm{d}}^{\mathrm{L}}\left(\boldsymbol{u}_{\mathrm{e}}\right)\right) G_{\mathrm{shear}}\left(m_{\mathrm{p},e}\right) \\ \Psi_{\mathrm{h,e}} &= \left(\overline{\Psi}_{\mathrm{h}}^{\mathrm{N}}\left(\gamma\boldsymbol{u}_{\mathrm{e}}\right) - \overline{\Psi}_{\mathrm{h}}^{\mathrm{L}}\left(\gamma\boldsymbol{u}_{\mathrm{e}}\right) + \overline{\Psi}_{\mathrm{h}}^{\mathrm{L}}\left(\boldsymbol{u}_{\mathrm{e}}\right)\right) K_{\mathrm{bulk}}\left(m_{\mathrm{p},e}\right)\end{aligned} \tag{2.56}$$

where γ is an indicator function obtained through a smooth Heaviside projection with a low threshold η_γ and a high steepness β_γ to better control for which level of density the linear strain energy function is used

$$\gamma = \frac{\tanh\left(\beta_\gamma\eta_\gamma\right) + \tanh\left(\beta_\gamma(m_{\mathrm{p}} - \eta_\gamma)\right)}{\tanh\left(\beta_\gamma\eta_\gamma\right) + \tanh\left(\beta_\gamma(1 - \eta_\gamma)\right)} \tag{2.57}$$

The functions $\overline{\Psi}_{\mathrm{d}}^{\mathrm{N}}$, $\overline{\Psi}_{\mathrm{d}}^{\mathrm{L}}$, $\overline{\Psi}_{\mathrm{h}}^{\mathrm{N}}$ and $\overline{\Psi}_{\mathrm{h}}^{\mathrm{L}}$ are normalized strain energy density functions describing deviatoric and hydrostatic components of hyperelastic models. The linear constitutive model of Eq. 2.51 may also be described by the following linear strain energy function

$$\overline{\Psi}^{\mathrm{L}}\left(\boldsymbol{u}\right) = G_{\mathrm{shear}}\underbrace{\left(\boldsymbol{\varepsilon}\left(\boldsymbol{u}\right) : \boldsymbol{\varepsilon}\left(\boldsymbol{u}\right) - \frac{1}{3}\mathrm{tr}\left(\boldsymbol{\varepsilon}\left(\boldsymbol{u}\right)\right)^2\right)}_{\overline{\Psi}_{\mathrm{d}}^{\mathrm{L}}(\boldsymbol{u})} + K_{\mathrm{bulk}}\underbrace{\left(\frac{1}{2}\mathrm{tr}\left(\boldsymbol{\varepsilon}\left(\boldsymbol{u}\right)\right)^2\right)}_{\overline{\Psi}_{\mathrm{h}}^{\mathrm{L}}(\boldsymbol{u})} \tag{2.58}$$

and the Neo-Hookean model of Eq. 2.33 may be rewritten in terms of G_{shear} and K_{bulk} as follows

$$\overline{\Psi}^{\mathrm{N}}\left(I_{\mathrm{C}},\, J_{\mathrm{F}}\right) = G_{\mathrm{shear}}\underbrace{\left(\frac{1}{2}(I_{\mathrm{C}} - 3) - \mathcal{V}_{\mathrm{d}}\left(J_{\mathrm{F}}\right)\right)}_{\overline{\Psi}_{\mathrm{d}}^{\mathrm{N}}} + K_{\mathrm{bulk}}\underbrace{\left(\frac{1}{2}\mathcal{V}\left(J_{\mathrm{F}}\right)\right)}_{\overline{\Psi}_{\mathrm{h}}^{\mathrm{N}}\left(J_{\mathrm{F}}\right)} \tag{2.59}$$

where I_{C} is the first invariant of the Green tensor, J_{F} is the volumetric change ($J_{\mathrm{F}} = \det\left(\boldsymbol{F}\right)$), $\mathcal{V}$ is a function related to the volume change which may have different forms such as

$$\begin{aligned}&\mathcal{V}_{\mathrm{SC}}\left(J_{\mathrm{F}}\right) = \frac{1}{2}\left({J_{\mathrm{F}}}^2 - 1\right) - \ln(J_{\mathrm{F}}) && \text{from Simo-Ciarlet (LAHUERTA et al., 2013)} \\ &\mathcal{V}_{\mathrm{BW}}\left(J_{\mathrm{F}}\right) = \ln(J_{\mathrm{F}})^2 && \text{from Bonet and Wood (2008)} \\ &\mathcal{V}\left(J_{\mathrm{F}}\right) = \left(J_{\mathrm{F}} - 1\right)^2 \\ &\mathcal{V}\left(J_{\mathrm{F}}\right) = \left(J_{\mathrm{F}} - \ln(J_{\mathrm{F}}) - 1\right)^2\end{aligned} \tag{2.60}$$

and $\mathcal{V}_{\mathrm{d}}$ is a function depending on $\mathcal{V}$ through the relation

$$\mathcal{V}_{\mathrm{d}}\left(J_{\mathrm{F}}\right) = \ln(J_{\mathrm{F}}) + \frac{1}{3}\mathcal{V}\left(J_{\mathrm{F}}\right) \tag{2.61}$$

2.4.5 Topology Optimization of Labyrinth Seals

This work is concerned with the leakage reduction in labyrinth seals, which can be expressed by the following functional for incompressible flows

$$Q_{\mathrm{v}}\left(\boldsymbol{v}\right) = \int_{\Gamma_{\mathrm{outlet}}} \boldsymbol{n} \cdot \boldsymbol{v} \, \mathrm{d}\Gamma \tag{2.62}$$

However, using leakage as the objective function is difficult for incompressible flows as it requires the use of pressure boundary conditions at inlet and outlet simultaneously. One alternative to minimizing the leakage is maximizing the head loss, which is given by

$$J(\boldsymbol{v},\, p) = -\frac{1}{Q_{\mathrm{v}}\left(\boldsymbol{v}\right)} \int_{\Gamma} \left(\frac{p}{g} + \frac{\boldsymbol{v} \cdot \boldsymbol{v}}{2g} \right) \left(\boldsymbol{n} \cdot \boldsymbol{v} \right) \, \mathrm{d}\Gamma \tag{2.63}$$

The loss coefficient concept may draw an equivalence between leakage minimization and head loss maximization. According to White (2011), the loss coefficient of a component may be calculated as the ratio of pressure head loss $\Delta p/g$ by velocity head $\boldsymbol{v} \cdot \boldsymbol{v}/(2g)$ as follows

$$K_{\mathrm{L}} = 2\frac{\Delta p}{\boldsymbol{v} \cdot \boldsymbol{v}} \tag{2.64}$$

Then, by taking the simplified flow model of a one-dimensional component with one inlet, one outlet, and a fully developed velocity profile as an example, the simplified loss coefficient is given by

$$K_{\mathrm{S}} = 2\,\frac{p_{\mathrm{out}} - p_{\mathrm{in}}}{{v_{\mathrm{avg}}}^2} \tag{2.65}$$

where p_{out}, p_{in}, and v_{avg} are the mean outlet pressure, mean inlet pressure, and mean velocity, respectively. For fixed pressure conditions in the inlet and outlet, the numerator of Eq. (2.65) is constant. Therefore, the loss coefficient of the simplified flow model is increased by lowering the velocity v_{avg}, i.e., by minimizing the leakage. On the other hand, if the velocity v_{avg} is fixed, the denominator of Eq. (2.64) is constant. Therefore, the loss coefficient is increased if the head loss of the simplified model is increased. From this analysis, the leakage minimization with the inlet pressure boundary condition is equivalent to the head loss maximization with the inlet velocity boundary condition.

During this work, the diodicity objective function (LIU et al., 2012; LIN et al., 2015; LIM et al., 2019) has also been explored to reduce leakage while avoiding the contact of rotor and stator parts (SOUZA, 2020; SÁ et al., 2021b). The approach was to combine geometry trimming proposed by Picelli et al. (2022) with diodicity (MOSCATELLI et al., 2022). However, the diodicity requires solving the physical problem twice, which considerably increases the computational cost for turbulent flows. Also, the diodicity involves two conflicting objectives, so the additional tuning of optimization parameters

is necessary to obtain interesting results. In fact, minimizing energy dissipation in the reverse direction is not important for labyrinth seal design and limits the actual objective of reducing leakage. Appendix A provides more details regarding the diodicity objective function.

For staggered and stepped labyrinth seals, the simultaneous optimization of the rotor and the stator may harness the interaction of these parts to generate improved designs. However, for conducing this simultaneous optimization, it is necessary to describe solid elements with different rotations. In this work, we propose to describe the different rotations with two Darcy terms. Two approaches are proposed to ensure a minimum gap size between stator and rotor, and avoid free-floating islands (Fig. 2.6), which may not be interesting in labyrinth seal design (due to manufacturing difficulties) and are problematic for topology optimization with FSI (JENKINS; MAUTE, 2016). The first approach is based on two discrete design variable fields and TOBS (MOSCATELLI et al., 2022). The second is based on one continuous design variable and interface identification method (MOSCATELLI et al., 2024).

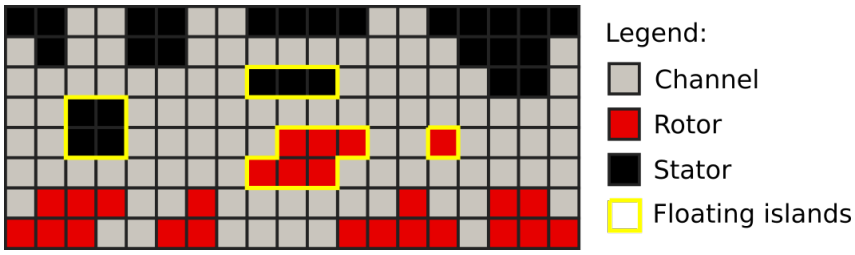

Figure 2.6 – Illustration of floating islands of solid material (highlighted with yellow frames) during the topology optimization of rotor-stator devices.

2.4.5.1 Rotor-Stator Algorithm

The rotor-stator algorithm proposed in Moscatelli et al. (2022) starts by dividing the solid domain Ω_s into stationary $\Omega_\mathrm{s}^\mathrm{s}$ and rotating $\Omega_\mathrm{s}^\mathrm{r}$ subdomains. This division is modeled with the aid of an additional design variable field β and the mapping of Table 2.1. As $\alpha = 1$ and $\beta = 1$ are mutually exclusive conditions, if the undesired phase is avoided, it is possible to introduce an additional Darcy term to the momentum equation to account for rotating solids as follows

$$(\boldsymbol{v}\cdot\nabla)\boldsymbol{v} - \nabla\cdot\boldsymbol{\sigma}_\mathrm{f} + \kappa(\alpha)\boldsymbol{v} + \kappa(\beta)(\boldsymbol{v} - \omega_\mathrm{r}\, r\, \boldsymbol{e}_\theta) = 0 \quad \text{in } {}^0\Omega \tag{2.66}$$

Table 2.1 – Mapping between design variables and element phases for the rotor-stator algorithm.

Subdomain	α	β	Element phase
$\boldsymbol{\Omega_s^s}$	**1**	**0**	**Stator (solid)**
$\boldsymbol{\Omega_f}$	**0**	**0**	**Fluid**
$\boldsymbol{\Omega_s^r}$	**0**	**1**	**Rotor (solid)**
-	**1**	**1**	**Undesired phase**

The undesired phase in which $\alpha = 1$ and $\beta = 1$ may be avoided by selecting the upper and lower bounds of $\Delta\alpha$ and $\Delta\beta$. The procedure followed in Moscatelli et al. (2022) for labyrinth seal design is to select $\Delta\alpha$ and $\Delta\beta$ such that the minimum gap is satisfied and that no floating islands (Fig. 2.6) of solid are introduced.

By considering the neighborhood V_d of an element E as the set of elements whose the ℓ_1-distance is equal to d (Fig. 2.7), it is possible to avoid floating islands by checking the state of V_1 and to impose a minimum gap $g_{\min}$ by checking V_d, where d is given by

$$d = \text{ceil}\left(\frac{g_{\min}}{h}\right) \tag{2.67}$$

where h is the element size and the ceil function returns the least integer that is greater than the argument.

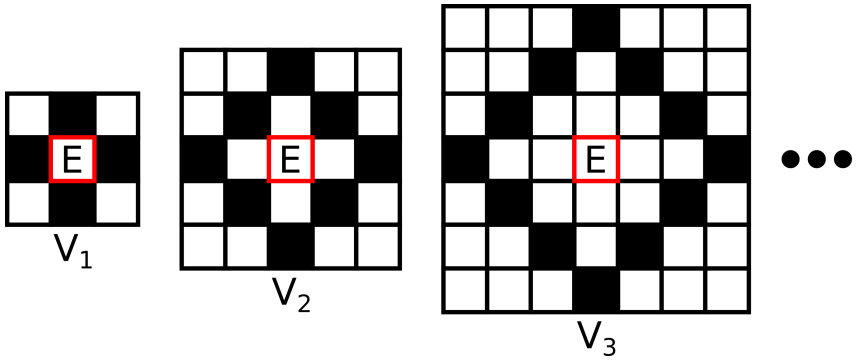

Figure 2.7 – Schematic representation of the neighborhoods V_d of element E for $d = 1, 2, 3$.

The solid islands are avoided by allowing only the following phase changes: 1) fluid elements close to rotor can change to rotor; 2) fluid elements close to stator can change to stator; 3) stator elements close to fluid can change to fluid; 4) rotor elements close to fluid can change to fluid. An illustration of the allowed changes for labyrinth seal design is presented in Fig. 2.8 where the elements that are allowed to change are marked with numbers.

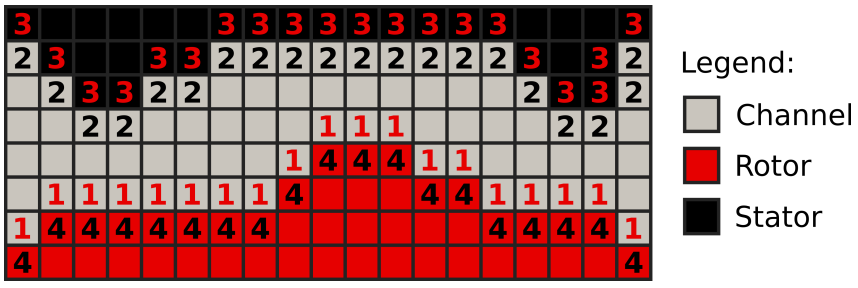

Figure 2.8 – Illustration of active elements during the optimization of a labyrinth seal. (1) Fluid elements that can change to rotor; (2) fluid elements that can change to stator; (3) stator elements that can change to fluid; (4) rotor elements that can change to fluid. Elements with black numbers are active during stator expansion/rotor contraction and elements with red numbers are active during rotor expansion/stator contraction.

The allowed changes described in Fig. 2.8 require the definition of the phases in the

boundary. This can be done by extending the domain on all sides by one element and by defining the phases of the introduced elements. Figure 2.9 presents an example of initialization for the boundaries. It is important to notice that the extended boundary elements are not part of the analysis and optimization. They are only used to complete the V_1 neighbourhood of elements at the border of the domain.

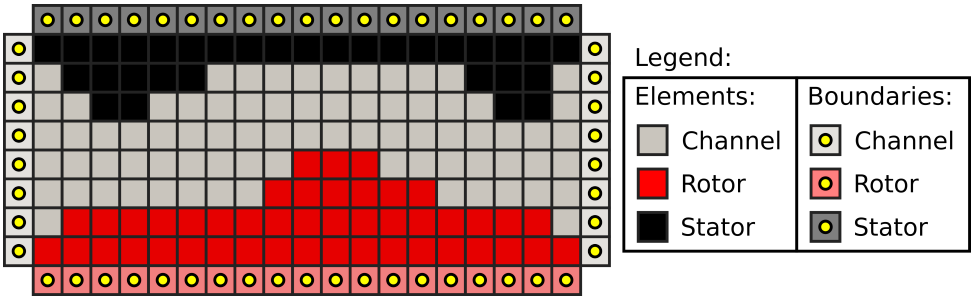

Figure 2.9 – Example of a possible boundary initialization for the labyrinth seal problem.

However, it is still possible to obtain solid islands if all elements of the design domain are allowed to change in each call to the integer linear optimization routine because adjacent elements can change simultaneously as Fig. 2.6 shows. As the logic to determine the allowed changes is based on the current state (i.e., there is no information about the next state), it is necessary to break the iteration into two steps to avoid adjacent elements of different phases changing at the same time. Therefore, each iteration of the labyrinth seal design is divided into two steps: stator expansion/rotor contraction and stator contraction/rotor expansion. During stator expansion/rotor contraction, fluid elements close to stator and rotor elements close to fluid elements are allowed to change. This corresponds to the black numbers in Fig. 2.8. During stator contraction/rotor expansion, fluid elements close to rotor elements are allowed to change to rotor and stator elements close to fluid elements are allowed to change to fluid. This corresponds to red numbers in Fig. 2.8. Then, each iteration of the TOBS for the rotor-stator algorithm is stated as

$$
\begin{aligned}
\min_{\Delta\alpha,\,\Delta\beta} \quad & \frac{\partial C}{\partial \alpha}\Delta\alpha + \frac{\partial C}{\partial \beta}\Delta\beta \\
\text{s.t.} \quad & F(\alpha,\,\beta,\,\boldsymbol{s}) = 0 \\
& \frac{\partial G_j}{\partial \alpha}\,\Delta\alpha + \frac{\partial G_j}{\partial \beta}\,\Delta\beta \leq \Delta G_j(\alpha,\,\beta,\,\boldsymbol{s}), \quad j \in [1,\,N_G] \\
& \left\|\Delta\alpha^{(k)}\right\|_1 \leq \beta_{\text{fl}} N_\alpha \\
& \left\|\Delta\beta^{(k)}\right\|_1 \leq \beta_{\text{fl}} N_\beta \\
& \Delta\alpha \in \mathcal{S}_\alpha \\
& \Delta\beta \in \mathcal{S}_\beta
\end{aligned}
\tag{2.68}
$$

where the sets $\mathcal{S}_\alpha$ and $\mathcal{S}_\beta$ indicate the allowed changes for the design variables. They are defined based on a combination of Table 2.2 and the logic discussed for Fig. 2.8.

Table 2.2 – Mapping between design variables, element phases and allowed changes for the rotor-stator algorithm.

Subdomain	α	β	Element phase	$\mathcal{S}_\alpha$	$\mathcal{S}_\beta$
Ω_s^s	1	0	Stator (solid)	{-1, 0}	{0, 1}
Ω_f	0	0	Fluid	{0, 1}	{0, 1}
Ω_s^r	0	1	Rotor (solid)	{0, 1}	{-1, 0}

2.4.5.2 Interface Identification Method

The work of Høghøj et al. (2020) proposes an interface identification technique for the design of heat exchangers by density-based topology optimization. The technique is based on erosion and dilation morphology operations and assures a solid interface between the coolant and the cooled fluids. Also, it controls the minimum size of the solid interface. This interface identification technique can also be extended to labyrinth seal design if the fluid channel is interpreted as an interface between the stator and rotor (MOSCATELLI et al., 2024).

The interface identification method is composed of a series of density filters (Eq. 2.46) and smooth Heaviside projections (Eq. 2.49) that can be grouped in two distinct steps: regularization and actual interface identification. The regularization step follows the three-field topology optimization approach (GUEST; PRÉVOST; BELYTSCHKO, 2004; SIGMUND, 2007; WANG; LAZAROV; SIGMUND, 2010), which consists of applying a density filter and a smooth Heaviside projection to design variable field m. In this work, the PDE-filter proposed by Lazarov and Sigmund (2010) and given by Eq. 2.46 is used with Dirichlet boundary conditions to obtain the filtered field m_f as follows

$$-{R_\mathrm{f}}^2\nabla^2 m_\mathrm{f} + m_\mathrm{f} = m \qquad \text{in } \Omega^\mathrm{m} \tag{2.69a}$$

$$m_\mathrm{f} = {m_\mathrm{f}}^* \qquad \text{on } \Gamma^\mathrm{m} \tag{2.69b}$$

The field ${m_\mathrm{f}}^*$ must be consistent with the locations of the stator, the rotor, and the channel. In this work, the convention is to set ${m_\mathrm{f}}^* = 0$ in the parts of Γ^m that are closer to the stator and to set ${m_\mathrm{f}}^* = 1$ in the parts of Γ^m that are closer to the rotor as shown in Fig. 2.10b. The design domain Ω^m may not occupy the whole fluid flow domain as described in Fig. 2.10, allowing the designer to select fixed fluid regions. The second operation of the regularization step is the smooth Heaviside projection of Eq. 2.49. The regularization produces a smooth interface for the interface identification step, as shown in the example of Fig. 2.11.

The objective of the interface identification step is to create a region with a minimum size around the transition from 0 to 1 in the projected field m_p. This minimum size is achieved by applying dilation and erosion morphology operations to m_p. These operations

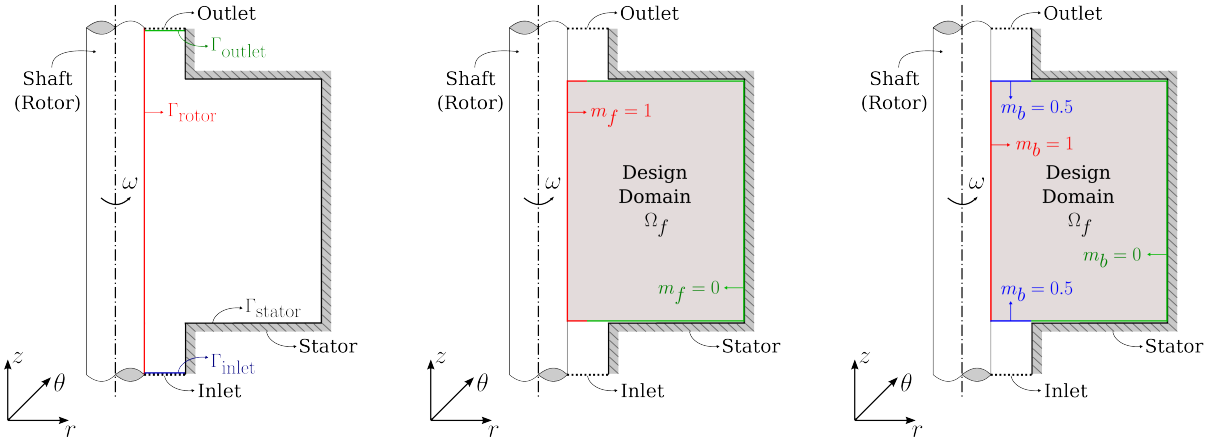

(a) Fluid flow problem **(b)** Filtering problem **(c)** Blurring problem

Figure 2.10 – Schematic representation of the boundary conditions involved in the interface identification method.

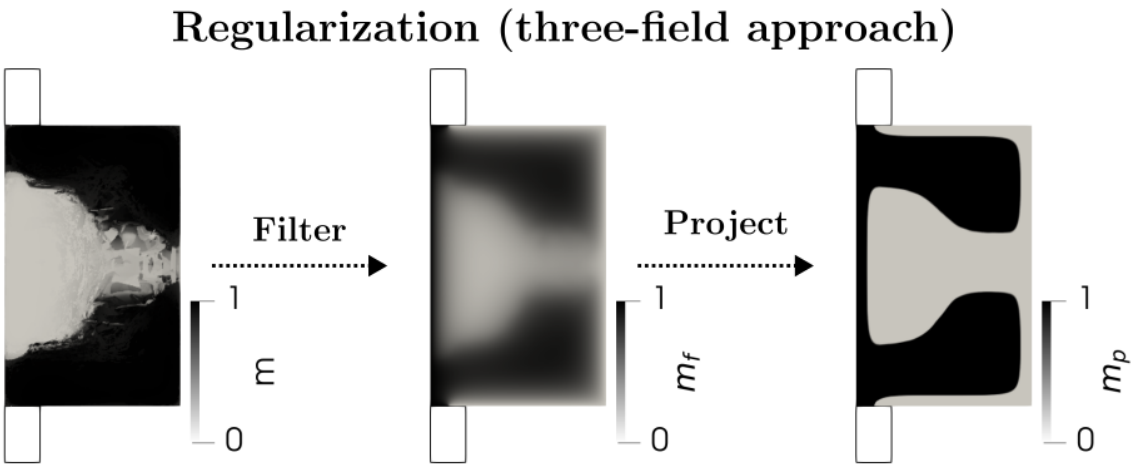

Figure 2.11 – Illustration of the regularization of a design variable field for the interface identification method.

also involve density filters and smooth Heaviside projections. The field m_p is filtered with radius $r_\mathrm{b} = 2\sqrt{3}R_\mathrm{b}$ as follows

$$-{R_\mathrm{b}}^2\nabla^2 m_\mathrm{b} + m_\mathrm{b} = m_\mathrm{p} \qquad \text{in } \Omega^\mathrm{m} \tag{2.70a}$$

$$m_\mathrm{b} = {m_\mathrm{b}}^* \qquad \text{on } \Gamma^\mathrm{m} \tag{2.70b}$$

where ${m_\mathrm{b}}^*$ is the input of the Dirichlet boundary condition, which must be chosen consistent with ${m_\mathrm{f}}^*$. In this work, the field ${m_\mathrm{b}}^*$ is set to 0 in the regions Γ^m that are over the stator, and equal to 1 where Γ^m is over the rotor. The parts of Γ^m that are not over the stator or over the rotor are set to 0.5 as illustrated in Fig. 2.10c.

The erosion operation consists of applying a smooth Heaviside projection to m_b with a threshold η_h in order to obtain the eroded field m_e. The new threshold η_h must be greater than η_th to make the transition to $m_\mathrm{e} = 1$ occur at larger values of m_b, causing a shrinkage

of the areas of m_b that are closer to 1. The erosion projection is given by

$$m_\mathrm{e} = \frac{\tanh\left(\beta_\mathrm{th}\eta_\mathrm{h}\right) + \tanh\left(\beta_\mathrm{th}\left(m_\mathrm{b} - \eta_\mathrm{h}\right)\right)}{\tanh\left(\beta_\mathrm{th}\eta_\mathrm{h}\right) + \tanh\left(\beta_\mathrm{th}(1 - \eta_\mathrm{h})\right)} \tag{2.71}$$

Similarly, the dilation operation consists of another smooth Heaviside projection to m_b to obtain m_d. This time, the threshold η_l must be lower than η_th to make the transition to $m_\mathrm{d} = 1$ occur at lower values of m_b, enlarging the areas of m_b that are closer to 1. The dilation projection is given by

$$m_\mathrm{d} = \frac{\tanh\left(\beta_\mathrm{th}\eta_\mathrm{l}\right) + \tanh\left(\beta_\mathrm{th}\left(m_\mathrm{b} - \eta_\mathrm{l}\right)\right)}{\tanh\left(\beta_\mathrm{th}\eta_\mathrm{l}\right) + \tanh\left(\beta_\mathrm{th}\left(1 - \eta_\mathrm{l}\right)\right)} \tag{2.72}$$

For assuring the conditions $\eta_\mathrm{h} > \eta_\mathrm{th}$ and $\eta_\mathrm{l} < \eta_\mathrm{th}$, a positive parameter $\Delta\eta$ is selected, and the erosion and dilation threshold are calculated as follows

$$\begin{aligned} \eta_\mathrm{h} &= \eta_\mathrm{th} + \Delta\eta \\ \eta_\mathrm{l} &= \eta_\mathrm{th} - \Delta\eta \end{aligned} \tag{2.73}$$

such that the condition $0 \leq \eta_\mathrm{l} < \eta_\mathrm{th} < \eta_\mathrm{h} \leq 1$ is satisfied. Finally, the stator and rotor fields are defined as

$$m_\mathrm{s} = 1 - m_\mathrm{d} \tag{2.74a}$$

$$m_\mathrm{r} = m_\mathrm{e} \tag{2.74b}$$

An example of the interface identification step is presented in Fig. 2.12, which continues the example from Fig. 2.11. The blurring of m_p produces intermediate values of m_b around the interface of m_p. Then, the dilation process enlarges the black areas while the dilation process shrinks them. The rotor field is taken as the eroded field itself, and the stator field is the complement of the dilated field (the black and white regions are inverted). These steps produce a fluid channel with the desired minimum thickness (gap) around the interface of m_p.

According to Høghøj et al. (2020), the minimum interface thickness is double the expression derived by Luo, Li and Liu (2019) for the infill structures. The multiplication by two arises because the method combines erosion and dilation, while the method proposed by Luo, Li and Liu (2019) applied only erosion. The minimum gap is given by

$$\begin{aligned} g_\mathrm{min} &= -2\, R_\mathrm{b} \ln\left(1 - 2\Delta\eta\right) \\ &= -\frac{r_\mathrm{b}}{\sqrt{3}} \ln\left(1 - 2\Delta\eta\right) \end{aligned} \tag{2.75}$$

This work considers $\Delta\eta = 0.45$, which yields $r_\mathrm{b} \approx 0.75\, g_\mathrm{min}$. Also, the physical filter

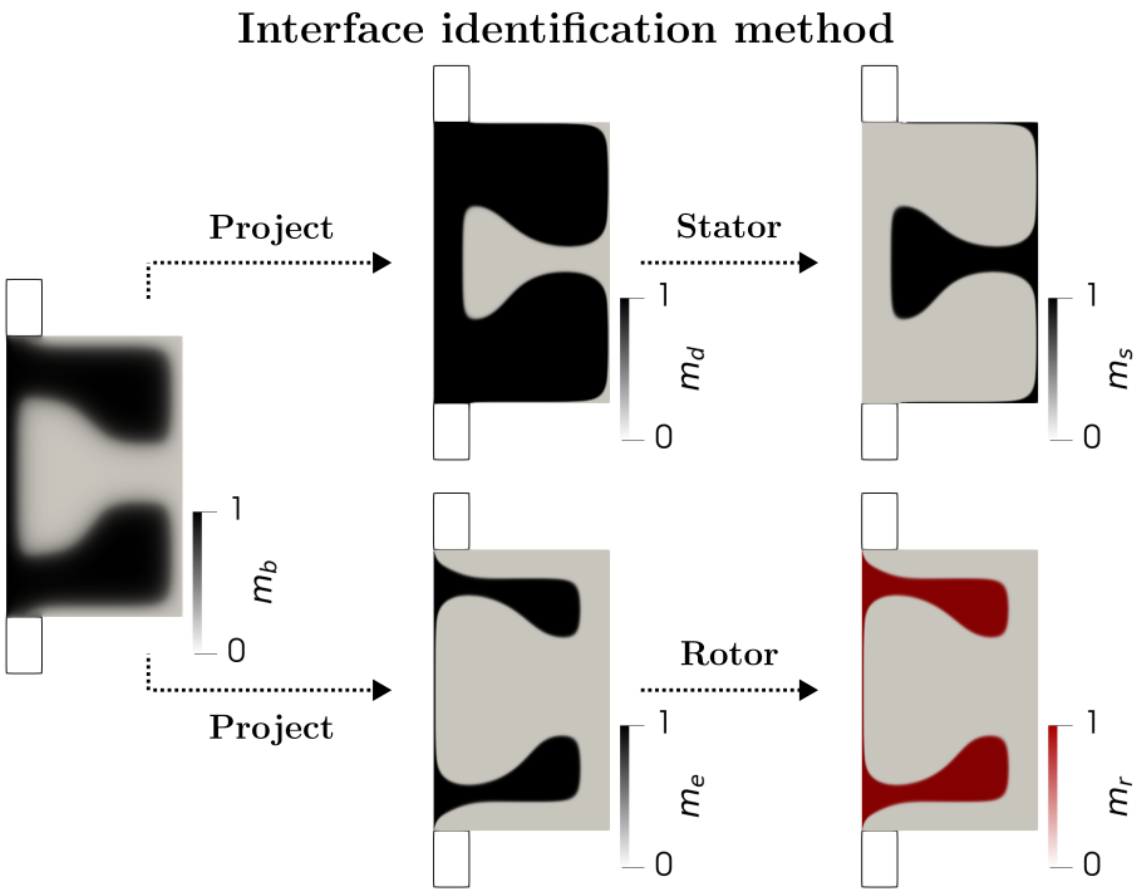

Figure 2.12 – Illustration of the operations involved in the actual interface identification step.

radius of Eq. (2.69) must be larger than the minimum gap size ($r_{\min} > g_{\min}$), and the relation $r_{\min} = 1.5\, g_{\min}$ is adopted in this work.

2.4.5.3 VFSI Connectivity Constraint

The interface identification method does not avoid free-floating islands (Fig. 2.6) as the rotor-stator algorithm. Therefore, connectivity constraints are necessary when using the interface identification method. One possibility is to devise a connectivity constraint based on FSI loads (SOUZA, 2020) because free-floating islands offer lower resistance than structural parts attached to walls. Here, the FSI formulation of Yoon (2010) is adapted to run as a staggered solver to reduce the computational cost. Also, one-way coupling from fluid to solid is considered because there are no advantages of using the monolithic approach or two-way coupling, as the accuracy of the displacement field is not important for the connectivity constraint. Actually, the monolithic approach and two-way coupling have disadvantages, which are increased computational costs and instabilities during the solution of the equilibrium equations.

For greater flexibility in tuning the constraint, fictitious parameters are used for the static equilibrium, such that the constraint will be named virtual fluid-structure constraint

(VFSI). The equilibrium equations for the VFSI are given by

$$\int_{0\Omega} \boldsymbol{\sigma}_{\mathrm{s}}(\boldsymbol{u}_f) : \boldsymbol{\varepsilon}(\boldsymbol{w}_u)\,\mathrm{d}\Omega = -\int_{0\Omega} \zeta\,(\nabla p \cdot \boldsymbol{w}_u)\;\mathrm{d}\Omega \tag{2.76}$$

where $\boldsymbol{u}_f$ is a fictitious displacement field to be used in the VFSI constraint and $\boldsymbol{w}_u$ is the test function. As a one-way staggered solver will be used, it is easy to include the FSI loads due to the velocity fields. Therefore, the equilibrium equations, including the velocity loads, will also be investigated for the VFSI constraint. In this case, the equilibrium is given by

$$\int_{0\Omega} \boldsymbol{\sigma}_{\mathrm{s}}(\boldsymbol{u}_f) : \boldsymbol{\varepsilon}(\boldsymbol{w}_u)\,\mathrm{d}\Omega = -\int_{0\Omega} \zeta\,(\nabla p \cdot \boldsymbol{w}_u)\;\mathrm{d}\Omega - \int_{0\Omega} \zeta\,\nu\left(\nabla^2 \boldsymbol{v} \cdot \boldsymbol{w}_u\right)\;\mathrm{d}\Omega \tag{2.77}$$

Structural compliance is the most studied measure of mechanical resistance in topology optimization. Therefore, it is chosen to define the VFSI constraint, and the fictitious compliance C_f is given by

$$C_f = \int_{0\Omega} \boldsymbol{\sigma}_{\mathrm{s}}(\boldsymbol{u}_f) : \boldsymbol{\varepsilon}(\boldsymbol{u}_f)\,\mathrm{d}\Omega \tag{2.78}$$

The actual VFSI constraint G_f is a normalized version of the fictitious compliance given by

$$G_f = \frac{C_f}{\overline{C}_f} - 1 \leq 0 \tag{2.79}$$

where $\overline{C}_f$ is the admissible value of C_f that is used to normalize the virtual compliance. In this work, the value of C_f for the initial guess is used for $\overline{C}_f$, corresponding to a compliance value for a material distribution without free-floating islands.

The behavior of the VFSI constraint may be studied by analyzing two bodies immersed in a fluid flow: a free-floating circle (Fig. 2.13) and a bar attached to the wall (Fig. 2.14). The velocity and pressure magnitudes are similar in both cases; however, the virtual displacement is considerably larger for the free-floating circle, as seen in Figs. 2.13d and 2.14d. The displacement gradients are also larger, making the virtual compliance value larger for the free-floating circle ($C_f = 26$) than for the supported bar ($C_f = 1.3 \times 10^{-13}$). This remarkable difference instigates testing if the VFSI constraint can control the arise of free-floating islands during optimization.

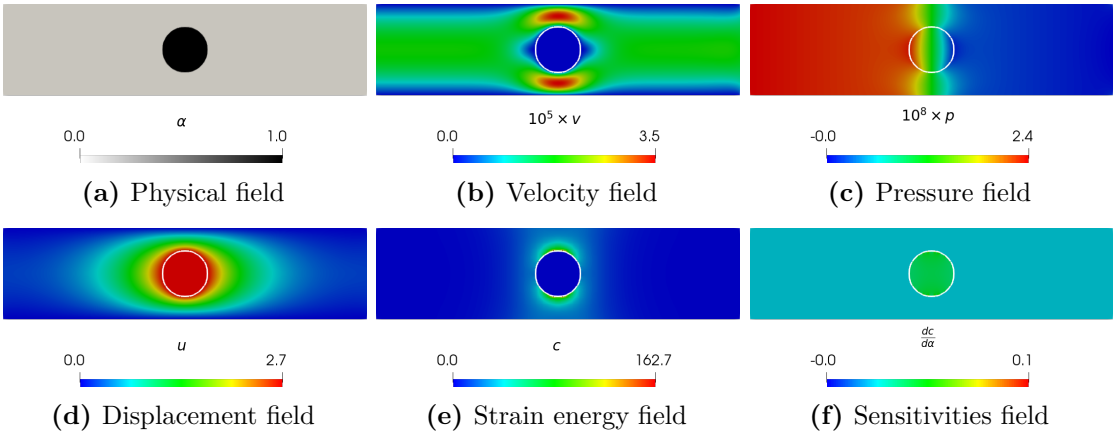

(a) Physical field **(b)** Velocity field **(c)** Pressure field

(d) Displacement field **(e)** Strain energy field **(f)** Sensitivities field

Figure 2.13 – Fields involved in the VFSI connectivity constraint for a circle inside a fluid flow channel. The virtual compliance is $C_f = 26$.

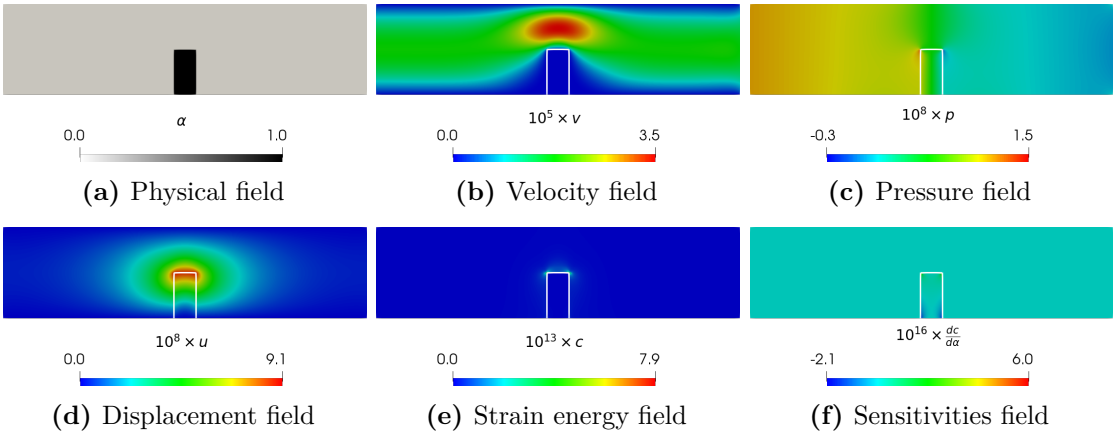

(a) Physical field **(b)** Velocity field **(c)** Pressure field

(d) Displacement field **(e)** Strain energy field **(f)** Sensitivities field

Figure 2.14 – Fields involved in the VFSI connectivity constraint for a cantilever inside a fluid flow channel. The virtual compliance is $C_f = 1.3 \times 10^{-13}$.

2.4.5.4 Virtual Temperature Method

The virtual temperature method (VTM) proposed by Liu et al. (2015) is explored in this work as an alternative connectivity constraint to avoid free-floating solid islands in the labyrinth seal design. The method consists of obtaining a virtual temperature field T_v from the solution of a thermal problem in which solid elements are heat sources, fluid elements are insulators, and the boundaries are heat sinks. This thermal problem may be written as follows

$$\nabla \cdot \left(k_\mathrm{t}\left(m_\mathrm{t}\right) \nabla T_\mathrm{v}\right) + Q\left(m_\mathrm{t}\right) = 0 \qquad \text{in } \Omega^\mathrm{m} \tag{2.80a}$$

$$T_\mathrm{v} = 0 \qquad \text{on } \Gamma^\mathrm{m} \tag{2.80b}$$

where k_t is the virtual thermal conductivity, Q is the virtual thermal heat source, and m_t

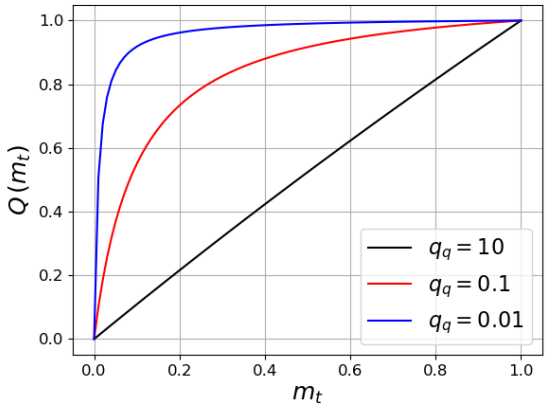

Figure 2.15 – Virtual heat generation for $Q_0 = 1$.

is the input of the VTM, which are given by

$$m_\mathrm{t} = m_\mathrm{s} + m_\mathrm{r} \tag{2.81a}$$

$$k_\mathrm{t}\left(m_\mathrm{t}\right) = k_0\, {m_\mathrm{t}}^{q_\mathrm{t}} \tag{2.81b}$$

$$Q\left(m_\mathrm{t}\right) = Q_0 \frac{m_\mathrm{t}\left(1+q_\mathrm{q}\right)}{m_\mathrm{t}+q_\mathrm{q}} \tag{2.81c}$$

where k_0 and Q_0 are the conductivity and heat generation of the solid parts, and q_t and q_q are penalization factors. The material interpolation for the virtual thermal conductivity k_t used in this work is the same of Liu et al. (2015). However, the material interpolation function for the virtual thermal heat source Q is modified from linear to concave to penalize free-floating islands with intermediate densities. The modification of Q interpolation is shown in Fig. 2.15.

The idea of the VTM is to limit the maximum value of T_v by an admissible temperature $\overline{T}_\mathrm{v}$ because the higher values would occur at floating solid islands (insulated heat sources). As the maximum function is not differentiable, a p-mean measure is used to approximate the max operator as follows

$$\begin{aligned} G_\mathrm{t} &= \max\left(T_\mathrm{v}\right) - \overline{T}_\mathrm{v} \\ &\approx \left(\frac{1}{M}\sum_{i=1}^{M}\left({T_\mathrm{v}}^{i}\right)^{p}\right)^{\frac{1}{p}} - \overline{T}_\mathrm{v} \leq 0 \end{aligned} \tag{2.82}$$

where it is noted that tuning $\overline{T}_\mathrm{v}$ is necessary to ensure the desired effect.

2.4.6 Topology Optimization of Inflatable Seals

Before designing inflatable seals, it is necessary to verify the consistency of the material models presented in Section 2.4.4 to handle pressure loads with structures undergoing large deformations. The verification considers compliance minimization under volume constraint

for literature benchmark problems. The structural compliance is given by

$$C_{\mathrm{s}}\left(\boldsymbol{u}\right) = \int_{0\Gamma_{\mathrm{n}}} \boldsymbol{t}^{*} \cdot \boldsymbol{u}\, \mathrm{d}\Gamma \tag{2.83}$$

while the volume constraint is

$$G_{V} = \frac{\int_{0\Omega} m_{\mathrm{p}}\, \mathrm{d}\Omega}{\int_{0\Omega} \mathrm{d}\Omega} - \overline{V} \leq 0 \tag{2.84}$$

This work approaches the design of inflatable seals by modeling them as compliant mechanisms. Then, the objective function selected for the design of the inflatable seals is the output port displacement (PEDERSEN; BUHL; SIGMUND, 2001), which may be written as

$$O\left(\boldsymbol{u}\right) = \frac{\int_{0\Gamma_{\mathrm{output}}} \boldsymbol{l}_{\mathrm{O}} \cdot \boldsymbol{u}\, \mathrm{d}\Gamma}{\int_{0\Gamma_{\mathrm{output}}} \mathrm{d}\Gamma} \tag{2.85}$$

where $\boldsymbol{l}_{\mathrm{O}}$ gives the output port movement direction.

2.5 Finite Element Method

The finite element method (FEM) is a numerical approach to the solution of partial differential equations. It consists of dividing the computational domain into a mesh of elements and approximating the fields by a linear combination of shape functions with compact support over the elements. The linear system of the FEM is obtained from a weak formulation of the problem and is solved for the degrees of freedom of the shape functions. Then, to obtain the finite element equations, it is necessary to derive the problem's weak formulation and apply the finite element discretization. This section presents the application of the FEM to the PDE filter (Eq. 2.46), VTM (Eq. 2.80), Navier-Stokes equations (Eq. 2.1), and RANS equations (Eq. 2.7) for illustrative purposes. As the input of FEniCS is the weak forms, Equations 2.29 and 2.77 are ready to use. The finite element formulations of the linear equations (PDE filter and VTM) are presented first because their solution is simpler than the solution of the nonlinear equations (Navier-Stokes and RANS).

2.5.1 PDE Filter

The PDE filter discretization starts by obtaining the weak form of Eq. 2.46. The first step is multiplying Eq. 2.46a by a test function w_m and integrating it over an element K of the mesh as follows

$$-{R_{\mathrm{f}}}^{2} \int_{K} \nabla^{2} m_{\mathrm{f}}\, w_m\, \mathrm{d}\Omega + \int_{K} m_{\mathrm{f}}\, w_m\, \mathrm{d}\Omega = \int_{K} m\, w_m\, \mathrm{d}\Omega \tag{2.86}$$

Then, integration by parts and the divergence theorem are applied to the first term of Eq. 2.86 to avoid second-order derivatives

$$\begin{aligned}\int_K \nabla^2 m_\mathrm{f}\, w_m \,\mathrm{d}\Omega &= \int_K \nabla\cdot\left(\nabla m_\mathrm{f}\, w_m\right)\,\mathrm{d}\Omega - \int_K \nabla m_\mathrm{f}\cdot\nabla w_m \,\mathrm{d}\Omega \\ &= \int_{\partial K} \boldsymbol{n}\cdot\left(\nabla m_\mathrm{f}\, w_m\right)\,\mathrm{d}\Gamma - \int_K \nabla m_\mathrm{f}\cdot\nabla w_m \,\mathrm{d}\Omega\end{aligned} \tag{2.87}$$

and the weak form of the PDE filter for an element K is obtained

$$R_\mathrm{f}{}^2\int_K \nabla m_\mathrm{f}\cdot\nabla w_m \,\mathrm{d}\Omega - R_\mathrm{f}{}^2\int_{\partial K}\left(\nabla m_\mathrm{f}\cdot\boldsymbol{n}\right) w_m \,\mathrm{d}\Gamma + \int_K m_\mathrm{f}\, w_m \,\mathrm{d}\Omega = \int_K m\, w_m \,\mathrm{d}\Omega \tag{2.88}$$

The next step is to sum the contribution of all the elements in the mesh

$$\begin{aligned}R_\mathrm{f}{}^2\int_{\Omega^\mathrm{m}} \nabla m_\mathrm{f}\cdot\nabla w_m \,\mathrm{d}\Omega - R_\mathrm{f}{}^2\int_{\Gamma_\mathrm{d}^\mathrm{m}}\left(\nabla m_\mathrm{f}\cdot\boldsymbol{n}\right) w_m \,\mathrm{d}\Gamma \\ - R_\mathrm{f}{}^2\int_{\Gamma_\mathrm{n}^\mathrm{m}}\left(\nabla m_\mathrm{f}\cdot\boldsymbol{n}\right) w_m \,\mathrm{d}\Gamma + \int_{\Omega^\mathrm{m}} m_\mathrm{f}\, w_m \,\mathrm{d}\Omega = \int_{\Omega^\mathrm{m}} m\, w_m \,\mathrm{d}\Omega\end{aligned} \tag{2.89}$$

The integral over $\Gamma_\mathrm{n}^\mathrm{m}$ vanishes when the Neumann boundary condition (Eq. 2.46c) is applied

$$R_\mathrm{f}{}^2\int_{\Omega^\mathrm{m}} \nabla m_\mathrm{f}\cdot\nabla w_m \,\mathrm{d}\Omega - R_\mathrm{f}{}^2\int_{\Gamma_\mathrm{d}^\mathrm{m}}\left(\nabla m_\mathrm{f}\cdot\boldsymbol{n}\right) w_m \,\mathrm{d}\Gamma + \int_{\Omega^\mathrm{m}} m_\mathrm{f}\, w_m \,\mathrm{d}\Omega = \int_{\Omega^\mathrm{m}} m\, w_m \,\mathrm{d}\Omega \tag{2.90}$$

The Dirichlet boundary condition (Eq. 2.46b) is imposed by the proper selection of the function spaces for the trial and test functions as follows

$$\begin{aligned}\mathcal{M} &= \{m \in \mathcal{H}^1(\Omega^m) : m = m_\mathrm{f}{}^* \text{ on } \Gamma_\mathrm{d}^\mathrm{m}\} \\ \mathcal{M}_0 &= \{m \in \mathcal{H}^1(\Omega^m) : m = 0 \text{ on } \Gamma_\mathrm{d}^\mathrm{m}\}\end{aligned} \tag{2.91}$$

Then, the solution of the density filter becomes: find $m_\mathrm{f} \in \mathcal{M}$ such that

$$R_\mathrm{f}{}^2\int_{\Omega^\mathrm{m}} \nabla m_\mathrm{f}\cdot\nabla w_m \,\mathrm{d}\Omega + \int_{\Omega^\mathrm{m}} m_\mathrm{f}\, w_m \,\mathrm{d}\Omega = \int_{\Omega^\mathrm{m}} m\, w_m \,\mathrm{d}\Omega, \qquad w_m \in \mathcal{M}_0 \tag{2.92}$$

The actual discretization starts by approximating the design and filtered fields by a linear combination of shape functions as follows

$$\begin{aligned}m\left(\boldsymbol{x}\right) &\approx \sum_{i=1}^{N_m} \xi_i\left(\boldsymbol{x}\right) M_i = \boldsymbol{\xi}^T\boldsymbol{m} \\ m_\mathrm{f}\left(\boldsymbol{x}\right) &\approx \sum_{i=1}^{N_m} \xi_i\left(\boldsymbol{x}\right) M_{f,i} = \boldsymbol{\xi}^T\boldsymbol{m}_\mathrm{f}\end{aligned} \tag{2.93}$$

The substitution of the finite element discretization into Eq. 2.92 for all shape functions

involved in the approximation of m and m_f results in the following system of equations

$$\begin{aligned} {R_\mathrm{f}}^2 \int_{\Omega^\mathrm{m}} \nabla \sum_{i=1}^{N_m} \xi_i M_{f,i} \cdot \nabla \xi_j \,\mathrm{d}\Omega + \int_{\Omega^\mathrm{m}} \sum_{i=1}^{N_m} \xi_i M_{f,i} \xi_j \,\mathrm{d}\Omega \\ = \int_{\Omega^\mathrm{m}} \sum_{i=1}^{N_m} \xi_i M_i \xi_j \,\mathrm{d}\Omega, \qquad j = 1, \ldots, N_m \end{aligned} \tag{2.94}$$

The matrix form of the linear system is easily seen by rearranging the equations as follows

$$\sum_{i=1}^{N_m} \left(\int_{\Omega^\mathrm{m}} {R_\mathrm{f}}^2 \nabla \xi_i \cdot \nabla \xi_j + \xi_i \xi_j \,\mathrm{d}\Omega \right) M_{f,i} = \sum_{i=1}^{N_m} \left(\int_{\Omega^\mathrm{m}} \xi_i \xi_j \,\mathrm{d}\Omega \right) M_i, \qquad j = 1, \ldots, N_m \tag{2.95}$$

where it is possible to define the matrix $\boldsymbol{K}_\mathrm{f}$ and vector $\boldsymbol{b}_\mathrm{f}$ to simplify the equation

$$\begin{aligned} K_{\mathrm{f},\,ij} &= \sum_{i=1}^{N_m} \left(\int_{\Omega^\mathrm{m}} {R_\mathrm{f}}^2 \nabla \xi_i \cdot \nabla \xi_j + \xi_i \xi_j \,\mathrm{d}\Omega \right) \\ b_{\mathrm{f},\,j} &= \sum_{i=1}^{N_m} \left(\int_{\Omega^\mathrm{m}} \xi_i \xi_j \,\mathrm{d}\Omega \right) M_i \end{aligned} \tag{2.96}$$

Finally, the density filter operation with PDE filter may be written as the solution of the following linear system

$$\boldsymbol{K}_\mathrm{f}\, \boldsymbol{m}_\mathrm{f} = \boldsymbol{b}_\mathrm{f} \tag{2.97}$$

2.5.2 Virtual Temperature Method

The same procedure used to obtain the weak form for the PDE filter is used for the VTM: Eq. 2.80a is multiplied by a test function w_t, integrated over the design domain Ω^m, and the divergence theorem is applied as follows

$$\begin{aligned} &\int_{\Omega^\mathrm{m}} \nabla \cdot \left(k_\mathrm{t}\left(m_\mathrm{t}\right) \nabla T_\mathrm{v} \right) w_t \,\mathrm{d}\Omega + \int_{\Omega^\mathrm{m}} Q\left(m_\mathrm{t}\right) w_t \,\mathrm{d}\Omega = 0 \\ &\int_{\Gamma^\mathrm{m}} \left(k_\mathrm{t}\left(m_\mathrm{t}\right) \boldsymbol{n} \cdot \nabla T_\mathrm{v} \right) w_t \,\mathrm{d}\Gamma - \int_{\Omega^\mathrm{m}} k_\mathrm{t}\left(m_\mathrm{t}\right) \nabla T_\mathrm{v} \cdot \nabla w_t \,\mathrm{d}\Omega + \int_{\Omega^\mathrm{m}} Q\left(m_\mathrm{t}\right) w_t \,\mathrm{d}\Omega = 0 \end{aligned} \tag{2.98}$$

As in the previous section, the Dirichlet boundary condition (Eq. 2.80b) is imposed by properly selecting the function spaces. As the Dirichlet boundary condition is homogeneous, only one function space definition is necessary

$$\mathcal{T} = \{ T_\mathrm{v} \in \mathcal{H}^1(\Omega^\mathrm{m}) : T_\mathrm{v} = 0 \text{ on } \Omega^\mathrm{m} \} \tag{2.99}$$

Then, the virtual temperature is found by solving the following variational problem:

find $T_{\mathrm{v}} \in \mathcal{T}$ such that

$$\int_{\Omega^{\mathrm{m}}} k_{\mathrm{t}}\left(m_{\mathrm{t}}\right) \nabla T_{\mathrm{v}} \cdot \nabla w_t \,\mathrm{d}\Omega = \int_{\Omega^{\mathrm{m}}} Q\left(m_{\mathrm{t}}\right) w_t \,\mathrm{d}\Omega, \qquad w_t \in \mathcal{T} \tag{2.100}$$

The numerical solution of Eq. 2.100 requires the discretization of the virtual temperature field, which is given by

$$T_{\mathrm{v}}\left(\boldsymbol{x}\right) \approx \sum_{i=1}^{N_t} \xi_i\left(\boldsymbol{x}\right) T_{\mathrm{v},\,i} = \boldsymbol{\xi}^T \boldsymbol{T}_{\mathrm{v}} \tag{2.101}$$

with $\xi_i \in \mathcal{T}, i = 1, \cdots, N_t$. The substitution of Eq. 2.101 into Eq. 2.100 gives

$$\begin{aligned} \int_{\Omega^{\mathrm{m}}} k_{\mathrm{t}}\left(m_{\mathrm{t}}\right) \nabla \sum_{i=1}^{N_t} \xi_i T_{\mathrm{v},\,i} \cdot \nabla \xi_j \,\mathrm{d}\Omega &= \int_{\Omega^{\mathrm{m}}} Q\left(m_{\mathrm{t}}\right) \xi_j \,\mathrm{d}\Omega, \qquad j = 1, \ldots, N_t \\ \sum_{i=1}^{N_t} \left(\int_{\Omega^{\mathrm{m}}} k_{\mathrm{t}}\left(m_{\mathrm{t}}\right) \nabla \xi_i \cdot \nabla \xi_j \,\mathrm{d}\Omega \right) T_{\mathrm{v},\,i} &= \int_{\Omega^{\mathrm{m}}} Q\left(m_{\mathrm{t}}\right) \xi_j \,\mathrm{d}\Omega, \qquad j = 1, \ldots, N_t \end{aligned} \tag{2.102}$$

where it is possible to identify and define the "stiffness" matrix $\boldsymbol{K}_{\mathrm{t}}$ and the "load" vector $\boldsymbol{q}_{\mathrm{t}}$ of the FEM as follows

$$\begin{aligned} K_{\mathrm{t},\,ij} &= \sum_{i=1}^{N_t} \left(\int_{\Omega^{\mathrm{m}}} k_{\mathrm{t}}\left(m_{\mathrm{t}}\right) \nabla \xi_i \cdot \nabla \xi_j \,\mathrm{d}\Omega \right) \\ q_{\mathrm{t},\,j} &= \int_{\Omega^{\mathrm{m}}} Q\left(m_{\mathrm{t}}\right) \xi_j \,\mathrm{d}\Omega \end{aligned} \tag{2.103}$$

Then, the degrees of freedom of the virtual temperature field are found by solving the following linear system

$$\boldsymbol{K}_{\mathrm{t}}\, \boldsymbol{T}_{\mathrm{v}} = \boldsymbol{q}_{\mathrm{t}} \tag{2.104}$$

2.5.3 Incompressible Navier-Stokes Equations

This work investigated two finite element approaches for solving the incompressible Navier-Stokes equations: the Continuous Galerkin (CG-FEM) and the Discontinuous Galerkin (DG-FEM). The idea was to explore which approach is better suited for receiving the solution from the finite volume method (FVM). As discussed in Appendix B, the DG-FEM formulation did not present advantages when interfacing with the finite volume method, so the CG-FEM formulation is used in this work with Taylor-Hood elements (TAYLOR; HOOD, 1973), i.e., quadratic and linear shape functions for velocity and pressure fields, respectively. Still, the DG-FEM formulation is presented here for completeness and to enable reproduction from the study of Appendix B.

In the CG-FEM approach, adjacent elements share some degrees of freedom, so the primal variables of the problem are $\mathcal{C}^0$-continuous across internal facets. Also, applying strong boundary conditions for the velocity is usual when using CG-FEM. Therefore, the

velocity test functions $\boldsymbol{w}_v$ must be zero at ${}^0\Gamma_{\mathrm{v}}$. By defining the following function spaces

$$\begin{aligned}
&\mathcal{V} = [\mathcal{H}({}^0\Omega)]^{n_{\mathrm{d}}} \\
&\mathcal{V}_0 = \{\boldsymbol{v} \in [\mathcal{H}({}^0\Omega)]^{n_{\mathrm{d}}} : \boldsymbol{v} = 0 \text{ on } {}^0\Gamma_{\mathrm{v}}\} \\
&\mathcal{Q} = \mathcal{L}_2({}^0\Omega)
\end{aligned} \tag{2.105}$$

the CG-FEM formulation for problem 2.1 is

$$\begin{aligned}
a(\nu;\, \boldsymbol{v},\, \boldsymbol{w}_v) + c(\boldsymbol{v};\, \boldsymbol{v},\, \boldsymbol{w}_v) + b(\boldsymbol{w}_v,\, p) = l(\boldsymbol{w}_v) \quad &\forall \boldsymbol{w}_v \in \mathcal{V}_0 \\
b(\boldsymbol{v},\, w_p) = 0 \qquad &\forall w_p \in \mathcal{Q}
\end{aligned} \tag{2.106}$$

where the forms are given by

$$\begin{aligned}
a(\nu;\, \boldsymbol{v},\, \boldsymbol{w}_v) &= \int_{{}^0\Omega} \frac{\nu}{2}(\nabla \boldsymbol{v} + \nabla \boldsymbol{v}^T) : (\nabla \boldsymbol{w}_v + \nabla \boldsymbol{w}_v{}^T)\, \mathrm{d}\Omega \\
b(\boldsymbol{v},\, p) &= -\int_{{}^0\Omega} p\, (\nabla \cdot \boldsymbol{v})\, \mathrm{d}\Omega \\
c(\boldsymbol{v}_c;\, \boldsymbol{v},\, \boldsymbol{w}_v) &= \int_{{}^0\Omega} ((\boldsymbol{v}_c \cdot \nabla)\, \boldsymbol{v}) \cdot \boldsymbol{w}_v\, \mathrm{d}\Omega \\
l(\boldsymbol{w}_v) &= \int_{{}^0\Gamma_{\mathrm{n}}} \boldsymbol{t}^* \cdot \boldsymbol{w}_v\, \mathrm{d}\Gamma
\end{aligned} \tag{2.107}$$

The fluid flow equations in weak form may also be written in mixed form by summing the linear momentum and continuity equations as follows

$$\begin{aligned}
F_{\mathrm{ns}}\,(\nu;\, \boldsymbol{v},\, p,\, \boldsymbol{w}_v,\, w_p) = a(\nu;\, \boldsymbol{v},\, \boldsymbol{w}_v) + c(\boldsymbol{v};\, \boldsymbol{v},\, \boldsymbol{w}_v) + b(\boldsymbol{w}_v,\, p) \\
+ b(\boldsymbol{v},\, w_p) - l(\boldsymbol{w}_v) = 0, \qquad \forall\, (\boldsymbol{w}_v,\, w_p) \in (\mathcal{V}_0,\, \mathcal{Q})
\end{aligned} \tag{2.108}$$

In the DG-FEM approach, adjacent elements do not share degrees of freedom, so the primal variables are discontinuous across internal facets. As the degrees of freedom are not located at the boundary of the computational domain, it is necessary to apply the boundary conditions in a weak sense. By applying the Nitsche's method, the DG-FEM formulation for problem 2.1 is

$$\begin{aligned}
a_{IP}(\nu;\, \boldsymbol{v},\, \boldsymbol{w}_v) + c(\boldsymbol{v};\, \boldsymbol{v},\, \boldsymbol{w}_v) + b_w(\boldsymbol{w}_v,\, p) = l_{IP}(\nu; \boldsymbol{w}_v) \quad &\forall \boldsymbol{w}_v \in \mathcal{V} \\
b_w(\boldsymbol{v},\, w_p) = l_C(w_p) \qquad &\forall w_p \in \mathcal{Q}
\end{aligned} \tag{2.109}$$

where the forms are

$$\begin{aligned} a_{IP}(\nu;\, \boldsymbol{v},\, \boldsymbol{w}_v) = a(\nu;\, \boldsymbol{v},\, \boldsymbol{w}_v) \\ - \int_{{}^0\Gamma_{\mathrm{v}} \cup {}^0\Gamma_{\mathrm{i}}} \left\{ \nu \left(\nabla \boldsymbol{v} + \nabla \boldsymbol{v}^T \right) \right\} : [\![\boldsymbol{n} \otimes \boldsymbol{w}_v]\!] \, \mathrm{d}\Omega \\ - \int_{{}^0\Gamma_{\mathrm{v}} \cup {}^0\Gamma_{\mathrm{i}}} \left\{ \nu \left(\nabla \boldsymbol{w}_v + \nabla \boldsymbol{w}_v{}^T \right) \right\} : [\![\boldsymbol{n} \otimes \boldsymbol{v}]\!] \, \mathrm{d}\Omega \\ + \int_{{}^0\Gamma_{\mathrm{v}} \cup {}^0\Gamma_{\mathrm{i}}} \gamma_{\mathrm{ip}} [\![\boldsymbol{n} \otimes \boldsymbol{v}]\!] : [\![\boldsymbol{n} \otimes \boldsymbol{w}_v]\!] \, \mathrm{d}\Gamma \end{aligned} \tag{2.110}$$

$$\begin{aligned} b_w(\boldsymbol{v},\, p) = b(\boldsymbol{v},\, p) \\ + \int_{{}^0\Gamma_{\mathrm{v}} \cup {}^0\Gamma_{\mathrm{i}}} \{p\} \, [\![\boldsymbol{n} \cdot \boldsymbol{v}]\!] \, \mathrm{d}\Gamma \end{aligned} \tag{2.111}$$

$$\begin{aligned} c_w(\boldsymbol{v}_c;\, \boldsymbol{v},\, \boldsymbol{w}_v) = \int_{{}^0\Gamma_{\mathrm{n}}} (\boldsymbol{n} \cdot \boldsymbol{v}_c)(\boldsymbol{v} \cdot \boldsymbol{w}_v) \, \mathrm{d}\Gamma \\ + \int_{{}^0\Gamma_{\mathrm{v}} \cup {}^0\Gamma_{\mathrm{i}}} \mathcal{H}^F(\boldsymbol{v}_c,\, \boldsymbol{v}) \cdot [\![\boldsymbol{w}_v]\!] \, \mathrm{d}\Gamma \\ - \int_{{}^0\Omega} ((\boldsymbol{v}_c \cdot \nabla)\boldsymbol{v}) \cdot \boldsymbol{w}_v \, \mathrm{d}\Omega \end{aligned} \tag{2.112}$$

$$\begin{aligned} l_{IP}(\nu;\, \boldsymbol{w}_v) = l(\boldsymbol{w}_v) \\ + \int_{{}^0\Gamma_{\mathrm{v}}} \gamma_{\mathrm{ip}} \left(\boldsymbol{v}^* \cdot \boldsymbol{w}_v \right) \, \mathrm{d}\Gamma \\ - \int_{{}^0\Gamma_{\mathrm{v}}} \left\{ \nu \left(\nabla \boldsymbol{w}_v + \nabla \boldsymbol{w}_v{}^T \right) \right\} : [\![\boldsymbol{n} \otimes \boldsymbol{v}^*]\!] \, \mathrm{d}\Omega \end{aligned} \tag{2.113}$$

$$l_C(w_p) = \int_{{}^0\Gamma_{\mathrm{v}}} w_p \left(\boldsymbol{n} \cdot \boldsymbol{v}^* \right) \, \mathrm{d}\Gamma \tag{2.114}$$

and γ_{ip} is a large constant, and ${}^0\Gamma_{\mathrm{i}}$ are the internal edges of the mesh. The Navier-Stokes equations are nonlinear and require an iterative solution algorithm. In this work, the Newton-Raphson method is used.

2.5.4 Reynolds-Averaged Navier-Stokes (RANS) Equations

The weak forms of the RANS equations are the same as the incompressible Navier-Stokes equations with the substitution of the instantaneous variables $\boldsymbol{v}$ and p by the time-averaged variables $\overline{\boldsymbol{v}}$ and $\overline{p}$, and the substitution of the molecular viscosity ν by the effective viscosity ν_{eff} as follows

$$\begin{aligned} a(\nu_{\mathrm{eff}};\, \overline{\boldsymbol{v}},\, \boldsymbol{w}_v) + c(\overline{\boldsymbol{v}};\, \overline{\boldsymbol{v}},\, \boldsymbol{w}_v) + b(\boldsymbol{w}_v, \overline{p}) = l(\boldsymbol{w}_v) \quad \forall \boldsymbol{w}_v \in \mathcal{V}_0 \\ b(\overline{\boldsymbol{v}},\, w_p) = 0 \qquad \forall w_p \in \mathcal{Q} \end{aligned} \tag{2.115}$$

Similarly, the mixed forms of the RANS equations are obtained by substituting $\overline{\boldsymbol{v}}$, $\overline{p}$,

and ν_{eff} into the mixed form of the Navier-Stokes equations

$$F_{\text{rans}} = F_{\text{ns}}\left(\nu_{\text{eff}};\, \overline{\boldsymbol{v}},\, \overline{p},\, \boldsymbol{w}_v,\, w_p\right) \tag{2.116}$$

The problem above is not closed because the turbulence model is not included. The weak form of the Spalart-Allmaras model may be written as follows

$$\begin{aligned} F_{\text{sa}}\left(\nu,\, \overline{\boldsymbol{v}};\, \tilde{\nu},\, w_{\tilde{\nu}}\right) = & \int_{0_\Omega} \left(\overline{\boldsymbol{v}} \cdot \nabla\tilde{\nu}\right) w_{\tilde{\nu}}\, \mathrm{d}\Omega - \int_{0_\Omega} c_{\text{b1}}\tilde{W}\tilde{\nu} w_{\tilde{\nu}}\, \mathrm{d}\Omega \\ & + \int_{0_\Omega} \left(\frac{\nu+\tilde{\nu}}{\sigma_{\tilde{\nu}}}\right) \nabla\tilde{\nu} \cdot \nabla w_{\tilde{\nu}}\, \mathrm{d}\Omega - \int_{0_\Omega} \frac{c_{\text{b2}}}{\sigma_{\tilde{\nu}}} \nabla\tilde{\nu} \cdot \nabla w_{\tilde{\nu}}\, \mathrm{d}\Omega \\ & + \int_{0_\Omega} c_{\text{w1}} f_{\text{w}} \left(\frac{\tilde{\nu}}{l_{\text{w}}}\right)^2 w_{\tilde{\nu}}\, \mathrm{d}\Omega + \int_{0_\Omega} \lambda_{\tilde{\nu}} \kappa_{\tilde{\nu}}\left(\alpha\right) \tilde{\nu} w_{\tilde{\nu}}\, \mathrm{d}\Omega = 0 \end{aligned} \tag{2.117}$$

Then, the closed RANS equations in mixed form are

$$F^{\text{sa}}_{\text{rans}} = F_{\text{rans}} + F_{\text{sa}} = 0, \qquad \forall\left(\boldsymbol{w}_v,\, w_p,\, w_{\tilde{\nu}}\right) \in \left(\mathcal{V},\, \mathcal{Q},\, \mathcal{N}\right) \tag{2.118}$$

where $\mathcal{N} = \mathcal{L}_2({}^0\Omega)$.

3 NUMERICAL IMPLEMENTATION

3.1 Topology Optimization Implementation

The numerical implementation of the topology optimization algorithm follows the flowchart presented in Fig. 3.1. The first step is selecting an initial guess for the design variables, which is an important step as most problems have a myriad of local minima and different results are obtained by starting with different initial guesses. Then, the forward problem (physics) is solved and the state variables are used to compute the objective function. Next, the sensitivity analysis is performed to obtain the derivatives for gradient-based optimization (SIGMUND, 2011). Here, the sensitivities are calculated following the discrete-adjoint approach using automatic differentiation. Then, the design variables are updated by a gradient-based optimization algorithm and the convergence (stopping criteria) is checked. In this work, the flowchart logic is implemented in Python due to its flexibility, extensive availability of scientific libraries, and open-source license, while the most computationally intensive parts of the method run in native libraries through just-in-time compilation or Python bindings.

The most common initial guess in fluid flow topology optimization is a domain composed of only fluid elements (which will be called pure fluid domain for brevity). At the same time, it is common to start from a solid domain in structural topology optimization. In this work, the pure fluid domain initial guess is mostly used. However, designs starting with features, such as teeth on rotor and/or stator, are also explored. The initial guesses are imposed by setting the values of the degrees of freedom of the design variable field

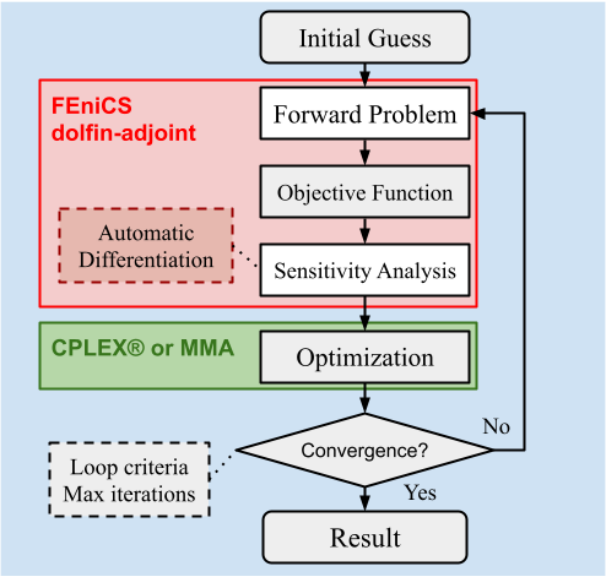

Figure 3.1 – Flowchart illustrating the topology optimization procedure used in this work

before the optimization starts. These values are kept constant until the optimization algorithm routine is called to update the design variable field. This process is repeated in each iteration until convergence is reached. The forward problem solution, the sensitivity analysis and the optimization are implemented with the theory presented in Chapter 2 and the tools described in Section 3.2. Two optimization algorithms are used depending on the characteristics of the design variables, with TOBS being used for discrete variables and MMA being used for continuous variables.

3.1.1 TOBS

Two optimization stopping criteria are commonly used in the TOBS approach. The first is the minimum change of objective function ϵ_C required to continue the optimization, which is proposed by Huang and Xie (2007) and calculated based on the last iterations. The second is the maximum number of iterations $n_{\max}$. However, the selection of ϵ_C is not trivial for challenging problems, such as the design of fluidic diodes and compliant mechanisms, because the first condition may be satisfied prematurely if the selected value of ϵ_C is "high", precluding further optimization, or may never be satisfied if ϵ_C is "low" and the optimization enters in a cycle of the same designs, as illustrated in Fig. 3.2. In this case, the optimization runs without improvements until the maximum number of iterations is reached, wasting computational resources. Therefore, selecting ϵ_C may become a time-consuming process. In fact, according to Sigmund and Maute (2013), selecting the convergence criteria is challenging in discrete density approaches of topology optimization. Therefore, it is important to investigate new convergence criteria for discrete design variables. The problems described above (stopping the optimization prematurely or never stopping the optimization) are circumvented with the stopping criteria proposed in Moscatelli et al. (2022), which consists of comparing the current design with the last w_S iterations and stopping the optimization in case of repetition. The window size w_S is restricted to avoid a high computational cost in the stopping criteria verification.

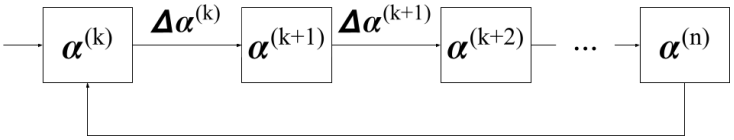

Figure 3.2 – Diagram showing a cycle between the same designs inside a topology optimization routine

3.1.2 MMA

The topology optimization with continuous design variables uses the MMA algorithm with two stopping criteria. The first criterion is that the change of at least one design variable must be larger than a tolerance ϵ_m for continuing the optimization. This stopping

criteria may be written as follows

$$\left\|\boldsymbol{m}^{(i+1)} - \boldsymbol{m}^{(i)}\right\|_{\infty} = \max\left\{\boldsymbol{m}^{(i+1)} - \boldsymbol{m}^{(i)}\right\} \leq \epsilon_m \tag{3.1}$$

where the superscript of the design variable array indicates the iteration number. The second stopping criterion is the maximum number of iterations $n_{\max}$.

3.2 Software Stack

Implementing the topology optimization algorithm of Fig. 3.1 requires simulating the physics, calculating the objective function and constraints, solving the sensitivities analysis, and running gradient-based mathematical optimization. This section describes the software stack used in this work to perform each task.

3.2.1 FEniCS

FEniCS is a framework for the solution of partial differential equations by the finite element method, allowing the simulation of arbitrary physical models that may be stated as a variational problem. Simulating arbitrary physics is possible because FEniCS provides a domain-specific language, named UFL (Unified Form Language), for defining discrete variational forms and functionals (ALNÆS et al., 2014). The UFL has a high-level notation close to mathematical description, providing flexibility for solving different equations and functionality for automatic differentiation (which is useful for obtaining Jacobians and functional sensitivities). The forms defined in UFL notation are converted to efficient C++ code in UFC (Unified Form-assembly Code) convention (ALNÆS et al., 2008) by the FEniCS form compiler (FFC). The FFC provides just-in-time automatic code generation, creating flexibility during scientific investigations.

The primary user interface of FEniCS is the DOLFIN module (LOGG; WELLS, 2010), which handles the finite element assembly and the communication of other components. DOLFIN also implements data structures and interfaces to third-party linear algebra back-ends, such as PETSc (BALAY et al., 2021b; BALAY et al., 2021a), providing a complete problem-solving environment.

The motivation for using FEniCS in this work is its interface to pyadjoint library through dolfin-adjoint framework (FARRELL et al., 2013; MITUSCH; FUNKE; DOKKEN, 2019), which eases the implementation of sensitivity analysis for complex models.

3.2.2 pyadjoint/dolfin-adjoint

The derivation of adjoint models from forward models is challenging for complex problems, such as the simulation of turbulent flows with RANS equations and turbulence closure models. One technique that facilitates this process is to obtain the discrete adjoint by algorithmic differentiation (AD). Still, the standard AD approach operates on the elementary instruction level, where instructions are typically native operations of the programming language, and the AD implementation must concern memory allocations, pointer analysis, I/O, and parallel communication. To avoid these difficulties, Farrell et al. (2013) proposed using AD on a higher level of abstraction, with the forward model described by a sequence of equation solves. They implemented this idea in the libadjoint library and integrated it into the FEniCS platform through the dolfin-adjoint framework, where the forward model was described as a sequence of variational problems solutions. Then, Mitusch, Funke and Dokken (2019) improved the abstraction by considering the forward model as a sequence of operations that are not necessarily in variational form. They call these operations blocks and this block abstraction allows users to implement the derivatives of parts of the forward model manually. A new software named pyadjoint has been introduced to replace the libadjoint library. The pyadjoint module builds a graph of blocks and apply the chain rule to compute the gradients. For example, this improved abstraction allows the implementation of the smooth Heaviside projection given by Eq. 2.49 (WANG; LAZAROV; SIGMUND, 2010), which is a local (non-integral) explicit operation. The version of dolfin-adjoint used in this work is 2019.1.2, which follows the approach of (MITUSCH; FUNKE; DOKKEN, 2019).

3.2.3 FEniCS TopOpt Foam

Although FEniCS provides flexibility for implementing the finite element method, some problems, such as the simulation of incompressible fluid flow, require specialized algorithms for their solution, as the direct use of Krylov methods for linear problems or variants of Newton's method for nonlinear problems may not be sufficient for obtaining a solution. Implementing these specialized algorithms is not trivial, while they are already available in open-source codes such as OpenFoam. However, these codes do not provide automatic differentiation in general. Therefore, combining existing implementations of specialized algorithms for challenging physical problems with dolfin-adjoint would be interesting.

The FEniCS TopOpt Foam (ALONSO; RODRIGUEZ; SILVA, 2021) provides an interface between FEniCS and OpenFoam and gives access to OpenFoam through a Python API. The forward problem is solved in OpenFoam, while the adjoint problem is solved in FEniCS, allowing the combination of specialized algorithms for fluid flow simulation and flexible automatic differentiation by the discrete adjoint method. This work

attempted to use FEniCS TopOpt Foam for the topology optimization of labyrinth seals with turbulent flow without success. The objective function oscillations during optimization led the design process to poor-performing results. Consequently, the results of Chapter 4 use FEniCS without OpenFoam. Some investigations regarding the attempt to use FEniCS TopOpt Foam in this work are presented in Appendix B.

3.2.4 CPLEX®

CPLEX® is a suite of high-performance implementations of mathematical programming algorithms, such as simplex and barrier interior point methods, for solving linear (LP), mixed-integer (MIP), and quadratic programming (QP) problems. In this work, the branch-and-bound (or branch-and-cut) search algorithm of CPLEX® is used for solving each TOBS iteration by integer linear programming (ILP) as recommended by Picelli, Sivapuram and Xie (2020) for efficiency and robustness. A branch-and-bound algorithm creates a search tree of continuous LP or QP nodes, which are solved and checked for integer solutions. If the integrality condition is not satisfied, two additional nodes may be created with additional constraints, known as *bounds*, that try to induce the integer design variables. This process is called a *branch*. The creation of branches and bounds continues until there are nodes to be investigated, i.e., nodes with optimal objective function values that do not satisfy the integer design variables requirement. This work uses the version 12.10 of CPLEX®.

3.2.5 Software Environment/Reproduction of Results

Executing the algorithm presented in the flowchart of Fig. 3.1 with the software described in previous sections requires an operating system and a set of dependency libraries. The installation and configuration of all these software components is complex and time-consuming, as it is for most scientific computing projects. Therefore, it is imperative to adopt a strategy that facilitates the setup of the software environment and consequently facilitates the reproduction of results. In this work, Docker containers technology is used as already suggested by (BOETTIGER, 2014).

Containers are a virtualization technology that shares the kernel of the host operating system between isolated instances of the software environment. Therefore, this virtualization approach makes containers lightweight, and some authors have shown that there are no performance penalties for running scientific software on containers (HALE et al., 2017). In this work, the Docker runtime is used to run the containers. Docker provides a utility to record the instructions necessary to build and configure the software environment through configuration files known as Dockerfiles. These configuration files are plain text files, so their evolution can be easily tracked with version control technologies, leveraging scientific reproduction.

3.3 Algorithms

The numerical solution of nonlinear problems is challenging and requires specialized algorithms because the sole use of numerical methods (such as Newton's method) may not be enough. This work uses continuation methods inspired by the physics of each problem and implementations of Newton's method provided in the PETSc library (BALAY et al., 2021b; BALAY et al., 2021a) to obtain solutions to nonlinear problems under non-trivial conditions.

3.3.1 Continuation for Navier-Stokes Equations

Solving the Navier-Stokes with a zero initial guess may be difficult, even for a moderate Reynolds number. One alternative to circumvent this problem is to use a better initial guess. In many cases, the solution of the same problem for lower Reynolds numbers is an appropriate initial guess, and it is easier to solve the Navier-Stokes equations for lower Reynolds numbers. For incompressible flows, the Reynolds number is given by $V_c\, L_c/\nu$ (Eq. 2.3), where L_c is a geometric parameter of the problem. As L_c can not be altered, the alternatives for reducing the Reynolds number are increasing ν or reducing V_c.

The algorithm used in this work does a continuation of the kinematic viscosity ν. It comprises an initial attempt to solve the Navier-Stokes equations and two nested continuation loops that are only run if the initial attempt fails. The objective of trying to solve directly with ν is to avoid wasting computational time with continuation if it is possible to obtain a solution starting from ν. However, if the initial attempt fails, the algorithm enters the first continuation loop, which consists of multiplying ν by a factor in the base of 10 and attempting to solve the problem again with $\nu_{1\text{st}} = (10^{p_\nu})\,\nu$, where p_ν is an integer greater than 0. If the attempt succeeds, $\nu_{1\text{st}}$ is divided by 10 and the problem is solved again with the solution of the previous step taken as the initial guess. The reduction of $\nu_{1\text{st}}$ continues while the solution attempts succeeds until the target kinematic viscosity ν is reached. The second continuation loop is only used if the solution fails inside the first continuation loop. In this case, the current kinematic viscosity $\nu_{1\text{st}}$ is multiplied by a factor in the base of 2 to obtain $\nu_{2\text{nd}} = (2^{q_\nu})\,\nu_{1\text{st}}$, where q_ν is an integer greater than 0. Then, the problem is solved with ν_{2nd} sequentially, with $\nu_{2\text{nd}}$ being divided by two at each step. The second loop continues until $\nu_{2\text{nd}}$ reaches $\nu_{1\text{st}}$. If the solution fails inside the second loop, the algorithm fails. This procedure is described as pseudo-code in Algorithm 1.

The inputs of the algorithm are the initial guess $\boldsymbol{s}_0$ for the state variables $\boldsymbol{s}$ (velocity and pressure fields), the target kinematic viscosity ν, and two configurable parameters $K^{1\text{st}}_{\text{cont}}$ and $K^{2\text{nd}}_{\text{cont}}$ for adjusting the number of continuation steps in each loop. These parameters are integers and must satisfy the following conditions: $K^{1\text{st}}_{\text{cont}} > 0$ and $0 < K^{2\text{nd}}_{\text{cont}} \leq 3$. In this work, three steps are allowed for each continuation loop ($K^{1\text{st}}_{\text{cont}} = K^{2\text{nd}}_{\text{cont}} = 3$), and

Fig. 3.3 illustrates one example of a solution where the initial attempt and the attempt for $\nu_{\text{try}} = 100\,\nu$ failed for three steps at each loop. The red arrows indicate unsuccessful solution attempts and the black arrows indicate successful ones.

The initial guess $\boldsymbol{s}_0$ is 0 for the first optimization iteration, and the solution for the previous material distribution is used as the initial guess in subsequent iterations. This approach is generally more robust and faster than starting from zero at each optimization iteration, according to numerical tests performed during this research.

Algorithm 1 Solution of the incompressible Navier-Stokes equations with continuation of kinematic viscosity ν.

Input: $\boldsymbol{s}_0$, ν, $K_{\text{cont}}^{\text{1st}}$, $K_{\text{cont}}^{\text{2nd}}$
Ensure: $K_{\text{cont}}^{\text{1st}} > 0$ and $0 < K_{\text{cont}}^{\text{2nd}} \leq 3$
Output: $\boldsymbol{s}$, err

$\boldsymbol{s} \leftarrow \boldsymbol{s}_0$
err $\leftarrow$ solve($\boldsymbol{s}$, ν)
if err **then**
    $\boldsymbol{s} \leftarrow 0$
    $p_\nu \leftarrow K_{\text{cont}}^{\text{1st}}$
    while $p_\nu \geq 0$ **do**
        $\nu_{\text{1st}} \leftarrow (10^{p_\nu})\,\nu$
        $\boldsymbol{s}_{\text{last}} \leftarrow \boldsymbol{s}$
        err $\leftarrow$ solve($\boldsymbol{s}$, ν_{1st})
        if err **then**
            $\boldsymbol{s} \leftarrow \boldsymbol{s}_{\text{last}}$
            $q_\nu \leftarrow K_{\text{cont}}^{\text{2nd}}$
            while $q_\nu \geq 0$ **do**
                $\nu_{\text{2nd}} \leftarrow (2^{\,q_\nu})\,\nu_{\text{1st}}$
                err $\leftarrow$ solve($\boldsymbol{s}$, ν_{2nd})
                if err **then**
                    exit
                $q_\nu \leftarrow q_\nu - 1$
        $p_\nu \leftarrow p_\nu - 1$

According to the tests performed in this work, the continuation of viscosity is faster than running pseudo-transient algorithms such as SIMPLE.

3.3.2 Load Increment for Nonlinear Solid Mechanics

This work applies Newton's method to solve the nonlinear solid mechanics equations. As in the case of the Navier-Stokes equations, it is necessary to use a continuation scheme if the problem's solution is not achieved within a single run of Newton's method. The strategy used here is to apply load continuation with fixed increments. First, the code attempts to solve the structural equilibrium with the full load to avoid wasting time with continuation if the solution may be achieved directly. If Newton's method does not converge, the algorithm starts to solve the problem with fractions l_{frac} of the total load,

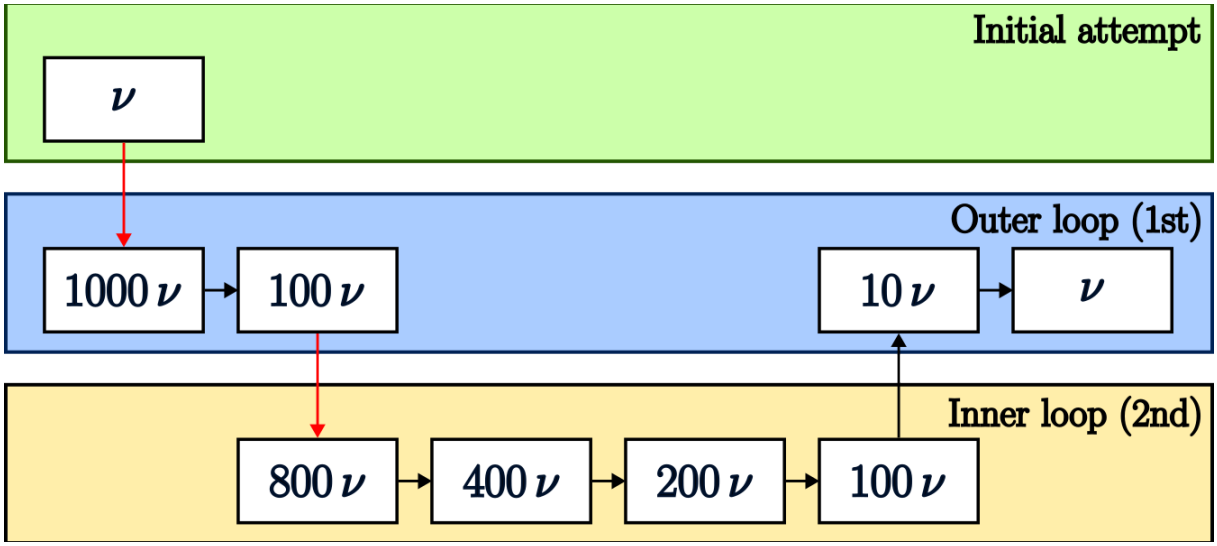

Figure 3.3 – Diagram showing one example of the continuation of the kinematic viscosity ν. Each white rectangle indicates a solution attempt with the corresponding kinematic viscosity value. The red arrows indicate unsuccessful solution attempts and the black arrows indicate successful ones. The sequence of kinematic viscosity values is obtained by following Algorithm 1 with $K_{\text{cont}}^{\text{1st}} = K_{\text{cont}}^{\text{2nd}} = 3$.

which is equivalent to solving the following modified version of Eq. 2.29

$$\int_\Omega D\,\Psi(\boldsymbol{u})[\boldsymbol{w_u}]\,\mathrm{d}\Omega - \int_\Omega l_{frac}\,\boldsymbol{s}\cdot\boldsymbol{w_u}\,\mathrm{d}\Omega - \int_\Gamma l_{frac}\,\boldsymbol{t}\cdot\boldsymbol{w_u}\,\mathrm{d}\Gamma = 0 \quad \forall \boldsymbol{w_u} \in \mathcal{U} \tag{3.2}$$

The initial guess of the displacement field is always set to zero at the beginning of the algorithm. Differently from the solution of Navier-Stokes described in Section 3.3.1, using the forward problem solution from the previous optimization iteration as an initial guess in the current iteration makes the solver less robust.

Algorithm 2 Solution of the structural equilibrium equations with continuation of the load for nonlinear solid mechanics.

Output: $\boldsymbol{s}$, err

$\boldsymbol{s} \leftarrow 0$
err $\leftarrow$ solve $(\boldsymbol{s}, 1)$
if err **then**
    $\boldsymbol{s} \leftarrow 0$
    $l_{frac} = 0.05$
    while $l_{frac} \leq 1$ **do**
        err $\leftarrow$ solve $(\boldsymbol{s}, l_{frac})$
        if err **then**
            exit
        $l_{frac} = l_{frac} + 0.05$

4 RESULTS

This section presents the topology optimization results of labyrinth seals, encompassing all the arrangements discussed in Section 1.1 and illustrated in Fig. 1.2. Each arrangement's boundary conditions and design domains are presented in Fig. 4.1. The analysis and optimization are carried out in a 2D axisymmetric domain with the geometrical parameters of Table 4.1. The equations are solved in a cylindrical coordinate system with an inertial reference frame (i.e., the reference frame is not rotating). The parameters of CO_2 at 25°C are considered for simulation (ν = 0.773 x 10^{-6} m^2/s). The other parameters, such as the maximum inlet axial velocity and the rotor angular velocity, may differ for each arrangement because the problems with a high rotor radius (staggered and stepped) are more difficult to solve due to the higher tangential velocities.

Table 4.1 – Geometrical parameters common to all the labyrinth seal problems.

Parameter	Value	Unit	Description
D	4	mm	Shaft diameter
L	16	mm	Design domain length
H	10	mm	Design domain height
e_L	3.2	mm	Inlet/outlet channel length
e_H	2	mm	Inlet/outlet channel height

The objective of this chapter is to present the advantages and disadvantages of the rotor-stator and interface identification method approaches without a direct comparison of the results. This comparison would require body-fitted extraction and analysis. However, the author did not find a unified body-fitted extraction technique suitable for both approaches. For example, the body-fitted techniques reported in (MOSCATELLI et al.,

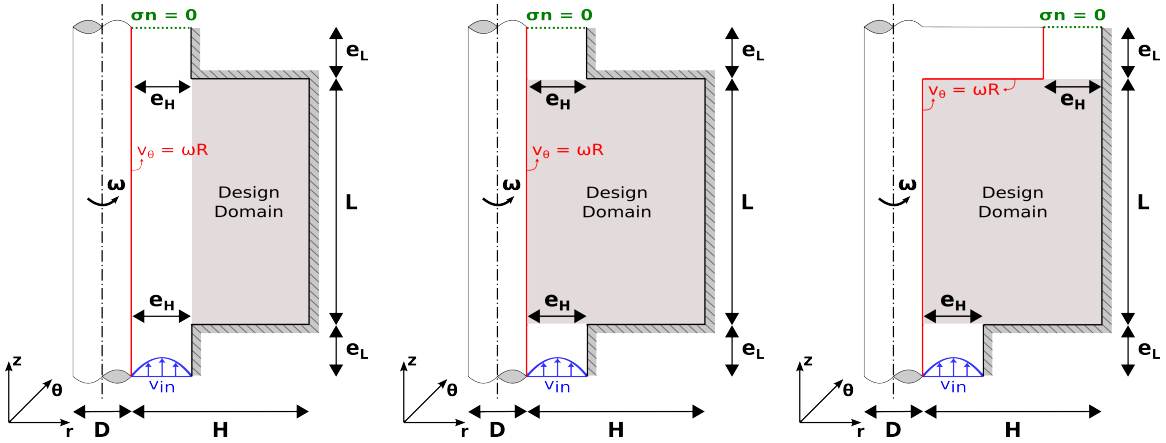

(a) Straight-through **(b)** Staggered **(c)** Stepped

Figure 4.1 – Boundary conditions and design domains for the topology optimization of different arrangements of labyrinth seals.

2022) and (MOSCATELLI et al., 2024) are different. These differences may affect the comparison, leading to wrong conclusions.

4.1 TOBS

The presentation of results starts with the designs obtained with the TOBS approach. The design of straight-through labyrinth seals is carried out with the standard TOBS approach adapted to fluid flows (SOUZA et al., 2021), while the staggered and stepped configurations require the modified approach described in Section 2.4.5.1 (MOSCATELLI et al., 2022). The results are also grouped into laminar and turbulent, with the laminar results being presented first.

4.1.1 Straight-through Labyrinth Seal in Laminar Flow

The design domain for the straight-through labyrinth seal (Fig. 4.1a) presents a non-design domain close to the rotor to keep a minimum distance between the rotor and the stator. The standard TOBS algorithm is applied with one design variable field because only the stator is optimized. The head loss is maximized subjected to the Navier-Stokes equations. Then, the linearized optimization problem solved at each iteration is written as follows

$$\begin{aligned} \max_{\Delta\alpha^{(k)}} \quad & \frac{\partial J}{\partial \alpha}\left(\boldsymbol{v}^{(k)},\, p^{(k)}\right)\Delta\alpha^{(k)} \text{ (with } J \text{ from Eq. 2.63)} \\ \text{s.t.} \quad & F_{\text{ns}}\left(\nu;\, \boldsymbol{v},\, p,\, \boldsymbol{w}_v,\, w_p\right) = 0, \quad \forall\left(\boldsymbol{w}_v,\, w_p\right) \in \left(\mathcal{V},\, \mathcal{Q}\right) \\ & \left\|\Delta\alpha^{(k)}\right\|_1 \leq \beta_{\text{fl}} N_\alpha \\ & \Delta\alpha^{(k)} \in \left\{-\alpha^{(k)}, 1-\alpha^{(k)}\right\} \end{aligned} \tag{4.1}$$

The result for laminar flow considers a parabolic inlet profile (Eq. 2.21 and Fig. 2.2b) with a maximum axial velocity of 0.77 m/s (Re = 100) and a rotation of 4000 rpm, which are around the maximum conditions that can be simulated during the optimization with the solver developed in this work for Navier-Stokes equations (see Section 3.3.1). The optimized design is a straight channel narrowed to the minimum gap size as shown in Fig. 4.2a for a flip limits of $\beta_{\text{fl}} = 10\%$. According to the convergence history (Fig. 4.2b), the head loss increases significantly in the first iteration and remains almost constant in the subsequent iterations. If the convergence history is zoomed after the first iteration, as shown in Fig. 4.2c, it is possible to see a small change in the head loss that makes the optimizer continue the optimization. Actually, these small changes are not relevant in practice as they only exist in the presence of the material model (Eq. 2.50). The Darcy number used in this section is $\text{Da} = 10^{-5}$ ($\kappa_{\max} = 7.7 \times 10^5$ 1/s).

According to the design history presented in Fig. 4.3, the optimizer places elements at the left edge of the design domain to prevent the flow from entering the chamber in the

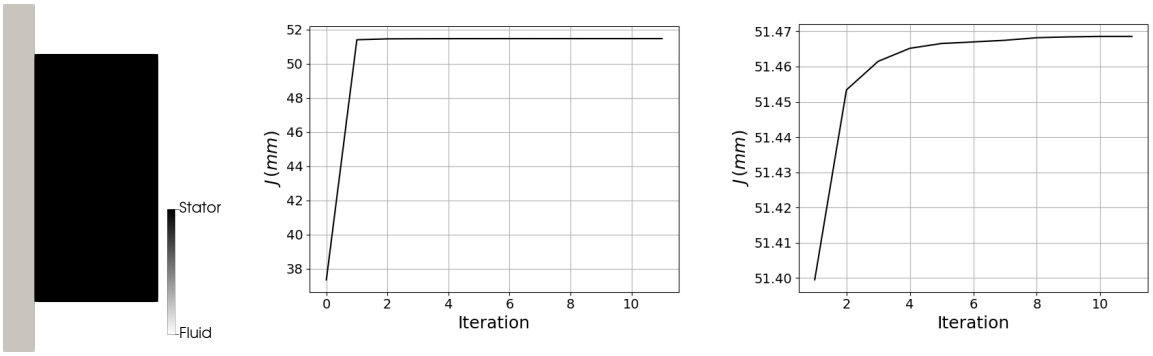

(a) Solution **(b)** Convergence history **(c)** Convergence history zoom

Figure 4.2 – Straight-through labyrinth seal design in laminar regime with $\beta_{fl} = 10\%$ (Re = 100 and $\omega_r = 4000$ rpm).

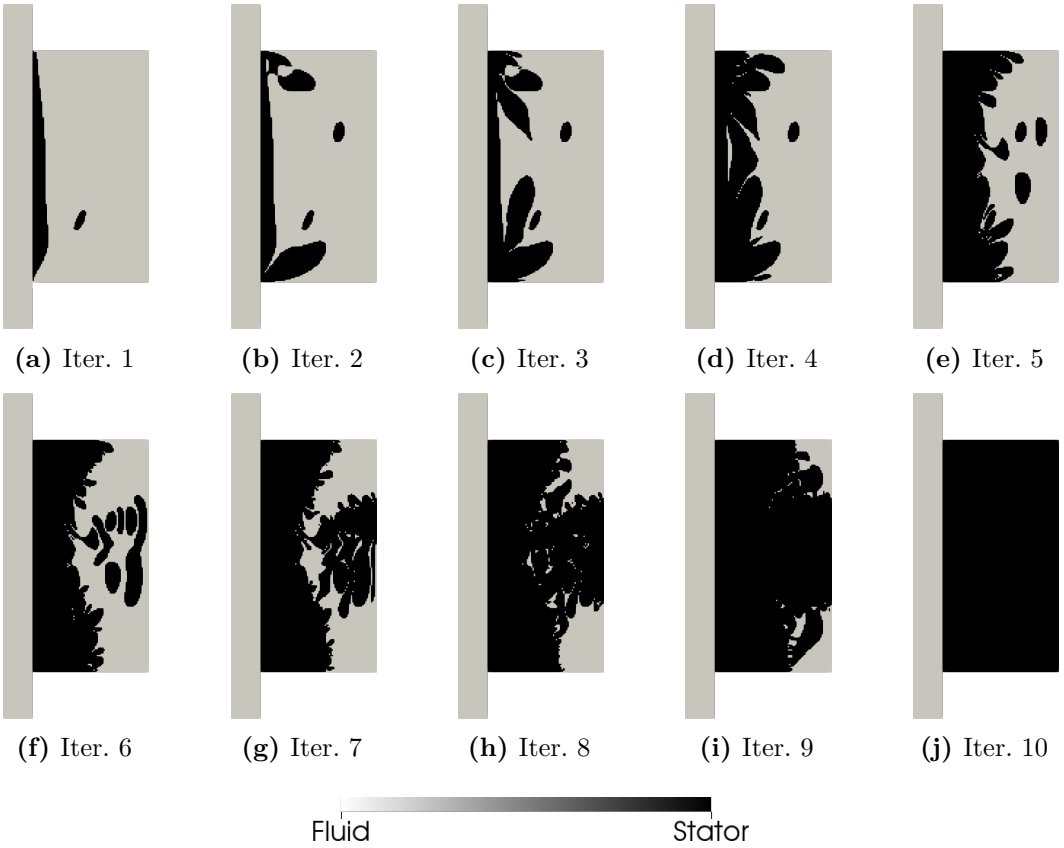

(a) Iter. 1 **(b)** Iter. 2 **(c)** Iter. 3 **(d)** Iter. 4 **(e)** Iter. 5

(f) Iter. 6 **(g)** Iter. 7 **(h)** Iter. 8 **(i)** Iter. 9 **(j)** Iter. 10

Figure 4.3 – Design history of the straight-through labyrinth seal optimized with TOBS for laminar flow (Re = 100 and 4000 rpm).

first iteration. Then, it fills the hole in the stator until there are only solid elements in the design domain. Again, the filling of the chamber only occurs because the material model indicates a small increase in head loss by adding solid material to the chamber.

One question that may arise is if the flip limit used to obtain the result of Fig. 4.2 is not large, leading to local minima. The answer to this question is "no" as the same result is obtained when β_{fl} is reduced to 1%, as shown in Fig. 4.4. The only difference is that more iterations are necessary. Also, some parts of the design domain are not filled because the expected objective function change becomes too small, as the number of allowed changes

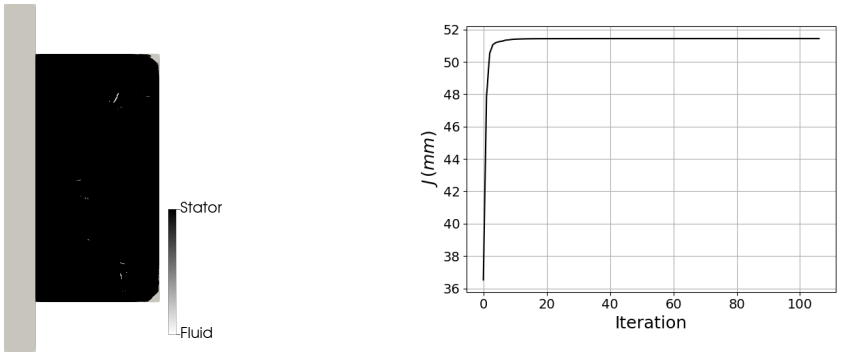

(a) Solution **(b)** Convergence history

Figure 4.4 – Straight-through labyrinth seal design in laminar regime with $\beta_{fl} = 1\%$ (Re = 100 and $\omega_r = 4000$ rpm).

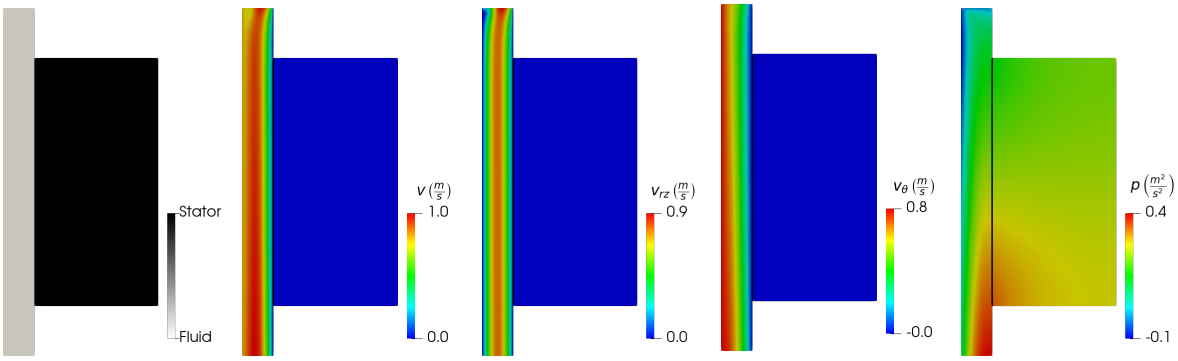

(a) Solution **(b)** Velocity **(c)** Plane velocity **(d)** Tangential velocity **(e)** Pressure

Figure 4.5 – Straight-through labyrinth seal design in laminar regime (Re = 100 and $\omega_r = 4000$ rpm).

is reduced.

The velocity and pressure fields for the labyrinth seal of Fig. 4.2a are presented in Fig. 4.5. The tangential velocity of the shaft plays an important role in the flow along the straight channel, as the velocity magnitude close to the shaft is close to the velocity at the centerline. The pressure drop occurs along the straight channel and there is some pressure drop in solid elements. According to the convergence graph (Fig. 4.2b), the straight channel is indeed more dissipative than other configurations with cavities along the labyrinth seal. As the fluid has no energy to enter the cavity, no recirculation is created in this region and the most prominent dissipation effect is associated with velocity gradients. Therefore, the optimal solution is the narrowest channel because the velocity gradient increases as the channel width decreases.

4.1.2 Staggered Labyrinth Seal in Laminar Flow

The staggered labyrinth seal is designed with the rotor-stator topology optimization algorithm (Section 2.4.5.1) with a minimum gap of $g_{\min} = e_H$. The head loss is maximized subjected to the Navier-Stokes equations. The linearized optimization problem solved at

each iteration is given by

$$\begin{aligned}
\max_{\Delta\alpha,\,\Delta\beta} \quad & \frac{\partial J}{\partial \alpha}\Delta\alpha + \frac{\partial J}{\partial \beta}\Delta\beta \text{ (with } J \text{ from Eq. 2.63)} \\
\text{s.t.} \quad & F_{\text{ns}}\left(\nu;\, \boldsymbol{v},\, p,\, \boldsymbol{w}_v,\, w_p\right) = 0, \quad \forall\left(\boldsymbol{w}_v,\, w_p\right) \in \left(\mathcal{V},\, \mathcal{Q}\right) \\
& \left\|\Delta\alpha^{(k)}\right\|_1 \leq \beta_{\text{fl}} N_\alpha \\
& \left\|\Delta\beta^{(k)}\right\|_1 \leq \beta_{\text{fl}} N_\beta \\
& \Delta\alpha \in \mathcal{S}_\alpha \\
& \Delta\beta \in \mathcal{S}_\beta
\end{aligned} \tag{4.2}$$

Initially, the same centerline velocity of the straight-through labyrinth seal is used (Re = 100); however, the shaft angular velocity is reduced to 1000 rpm. The result by starting with a pure fluid initial guess is presented in Fig. 4.6 with the rotor represented in red and the stator in black. The optimized result (Fig. 4.6a) is a curved channel constricted up to the minimum-allowed gap. There is a chamber along the channel; however, it does not improve the head loss. The optimizer does not remove the chamber because it has no effect on the objective function. The convergence graph presents a smooth convergence as seen in Fig. 4.6d. The Darcy number used in this section is lower ($\text{Da} = 10^{-10}$) than in the previous section ($\text{Da} = 10^{-5}$) because the numerical experiments showed that the solution of Eq. 2.4 with non-zero rotation is facilitated when using binary design variables and lower Darcy numbers. The flip limits of each optimization substep is $\beta_{\text{fl}} = 0.5\%$.

The velocity field is presented in Fig. 4.6b, where the rotor contour is drawn in white and the stator contour in black. It is seen that the velocity magnitude of rotor elements increases with the radial coordinate, while the velocity of stator elements is zero due to the use of two Darcy terms with different velocities. From Fig. 4.6c, it is noticed that the pressure drops along the channel, and the higher local drops occur in the connection of the design domain to the inlet and outlet channels. In fact, the distance between the rotor and the stator in these regions is lower than the minimal gap due to the way the neighborhoods are defined in Fig. 2.7 (with the ℓ_1-distance). It may be necessary to fix the neighborhood definition if this minimum gap violation is problematic. On the other hand, if a lower gap is acceptable in diagonal directions, this can be used to increase the pressure drop at some regions of the domain and to increase the conversion of pressure head to velocity head (kinetic energy) at the entrance of cavities, where the generation of turbulent eddies is desired.

The effect of the inlet velocity in the optimization result is accessed by running the rotor-stator algorithm for different inlet Reynolds numbers as seen in Fig. 4.7, where the optimized designs are presented with the streamlines of plane rz. For Re = 1 (Fig. 4.7a), the result is a channel constricted to the minimum gap size because fluid flows with low

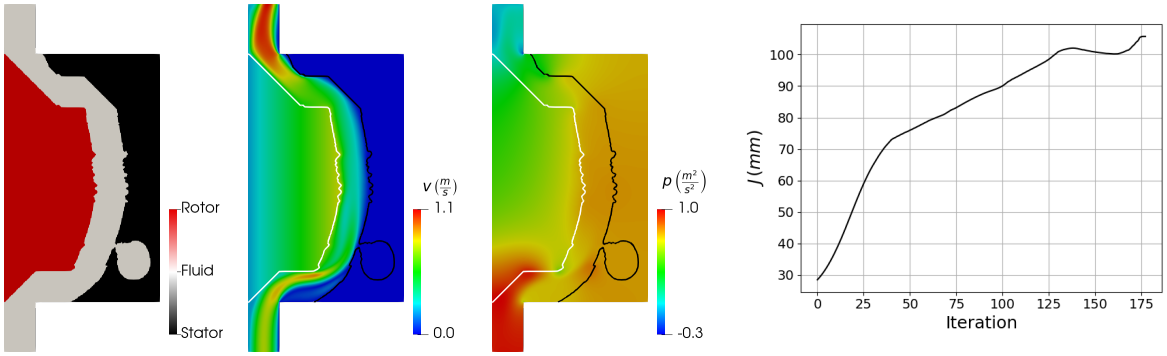

(a) Result **(b)** Velocity **(c)** Pressure **(d)** Convergence history

Figure 4.6 – Staggered labyrinth seal design in laminar regime with rotor-stator algorithm (Re = 100 and $\omega_r = 1000$ rpm).

Reynolds numbers do not form recirculation zones where additional viscous dissipation would occur. In these flows, the factors that contribute to the increase of the head loss are the magnitude of the velocity gradients and the length of the streamlines, so the stricter the passage and the longer the channel, the higher the head loss. As the inlet Reynolds number increases (Figs. 4.7b and 4.7c), the optimized designs present larger chambers with recirculation zones, which contribute to head loss by creating fluid motion that is not related to the leakage. The recirculation zones also constrained the streamlines that connect the inlet to the outlet of the seal, maintaining the velocity gradient even with the larger distance between the rotor and stator. Figure 4.7 also presents the 3D representation of the labyrinth seals for a better visualization of the results.

For low Reynolds numbers, the expected solution is a long channel constricted to the minimum gap size because the flow does not have recirculation zones. Therefore, it is possible to create intuitive solutions to benchmark the result from Fig. 4.7a as seen in Fig. 4.8. The designs of Figs. 4.8a and 4.8b have the same gap size ($g_{min} = e_H$) used to obtain Fig. 4.7a with the rotor-stator algorithm. It is seen that the head loss of the optimized result (Fig. 4.7a) is higher than the head loss of the benchmark designs (Figs. 4.8a and 4.8b), what is not expected at first sight. By examining Fig. 4.7a again, it is possible to observe that the inclined channels have a smaller gap size than the selected minimum gap ($g_{min} = e_H$). In fact, the gap size for the inclined channels is equal to $\sqrt{2}e_H/2 \approx 0.7$ due to the way the element neighborhood is defined (Fig. 2.7). So, the optimizer tries to maximize the length of the inclined channels for low Reynolds numbers. If the optimized solution is compared to benchmark designs with $g_{min} = \sqrt{2}e_H/2$, such as the ones presented in Figs. 4.8c and 4.8d, the head loss is lower. This anisotropy of the gap size could be alleviated by selecting more appropriate element neighborhoods. However, due to the binary nature of the problem, the gap minimum size will never be exactly uniform, although the anisotropy will be less pronounced in finer meshes.

The effect of the angular velocity is accessed by running the rotor-stator algorithm for different values of shaft angular velocities, and the results are presented in Fig. 4.9. The

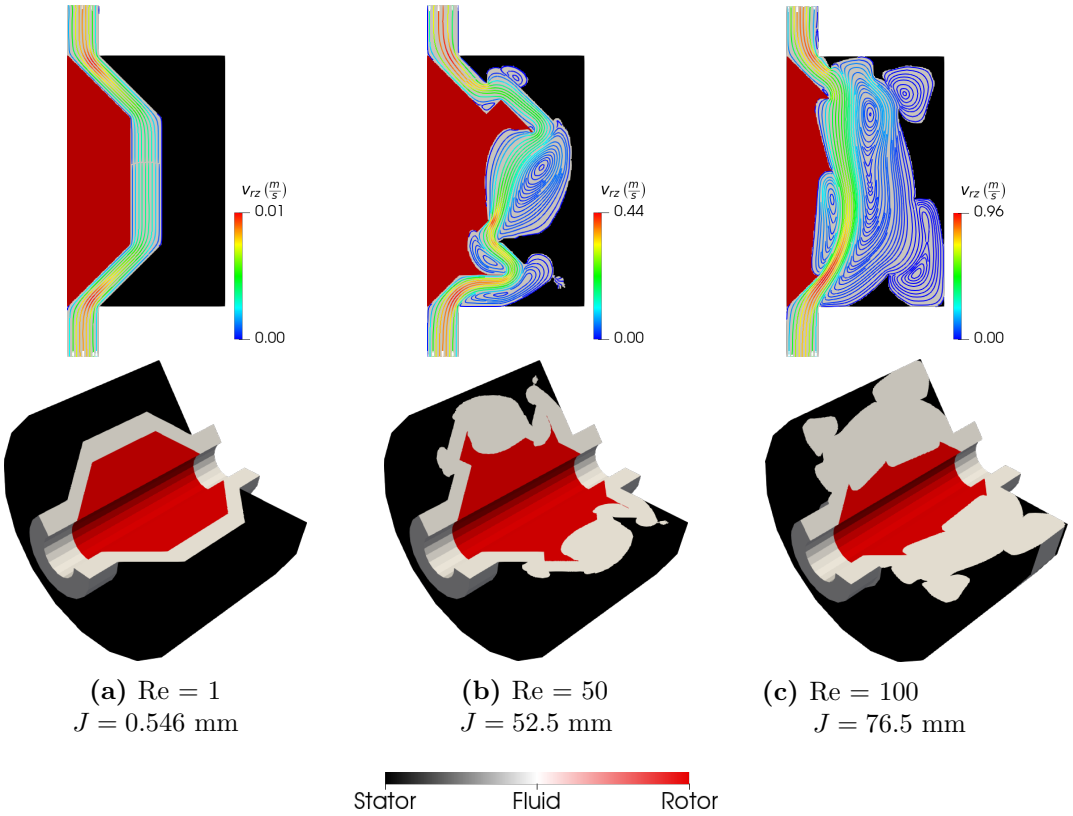

(a) Re = 1
$J = 0.546$ mm

(b) Re = 50
$J = 52.5$ mm

(c) Re = 100
$J = 76.5$ mm

Figure 4.7 – Effect of the Reynolds number on the staggered labyrinth seal design using the rotor-stator algorithm. The angular velocity is $\omega_r = 0$ rpm. The streamlines are plotted over the results.

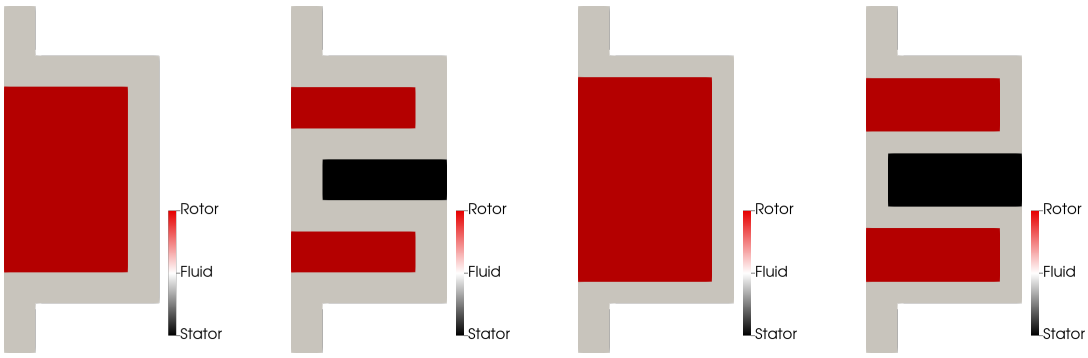

(a) $J = 0.344$ mm **(b)** $J = 0.520$ mm **(c)** $J = 0.724$ mm **(d)** $J = 1.33$ mm

Figure 4.8 – Reference designs for the staggered labyrinth seal. The head losses are evaluated at Re = 1 and $\omega_r = 0$ rpm.

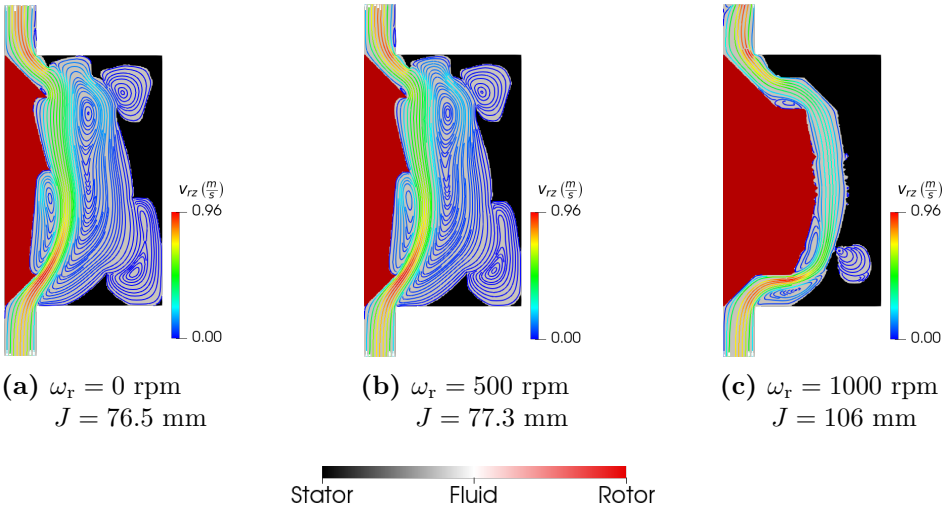

(a) $\omega_r = 0$ rpm, $J = 76.5$ mm **(b)** $\omega_r = 500$ rpm, $J = 77.3$ mm **(c)** $\omega_r = 1000$ rpm, $J = 106$ mm

Figure 4.9 – Effect of the shaft angular velocity on the staggered labyrinth seal design using the rotor-stator algorithm. The inlet Reynolds number is Re = 100.

inlet Reynolds number is fixed as Re = 100. For $\omega_r = 50$ rpm (Fig. 4.9b), the optimized result is almost the same as for the static shaft ($\omega_r = 0$ rpm), indicating that the axial and radial flows are still dominant for head loss. The optimized result is different for $\omega_r = 100$ rpm (Fig. 4.9c), indicating that the tangential velocity is also relevant for head loss. The undesired tendency to create inclined channels is still present. However, the optimizer also explores the increase of the rotor diameter, as seen in the parts of the channel that are in the radial direction.

It is interesting to investigate the effect of the initial guess in the rotor-stator algorithm, so the staggered labyrinth seal is also optimized by starting with one stator tooth, and the results are presented in Fig. 4.10. The optimizer enlarges the rotor tooth and places stator elements around it. The enlargement is uneven in the upstream and downstream directions of the tooth. In the upstream direction (or inlet direction), the fluid channel is constricted to the minimum gap size. In the downstream direction (or outlet direction), the tooth is more enlarged at the tip, creating a recirculation zone. However, the streamlines (Fig. 4.10d) show that the flow at the recirculation zone has low velocities because the fluid does not have enough energy to enter the recirculation zone.

Then, the staggered labyrinth seal is optimized by starting with two teeth, as shown in Fig. 4.11. The rotor tooth is similar in topology to the result starting with one tooth (Fig. 4.10b), being smaller in the axial direction. The stator tooth presents sharp 45° wedges, and the wedge at the tip of the tooth constricts the flow and creates a recirculation zone downstream. This mechanism is interesting in improving head loss in labyrinth seals as it reduces the actual gap by constraining the streamlines connected to the outlet with the recirculation zones.

Table 4.2 compares the results obtained for the staggered configuration by presenting the initial head loss J_0, the final head loss J, and the head loss gain. It is seen that the

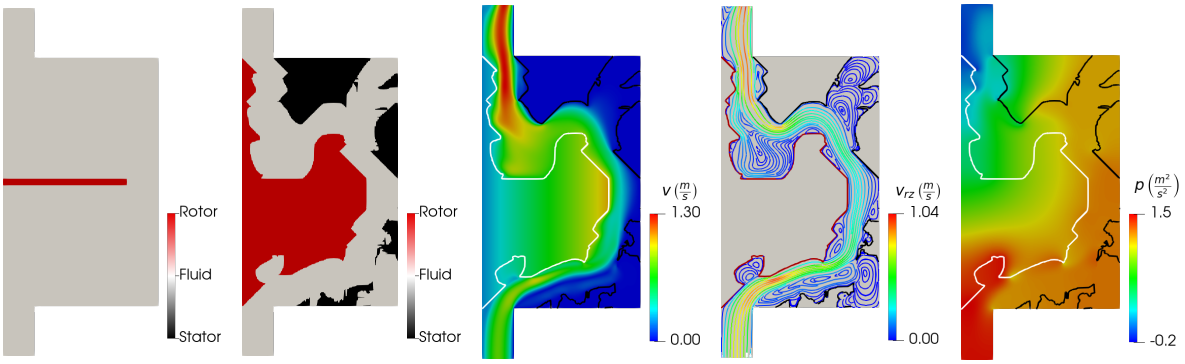

(a) Initial guess **(b)** Result **(c)** Velocity **(d)** Streamlines **(e)** Pressure

Figure 4.10 – Staggered labyrinth seal optimization with rotor-stator algorithm and an initial guess with one rotor tooth (Re = 100 and ω_r = 1000 rpm).

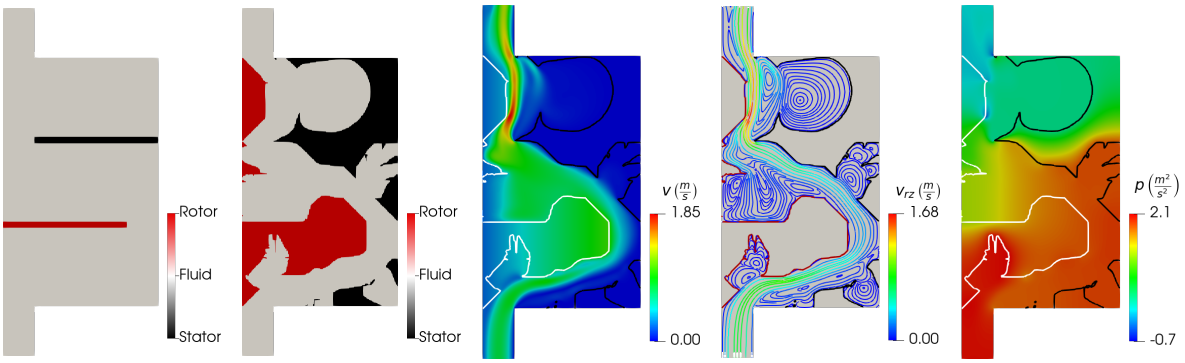

(a) Initial guess **(b)** Result **(c)** Velocity **(d)** Streamlines **(e)** Pressure

Figure 4.11 – Staggered labyrinth seal optimization with rotor-stator algorithm and an initial guess with one stator tooth and rotor tooth (Re = 100 and ω_r = 1000 rpm).

Table 4.2 – Comparison of staggered labyrinth seal objective function values for different initial guesses.

Initial guess	Results	J_0 (mm)	J (mm)	J/J_0
Pure fluid	Fig. 4.6	28.4	106	3.72
1 tooth	Fig. 4.10	91.8	159	1.74
2 teeth	Fig. 4.11	125	255	2.04

result obtained by starting with two teeth has a higher head loss, so the 45° wedge is efficient in improving the head loss. Also, the initial guess is relevant to guide the optimizer towards more optimized designs. The gain is higher when starting from a pure fluid domain because the initial head loss is low.

4.1.3 Stepped Labyrinth Seal in Laminar Flow

The stepped labyrinth seal is also optimized with the rotor-stator algorithm presented in Section 2.4.5.1 and the same optimization problem of the staggered case (Eq. 4.2) is solved. As the outlet has a higher radial coordinate for the stepped configuration, the problem becomes more challenging to solve, and the maximum angular velocity reached

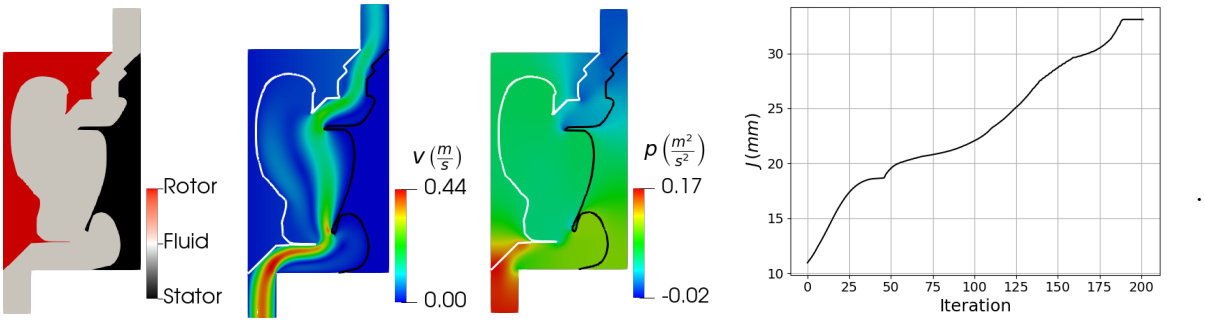

(a) Result **(b)** Velocity **(c)** Pressure **(d)** Convergence history

Figure 4.12 – Stepped labyrinth seal design in laminar regime with rotor-stator algorithm (Re = 50 and $\omega_r = 50$ rpm). The final head loss is $J = 33.1$ mm.

with the laminar solver is 50 rpm. Also, the maximum centerline velocity of the parabolic profile is reduced to 0.39 m/s (Re = 50). The other parameters are the same as for the staggered example. The optimization result is presented in Fig. 4.12 with the velocity and pressure fields. The rotor constricts the flow entering the design domain, increasing its velocity. Then, the flow is guided by a thin rotor tooth towards an inclined stator tooth that splits the flow into streamlines connected to the outlet and recirculation. The downstream flow encounters other obstacles until reaching the outlet. The optimization ends after 201 iterations. The velocity field for the stepped labyrinth seal result (Fig. 4.12b) has features that are commonly explored in labyrinth seal design (SNECK, 1974): restrictions that convert the available pressure head into kinetic energy, which is dissipated in the intervening chambers. Figure 4.12c shows a significant pressure drop in the second stator tooth without an increase in velocity, indicating head loss. The convergence curve grows monotonically.

The influence of the inlet velocity on the optimized design is studied by running the rotor-stator algorithm with Re equals 1, 25, and 50, and $\omega_r = 0$. The results are presented in Fig. 4.13. For Re = 1, the fluid does not have the necessary energy to develop recirculation regions, so the result is a channel constricted to the minimum gap size. The diagonal direction is favored due to the smaller gap size in this direction, as discussed in the previous section. For Re = 25, the result already presents chambers for recirculation; however, most of the fluid path is constricted to the minimum gap size. For Re = 50, there are more recirculation zones and the channel constrictions are concentrated at the inlet and outlet of the design domain. The effect of the angular velocity was not accessed because ω_r could not be increased beyond 50 rpm. The results of Figs. 4.13c and 4.12a are similar, indicating that for Re = 50 and $\omega_r = 50$ rpm, the effect of the angular velocity is secondary. Still, the angular velocity increases the head loss as seen by comparing the similar results of Figs. 4.12a and 4.13c, which have $J = 33.1$ and $J = 28.7$ mm, respectively.

Then, the stepped seal is optimized by starting with one rotor tooth, as seen in Fig. 4.14. The result presents a more constricted channel than the result for the pure fluid

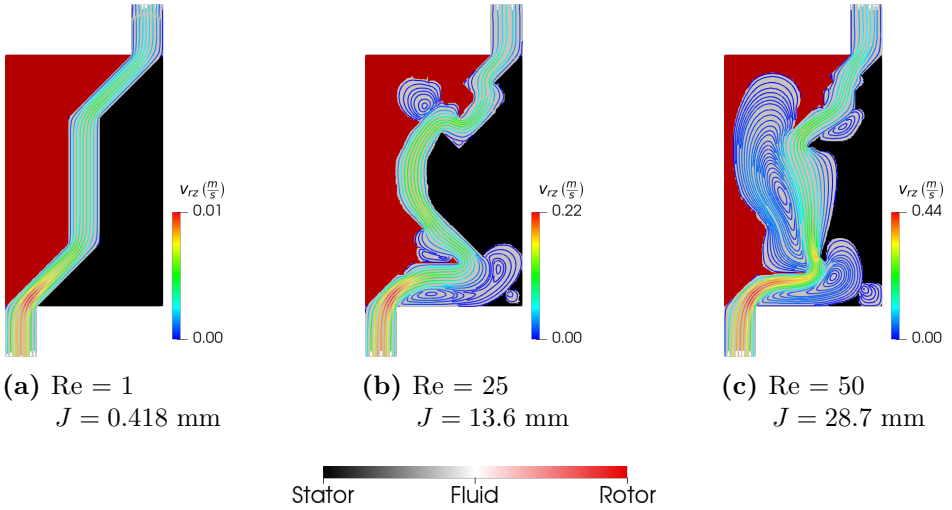

(a) Re = 1, $J = 0.418$ mm **(b)** Re = 25, $J = 13.6$ mm **(c)** Re = 50, $J = 28.7$ mm

Figure 4.13 – Effect of the Reynolds number on the stepped labyrinth seal design using the rotor-stator algorithm. The angular velocity is $\omega_r = 0$ rpm. The streamlines are plotted over the results.

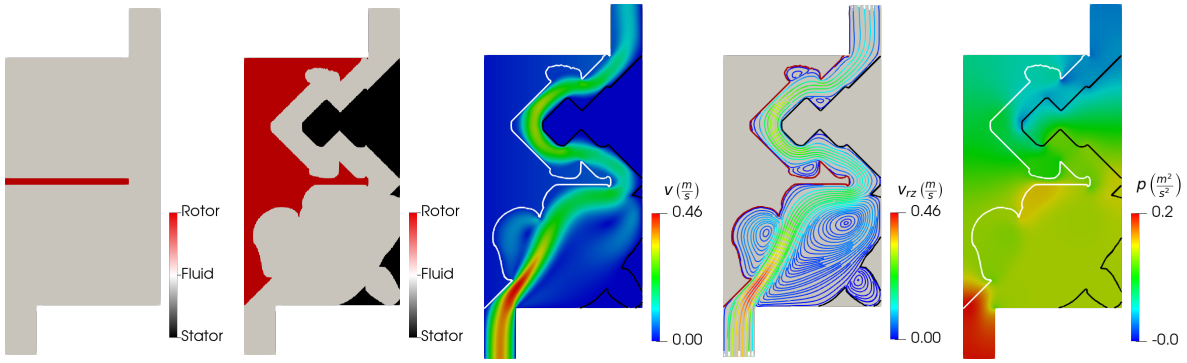

(a) Initial guess **(b)** Result **(c)** Velocity **(d)** Streamlines **(e)** Pressure

Figure 4.14 – Stepped labyrinth seal optimization with rotor-stator algorithm and an initial guess with one rotor tooth (Re = 50 and $\omega_r = 50$ rpm). The final head loss is $J = 37.0$ mm.

initial guess (Fig. 4.12a), with an increase in head loss from 33.1 to 37.0 mm. The larger head loss is caused by the longer inclined channel, which has a lower gap size. As the rotor diameter is larger, the increase of tangential velocity with radial coordinate becomes clearer. The optimization ends after 167 iterations.

The result obtained by starting with two teeth is presented in Fig. 4.15. The initial head loss is 25.3 mm, which is more than twice the head loss of the previous initial guesses. The improvement in the initial head loss occurs because the second tooth deviates the flow from the outlet. The final head loss is 53.1 mm, which is also high. The optimized solution presents two small stator teeth, one close to the outlet and the other to the rotor tooth. These small stator teeth promote additional constriction and split the flow in the main flow and in recirculation zones, as seen in the streamlines plot (Fig. 4.15d). The optimization ends after 110 iterations.

Table 4.3 summarizes the comparison of the stepped results for different initial guesses. As for the staggered labyrinth seal, the result obtained by starting with two teeth presents

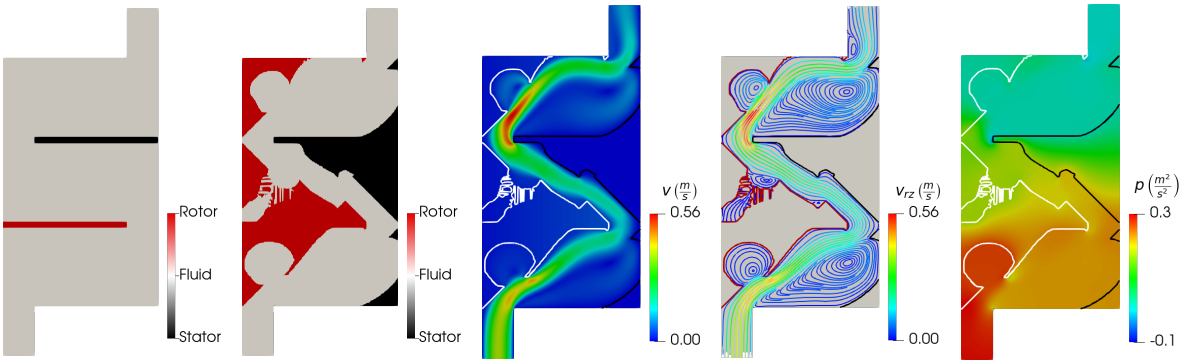

(a) Initial guess **(b)** Solution **(c)** Velocity **(d)** Streamlines **(e)** Pressure

Figure 4.15 – Stepped labyrinth seal optimization with rotor-stator algorithm and an initial guess with one stator tooth and rotor tooth (Re = 50 and $\omega_r = 50$ rpm). The final head loss is $J = 53.1$ mm.

Table 4.3 – Comparison of stepped labyrinth seal objective function values for different initial guesses.

Initial guess	Results	J_0 (mm)	J (mm)	J/J_0
Pure fluid	Fig. 4.12	10.9	33.1	3.02
1 tooth	Fig. 4.14	12.6	37.0	2.94
2 teeth	Fig. 4.15	25.3	53.1	2.10

a higher head loss. The results starting with pure fluid domain and one tooth present similar values at the initial and final designs, showing that the tooth does not contribute considerably to the head loss. Although the tooth guides imposes an annular orifice to the flow, it also guides the fluid towards the outlet.

4.1.4 Straight-through Labyrinth Seal in Turbulent Flow

The first arrangement optimized for turbulent flow is the straight-through (Fig. 4.1a). The design follows the standard TOBS approach for fluid flow topology optimization, with the optimization problem written as

$$\begin{aligned} \max_{\Delta\alpha^{(k)}} \quad & \frac{\partial J}{\partial \alpha}\left(\overline{\boldsymbol{v}}^{(k)}, \overline{p}^{(k)}\right)\Delta\alpha^{(k)} \text{ (with } J \text{ from Eq. 2.63)} \\ \text{s.t.} \quad & F_{\text{rans}}\left(\nu_{\text{eff}}; \overline{\boldsymbol{v}}, \overline{p}, \tilde{\nu}, \boldsymbol{w}_v, w_p, w_{\tilde{\nu}}\right) = 0, \quad \forall\left(\boldsymbol{w}_v, w_p, w_{\tilde{\nu}}\right) \in \left(\mathcal{V}, \mathcal{Q}, \mathcal{N}\right) \\ & \left\|\Delta\alpha^{(k)}\right\|_1 \leq \beta_{\text{fl}} N_\alpha \\ & \Delta\alpha^{(k)} \in \left\{-\alpha^{(k)}, 1-\alpha^{(k)}\right\} \end{aligned} \tag{4.3}$$

The straight-through results in turbulent flow are presented in Fig. 4.16. The inlet velocity is increased to 3.86 m/s (Re = 500), the rotation is increased to 10000 rpm, and the RANS equations with Spalart-Allmaras model are used to simulate the fluid flow. For higher velocities, the turbulent eddies are the main mechanism of energy dissipation and head loss. Therefore, the optimizer does not constrict the channel to the minimum gap size

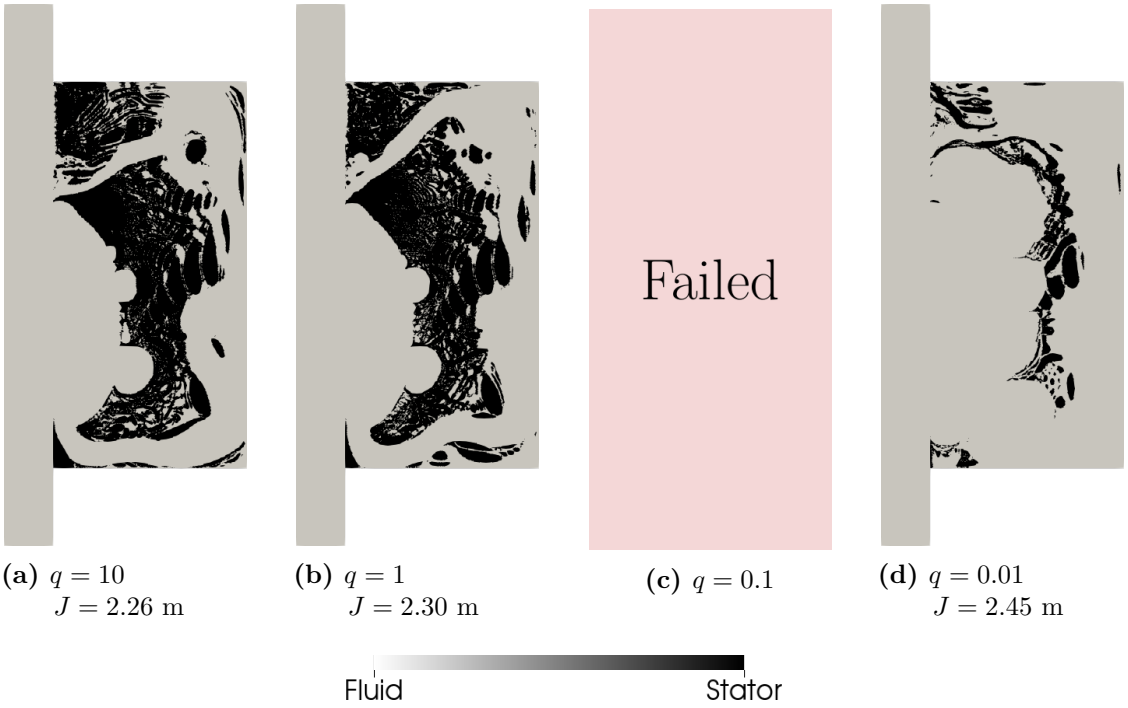

(a) $q = 10$, $J = 2.26$ m **(b)** $q = 1$, $J = 2.30$ m **(c)** $q = 0.1$ **(d)** $q = 0.01$, $J = 2.45$ m

Figure 4.16 – Straight-through labyrinth seal design in turbulent regime with TOBS algorithm (Re = 500 and $\omega_r = 10000$ rpm).

as in the result for laminar flow (Fig. 4.2) because the turbulent eddies require a cavity to develop. The obtained design is in accordance with the literature experience on the physics of labyrinth seals (SNECK, 1974).

For turbulent flow, the solution of the governing equations is harder than for laminar flow, increasing the difficulty of obtaining optimization results. In Fig. 4.16c, the optimization for $q_c = 0.1$ failed at iteration 58 because the solution of the fluid flow equations did not converge. For the other choices of q_c, the optimization ran successfully for 150 iterations, being stopped because the maximum number of iterations was reached (the maximum number of iterations is reduced for turbulent flow because the time to solve the fluid flow equations increases considerably).

The objective function history is oscillatory for the straight-through design in turbulent flow according to Fig. 4.17, which presents the convergence curves for the valid results of Fig. 4.16. The oscillations are due to the large steps involved in the TOBS approach (going from 0 to 1 or from 1 to 0) and the number of elements that are allowed to change during each optimization step. As the large steps are inherent to the TOBS approach, the alternative for reducing the oscillations is to reduce the number of elements allowed to flip during each optimization iteration by lowering β_{fl}.

Figure 4.18 shows the effect of reducing the flip limits to 0.25% for $q_c = 0.01$. It is seen that the objective function oscillations are reduced in the convergence graph; however, there are fewer solid elements in the final design when compared to the results of Fig. 4.16. Again, the maximum number of iterations was reached. By analyzing the iterations (second

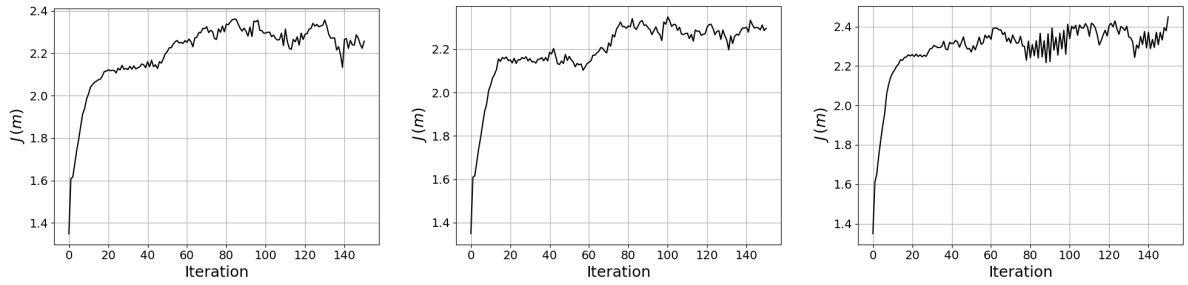

(a) Convergence for Fig. 4.16a **(b)** Convergence for Fig. 4.16b **(c)** Convergence for Fig. 4.16d

Figure 4.17 – Objective function history for the TOBS results of straight-through labyrinth seal optimization in turbulent flow.

row of Fig. 4.18), the optimization oscillated between similar designs with a localized change in the region highlighted by the red ellipses. Therefore, working with a lower flip limits parameter is not viable.

Figure 4.19 presents the velocity, pressure, and turbulent kinematic viscosity for the result of Fig. 4.16d. The higher values of turbulent kinematic viscosity occur in the chamber of the labyrinth seal, indicating that the turbulent eddies are concentrated in this region. The maximum value of ν_T is around 5.8×10^{-4} m^2/s, which is two orders of magnitude higher than the molecular kinematic viscosity of CO_2 at 15°C ($\nu = 7.7 \times 10^{-6}$ m^2/s), indicating that the turbulent dissipation dominates the head loss for Re = 500 and $\omega_\mathrm{r} = 10000$ rpm.

4.1.5 Staggered Labyrinth Seal in Turbulent Flow

The staggered labyrinth seal in turbulent flow is optimized with the rotor-stator algorithm (Section 2.4.5.1), and the RANS equations closed with the Spalart-Allmaras turbulence model are used to describe the fluid flow. Then, the optimization problem is given by

$$
\begin{aligned}
\max_{\Delta\alpha,\,\Delta\beta} \quad & \frac{\partial J}{\partial \alpha}\Delta\alpha + \frac{\partial J}{\partial \beta}\Delta\beta \text{ (with } J \text{ from Eq. 2.63)} \\
\text{s.t.} \quad & F_\mathrm{rans}\left(\nu_\mathrm{eff};\, \overline{\boldsymbol{v}},\, \overline{p},\, \tilde{\nu},\, \boldsymbol{w}_v,\, w_p,\, w_{\tilde{\nu}}\right) = 0, \quad \forall \left(\boldsymbol{w}_v,\, w_p,\, w_{\tilde{\nu}}\right) \in \left(\mathcal{V},\, \mathcal{Q},\, \mathcal{N}\right) \\
& \left\|\Delta\alpha^{(k)}\right\|_1 \leq \beta_\mathrm{fl} N_\alpha \\
& \left\|\Delta\beta^{(k)}\right\|_1 \leq \beta_\mathrm{fl} N_\beta \\
& \Delta\alpha \in \mathcal{S}_\alpha \\
& \Delta\beta \in \mathcal{S}_\beta
\end{aligned}
\tag{4.4}
$$

The FEniCS TopOpt FOAM software is used to solve the fluid flow equations because the algorithm described in Section 3.3.1 failed even for moderate turbulent conditions. The SIMPLEC algorithm of OpenFoam is used to solve the fluid flow equations. The maximum

(a) Solution

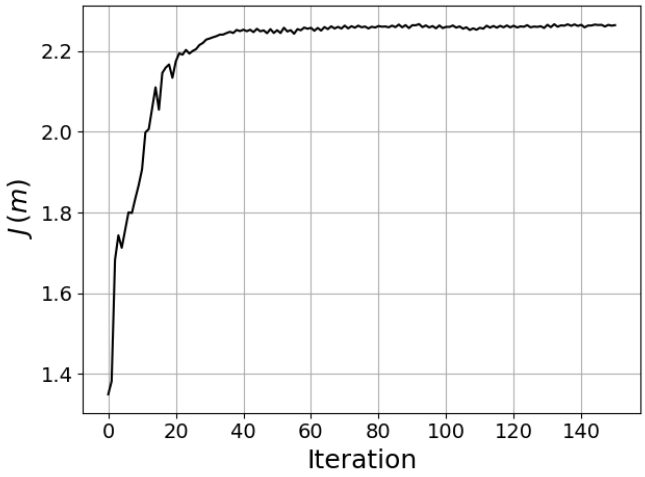

(b) Convergence

(c) Iter. 20 **(d)** Iter. 40 **(e)** Iter. 60 **(f)** Iter. 80 **(g)** Iter. 100 **(h)** Iter. 120

Figure 4.18 – Effect of reducing the flip limits to 0.25% for $q = 0.01$ for the straight-through labyrinth seal design in turbulent flow with TOBS (Re = 500 and $\omega_r = 10000$ rpm).

(a) Result

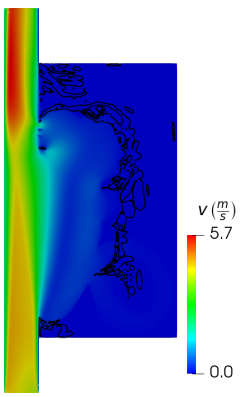

(b) Velocity

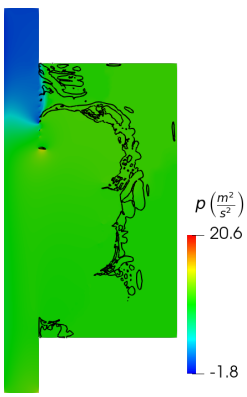

(c) Pressure

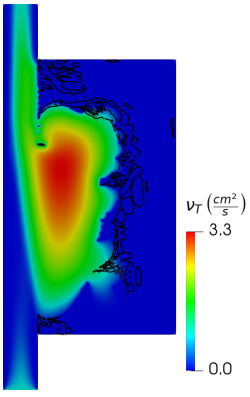

(d) Turbulent viscosity

Figure 4.19 – Velocity, pressure, and turbulent kinetic viscosity for the straight-through result in turbulent regime with TOBS and $q_c = 0.01$ (Re = 500 and $\omega_r = 10000$ rpm).

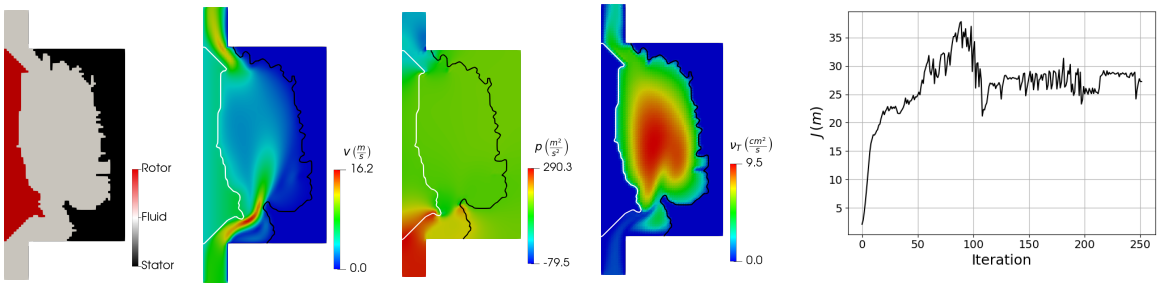

(a) Result **(b)** Velocity **(c)** Pressure **(d)** Turbulent viscosity **(e)** Convergence history

Figure 4.20 – Staggered labyrinth seal optimization in turbulent regime with rotor-stator algorithm (Re = 1000 and $\omega_r = 10000$ rpm). The final head loss is $J = 27.2$ m.

inlet axial velocity is 7.7 m/s (Re = 1000) and the shaft angular velocity is $\omega_r = 10000$ rpm. The element size is increased to 0.2 mm in order to reduce the computational cost. Figure 4.20 presents the optimization result, the flow variables, and the convergence history. It is seen that the optimized design does not emphasize on narrow channels, as observed for laminar flow (Fig. 4.6). This is expected because turbulent eddies require space to develop. The objective function oscillated considerably and the optimization stopped because the maximum number of iterations was reached. Therefore, the objective function did not converge. The maximum value of the objective function occurred in an intermediate iteration and it is 38.7% higher than the final value. The oscillations are related to the binary nature of the design variables (as in Section 4.1.4) and the projection from FEniCS to OpenFoam (see Appendix B).

4.1.6 Stepped Labyrinth Seal in Turbulent Flow

The same approach described in the previous section is applied to optimize the staggered labyrinth seal in turbulent flow. The results are presented in Fig. 4.21 for Re = 1000 and $\omega_r = 10000$ rpm. As for the staggered seal in turbulent regime, the convergence curve is oscillatory and the optimization ended due to the maximum number of iterations. Again, the objective function did not converge. The final material distribution presents two chambers and the flow is accelerated at the entrance of the first chamber, where most of the turbulent dissipation occurs. The final head loss is $J = 9.62$ m, which is a low value obtained after an oscillation.

It is also interesting to study the oscillations of Fig. 4.21e from a physical perspective. This study may be made by analyzing the material distributions at the peaks of Fig. 4.21e, which corresponds to iterations 45, 152 and 248. The material distributions present differences concerning the chambers size, number of small teeth, and location of teeth. However, the head loss difference between the peaks is lower than the head loss difference between the third peak and the last iteration, which presents similar material distributions. The core difference is one rotor tooth at the entrance of the design domain, which is absent

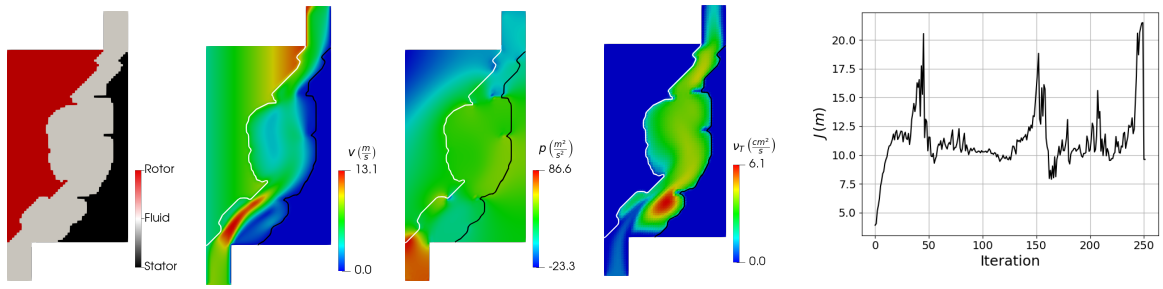

(a) Result **(b)** Velocity **(c)** Pressure **(d)** Turbulent viscosity **(e)** Convergence history

Figure 4.21 – Stepped labyrinth seal optimization in turbulent regime with rotor-stator algorithm (Re = 1000 and $\omega_r = 10000$ rpm). The final head loss is $J = 9.62$ m.

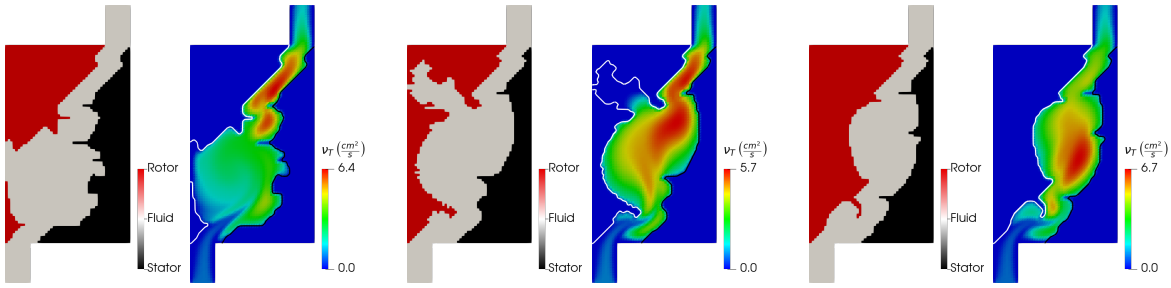

(a) Iter. 45 $J = 20.5$ m **(b)** Iter. 152 $J = 18.8$ m **(c)** Iter. 248 $J = 21.5$ m

Figure 4.22 – Material distribution and turbulent kinetic energy of the peaks of the convergence curve of stepped labyrinth seal optimization in turbulent regime with rotor-stator algorithm (Re = 1000 and $\omega_r = 10000$ rpm).

in the final design. The differences show how sensitive the turbulent flow is regarding design changes and provide an understanding of the oscillations. As the material distribution is discrete and there are thin structural members, the flow obstacles may be removed between iterations, leading to high objective function changes.

4.2 Continuous Design Variables

The labyrinth seal arrangements described in Fig. 4.1 are also optimized with continuous design variables. Similarly to the discrete approach, the straight-through labyrinth seal may be approached with standard fluid flow topology optimization algorithms (BORRVALL; PETERSSON, 2003), while the staggered and stepped arrangements require the specialized formulation presented in Section 2.4.5.2 (MOSCATELLI et al., 2024). Again, the results are grouped into laminar and turbulent.

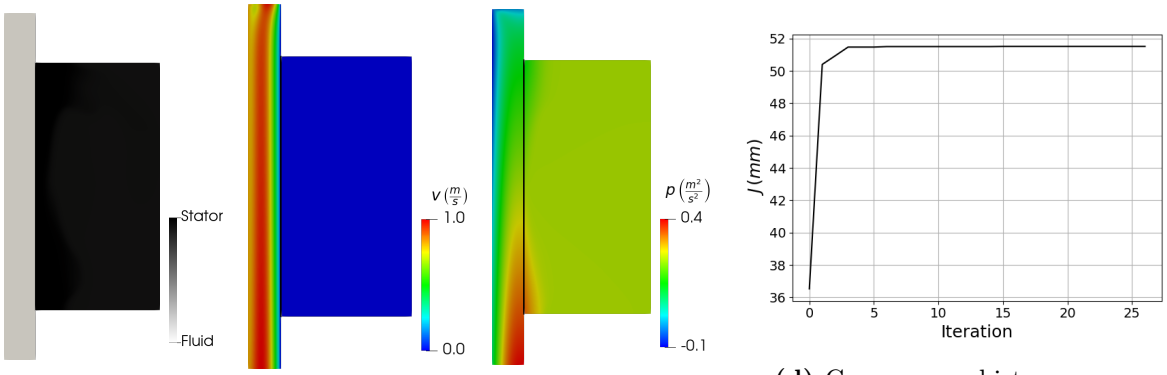

(a) Solution **(b)** Velocity **(c)** Pressure **(d)** Convergence history zoom

Figure 4.23 – Straight-through labyrinth seal design in laminar regime with MMA (Re = 100 and ω_r = 4000 rpm). The final head loss is 51.5 mm.

4.2.1 Straight-through Labyrinth Seal in Laminar Flow

The straight-through labyrinth seal optimization with continuous design variables and laminar flow is performed by solving the following optimization problem

$$\begin{aligned} \max_{m} \quad & J(\boldsymbol{v},\, p) \text{ (with } J \text{ from Eq. 2.63)} \\ \text{s.t.} \quad & F_{\text{ns}}\left(\nu;\, \boldsymbol{v},\, p,\, \boldsymbol{w}_v,\, w_p\right) = 0, \quad \forall\, (\boldsymbol{w}_v,\, w_p) \in (\mathcal{V},\, \mathcal{Q}) \\ & m \in [0,\, 1] \end{aligned} \tag{4.5}$$

The inlet velocity and shaft rotation are the same as the optimization with TOBS (Section 4.1.1), which are 0.77 m/s (Re = 100) and ω_r = 4000 rpm. Figure 4.23 shows that the same straight channel constricted to the minimum gap size is obtained (as in Fig. 4.2). The convergence curve is smooth, the final head loss is reached in about 5 iterations, and the optimization converges after 26 iterations. The result from Fig. 4.23 corroborates that the straight channel is the optimum solution under low and moderate Reynolds numbers.

4.2.2 Staggered Labyrinth Seal in Laminar Flow

For continuous design variables, the staggered labyrinth seal is designed with the interface identification method presented in Section 2.4.5.2. The first case considers a flow with low energy (Re = 1 and ω_r = 0 rpm), in which the main head loss mechanism is viscous dissipation due to high-velocity gradients. The expected result is a long channel constricted to the minimum gap size because a strict flow passage increases the velocity gradients, and a long path represents more dissipation regions. The optimization problem of Eq. 4.5 is solved for this first case.

Figure 4.24 presents the optimization result, the velocity and pressure fields, and the convergence curve. The white and black contours in the velocity and pressure fields are the isolines for $m_r = 0.5$ and $m_s = 0.5$, respectively. It is seen that the proposed algorithm produces an expected solution. Regarding the optimization parameters used to obtain this

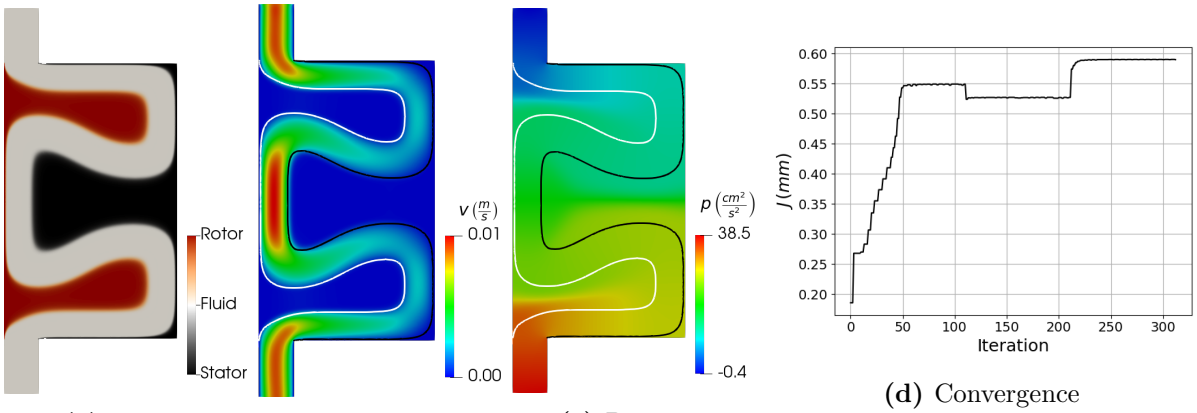

(a) Result **(b)** Velocity **(c)** Pressure **(d)** Convergence

Figure 4.24 – Staggered labyrinth seal optimization with the interface identification method without additional constraints (Re = 1 and $\omega_r = 0$ rpm), resulting in an head loss of 0.590 mm.

result, the material model convexity is $q_c = 10^{-4}$ and the Darcy number is $\mathrm{Da} = 10^{-5}$. The steepness parameter β_{th} starts at 8, and it is doubled after each continuation step until it reaches the value of 64. The MMA move limits are 0.2, the minimum iteration change is $\epsilon_m = 0.01$ (Eq. 3.1), and the maximum number of iterations per continuation step is 100.

The staggered labyrinth seal is also optimized with the same parameters of Fig. 4.24 and different minimum gaps g_{min} to show that the interface identification method is capable of controlling the minimum gap size. The results are presented in Figs. 4.24 and 4.25 for different ratios of minimum gap g_{min} to inlet size e_H. The optimizer has less freedom to create complex forms for larger gap sizes, as seen in Figs. 4.25a, 4.25b, and 4.25c. As the minimum gap is reduced, the optimization result becomes more tortuous, and the head loss is increased.

Figure 4.26 presents a graphical representation of the head loss trend as the minimum gap size is reduced. As discussed before, the increase in head loss is due to a combination of narrower channels and longer fluid flow paths. For stricter passages, the velocity gradient magnitude is larger, which improves the local viscous dissipation as this dissipation is related to the square of the velocity gradient. Therefore, the head loss has a trend close to a quadratic or exponential growth as the minimum gap size is reduced.

Before proceeding to the optimization of staggered and stepped labyrinth seals with rotation, it is necessary to choose a connectivity constraint for the interface identification method because free-floating solid islands may appear in the optimization result, as shown in Fig. 4.27. These islands are undesirable because they may not be realized physically without the introduction of supporting structures, which are also undesirable because they may compromise the performance of the optimization result. Figure 4.28 shows the velocity and streamlines fields for the results with $\omega_r = 100$ rpm (first line of Fig. 4.27). It is seen that the velocity increases with radial direction as desired. However, there may be fluid flow seepage through the thin structural members. In this case, minimum length constraints

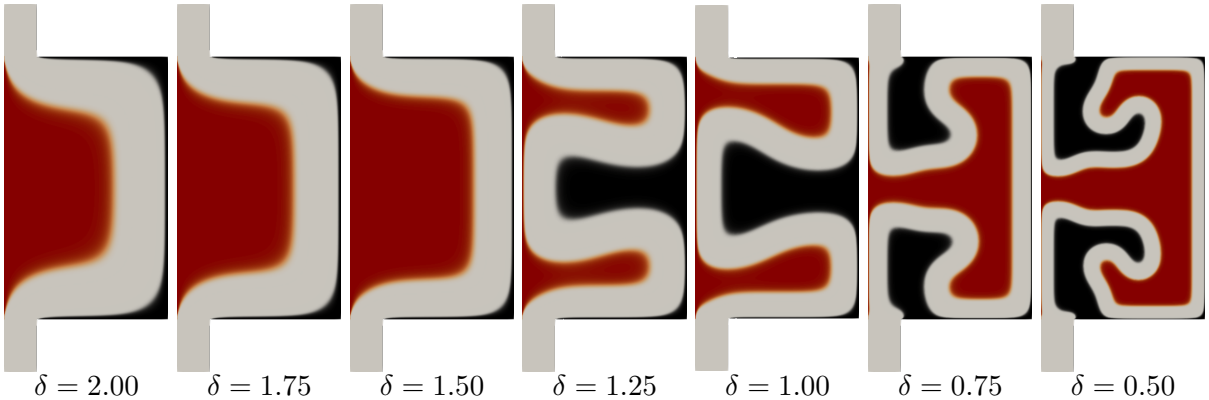

$\delta = 2.00$	$\delta = 1.75$	$\delta = 1.50$	$\delta = 1.25$	$\delta = 1.00$	$\delta = 0.75$	$\delta = 0.50$
$J = 0.19$mm	$J = 0.21$mm	$J = 0.24$mm	$J = 0.35$mm	$J = 0.59$mm	$J = 1.24$mm	$J = 4.25$mm
(a)	**(b)**	**(c)**	**(d)**	**(e)**	**(f)**	**(g)**

Figure 4.25 – Minimum gap size control of the staggered labyrinth seal for different ratios $g_{\min}$ and e_{H} (Re = 1 and $\omega_{\mathrm{r}} = 0$ rpm).

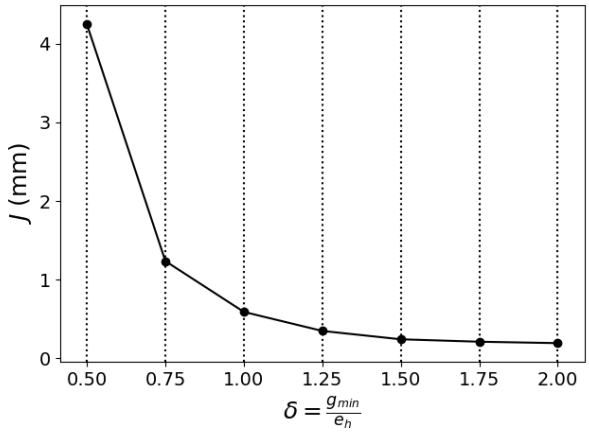

Figure 4.26 – Objective function trend for different ratios of minimum gap size $g_{\min}$ to inlet size e_{H} (Re = 1 and $\omega_{\mathrm{r}} = 0$ rpm).

may be added to the optimization problem to circumvent the seepage (MOSCATELLI et al., 2024).

The following sections present tests regarding the connectivity constraints discussed in sections 2.4.5.3 (VFSI) and 2.4.5.4 (VTM). The objective is to select one of these constraints for the rest of the work. The selection will be based on the ability to avoid free-floating islands, the possibility of not over-constraining the optimization, and the easiness of calibration.

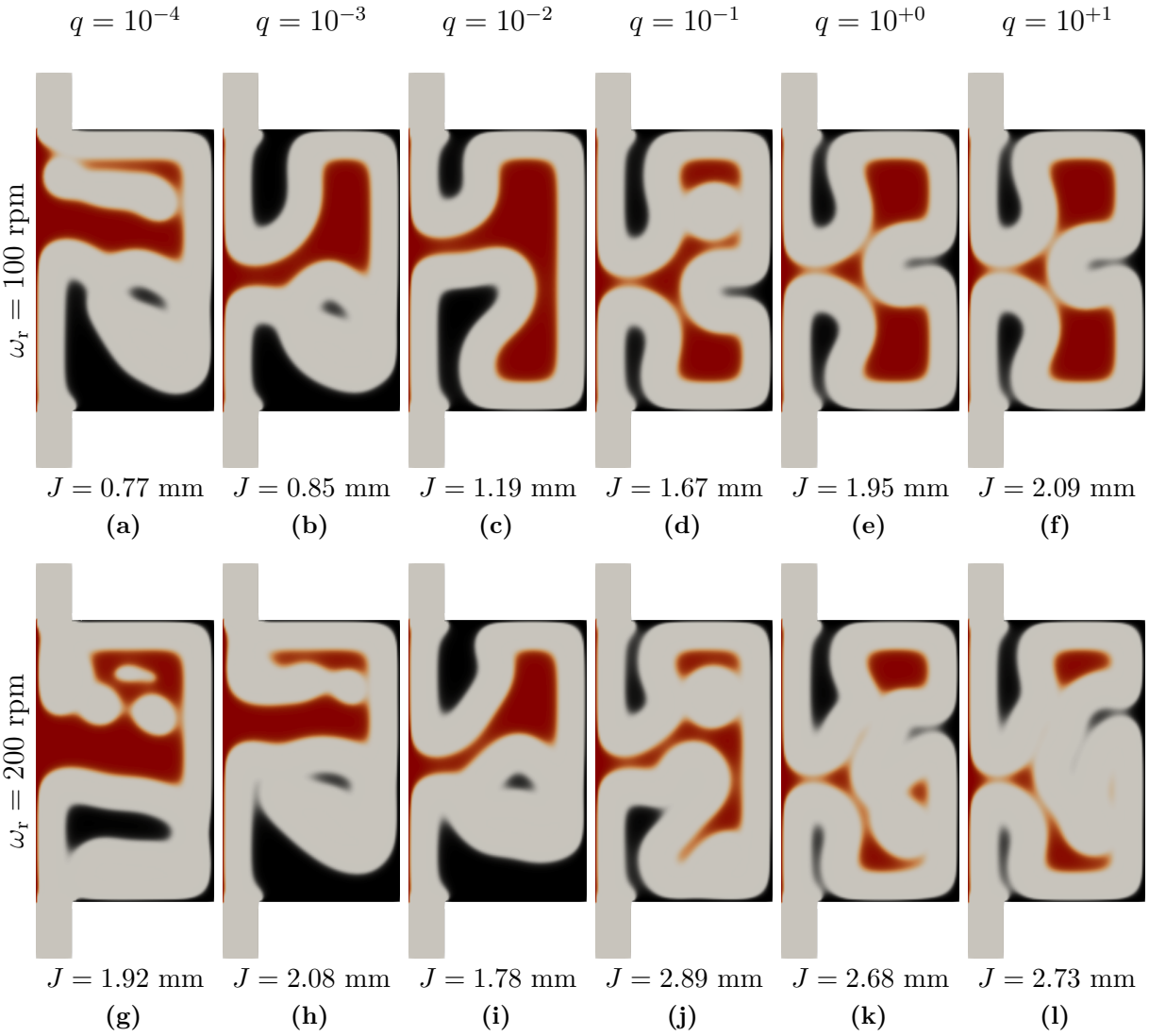

Figure 4.27 – Topology optimization of staggered labyrinth seal by interface identification method without connectivity constraints (Re = 1).

4.2.2.1 Fluid-Structure Interaction (VFSI)

The VFSI constraint is included in the design process by adding the inequality $G_f \leq 0$ to the optimization problem of Eq. 4.5, resulting in the following problem

$$\begin{aligned} \max_{m} \quad & J(\boldsymbol{v},\, p) \text{ (with } J \text{ from Eq. 2.63)} \\ \text{s.t.} \quad & F_{\text{ns}}\left(\nu;\, \boldsymbol{v},\, p,\, \boldsymbol{w}_v,\, w_p\right) = 0, \quad \forall\, (\boldsymbol{w}_v,\, w_p) \in (\mathcal{V},\, \mathcal{Q}) \\ & G_f \leq 0 \\ & m \in [0,\, 1] \end{aligned} \tag{4.6}$$

First, the VFSI constraint is tested with pressure loads only (Eq. 2.76) and the results for $\omega_r = 100$ rpm are presented in Fig. 4.29. Each line presents one admissible value $\overline{C}_f$ for the constraint, and each column one value of the material model convexity q_c. It is seen that in most cases, the free-floating islands are avoided; however, in some cases (such

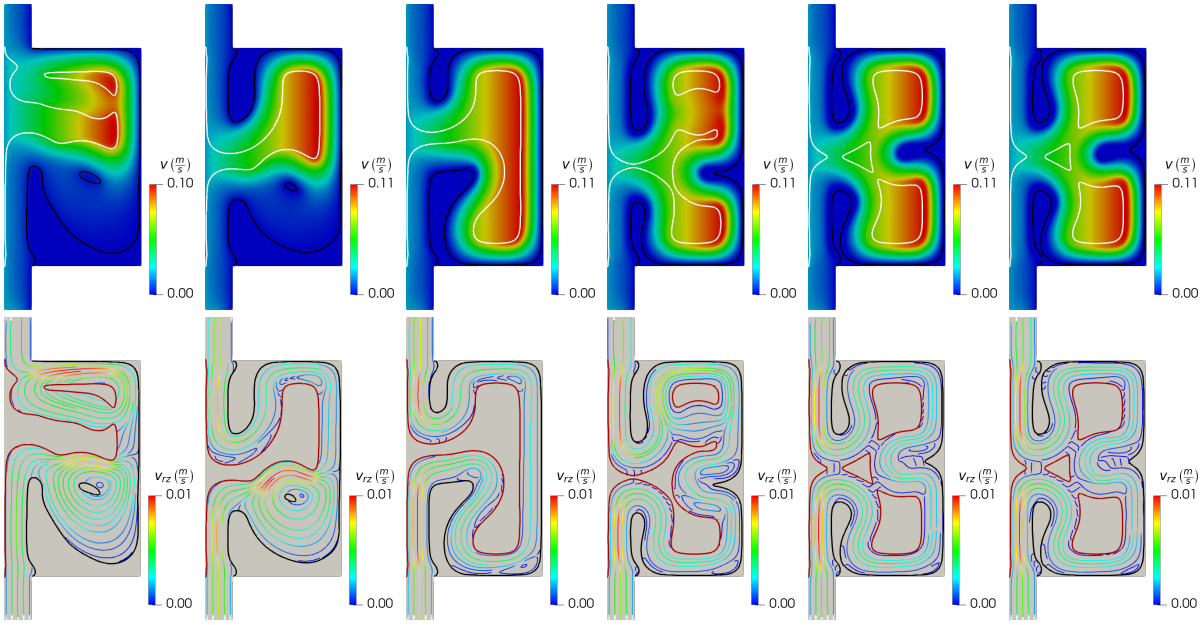

(a) $q_c = 10^{-4}$ **(b)** $q_c = 10^{-3}$ **(c)** $q_c = 10^{-2}$ **(d)** $q_c = 10^{-1}$ **(e)** $q_c = 10^{+0}$ **(f)** $q_c = 10^{+1}$

Figure 4.28 – Velocity and streamlines of the staggered labyrinth seals designed by interface identification method without connectivity constraints (Re = 1 and $\omega_r = 100$ rpm).

as in Figs. 4.29h and 4.29n), the islands are still present. Also, when comparing the first line of Fig. 4.27 with Fig. 4.29, it is noted that the VFSI constraint is over-constraining the problem as the objective function values of Fig. 4.27 are considerably higher than the objective function values of Fig. 4.29. Also, it is hard to identify a pattern of the constraint behavior as $\overline{C}_f$ is changed. Therefore, the VFSI with pressure loads only does not met any of the goals of the connectivity constraint.

Figure 4.30 presents the attempt to avoid free-floating islands by including the FSI velocity loads (Eq. 2.77). For most cases, there are no significant differences from Fig. 4.29 as seen by inspecting the material distributions and objective functions for the same q_c and $\overline{C}_f$. Therefore, adding the velocity loads does not improve the behavior of the VFSI constraint. The bad performance of the VFSI as a connectivity constraint is possibly related to the dependence on the fluid flow. For a given fluid flow, there may be regions with high and low FSI loads. The admissible constraint $\overline{C}_f$ for each region will differ, making calibration hard. It may also be the case that free-floating islands will never be avoided in regions with low pressure and velocity gradients. Therefore, an alternative connectivity constraint is necessary. The inclusion of FSI would only be interesting if other design criteria beyond maximizing head loss are required, such as increasing resonance frequency and limiting stress levels.

4.2.2.2 Virtual Temperature Method (VTM)

As the VFSI constraint failed to remove the free-floating islands and hindered the optimization, it is necessary to test another connectivity constraint. The VTM from (LIU

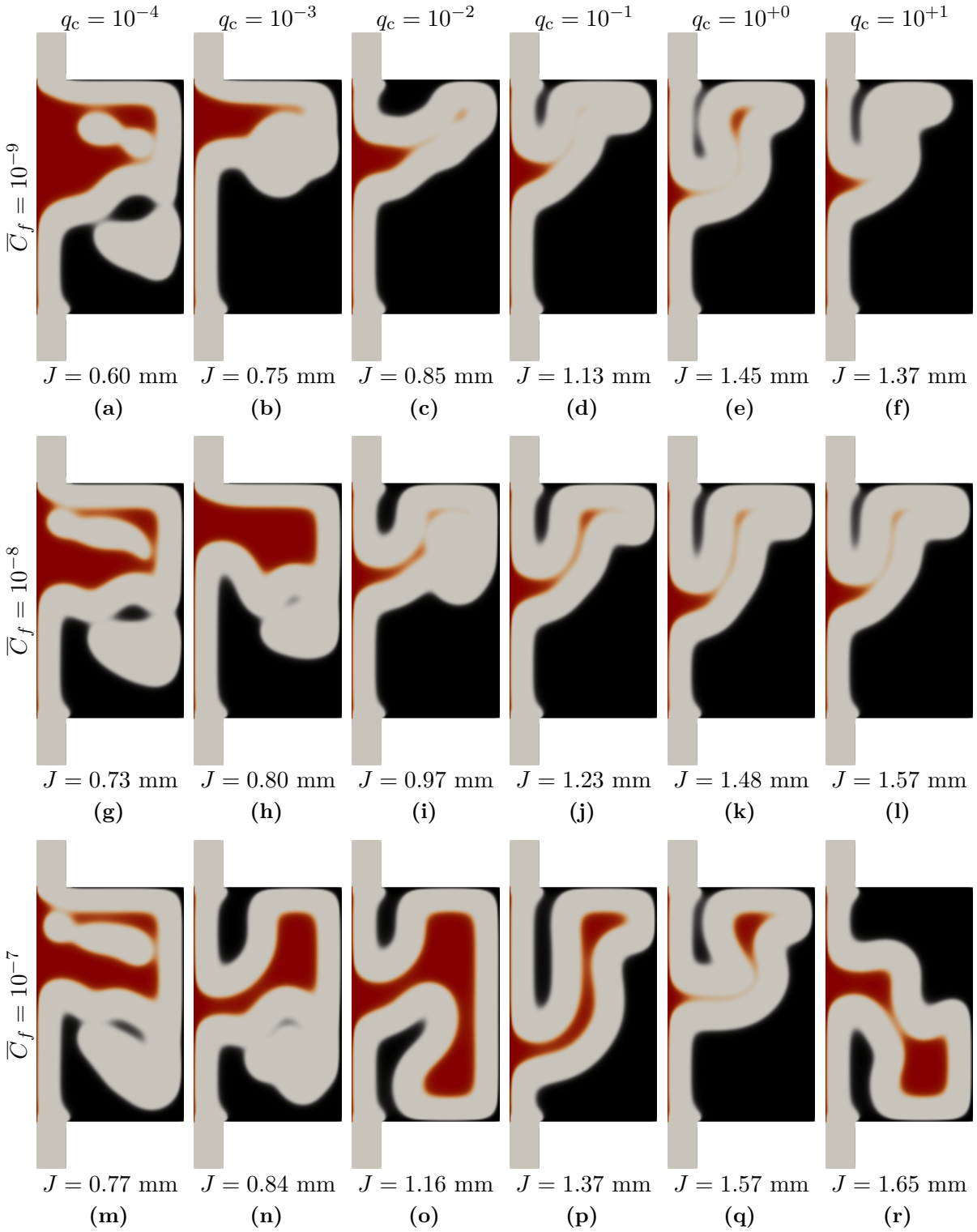

Figure 4.29 – Topology optimization of staggered labyrinth seals by interface identification with VFSI connectivity constraint based on pressure loads only (Re = 1).

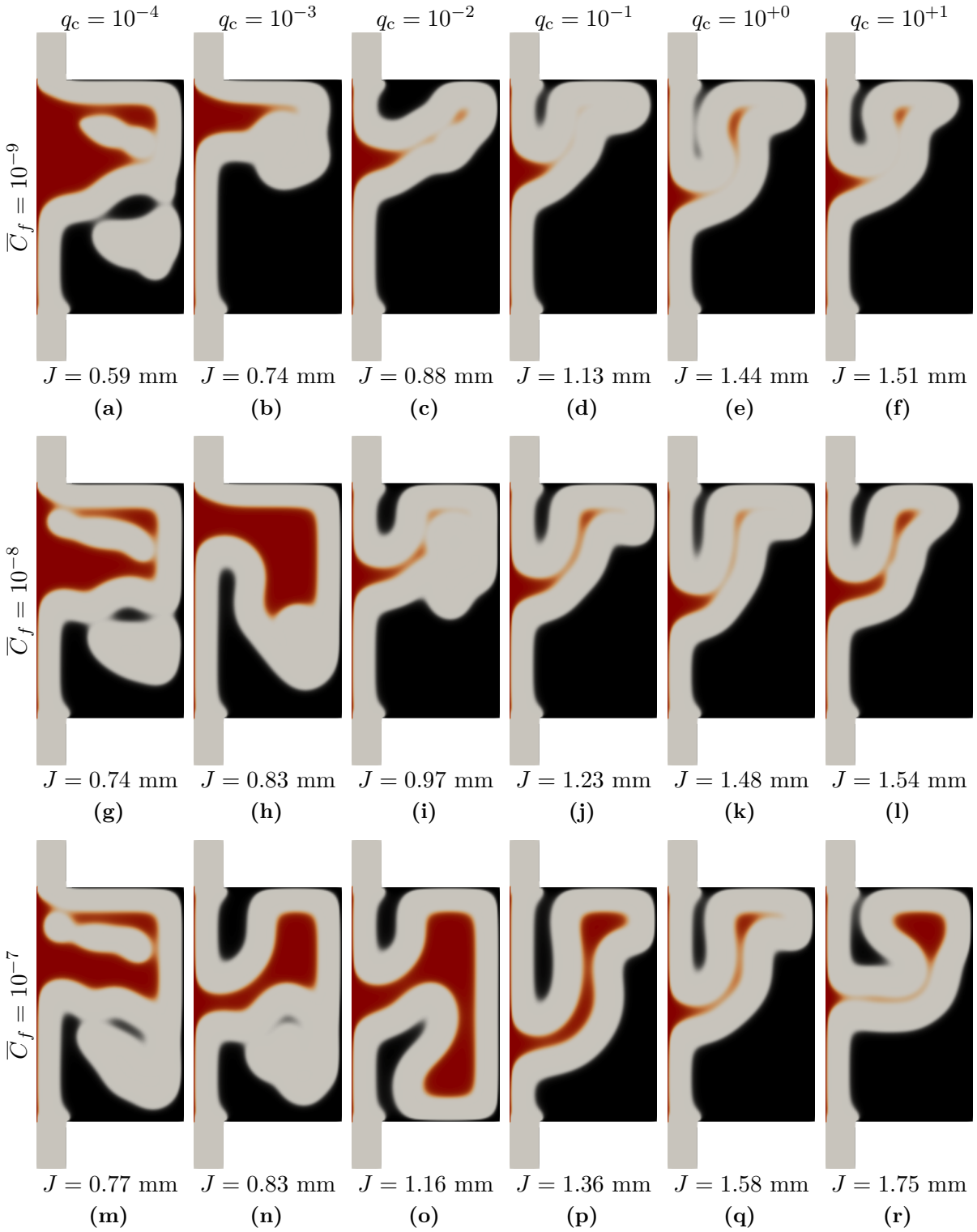

Figure 4.30 – Topology optimization of staggered labyrinth seals by interface identification with VFSI connectivity constraint based on velocity and pressure loads (Re = 1).

et al., 2015) was chosen as an alternative and the optimization problem is now given by

$$\begin{aligned} \max_{m} \quad & J(\boldsymbol{v},\, p) \text{ (with } J \text{ from Eq. 2.63)} \\ \text{s.t.} \quad & F_{\text{ns}}\left(\nu;\, \boldsymbol{v},\, p,\, \boldsymbol{w}_v,\, w_p\right) = 0, \quad \forall\, (\boldsymbol{w}_v,\, w_p) \in (\mathcal{V},\, \mathcal{Q}) \\ & G_{\text{t}} \leq 0 \\ & m \in [0,\, 1] \end{aligned} \tag{4.7}$$

Figure 4.31 presents the tests for different values of the calibration constant T_c and the material model convexity q_{c}. The shaft angular velocity is 100 rpm, as in the previous section. The first line of Fig. 4.31 shows that the VTM constraint is capable of avoiding the free-floating islands; however, the constraint limits the optimization if a low admissible temperature is used (compare the head loss of Figs. 4.27 and 4.31 for the same q_{c}). Then, the second line of Fig. 4.31 shows that it is possible to find an admissible temperature value that avoids the islands without limiting the optimization. Finally, the third line of Fig. 4.31 illustrates that a high value of admissible temperature does not avoid the floating islands.

The tests presented in Fig. 4.31 also show that the VTM constraint is easier to calibrate than the VFSI constraint. As the calibration constant T_c is increased, the optimization results go from over-constrained results without islands to not constrained results with islands, making it possible to use an intermediary value of T_c that allows optimized results without islands. The easiness of calibration is possibly related to the linear nature of the heat transfer problem of Eq. 2.80. As the VTM constraint provided better results, it was chosen for the optimization of the staggered and stepped labyrinth seals.

4.2.3 Stepped Labyrinth Seal in Laminar Flow

The stepped seal in laminar flow is optimized with the interface identification method (Section 2.4.5.2) and VTM constraint (Section 2.4.5.4 and Eq. 4.7). First, the influence of the shaft rotation is evaluated by solving the problem from Fig. 4.1c with different values of ω_{r} and q_{c}, as seen in Fig. 4.32. The inlet Reynolds number is $\text{Re} = 1$, allowing the rotation to be the dominant effect during optimization. The results depend on the material model's convexity, and high convexity (low q_{c}) is inappropriate for optimization with rotation, according to Figs. 4.32f, 4.32g, 4.32k, and 4.32l. Low convexity may result in thin structural parts, as seen in the last column of Fig. 4.32 ($q_{\text{c}} = 1$). The results for 200 rpm show that the interface identification method does not impose a fluid channel with uniform length, as the lower right part of the design domain presents fluid regions larger than the minimum gap. The ability to model non-uniform fluid channels is especially important for turbulent flows because larger chambers may facilitate the development of turbulent eddies.

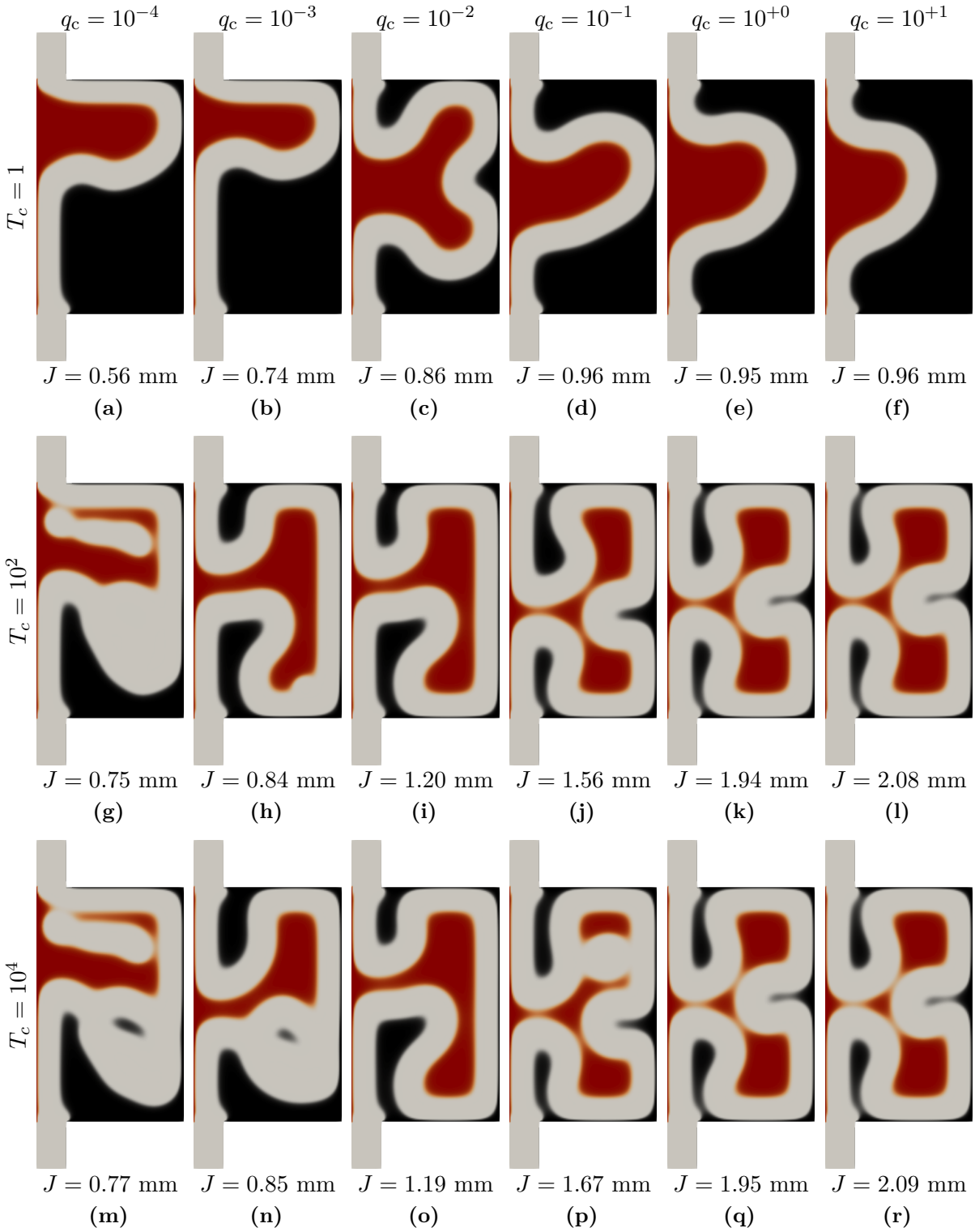

Figure 4.31 – Effect of the VTM calibration factor T_c on the topology optimization of staggered labyrinth seals (Re = 1).

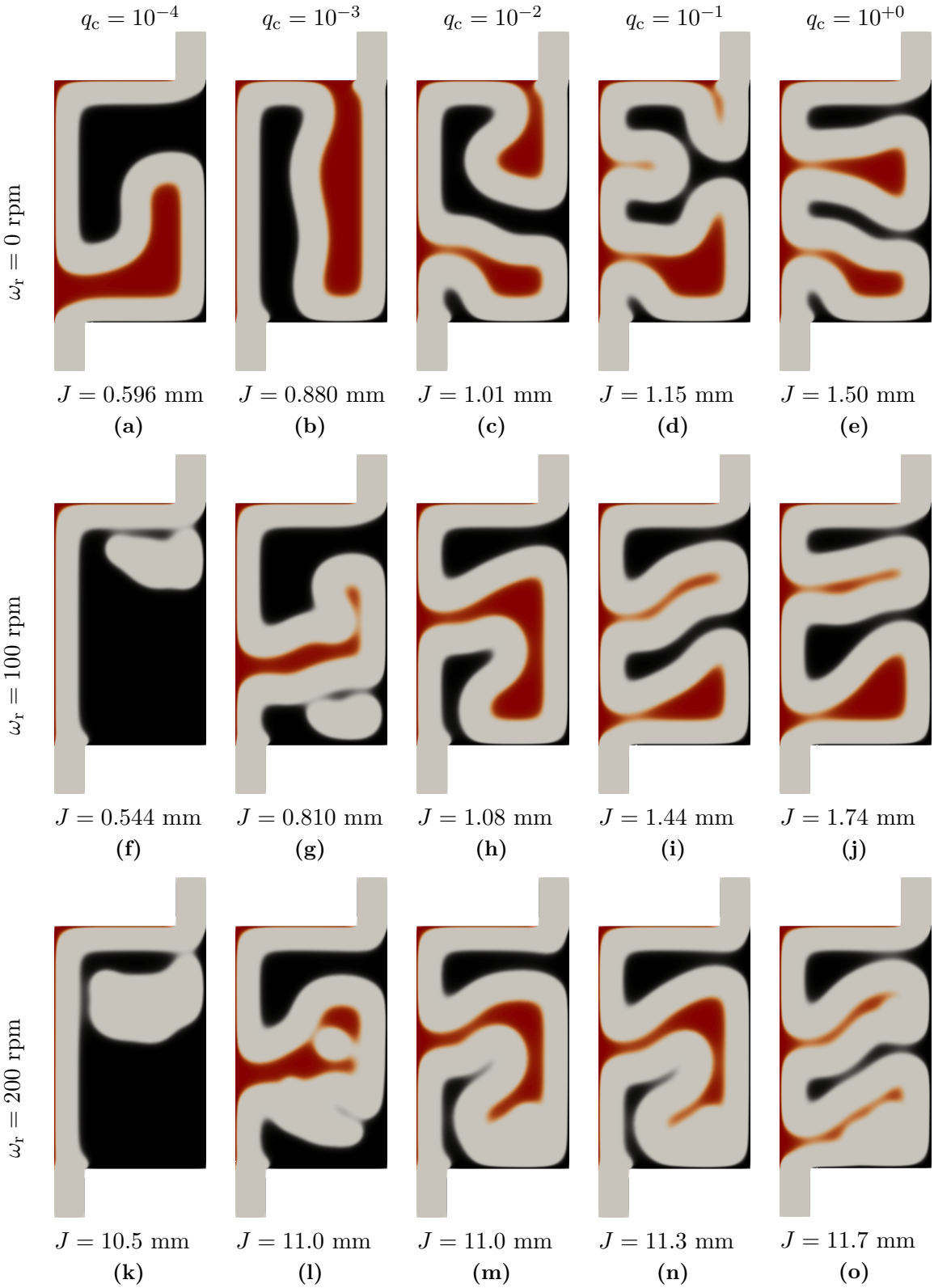

Figure 4.32 – Effect of the angular velocity on the topology optimization of stepped labyrinth seals with interface identification method (Re = 1).

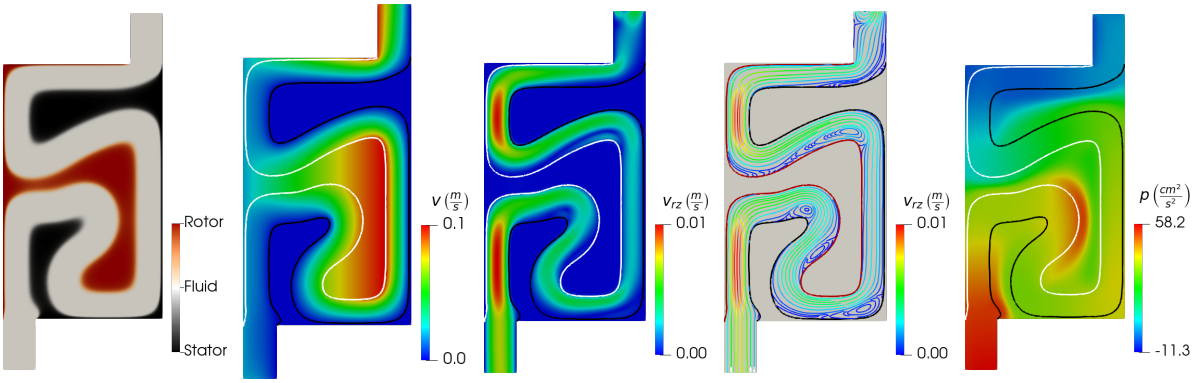

(a) Result **(b)** Velocity **(c)** rz velocity **(d)** Streamlines **(e)** Pressure

Figure 4.33 – Stepped labyrinth seal state variables for Re = 1, $\omega_r = 100$ rpm, and $q_c = 0.01$.

Figure 4.33 shows the state variables for Re = 1, $\omega_r = 100$ rpm, and $q_c = 0.01$, which produced a result with rotor and stator sizes that enable the visualization of the rotation effect. The velocity magnitude increases with the radial coordinate according to Fig. 4.33b. The streamlines that connect the inlet to the outlet are constrained by recirculating zones along the seal (Fig. 4.33d). The pressure does not decrease continuously along the seal as in Fig. 4.24c. There is a pressure increase when the flow passes through the inner part of the hook-shaped rotor (Fig. 4.33e).

Then, the influence of the inlet velocity is studied by keeping the shaft stationary ($\omega_r = 0$) and varying the inlet Reynolds number, as shown in Fig. 4.34. Most results are narrow channels and the channel length increases as the material model interpolation becomes less convex (q_c increases). The results for $q_c = 1$ present stator and rotor teeth that deviate the flow several times. Again, the minimum size of the structural parts decreases as q_c increases.

Finally, the effect of moderate rotations and inlet velocities is accessed by running the optimization with Re = 100 and $\omega_r = 100$ rpm, as seen in Fig. 4.35. The results are closer to the second line of Fig. 4.34 than to the second line of Fig. 4.32, showing a dominance of the inlet velocity.

4.2.4 Straight-through Labyrinth Seal in Turbulent Flow

Most of the results of previous sections are labyrinth seals constricted to the minimum gap size because viscous dissipation due to high-velocity gradients is the main mechanism for obtaining head loss when the fluid does not have enough energy to form turbulent eddies. This section explores optimization cases with turbulent flow, which is the real condition for labyrinth seals operating with GHGs. The RANS equations closed with the Spalart-Allmaras turbulence model are used with $\tilde{\nu}_{in} = 10^{-4}$. Then, the optimization

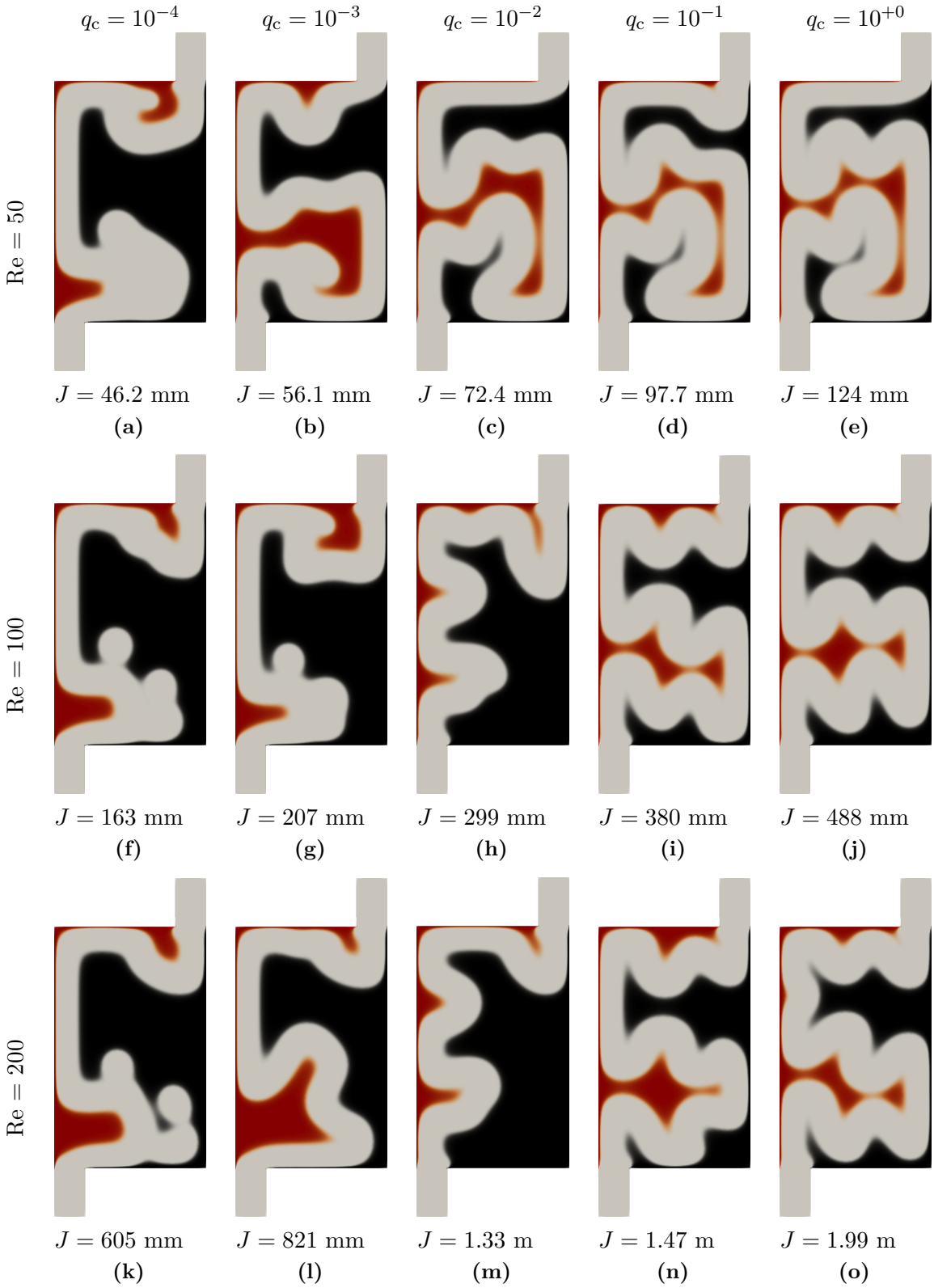

Figure 4.34 – Effect of the inlet velocity on the topology optimization of stepped labyrinth seals with interface identification method ($\omega_r = 0$ rpm).

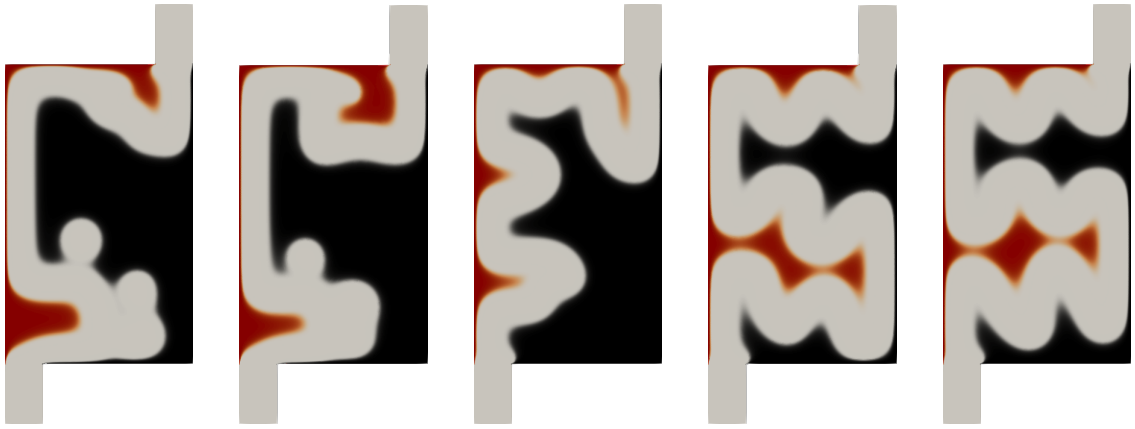

$J = 163$ mm **(a)** $q_c = 10^{-4}$ | $J = 207$ mm **(b)** $q_c = 10^{-3}$ | $J = 298$ mm **(c)** $q_c = 10^{-2}$ | $J = 381$ mm **(d)** $q_c = 10^{-1}$ | $J = 489$ mm **(e)** $q_c = 10^{+0}$

Figure 4.35 – Stepped labyrinth seal optimization with interface identification method (Re = 100 and $\omega_r = 0$ rpm).

problem for the straight-through labyrinth seal in turbulent flow is given by

$$\begin{aligned} \max_{m} \quad & J(\overline{\boldsymbol{v}}, \overline{p}) \text{ (with } J \text{ from Eq. 2.63)} \\ \text{s.t.} \quad & F_{\text{rans}}\left(\nu_{\text{eff}}; \overline{\boldsymbol{v}}, \overline{p}, \tilde{\nu}, \boldsymbol{w}_v, w_p, w_{\tilde{\nu}}\right) = 0, \quad \forall\left(\boldsymbol{w}_v, w_p, w_{\tilde{\nu}}\right) \in (\mathcal{V}, \mathcal{Q}, \mathcal{N}) \\ & m \in [0, 1] \end{aligned} \tag{4.8}$$

First, a study regarding the influence of the inlet velocity in the magnitude of the turbulent viscosity is performed, as seen in Fig. 4.36. The shaft is not rotating to simplify the interpretation of results. It is possible to observe that for Re = 100, which is the condition of Section 4.2.1, the Spalart-Allmaras turbulence model does not identify the formation of turbulent eddies inside the design domain. The absence of turbulent eddies corroborates that the straight channel constricted to the minimum gap size is the optimal solution for low to moderate Reynolds numbers. For Re = 250 and 500, there is turbulent dissipation inside the design domain. Therefore, it is possible to use Re = 500 as a starting point for the labyrinth seal optimization in turbulent flow.

Figure 4.37 presents the state variables and the sensitivities for Re = 500 and $\omega_r =$ 10000 rpm. The pressure field has maximum and minimum values in the connection of the chamber to the inlet and outlet tube, respectively. These maximum and minimum values are high and low compared to the other values inside the design domain, which may indicate numerical artifacts. Therefore, some experiments chamfering the corners and using different meshes were performed. After analyzing the results of the experiments, it was found that the issue is associated with the turbulent velocity profile (Eq. 2.22) as it is alleviated with the use of a parabolic profile (Eq. 2.21), as seen in Fig. 4.38. However, we proceed with the "almost constant" profile because it is more appropriate for turbulent flows.

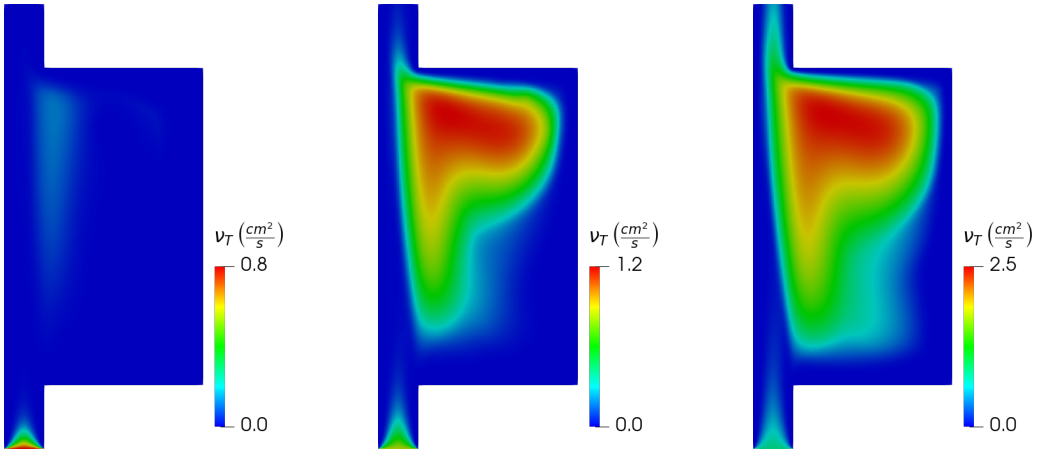

(a) Re = 100 **(b)** Re = 250 **(c)** Re = 500

Figure 4.36 – Effect of the inlet velocity (through inlet Reynolds number) in the turbulent viscosity of the straight-through labyrinth seal.

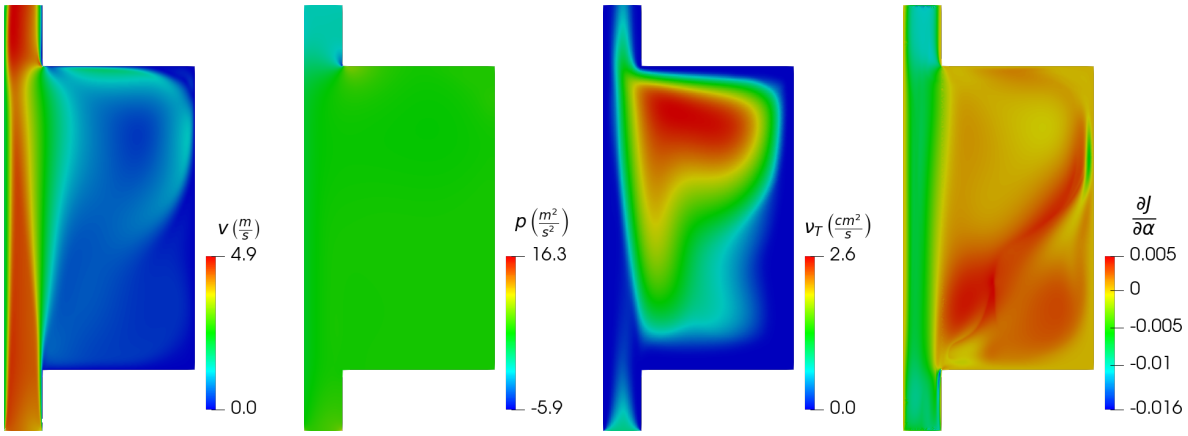

(a) Velocity **(b)** Pressure **(c)** Turbulent viscosity **(d)** Sensitivities

Figure 4.37 – State variables and sensitivities for a fully developed turbulent velocity profile at the inlet.

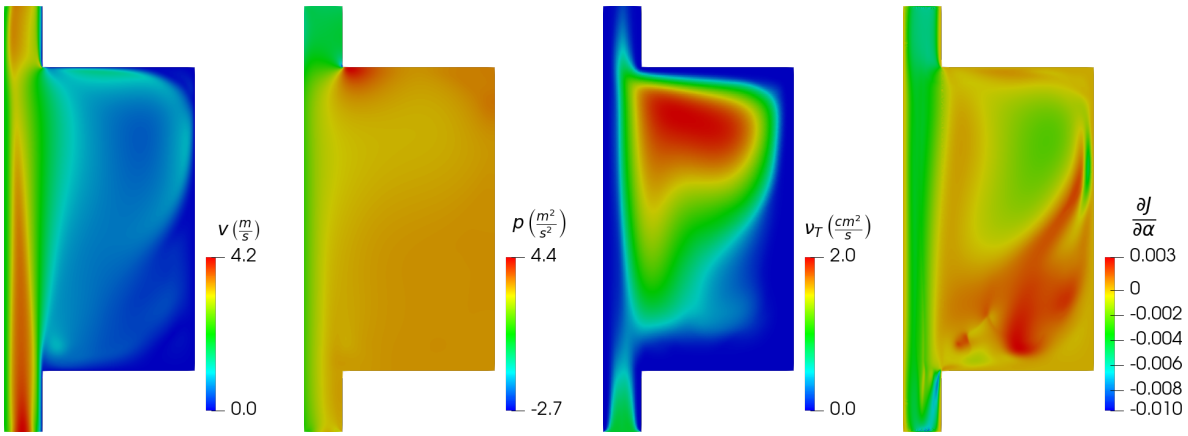

(a) Velocity **(b)** Pressure **(c)** Turbulent viscosity **(d)** Sensitivities

Figure 4.38 – State variables and sensitivities for a parabolic velocity profile at the inlet.

Figure 4.39 presents the influence of the convexity q_c and the steepness β_{th} in the topology optimization of straight-through labyrinth seals in turbulent flow. The parameter β_{th} is kept constant because continuation did not improve the results, and it increased the number of iterations. In general, the results present one large chamber followed by smaller chambers. The big chamber also presents smaller chambers attached to it. It is concluded that the intermediate densities are not penalized because there are considerable intermediate densities for the low β_{th} results.

The velocity, pressure, and turbulent viscosity fields of the result from Fig. 4.39r are presented in Fig. 4.40 with the black contour line indicating the solid frontier. The turbulent viscosity field helps understand the results from Fig. 4.39. The turbulent dissipation is concentrated in the chambers, being larger in the first chamber. The size of each chamber is associated with the remaining energy in the fluid flow because the larger the chamber, the higher the energy required to enter the chamber and form turbulent eddies. As there is turbulent energy dissipation in each chamber, the size of the chambers diminishes downstream.

Another important output to investigate is the objective function history. Figure 4.41 presents the convergence curves for $q_c = 0.01$ and different values of β_{th}, which corresponds to the study of the last line of Fig. 4.39. It is seen that the oscillations in the objective function graph increase for higher values of the steepness β_{th} of the smooth Heaviside projection. Therefore, it may be necessary to use the continuation of β_{th} for higher flow velocities.

4.2.5 Staggered Labyrinth Seal in Turbulent Flow

The staggered seal in turbulent flow is optimized with the interface identification method (Section 2.4.5.2) and VTM constraint (Section 2.4.5.4). Then, Equation 4.7 is modified to include the weak form of the RANS equations with Spalart-Allmaras turbulence model, as follows

$$\begin{aligned} \max_{m} \quad & J(\overline{\boldsymbol{v}},\, \overline{p}) \text{ (with } J \text{ from Eq. 2.63)} \\ \text{s.t.} \quad & F_{\text{rans}}\left(\nu_{\text{eff}};\, \overline{\boldsymbol{v}},\, \overline{p},\, \tilde{\nu},\, \boldsymbol{w}_v,\, w_p,\, w_{\tilde{\nu}}\right) = 0, \quad \forall\, (\boldsymbol{w}_v,\, w_p,\, w_{\tilde{\nu}}) \in (\mathcal{V},\, \mathcal{Q},\, \mathcal{N}) \\ & G_{\text{t}} \leq 0 \\ & m \in [0,\, 1] \end{aligned} \tag{4.9}$$

The inlet velocity is 3.86 m/s (Re = 500) as for the straight-through labyrinth seal because this velocity already provides turbulent eddies in the design domain (Fig. 4.36). Figure 4.42 presents a study of the influence of the rotation and the material model convexity on the optimization result. The designs do not present large open chambers as in the case of the staggered labyrinth seal, and the optimization fails for some combinations

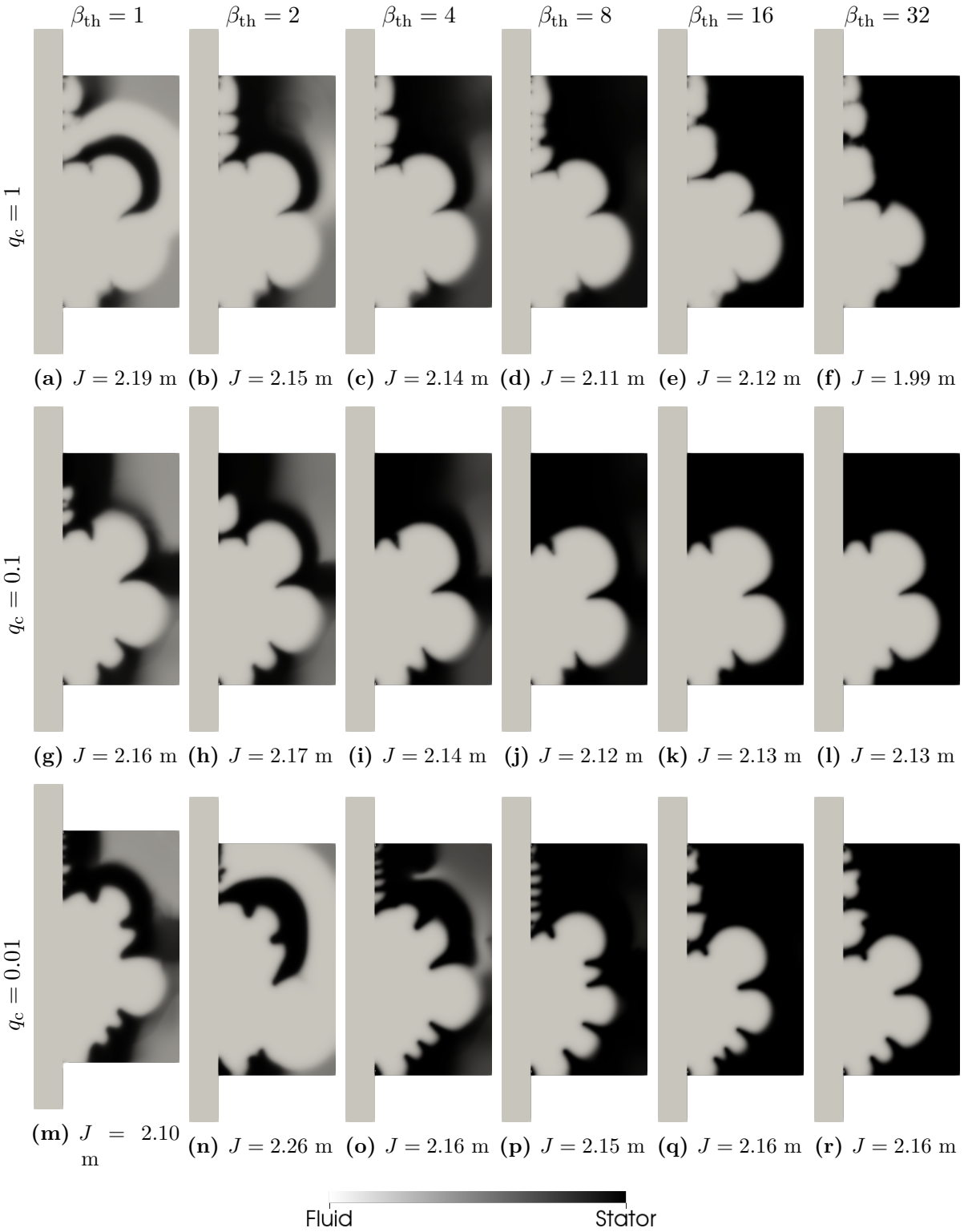

(a) $J = 2.19$ m **(b)** $J = 2.15$ m **(c)** $J = 2.14$ m **(d)** $J = 2.11$ m **(e)** $J = 2.12$ m **(f)** $J = 1.99$ m

(g) $J = 2.16$ m **(h)** $J = 2.17$ m **(i)** $J = 2.14$ m **(j)** $J = 2.12$ m **(k)** $J = 2.13$ m **(l)** $J = 2.13$ m

(m) $J = 2.10$ m **(n)** $J = 2.26$ m **(o)** $J = 2.16$ m **(p)** $J = 2.15$ m **(q)** $J = 2.16$ m **(r)** $J = 2.16$ m

Figure 4.39 – Influence of q_c and β_{th} in the topology optimization of straight-through labyrinth seals in turbulent flow with MMA (Re = 500 and $\omega_r = 10000$ rpm).

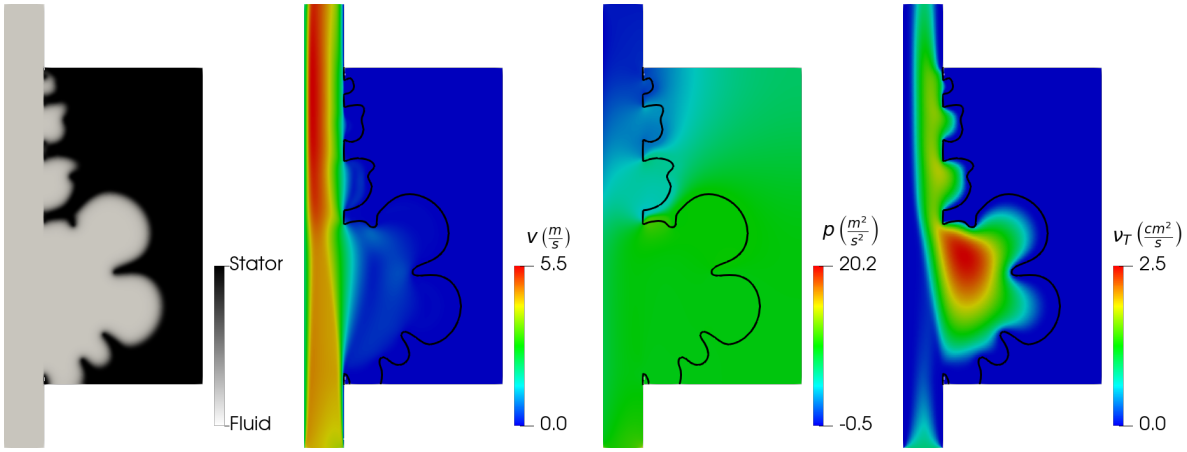

(a) Solution **(b)** Velocity **(c)** Pressure **(d)** Turbulent viscosity

Figure 4.40 – State variables for straight-through labyrinth seal design with $q_c = 0.01$ and $\beta_{th} = 32$ (Re = 500 and $\omega_r = 10000$ rpm).

of q_c and ω_r, showing that the design of the staggered seal is more challenging than the design of the straight-through seal. The failures are related to non-convergence of the fluid flow simulations, which are probably more associated with hard-to-analyze material distributions than to the parameters q_c and ω_r as there is no failure pattern (such as the optimization is constantly failing for $q_c = 0.01$).

Three designs of Fig. 4.42 are worth inspecting with more attention. First, the results from Figs. 4.42g and 4.42j are almost identical, although they were obtained with and without rotation. Also, the material distribution is a long, tortuous channel constricted to the minimum gap size. However, the result for the straight-through labyrinth seal (Fig. 4.39) indicated that a large chamber is more interesting for developing turbulent eddies. Second, the result of Fig. 4.42i is similar to the other two results although it presents a larger chamber close to the inlet.

Figure 4.43 presents the state variables and head loss convergence history for the result obtained for $q_c = 0.1$ and $\omega_r = 1500$ rpm (Fig. 4.42j). The velocity field shows that the flow is constricted beyond the minimum gap size of the channel in some regions. By inspecting the turbulent viscosity field, it is possible to see that some constrictions are associated with the development of turbulent eddies, which are formed in regions where the flow is deviated by the stator or rotor geometry. Therefore, the turbulent eddies may also be promoted by deviating the flow in addition to being generated at large chambers. The convergence history presents oscillations concentrated after the continuation steps, indicating that a smooth updating strategy may be more appropriate than doubling β_{th} after each continuation step.

A closer inspection of Fig. 4.43 shows that the isolines at $m_r = m_s = 0.5$ are not compatible with the velocity and turbulent viscosity fields. For higher radial coordinates, small values of m_r affect the flow field considerably due to the convexity of the material

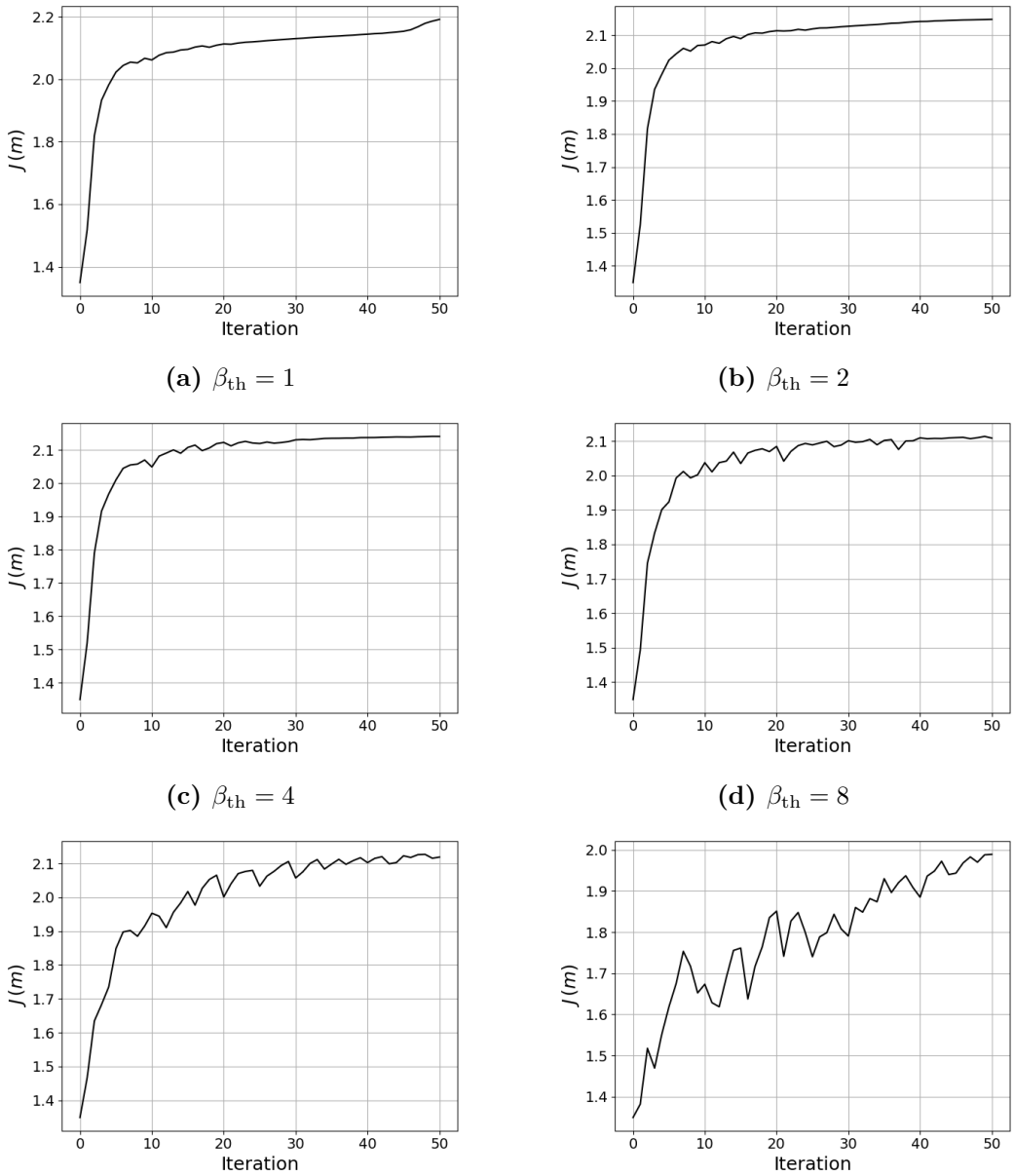

(a) $\beta_{\text{th}} = 1$ **(b)** $\beta_{\text{th}} = 2$

(c) $\beta_{\text{th}} = 4$ **(d)** $\beta_{\text{th}} = 8$

(e) $\beta_{\text{th}} = 16$ **(f)** $\beta_{\text{th}} = 32$

Figure 4.41 – Objective function history for the straight-through labyrinth seal with $q_{\text{c}} = 0.01$.

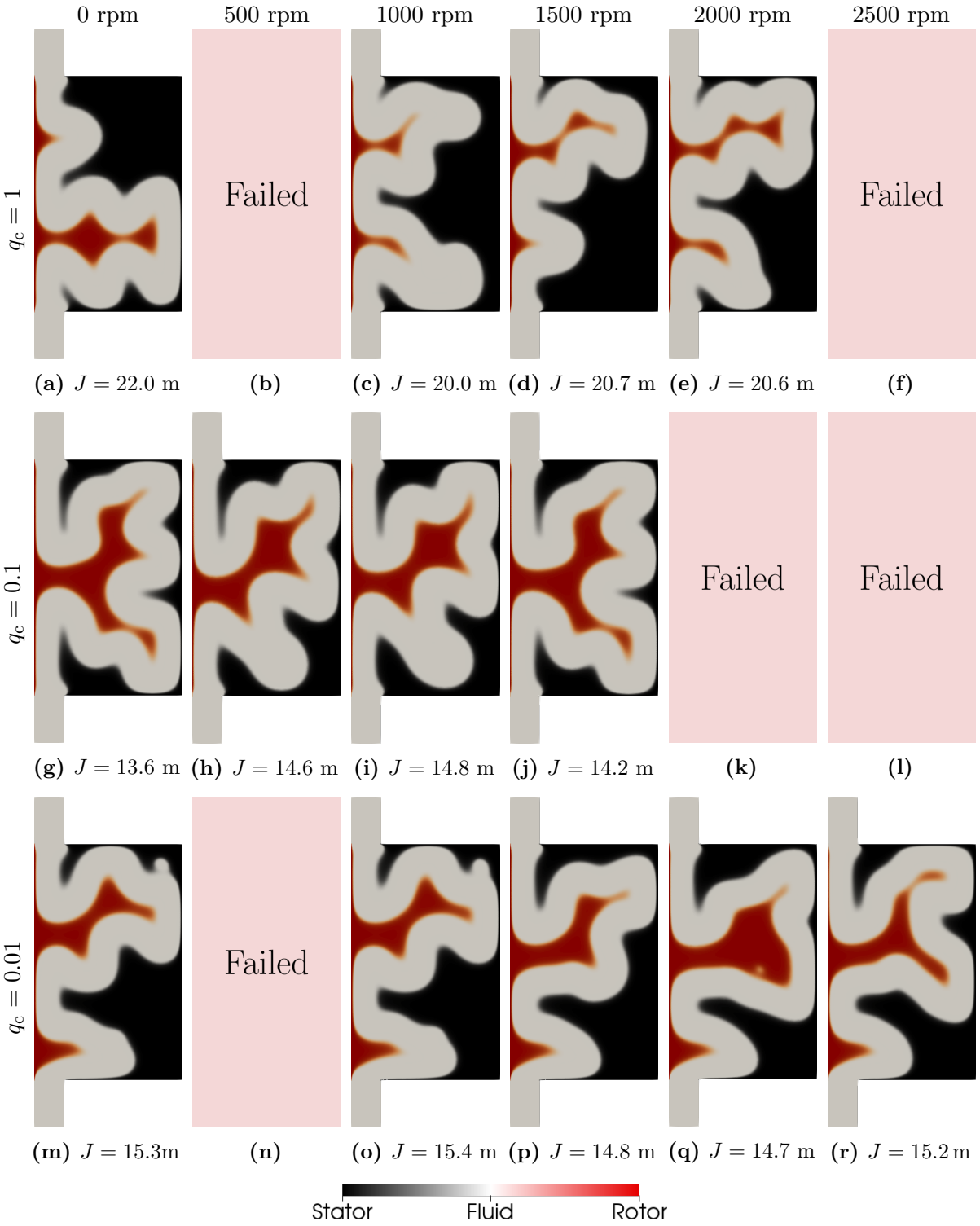

Figure 4.42 – Staggered labyrinth seal design in turbulent regime with interface identification method and VTM constraint (Re = 500 and different angular velocities).

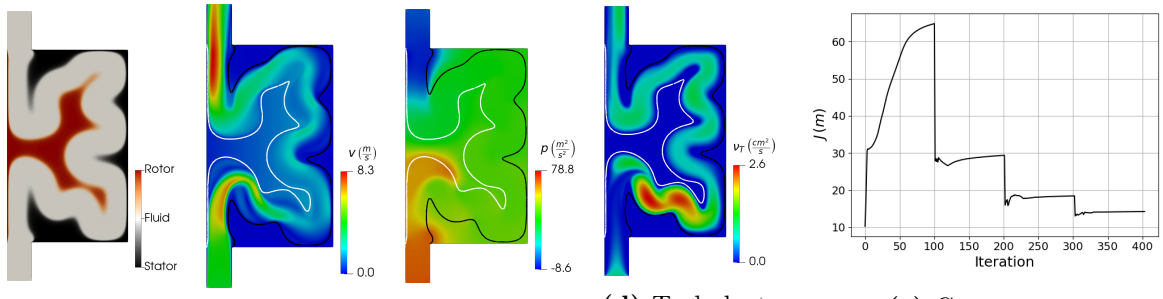

(a) Result **(b)** Velocity **(c)** Pressure **(d)** Turbulent viscosity **(e)** Convergence history

Figure 4.43 – Staggered labyrinth seal optimization in turbulent regime with interface identification method and $q_c = 0.1$ (Re = 500 and $\omega_r = 1500$ rpm). The final head loss is $J = 14.2$ m.

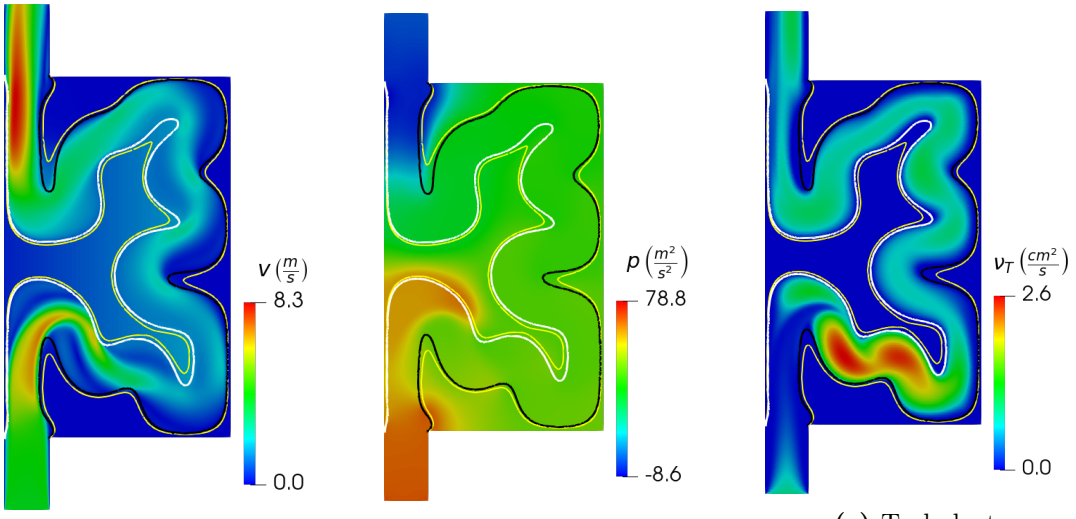

(a) Velocity **(b)** Pressure **(c)** Turbulent viscosity

Figure 4.44 – Staggered labyrinth seal in turbulent flow with isolines at $m_r = m_s = 0.5$ (yellow), $m_r = 0.1$ (white), and $m_s = 0.1$ (black).

model; however, the isolines at $m_r = 0.5$ do not delimit this influence. Also, for lower radial coordinates, small values of m_s have the same effect. Therefore, it is more appropriate to use a different isoline level for interpreting the results as shown in Fig. 4.44, where the isolines at $m_r = m_s = 0.5$ are drawn in yellow, and the new isolines at $m_r = m_s = 0.1$ are drawn in white and black. The shift from the yellow to the black and white isolines improves the capture of the material model influence.

Next, the influence of the rotation is accessed by inspecting the state variables of the result from Fig. 4.42g, which was obtained with $\omega_r = 0$. The velocity, pressure, and kinematic viscosity are presented in Fig. 4.45, with the isolines drawn at $m_r = m_s = 0.1$ to capture the influence of the material model better. The turbulent viscosity is similar to Fig. 4.43d, indicating that the shaft rotation is not the deciding factor for forming turbulent eddies. Still, the head loss of the result with $\omega_r = 1500$ rpm is slightly larger, showing some contribution of the rotation to increase the head loss. The convergence history presents the same features of the result with rotation, corroborating that a smoother continuation

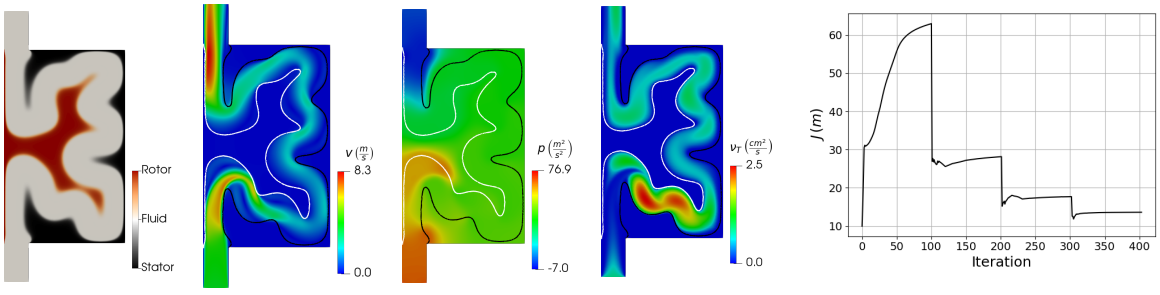

(a) Result **(b)** Velocity **(c)** Pressure **(d)** Turbulent viscosity **(e)** Convergence history

Figure 4.45 – Staggered labyrinth seal optimization in turbulent regime with interface identification method and $q_c = 0.1$ (Re $= 500$ and $\omega_r = 0$ rpm). The isolines are at $m_r = m_s = 0.1$. The final head loss is $J = 13.6$ m.

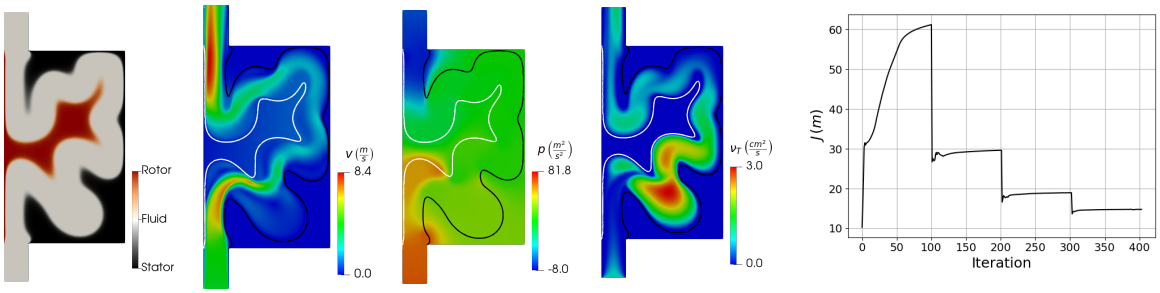

(a) Result **(b)** Velocity **(c)** Pressure **(d)** Turbulent viscosity **(e)** Convergence history

Figure 4.46 – Staggered labyrinth seal optimization in turbulent regime with interface identification method and $q_c = 0.1$ (Re $= 500$ and $\omega_r = 1000$ rpm). The isolines are at $m_r = m_s = 0.1$. The final head loss is $J = 14.8$ m.

strategy should be investigated.

Finally, the influence of the chamber from Fig. 4.42i is studied by inspecting the state variable fields. The chamber concentrates the larger values of turbulent kinetic viscosity, and the head loss is greater than in the result for 1500 rpm, although the angular velocity is lower (1000 rpm), showing the importance of the chambers in improving turbulent dissipation. The pressure drops in the three cases (Figs. 4.42g, 4.42i, and 4.42j) are associated with increases in the velocity. Therefore, they are not dissipative because the pressure head is converted into velocity head.

4.2.6 Stepped Labyrinth Seal in Turbulent Flow

The stepped seal in turbulent flow is also optimized with the interface identification method (Section 2.4.5.2) and VTM constraint (Section 2.4.5.4). Therefore, Equation 4.9 is solved to design the stepped seal in turbulent flow. The same study regarding the influence of material model convexity q_c and shaft rotation ω_r is performed for the stepped seal, and the results are presented in Fig. 4.47. As the radial coordinate of the outlet is larger, the fluid flow with large rotations is more difficult to simulate in the stepped seal than in the staggered seal. In consequence, the results for 2000 and 2500 rpm failed. For the other

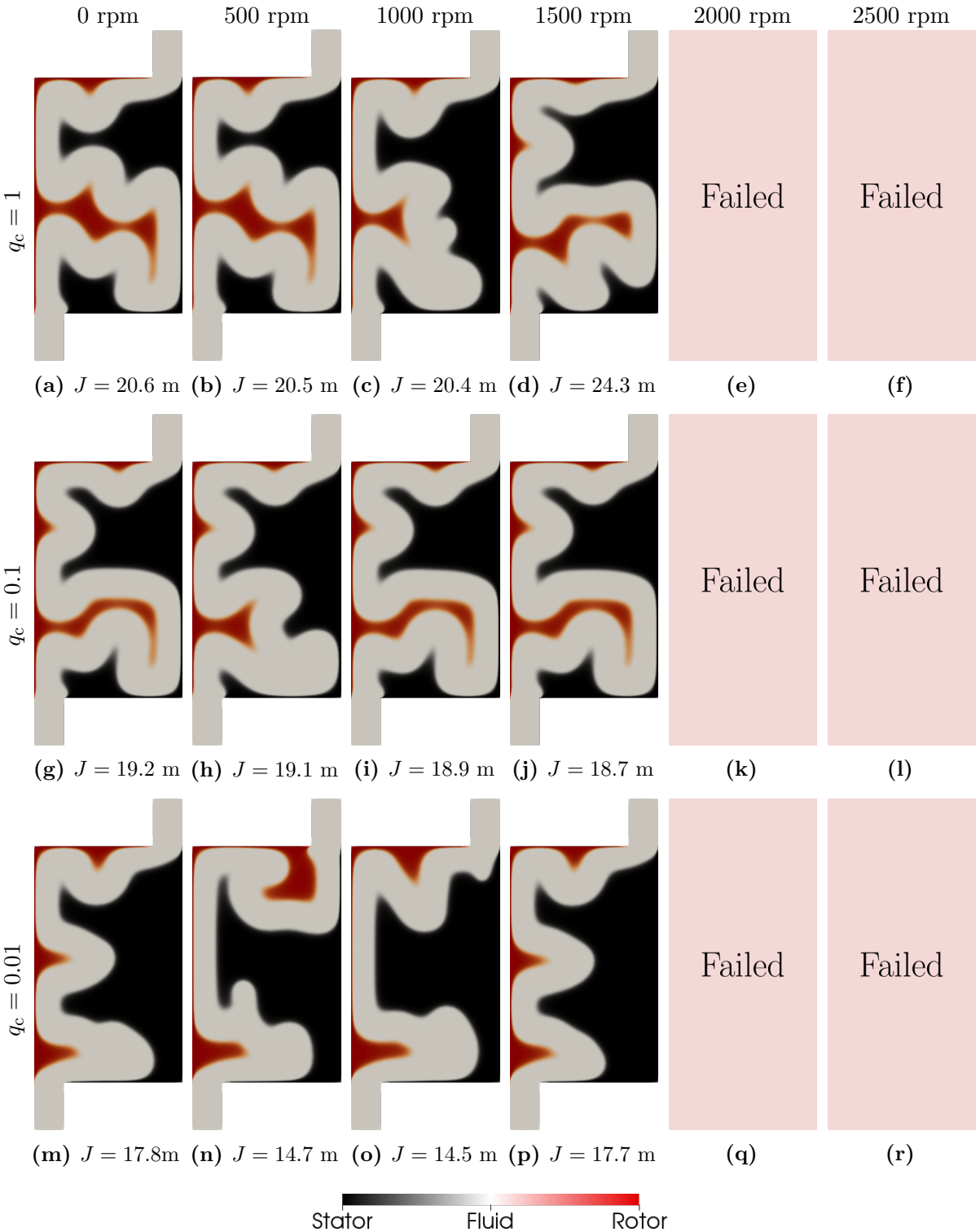

Figure 4.47 – Stepped labyrinth seal design in turbulent regime with interface identification method and VTM constraint (Re = 500 and different angular velocities).

angular velocities, most of the results are tortuous paths that deviate the flow multiple times to form turbulent eddies.

Figure 4.48 shows the velocity, pressure, and turbulent viscosity fields for the result with $q_c = 0.1$ and $\omega_r = 1500$ rpm (Fig. 4.47j). As in the staggered seal, the turbulent viscosity is higher in the parts of the design domain where the flow is deviated by the

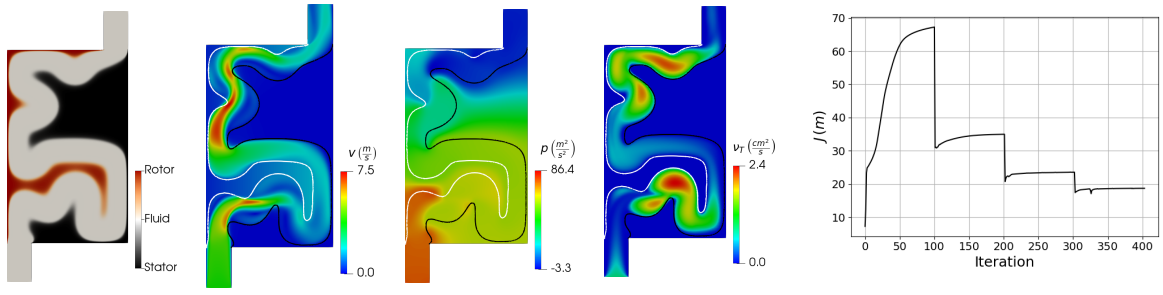

(a) Result **(b)** Velocity **(c)** Pressure **(d)** Turbulent viscosity **(e)** Convergence history

Figure 4.48 – Stepped labyrinth seal optimization in turbulent regime with interface identification method and $q_c = 0.01$ (Re = 500 and $\omega_r = 1500$ rpm). The final head loss is $J = 18.7$ m.

rotor or stator geometry. Also, the velocity field shows that the flow towards the outlet is constricted in regions with high turbulent viscosity. The objective function oscillates less after the continuation steps than in the staggered seal example. The isolines of m_r and m_s are drawn at 0.1 according to the previous section's discussion. These isolines envelop the turbulent viscosity field appropriately. However, there is some seepage in parts of the velocity field, showing the increased difficulty of calibrating the material model parameters in turbulent flow.

4.3 Inflatable Seals

This section presents topology optimization results with the solid material models described in Section 2.4.4 for solids with large deformations subjected to pressure loads. These results are the first step towards designing inflatable seals with topology optimization and combining the concepts of labyrinth seals with inflatable seals. One critical remark is that the discrete filter given by Eq. 2.48 is used for density filtering instead of the PDE filter given by Eq. 2.46. The rationale for this change is presented in Appendix C.

4.3.1 Topology Optimization with Finite Deformation and Pressure Loads

The internally pressurized lid is the first study regarding structural topology optimization with finite deformation and pressure loads. The idea is to check how including the geometrical and material nonlinearities affects the optimized result of a well-known topology optimization benchmark (DU; OLHOFF, 2004; SIGMUND; CLAUSEN, 2007). The optimization problem consists of minimizing the structural compliance under a volume

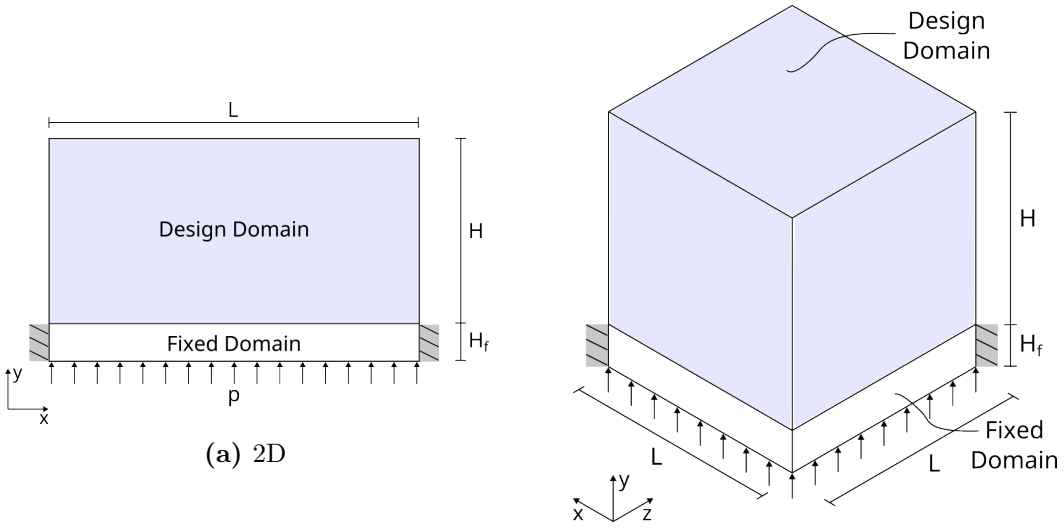

(a) 2D **(b)** 3D

Figure 4.49 – Design domain and boundary conditions of the internally pressurized lid benchmark.

constraint, which may written as follows

$$\begin{aligned} \min_{m} \quad & C_{\mathrm{s}}\left(\boldsymbol{u}\right) \\ \text{s.t.} \quad & D\,\Pi(\boldsymbol{u})[\boldsymbol{w}_u] = 0 \quad \forall \boldsymbol{w}_u \in \mathcal{U} \\ & G_V \leq 0 \\ & m \in [0,\, 1] \end{aligned} \tag{4.10}$$

The design domain and boundary conditions of the internally pressurized lid in 2D and 3D are presented in Fig. 4.49. The geometrical parameters are $L = 0.2$ m, $H = 0.1$ m, and $H_f = 0$ m (after numerical tests, it was noted that the fixed fluid region at the bottom of the domain is unnecessary). The pressure load is $P = 0.1$ GPa and the solid is nylon with a Young's modulus of 3 GPa and a Poisson's ratio of 0.4. The mesh is composed of 200x100 quadrilateral elements of degree 1, the density filter radius is $r_{\min} = 2$ mm, the threshold of the projection is $\eta_{\mathrm{th}} = 0.5$, and the volume fraction is 0.25. The slope of the smooth Heaviside projection β_{th} and SIMP penalization exponent P_{simp} follow the update strategy presented by Wang et al. (2014). The slope β_{th} starts at 1 and ends at 32, while the exponent P_{simp} starts at 1 and ends at 3. The same problem is optimized with the linear and nonlinear models for comparison. In fact, the continuation of P_{simp} is only important for the nonlinear optimization. The indicator function (Eq. 2.57) is obtained with $\eta_\gamma = 0.01$ and $\beta_\gamma = 500$.

Figure 4.50 presents the result of the linear constitutive model (Eq. 2.51), with the deformed configuration and the convergence curve. The solid is assumed to be under plane strain. The optimized result is a round structure in accordance with the literature on design-dependent pressure loads for small deformations (KUMAR; FROUWS; LANGELAAR, 2020). However, the deformation is high for the linear analysis to be

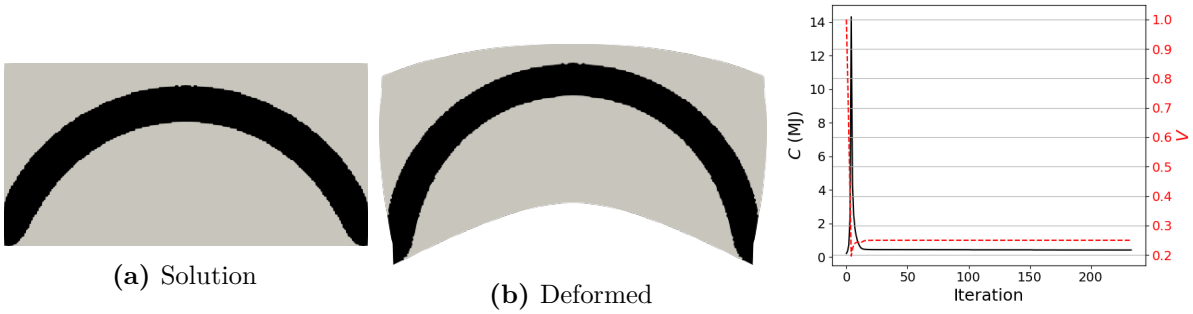

(a) Solution **(b)** Deformed **(c)** Convergence

Figure 4.50 – Design of an internally pressurized lid with linear constitutive model. The final objective function value is $C_s = 0.42$ MJ.

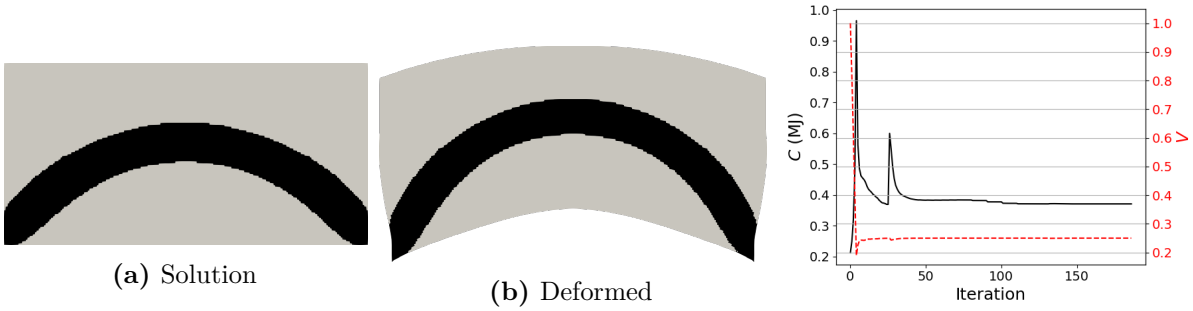

(a) Solution **(b)** Deformed **(c)** Convergence

Figure 4.51 – Design of an internally pressurized lid with Neo-Hookean constitutive model. The final objective function value is $C_s = 0.37$ MJ.

accurate. When running the same problem with a nonlinear solver and Neo-Hookean constitutive model, the optimized result is a flatter structure according to Fig. 4.51. The convergence of the nonlinear study is more oscillatory than the convergence of the linear result. Therefore, tuning the MMA optimizer better may be necessary if the oscillations become problematic.

The same study is performed in 3D and presented in Figs. 4.52 and 4.53. Only one-quarter of the design domain is used for analysis and optimization to reduce the computational cost. The mesh is relatively coarser than in the 2D examples, consisting of 25x25x25 hexahedral elements of order 1. Figures 4.52a and 4.53a show the xy view of the design domain, while Figs. 4.52b and 4.53b present the 3D result with one quarter trimmed to show the internal part of the structure. Again, the nonlinear result is flatter, although the difference is more subtle than in the 2D result. Also, the convergence curve of the nonlinear case (Fig. 4.53) is more oscillatory than the convergence of the linear case (Fig. 4.52c).

The second study involves the piston head benchmark problem, and the focus is to evaluate the behavior under compression and traction by running the topology optimization algorithm with positive and negative pressures. Again, Equation 4.10 provides the mathematical description of the optimization problem. Figure 4.54 presents the design

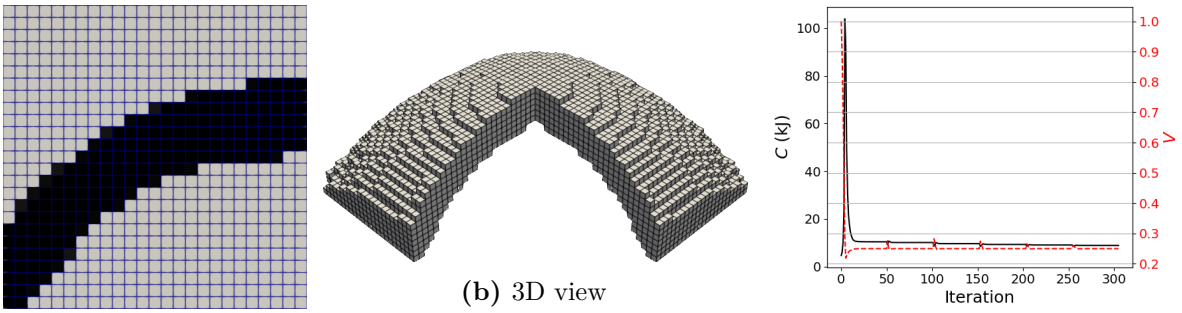

(a) 2D view **(b)** 3D view **(c)** Convergence

Figure 4.52 – Design of an internally pressurized lid in 3D with linear constitutive model. The final objective function value is $C_s = 8.9$ kJ.

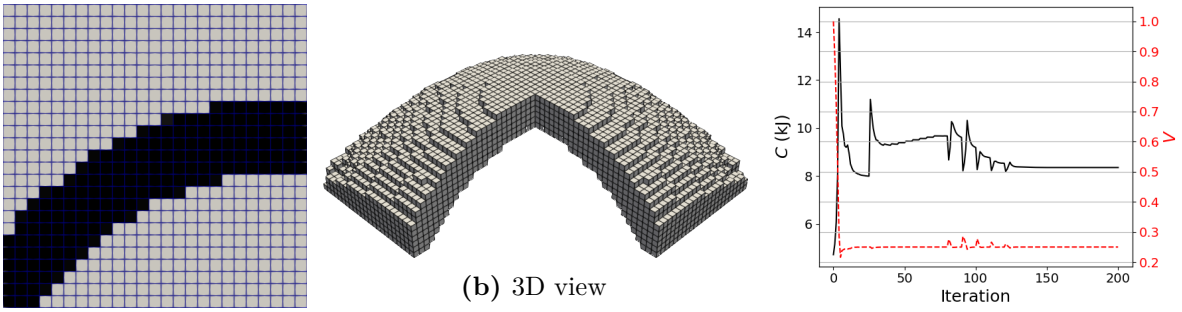

(a) 2D view **(b)** 3D view **(c)** Convergence

Figure 4.53 – Design of an internally pressurized lid in 3D with Neo-Hookean constitutive model. The final objective function value is $C_s = 8.4$ kJ.

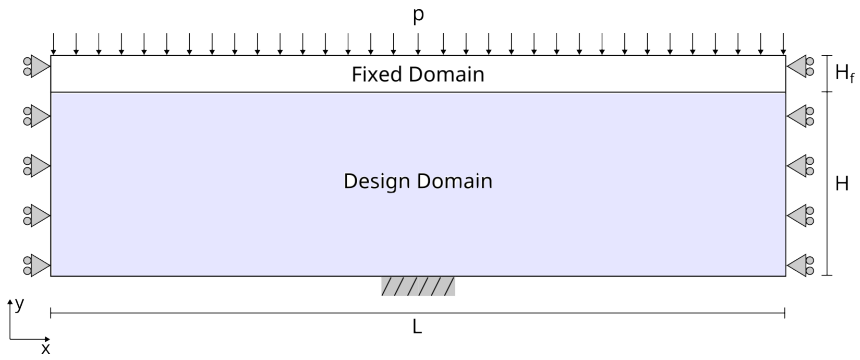

Figure 4.54 – Design domain and boundary conditions for the piston head optimization case.

domain and boundary conditions of the problem. The geometrical parameters of the problem are $L = 0.12$ m, $H = 0.04$ m, and $H_f = 0$. The lower support size is $L/10$. The mesh is composed of 240x160 quadrilateral elements of order 1. The material is nylon with the same parameters as the internally pressurized lid design. The density filter radius is $r_{\text{min}} = 2$ mm, the projection threshold is $\eta_{\text{th}} = 0.5$, and the projection slope starts at $\beta_{\text{th}} = 1$ and ends at 8. The SIMP penalization P_{simp} is constant and equals 3 for the linear analysis, while it starts at 1 and ends at 3 for the nonlinear analysis. The indicator function is calculated with $\eta_\gamma = 0.01$ and $\beta_\gamma = 500$.

Figure 4.55 presents the piston head designs, with the nonlinear results in the first

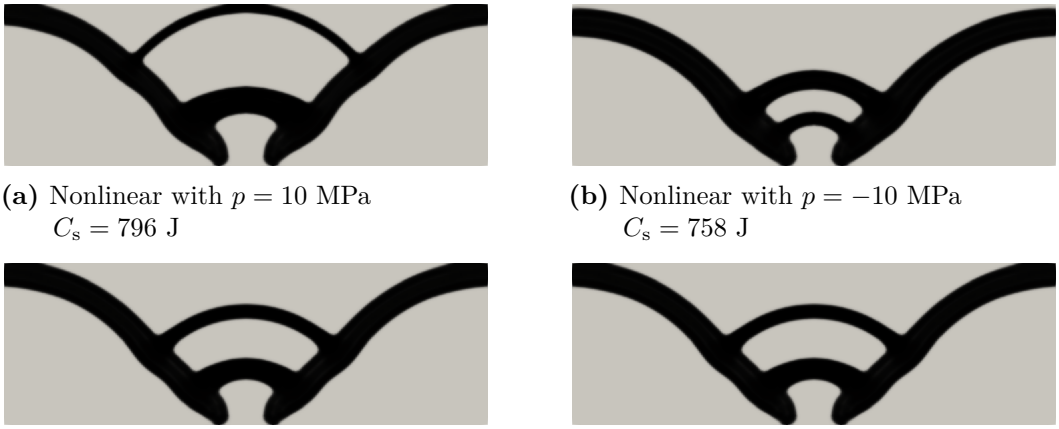

(a) Nonlinear with $p = 10$ MPa
$C_s = 796$ J

(b) Nonlinear with $p = -10$ MPa
$C_s = 758$ J

(c) Linear with $p = 10$ MPa
$C_s = 766$ J

(d) Linear with $p = -10$ MPa
$C_s = 766$ J

Figure 4.55 – Design of a piston head with linear and Neo-Hookean constitutive models. The behavior under compression and traction is evaluated by running the topology optimization algorithm with positive and negative pressures.

row and the linear results in the second row. It is seen that the topology of the nonlinear results change when the pressure load is positive (compression) or negative (traction). In contrast, the same result is obtained for the linear optimization with positive or negative pressures. All results present the same topology consisting of two arms connecting the lower support to the lateral rollers and two arcs that connect the arms and form two chambers. The nonlinear result with positive pressure (Fig. 4.55a) presents the arcs at the upper part of the design domain and larger chambers. The arcs of the nonlinear result with negative pressure (Fig. 4.55a) are concentrated at the design domain's lower part, creating smaller chambers. The linear results (Figs. 4.55c and 4.55d) are between the nonlinear results with positive and negative pressures.

4.3.2 Topology Optimization of Inflatable Seals

The design of inflatable seals involves selecting undeformed and actuated configurations for the seal, with the movement being defined by the flexibility of each part of the seal. This design process is similar to the design of a compliant mechanism. Therefore, it is possible to model inflatable seals as compliant mechanisms and to use the topology optimization formulations developed for compliant mechanisms in the design of the inflatable seals. In this work, the maximization of the output port displacement is selected as the design goal and the optimization problem is given by

$$\begin{aligned} \max_{m} \quad & O\left(\boldsymbol{u}\right) \\ \text{s.t.} \quad & D\,\Pi(\boldsymbol{u})[\boldsymbol{w}_u] = 0 \quad \forall \boldsymbol{w}_u \in \mathcal{U} \\ & m \in [0,\, 1] \end{aligned} \tag{4.11}$$

This section explores two movements that are interesting when designing inflatable

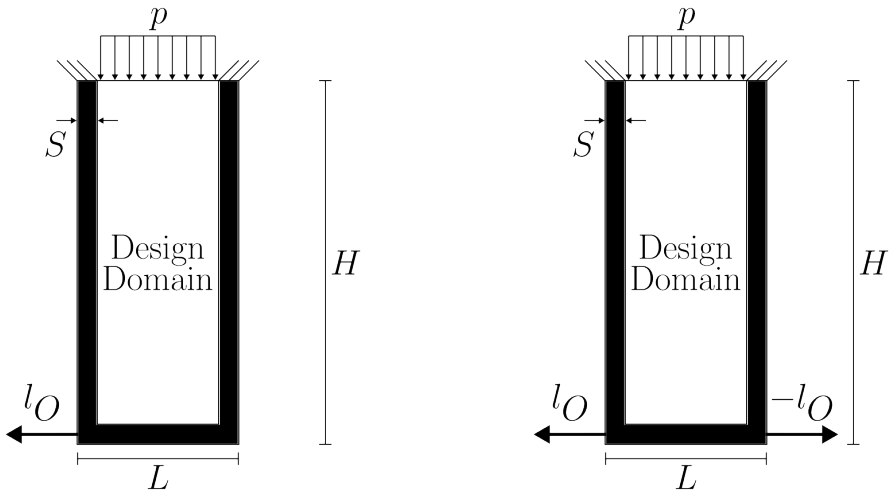

(a) Bending **(b)** Opening

Figure 4.56 – Design domains of inflatable seals.

labyrinth seals. The first movement is the bending of the seal in a desired direction, which may be used to incline the teeth according to angles of maximum head loss. The second movement is the opening of the tip of the tooth, which may be used to reach configurations that can not be assemble directly, such as illustrated in Fig. 1.4b. The design domains for the bending and opening inflatable seals are shown in Fig. 4.56. The design domain is surrounded by fixed solid regions in the right, left, and lower edges. The upper edge is under the actuation of a pressure of $P = 10$ kPa. The inflatable seal measures 80x180 mm and the material is a elastomer with a Young's modulus of 10 MPa and a Poisson's ratio of 0.4. The thickness of the fixed solid region is $S = 10$ mm. The mesh is discretized in 80x180 elements (including the fixed solid regions). The output direction is $\boldsymbol{l}_{\mathrm{O}} = (-1,\, 0)$.

The bending inflatable seal must move its left lower tip in the left direction. Figure 4.57 presents the optimization result, the deformed configuration, and the convergence curve for the optimization considering a linear constitutive model. The optimized design presents a large solid distribution at the left wall, making the right wall deform more than the left wall, making the inflatable seal bend towards the left direction. The jumps in the objective function graph are related to the continuation of the parameter β_{th}. Figure 4.58 presents the results with Neo-Hookean constitutive model. The output displacement is lower in the nonlinear case because the the stiffness increases with the deformation for nonlinear models.

The opening inflatable seal must move both lower tips of the seal in opposite directions as shown in Fig. 4.56b. The topology optimization results with linear and Neo-Hookean constitutive models are presented in Figs. 4.59 and 4.60. Again, the optimized designs present similar material distributions. It is noted that the output displacement is low in both cases, showing the difficulty of achieving the specified movement. In future works, the use of multiple materials or fiber reinforcements could be explored to help achieving

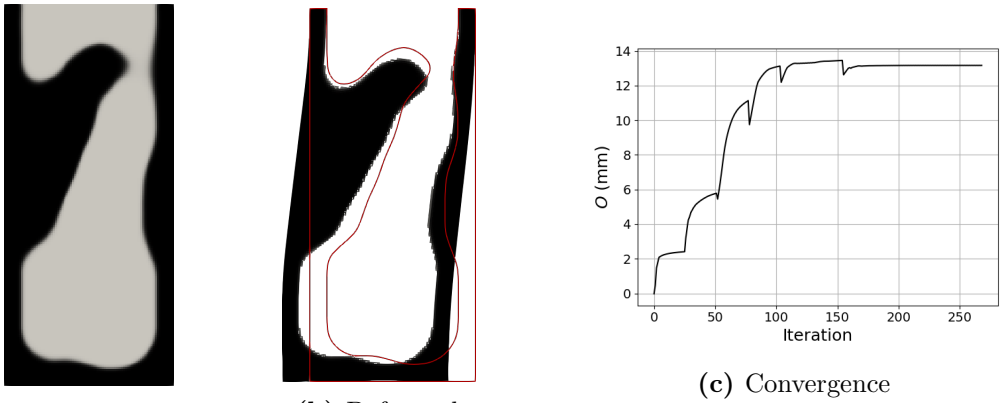

(a) Solution **(b)** Deformed **(c)** Convergence

Figure 4.57 – Design of a bending inflatable seal with linear constitutive model. The final objective function value is $O = 13.2$ mm.

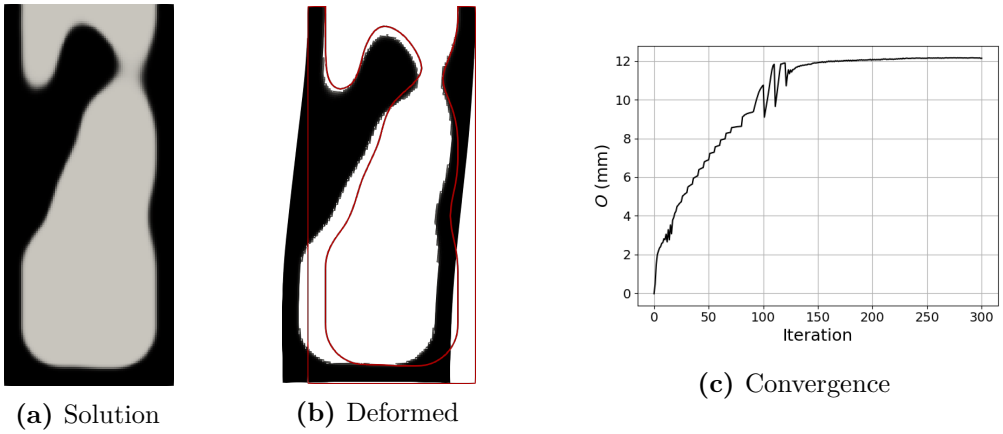

(a) Solution **(b)** Deformed **(c)** Convergence

Figure 4.58 – Design of a bending inflatable seal with Neo-Hookean constitutive model. The final objective function value is $O = 12.1$ mm.

the specified movement.

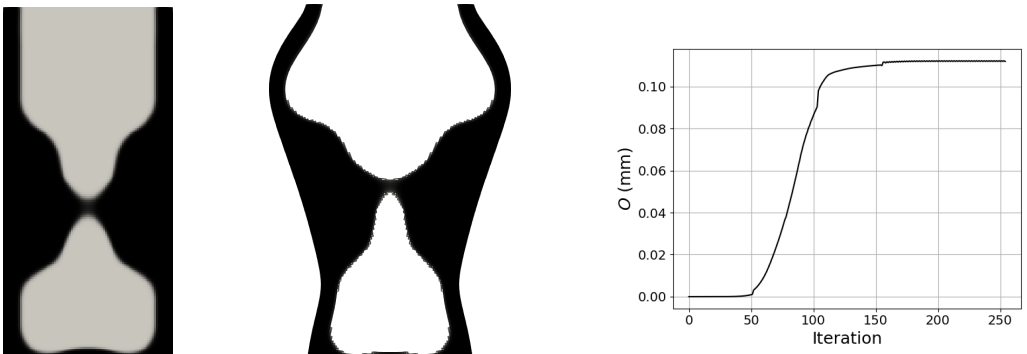

(a) Solution **(b)** Deformed **(c)** Convergence

Figure 4.59 – Design of a opening inflatable seal with linear constitutive model. The final objective function value is $O = 0.112$ mm. The deformed configuration is magnified 10 times.

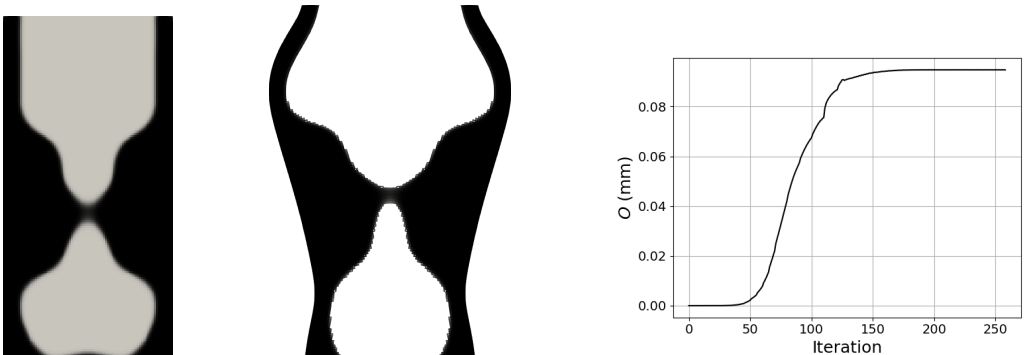

(a) Solution **(b)** Deformed **(c)** Convergence

Figure 4.60 – Design of a opening inflatable seal with Neo-Hookean constitutive model. The final objective function value is $O = 0.095$ mm. The deformed configuration is magnified 10 times.

5 DISCUSSION & CONCLUSIONS

This work presents the topology optimization of labyrinth seals in straight-through, staggered, and stepped arrangements. The straight-through optimization is achieved by designing only the stator and fixing a non-design domain close to the shaft. The staggered and stepped configurations require specialized formulations capable of imposing a minimum distance between the stator and rotor (i.e., avoiding the channel closure), avoiding free-floating islands, and assigning different velocities to stator and rotor elements. Therefore, two topology optimization algorithms are proposed to design staggered and stepped labyrinth seals. The optimizations of all arrangements are presented for laminar and turbulent flows. The laminar flow studies are based on the Navier-Stokes equations, while the turbulent studies are based on the RANS equations closed with Spalart-Allmaras model. The wall distance required by the Spalart-Allmaras model is calculated with a modified Eikonal equation.

The result of the straight-through design in laminar flow is a straight channel constricted to the minimum gap size. The same result is obtained with discrete and continuous design variables, which is expected because the constriction of the channel increases the velocity gradients, and the viscous energy dissipation due to velocity gradients is the dominant head loss mechanism in laminar flow. The objective function history presents smooth growth, showing that the design does not result from bad convergence. On the other hand, the discrete approach suffered from oscillations for turbulent flow. The oscillations are associated with linearization errors and the number of design variable changes ("step size"). Reducing the number of allowed design variable changes through the parameter β_{fl} was not viable because the optimization oscillated among similar designs. The continuous approach created open chambers with diminishing size in the downstream direction because the turbulent eddies require space to develop, and the space size depends on the flow's energy. As the fluid loses energy within each chamber, the optimal size of the chamber decreases in the downstream direction. The optimization with low β_{th} values is smooth and presents intermediate pseudo-densities, while the optimization with high β_{th} values is oscillatory and produces designs with clear interfaces. One possible improvement is to use smooth continuation strategies, such as the update schemes applied to the design of nonlinear structures under pressure loads. These smooth continuation strategies would not increase the number of iterations substantially. Another possible improvement is devising penalization strategies for intermediate pseudo-densities, such as the use of SIMP interpolation in compliance minimization with volume constraints. This last approach would avoid high β_{th} values.

The first algorithm for staggered and stepped seal optimization is based on discrete design variables and consists of an extension of the TOBS method. It was named rotor-stator algorithm, and it uses two design variable fields to model the stator and rotor separately. The allowed design changes depend on the neighbors of each element, allowing the control of the minimum gap size, avoiding free-floating islands, and circumventing the overlapping of stator and rotor elements. A new Darcy term is added to the momentum equation to model the rotor angular velocity inside the design domain. The discrete nature of the formulation produces clear interfaces, which allow modeling and designing sharp features, which are efficient for inducing recirculation and turbulent eddies. However, this advantage also introduces difficulties in simulating crisp designs in turbulent flow. The laminar results are channels constricted to the minimum gap size for low Reynolds numbers and a combination of constricted channels and chambers for moderate Reynolds. The results are highly dependent on the initial guess. The convergence is monotonic and smooth for laminar flows. The turbulent flow optimization demanded using FEniCS TopOpt FOAM to bridge the OpenFoam simulation with FEniCS sensitivity analysis. However, the turbulent convergence curves are oscillatory, and the optimization only ends due to the maximum number of iterations. On the other hand, the discrete nature of the formulation is well-suited for geometry trimming procedures (PICELLI et al., 2022), which avoids mixing FEM and FVM. In its current form, the minimum gap is anisotropic because the ℓ_1-distance is used in the definition of the neighborhood.

The second algorithm for staggered and stepped seal optimization uses continuous design variables and considers the fluid as the interface between the rotor and stator. An interface identification method developed for the design of heat exchangers is extended to the design of labyrinth seals. One design variable field goes through a series of filters and projections to create two non-overlapping fields for the stator and rotor. As in the first algorithm, a new Darcy term is added to the momentum equation to model the rotor angular velocity. The interface identification method itself does not avoid solid free-floating islands, so the virtual temperature method (VTM) is used as a connectivity constraint. The laminar results are channels constricted to the minimum gap size with longer lengths than for the discrete algorithm. For turbulent flow, the optimizer explores two mechanisms for generating turbulence: open chambers of appropriate size and curved geometries to deviate the flow, inducing recirculation. This last mechanism is more prevalent in the results, possibly due to the level of turbulence considered in this work. However, the continuous approach is not capable of creating sharp edges due to the filtering operations. The results of the continuous approach are dependent on the material model parameters, such as the convexity q_c.

Regarding the differences between the rotor-stator and the interface identification methods, the first aspect worth mentioning is that the algorithms result in different

optimization problems. Therefore, they are expected to produce different optimization results. The rotor-stator algorithm keeps only part of the elements active during each optimization step, while the interface identification method keeps the whole design domain active. Another difference between the algorithms is the computational cost. At first glance, the rotor-stator method requires more computational effort because it solves the forward and adjoint problem twice at each optimization step. Also, the branch-and-bound algorithm is slower than MMA. However, the rotor-stator algorithm stops within fewer iterations than the interface identification algorithm. In this work, the interface identification examples took more computational time because the maximum number of iterations at each continuation step was kept high to allow complete exploration of the design. If the stopping criteria of the interface identification method are changed, then this algorithm becomes faster.

This work also investigated the inclusion of FSI formulations during the topology optimization of labyrinth seals. The study explored using FSI to avoid free-floating solid islands as in the work of Souza et al. (2021). However, structural compliance is included as a constraint instead of as an objective function. The formulation of Yoon (2010) is adapted to run as a staggered solver in an one-way coupling. This adaption reduces the computational cost and presents no disadvantages, as the accuracy of the displacement field is not important. The performance of the VFSI constraint was inferior than the VTM constraint. Therefore, the author recommends using the VTM as a connectivity constraint.

The design of inflatable seals by topology optimization is initiated by establishing the necessary models to treat pressure loads with finite deformation. The neo-hookean constitutive model is decomposed into deviatoric and hydrostatic components to enable transmitting loads in normal direction. The material model interpolates the strain energy density function of the deviatoric and hydrostatic parts separately. A smooth convergence of the parameter β_{th} is used. The formulation is applied to benchmark problems of topology optimization with pressure loads (internally pressurized lid and piston head). The next step is to include the desired deformation in the topology optimization algorithm, such as in the works of Pedersen, Buhl and Sigmund (2001) and Li and Zhang (2023).

Regarding the fluid flow simulations, combining the forward solution from OpenFoam and the adjoint analysis from FEniCS is successful. However, attention to the level of artificial seepage in the solid domain is required. The artificial seepage is introduced by the projection from FVM to FEM. Also, the objective function convergence is less smooth than using an approach with FEM for forward and adjoint analysis. Iterative algorithms such as SIMPLE may be more robust for high Reynolds numbers and faster for large problems. However, in general, these algorithms are slower for low Reynolds numbers, significantly impacting topology optimization duration as the forward problem is solved several times.

Analyzing and optimizing labyrinth seals is difficult for turbulent flow because the

number of eddies increases as the optimization evolves. This increase is in contrast to the problems commonly solved in fluid flow topology optimization literature, which seeks to minimize energy dissipation and, therefore, reduce the number of turbulent eddies along the optimization. Therefore, the labyrinth seal design is an important benchmark for future turbulent flow topology optimization algorithms.

Finally, the proposed approaches successfully optimized straight-through, staggered, and stepped labyrinth seals in incompressible turbulent flows. The obtained designs present unconventional features, such as the diminishing chamber size in straight-through arrangement and the teeth with curves along the radial direction in the staggered and stepped arrangements. These unconventional features corroborate the importance of applying topology optimization to design labyrinth seals. Even if physical experiments show that these features are not optimal, the model's accuracy may be increased with other turbulence models and compressible flow to make the optimization results more physically appealing.

5.1 Future Work

The author suggests that future work should focus on running the proposed formulations with other turbulence closure models, such as the $k-\omega$ SST model, which is accurate for modeling labyrinth seals according to the experimental validation of Wein et al. (2020) (if the model parameters are correctly adjusted). Also, the proposed formulations should be executed with compressible flows to increase the model's accuracy and allow leakage minimization as the optimization problem goal. The optimization results should also be tested experimentally.

For the rotor-stator algorithm, it would be interesting to change the norm of the neighborhood definition. Also, including minimum length constraints would avoid extremely thin members, which are not physically feasible and may be the reason for high oscillations during optimization in turbulent regimes.

For the continuous approach to design staggered and stepped seals, the author suggests testing smooth continuation strategies to update β_{th} in turbulent flow. Also, including minimum length geometric constraint is essential as some results may present unfeasible thin structural members. In Moscatelli et al. (2024), the minimum length geometric constraint of Zhou et al. (2015) is used; however, this constraint is hard to calibrate and may only be activated after the optimization is close to the final solution, which is undesired features. Therefore, there is open room for investigating other minimum length constraints for the design of labyrinth seals with the interface identification method.

A feature in most staggered and stepped labyrinth seal designs with the discrete

approach is a 45° ramp close to the inlet and outlet channels. The distance of the rotor and the stator for these features is lower than the minimal gap due to the use of ℓ_1-distance to define the neighborhoods. Another line of research is to check if the minimum gap in the diagonal direction may be lower than in radial or axial directions. If the diagonal gap may be lower, it is possible to introduce ramps close to the teeth to improve labyrinth seal performance. The gap in the diagonal direction may be reduced by introducing elastomeric annular rings close to the teeth, as shown in Fig. 5.1. If elastomeric materials are used, the rings may also act as a safety mechanism against rubs.

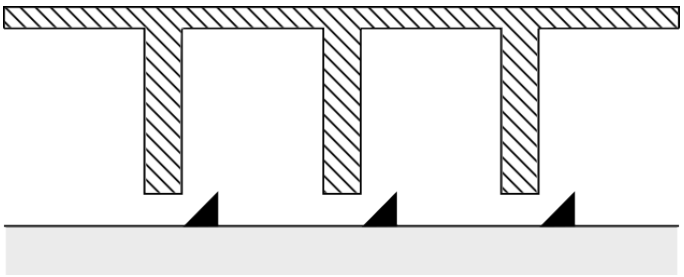

Figure 5.1 – Conceptual idea of reducing the labyrinth seal gap in diagonal direction close to the teeth.

REFERENCES

ALEXANDERSEN, J.; ANDREASEN, C. S. A review of topology optimisation for fluid-based problems. **Fluids**, MDPI AG, v. 5, n. 1, p. 29, mar. 2020. Available from Internet: <https://doi.org/10.3390/fluids5010029>. Cited 2 times in pages 32 and 39.

ALNÆS, M. S.; LOGG, A.; MARDAL, K.-A.; SKAVHAUG, O.; LANGTANGEN, H. P. Unified framework for finite element assembly. 2008. Available from Internet: <https://arxiv.org/abs/1205.3039>. Cited in page 79.

ALNÆS, M. S.; LOGG, A.; ØLGAARD, K. B.; ROGNES, M. E.; WELLS, G. N. Unified form language. **ACM Transactions on Mathematical Software**, Association for Computing Machinery (ACM), v. 40, n. 2, p. 1–37, fev. 2014. Available from Internet: <https://doi.org/10.1145/2566630>. Cited in page 79.

ALONSO, D. H.; RODRIGUEZ, L. F. G.; SILVA, E. C. N. Flexible framework for fluid topology optimization with OpenFOAM® and finite element-based high-level discrete adjoint method (FEniCS/dolfin-adjoint). **Structural and Multidisciplinary Optimization**, Springer Science and Business Media LLC, v. 64, n. 6, p. 4409–4440, set. 2021. Available from Internet: <https://doi.org/10.1007/s00158-021-03061-4>. Cited 3 times in pages 46, 80, and 151.

ALONSO, D. H.; SAENZ, J. S. R.; PICELLI, R.; SILVA, E. C. N. Topology optimization method based on the wray–agarwal turbulence model. **Structural and Multidisciplinary Optimization**, Springer Science and Business Media LLC, v. 65, n. 3, fev. 2022. Available from Internet: <https://doi.org/10.1007/s00158-021-03106-8>. Cited in page 33.

ALONSO, D. H.; Sá, L. F. N. de; SAENZ, J. S. R.; SILVA, E. C. N. Topology optimization applied to the design of 2d swirl flow devices. **Structural and Multidisciplinary Optimization**, Springer Science and Business Media LLC, v. 58, n. 6, p. 2341–2364, out. 2018. ISSN 1615-1488. Available from Internet: <http://dx.doi.org/10.1007/s00158-018-2078-0>. Cited in page 40.

BALAY, S.; ABHYANKAR, S.; ADAMS, M. F.; BROWN, J.; BRUNE, P.; BUSCHELMAN, K.; DALCIN, L.; DENER, A.; EIJKHOUT, V.; GROPP, W. D.; KAUSHIK, D.; KNEPLEY, M. G.; MAY, D. A.; MCINNES, L. C.; MILLS, R. T.; MUNSON, T.; RUPP, K.; SANAN, P.; SMITH, B. F.; ZAMPINI, S.; ZHANG, H.; ZHANG, H. **PETSc Users Manual**. [S.l.], 2021. Cited 2 times in pages 79 and 82.

BALAY, S.; ABHYANKAR, S.; ADAMS, M. F.; BROWN, J.; BRUNE, P.; BUSCHELMAN, K.; DALCIN, L.; DENER, A.; EIJKHOUT, V.; GROPP, W. D.; KAUSHIK, D.; KNEPLEY, M. G.; MAY, D. A.; MCINNES, L. C.; MILLS, R. T.; MUNSON, T.; RUPP, K.; SANAN, P.; SMITH, B. F.; ZAMPINI, S.; ZHANG, H.; ZHANG, H. **PETSc Web page**. 2021. Https://petsc.org/. Cited 2 times in pages 79 and 82.

BARDINA, J. E.; HUANG, P. G.; COAKLEY, T. J. **Turbulence Modeling Validation, Testing, and Development**. Moffett Field, California 94035-1000, 1997. Available from Internet: <https://ntrs.nasa.gov/citations/19970017828>. Cited in page 46.

BELLAOUAR, A.; KOPEY, B. V.; ABDELBAKI, N. Methods of the rational choice of a labyrinth seal design for gas pumping unit. **Mechanika**, Kaunas University of Technology (KTU), v. 19, n. 1, mar. 2013. ISSN 1392-1207. Available from Internet: <http://dx.doi.org/10.5755/j01.mech.19.1.3611>. Cited in page 27.

BENDSØE, M. P. Optimal shape design as a material distribution problem. **Structural Optimization**, Springer Science and Business Media LLC, v. 1, n. 4, p. 193–202, dez. 1989. Available from Internet: <https://doi.org/10.1007/bf01650949>. Cited in page 31.

BENDSØE, M. P.; KIKUCHI, N. Generating optimal topologies in structural design using a homogenization method. **Computer Methods in Applied Mechanics and Engineering**, Elsevier BV, v. 71, n. 2, p. 197–224, nov. 1988. Available from Internet: <https://doi.org/10.1016/0045-7825(88)90086-2>. Cited in page 31.

BOETTIGER, C. An introduction to docker for reproducible research, with examples from the r environment. arXiv, 2014. Available from Internet: <https://arxiv.org/abs/1410.0846>. Cited in page 81.

BONET, J.; WOOD, R. D. **Nonlinear Continuum Mechanics for Finite Element Analysis**. [S.l.]: Cambridge University Press, 2008. ISBN 978-0-521-83870-2. Cited 2 times in pages 34 and 58.

BORRVALL, T.; PETERSSON, J. Topology optimization of fluids in stokes flow. **International Journal for Numerical Methods in Fluids**, Wiley, v. 41, n. 1, p. 77–107, 2003. Available from Internet: <https://doi.org/10.1002/fld.426>. Cited 6 times in pages 32, 43, 53, 55, 101, and 151.

BOURDIN, B. Filters in topology optimization. **International Journal for Numerical Methods in Engineering**, Wiley, v. 50, n. 9, p. 2143–2158, fev. 2001. ISSN 1097-0207. Available from Internet: <http://dx.doi.org/10.1002/nme.116>. Cited in page 54.

BOURDIN, B.; CHAMBOLLE, A. Design-dependent loads in topology optimization. **ESAIM: Control, Optimisation and Calculus of Variations**, EDP Sciences, v. 9, p. 19–48, jan. 2003. Available from Internet: <https://doi.org/10.1051/cocv:2002070>. Cited in page 32.

BRUNS, T.; SIGMUND, O. Toward the topology design of mechanisms that exhibit snap-through behavior. **Computer Methods in Applied Mechanics and Engineering**, Elsevier BV, v. 193, n. 36-38, p. 3973–4000, set. 2004. Available from Internet: <https://doi.org/10.1016/j.cma.2004.02.017>. Cited in page 35.

BRUNS, T.; TORTORELLI, D. Topology optimization of geometrically nonlinear structures and compliant mechanisms. In: **7th AIAA/USAF/NASA/ISSMO Symposium on Multidisciplinary Analysis and Optimization**. American Institute of Aeronautics and Astronautics, 1998. Available from Internet: <https://doi.org/10.2514/6.1998-4950>. Cited in page 34.

BRUNS, T. E.; TORTORELLI, D. A. Topology optimization of non-linear elastic structures and compliant mechanisms. **Computer Methods in Applied Mechanics and Engineering**, Elsevier BV, v. 190, n. 26-27, p. 3443–3459, mar. 2001. Available from Internet: <https://doi.org/10.1016/s0045-7825(00)00278-4>. Cited 2 times in pages 34 and 54.

BRUNS, T. E.; TORTORELLI, D. A. An element removal and reintroduction strategy for the topology optimization of structures and compliant mechanisms. **International Journal for Numerical Methods in Engineering**, Wiley, v. 57, n. 10, p. 1413–1430, 2003. Available from Internet: <https://doi.org/10.1002/nme.783>. Cited in page 34.

BUHL, T.; PEDERSEN, C.; SIGMUND, O. Stiffness design of geometrically nonlinear structures using topology optimization. **Structural and Multidisciplinary Optimization**, Springer Science and Business Media LLC, v. 19, n. 2, p. 93–104, abr. 2000. Available from Internet: <https://doi.org/10.1007/s001580050089>. Cited in page 34.

CHEN, B.-C.; KIKUCHI, N. Topology optimization with design-dependent loads. **Finite Elements in Analysis and Design**, Elsevier BV, v. 37, n. 1, p. 57–70, jan. 2001. ISSN 0168-874X. Available from Internet: <http://dx.doi.org/10.1016/s0168-874x(00)00021-4>. Cited in page 57.

De Leon, D. M.; GONÇALVES, J. F.; SOUZA, C. E. de. Stress-based topology optimization of compliant mechanisms design using geometrical and material nonlinearities. **Structural and Multidisciplinary Optimization**, Springer Science and Business Media LLC, mar. 2020. Available from Internet: <https://doi.org/10.1007/s00158-019-02484-4>. Cited in page 35.

DEATON, J. D.; GRANDHI, R. V. A survey of structural and multidisciplinary continuum topology optimization: post 2000. **Structural and Multidisciplinary Optimization**, Springer Science and Business Media LLC, v. 49, n. 1, p. 1–38, jul. 2013. Available from Internet: <https://doi.org/10.1007/s00158-013-0956-z>. Cited in page 39.

DILGEN, S. B.; DILGEN, C. B.; FUHRMAN, D. R.; SIGMUND, O.; LAZAROV, B. S. Density based topology optimization of turbulent flow heat transfer systems. **Structural and Multidisciplinary Optimization**, Springer Science and Business Media LLC, v. 57, n. 5, p. 1905–1918, mar. 2018. Available from Internet: <https://doi.org/10.1007/s00158-018-1967-6>. Cited in page 33.

DU, J.; OLHOFF, N. Topological optimization of continuum structures with design-dependent surface loading - Part I: new computational approach for 2D problems. **Structural and Multidisciplinary Optimization**, v. 27, n. 3, p. 151–165, may 2004. ISSN 1615-147X. Available from Internet: <http://link.springer.com/10.1007/s00158-004-0379-y>. Cited 2 times in pages 57 and 124.

EGLI, A. The leakage of steam through labyrinth seals. **Journal of Fluids Engineering**, ASME International, v. 57, n. 3, p. 115–122, abr. 1935. ISSN 0097-6822. Available from Internet: <http://dx.doi.org/10.1115/1.4019911>. Cited in page 27.

EHRICH, F. Aeroelastic instability in labyrinth seals. **Journal of Engineering for Power**, ASME International, v. 90, n. 4, p. 369–374, out. 1968. ISSN 0022-0825. Available from Internet: <http://dx.doi.org/10.1115/1.3609221>. Cited in page 27.

EPA. Inventory of u.s. greenhouse gas emissions and sinks 1990 – 2009. abr. 2011. Cited 2 times in pages 26 and 38.

FARRELL, P. E.; HAM, D. A.; FUNKE, S. W.; ROGNES, M. E. Automated derivation of the adjoint of high-level transient finite element programs. **SIAM Journal on Scientific**

Computing, Society for Industrial & Applied Mathematics (SIAM), v. 35, n. 4, p. C369–C393, jan. 2013. Available from Internet: <https://doi.org/10.1137/120873558>. Cited 2 times in pages 79 and 80.

FLITNEY, R. **Seals and Sealing Handbook**. 6. ed. [S.l.]: Elsevier, 2014. ISBN 978-0-08-099416-1. Cited 3 times in pages 26, 28, and 39.

GERSBORG-HANSEN, A.; SIGMUND, O.; HABER, R. Topology optimization of channel flow problems. **Structural and Multidisciplinary Optimization**, Springer Science and Business Media LLC, v. 30, n. 3, p. 181–192, jun. 2005. Available from Internet: <https://doi.org/10.1007/s00158-004-0508-7>. Cited in page 32.

GRESHO, P. M.; SANI, R. L. On pressure boundary conditions for the incompressible navier-stokes equations. **International Journal for Numerical Methods in Fluids**, Wiley, v. 7, n. 10, p. 1111–1145, out. 1987. ISSN 1097-0363. Available from Internet: <http://dx.doi.org/10.1002/fld.1650071008>. Cited in page 44.

GUEST, J. K.; PRÉVOST, J. H. Topology optimization of creeping fluid flows using a darcy–stokes finite element. **International Journal for Numerical Methods in Engineering**, Wiley, v. 66, n. 3, p. 461–484, 2006. Available from Internet: <https://doi.org/10.1002/nme.1560>. Cited in page 32.

GUEST, J. K.; PRÉVOST, J. H.; BELYTSCHKO, T. Achieving minimum length scale in topology optimization using nodal design variables and projection functions. **International Journal for Numerical Methods in Engineering**, Wiley, v. 61, n. 2, p. 238–254, ago. 2004. Cited 2 times in pages 55 and 63.

HALE, J. S.; LI, L.; RICHARDSON, C. N.; WELLS, G. N. Containers for portable, productive, and performant scientific computing. **Computing in Science & Engineering**, Institute of Electrical and Electronics Engineers (IEEE), v. 19, n. 6, p. 40–50, nov. 2017. Available from Internet: <https://doi.org/10.1109/mcse.2017.2421459>. Cited in page 81.

HIRANO, T.; GUO, Z.; KIRK, R. G. Application of computational fluid dynamics analysis for rotating machinery—part ii: Labyrinth seal analysis. **Journal of Engineering for Gas Turbines and Power**, ASME International, v. 127, n. 4, p. 820–826, set. 2005. ISSN 1528-8919. Available from Internet: <http://dx.doi.org/10.1115/1.1808426>. Cited in page 27.

HØGHØJ, L. C.; NØRHAVE, D. R.; ALEXANDERSEN, J.; SIGMUND, O.; ANDREASEN, C. S. Topology optimization of two fluid heat exchangers. **International Journal of Heat and Mass Transfer**, Elsevier BV, v. 163, p. 120543, dez. 2020. Cited 2 times in pages 63 and 65.

HUANG, X.; XIE, Y. Convergent and mesh-independent solutions for the bi-directional evolutionary structural optimization method. **Finite Elements in Analysis and Design**, Elsevier BV, v. 43, n. 14, p. 1039–1049, out. 2007. Available from Internet: <https://doi.org/10.1016/j.finel.2007.06.006>. Cited in page 78.

HøGHøJ, L. C.; CONLAN-SMITH, C.; SIGMUND, O.; ANDREASEN, C. S. Simultaneous shape and topology optimization of wings. **Structural and Multidisciplinary Optimization**, Springer Science and Business Media LLC, v. 66, n. 5, abr. 2023. ISSN

1615-1488. Available from Internet: <http://dx.doi.org/10.1007/s00158-023-03569-x>. Cited in page 38.

JENKINS, N.; MAUTE, K. Level set topology optimization of stationary fluid-structure interaction problems. **Structural and Multidisciplinary Optimization**, Springer Science and Business Media LLC, v. 52, n. 1, p. 179–195, mar. 2015. Available from Internet: <https://doi.org/10.1007/s00158-015-1229-9>. Cited 4 times in pages 7, 36, 37, and 38.

JENKINS, N.; MAUTE, K. An immersed boundary approach for shape and topology optimization of stationary fluid-structure interaction problems. **Structural and Multidisciplinary Optimization**, Springer Science and Business Media LLC, v. 54, n. 5, p. 1191–1208, maio 2016. Available from Internet: <https://doi.org/10.1007/s00158-016-1467-5>. Cited 2 times in pages 38 and 60.

JOG, C. Distributed-parameter optimization and topology design for non-linear thermoelasticity. **Computer Methods in Applied Mechanics and Engineering**, Elsevier BV, v. 132, n. 1-2, p. 117–134, maio 1996. Available from Internet: <https://doi.org/10.1016/0045-7825(95)00990-6>. Cited in page 34.

KEMMLER, R.; LIPKA, A.; RAMM, E. Large deformations and stability in topology optimization. **Structural and Multidisciplinary Optimization**, Springer Science and Business Media LLC, v. 30, n. 6, p. 459–476, jul. 2005. Available from Internet: <https://doi.org/10.1007/s00158-005-0534-0>. Cited in page 35.

KLARBRING, A.; STRöMBERG, N. Topology optimization of hyperelastic bodies including non-zero prescribed displacements. **Structural and Multidisciplinary Optimization**, Springer Science and Business Media LLC, v. 47, n. 1, p. 37–48, jun. 2012. Available from Internet: <https://doi.org/10.1007/s00158-012-0819-z>. Cited in page 35.

KONTOLEONTOS, E. A.; PAPOUTSIS-KIACHAGIAS, E. M.; ZYMARIS, A. S.; PAPADIMITRIOU, D. I.; GIANNAKOGLOU, K. C. Adjoint-based constrained topology optimization for viscous flows, including heat transfer. **Engineering Optimization**, Informa UK Limited, v. 45, n. 8, p. 941–961, ago. 2013. Available from Internet: <https://doi.org/10.1080/0305215x.2012.717074>. Cited in page 33.

KREISSL, S.; PINGEN, G.; EVGRAFOV, A.; MAUTE, K. Topology optimization of flexible micro-fluidic devices. **Structural and Multidisciplinary Optimization**, Springer Science and Business Media LLC, v. 42, n. 4, p. 495–516, jun. 2010. ISSN 1615-1488. Available from Internet: <http://dx.doi.org/10.1007/s00158-010-0526-6>. Cited in page 37.

KUBO, S.; KOGUCHI, A.; YAJI, K.; YAMADA, T.; IZUI, K.; NISHIWAKI, S. Level set-based topology optimization for two dimensional turbulent flow using an immersed boundary method. **Journal of Computational Physics**, Elsevier BV, v. 446, p. 110630, dez. 2021. Available from Internet: <https://doi.org/10.1016/j.jcp.2021.110630>. Cited in page 33.

KUMAR, P.; FROUWS, J. S.; LANGELAAR, M. Topology optimization of fluidic pressure-loaded structures and compliant mechanisms using the darcy method. **Structural and Multidisciplinary Optimization**, Springer Science and Business Media LLC, v. 61, n. 4, p. 1637–1655, jan. 2020. ISSN 1615-1488. Available from Internet: <http://dx.doi.org/10.1007/s00158-019-02442-0>. Cited 2 times in pages 57 and 125.

LAHUERTA, R. D.; SIMÕES, E. T.; CAMPELLO, E. M. B.; PIMENTA, P. M.; SILVA, E. C. N. Towards the stabilization of the low density elements in topology optimization with large deformation. **Computational Mechanics**, Springer Science and Business Media LLC, v. 52, n. 4, p. 779–797, mar. 2013. Available from Internet: <https://doi.org/10.1007/s00466-013-0843-x>. Cited 2 times in pages 35 and 58.

LAZAROV, B. S.; SIGMUND, O. Filters in topology optimization based on helmholtz-type differential equations. **International Journal for Numerical Methods in Engineering**, Wiley, v. 86, n. 6, p. 765–781, dez. 2010. Cited 2 times in pages 54 and 63.

LEE, E.; MARTINS, J. R. Structural topology optimization with design-dependent pressure loads. **Computer Methods in Applied Mechanics and Engineering**, Elsevier BV, v. 233–236, p. 40–48, ago. 2012. ISSN 0045-7825. Available from Internet: <http://dx.doi.org/10.1016/j.cma.2012.04.007>. Cited in page 57.

LI, W.; ZHANG, X. S. Arbitrary curvature programming of thermo-active liquid crystal elastomer via topology optimization. **Computer Methods in Applied Mechanics and Engineering**, Elsevier BV, v. 417, p. 116393, dez. 2023. ISSN 0045-7825. Available from Internet: <http://dx.doi.org/10.1016/j.cma.2023.116393>. Cited in page 134.

LIM, D. K.; SONG, M. S.; CHAE, H.; KIM, E. S. Topology optimization on vortex-type passive fluidic diode for advanced nuclear reactors. **Nuclear Engineering and Technology**, Elsevier BV, v. 51, n. 5, p. 1279–1288, ago. 2019. Available from Internet: <https://doi.org/10.1016/j.net.2019.03.018>. Cited in page 59.

LIN, S.; ZHAO, L.; GUEST, J. K.; WEIHS, T. P.; LIU, Z. Topology optimization of fixed-geometry fluid diodes. **Journal of Mechanical Design**, ASME International, v. 137, n. 8, ago. 2015. Available from Internet: <https://doi.org/10.1115/1.4030297>. Cited 2 times in pages 59 and 149.

LIU, S.; LI, Q.; CHEN, W.; TONG, L.; CHENG, G. An identification method for enclosed voids restriction in manufacturability design for additive manufacturing structures. **Frontiers of Mechanical Engineering**, Springer Science and Business Media LLC, v. 10, n. 2, p. 126–137, jun. 2015. Cited 4 times in pages 42, 68, 69, and 109.

LIU, Z.; DENG, Y.; LIN, S.; XUAN, M. Optimization of micro venturi diode in steady flow at low reynolds number. **Engineering Optimization**, Informa UK Limited, v. 44, n. 11, p. 1389–1404, mar. 2012. Available from Internet: <https://doi.org/10.1080/0305215x.2011.652100>. Cited in page 59.

LOGG, A.; WELLS, G. N. DOLFIN: Automated finite element computing. **ACM Transactions on Mathematical Software**, Association for Computing Machinery (ACM), v. 37, n. 2, p. 1–28, abr. 2010. Available from Internet: <https://doi.org/10.1145/1731022.1731030>. Cited in page 79.

LUNDGAARD, C.; ALEXANDERSEN, J.; ZHOU, M.; ANDREASEN, C. S.; SIGMUND, O. Revisiting density-based topology optimization for fluid-structure-interaction problems. **Structural and Multidisciplinary Optimization**, Springer Science and Business Media LLC, v. 58, n. 3, p. 969–995, abr. 2018. Available from Internet: <https://doi.org/10.1007/s00158-018-1940-4>. Cited in page 38.

LUO, Y.; LI, Q.; LIU, S. Topology optimization of shell–infill structures using an erosion-based interface identification method. **Computer Methods in Applied Mechanics and Engineering**, Elsevier BV, v. 355, p. 94–112, out. 2019. Cited in page 65.

MAFFEI, F. S.; Sá, L. F. Nogueira de; MOSCATELLI, E.; PICELLI, R.; MENEGHINI, J. R.; SILVA, E. C. N. Integer programming topology optimization for subsonic compressible flows with geometry trimming. **International Journal of Heat and Mass Transfer**, Elsevier BV, v. 201, p. 123614, fev. 2023. ISSN 0017-9310. Available from Internet: <http://dx.doi.org/10.1016/j.ijheatmasstransfer.2022.123614>. Cited in page 40.

MITUSCH, S.; FUNKE, S.; DOKKEN, J. dolfin-adjoint 2018.1: automated adjoints for FEniCS and firedrake. **Journal of Open Source Software**, The Open Journal, v. 4, n. 38, p. 1292, jun. 2019. Available from Internet: <https://doi.org/10.21105/joss.01292>. Cited 2 times in pages 79 and 80.

MOSCATELLI, E.; ALONSO, D. H.; SÁ, L. F. N. de; PICELLI, R.; SILVA, E. C. N. Topology optimisation for rotor-stator fluid flow devices. **Structural and Multidisciplinary Optimization**, Springer Science and Business Media LLC, v. 65, n. 5, abr. 2022. Available from Internet: <https://doi.org/10.1007/s00158-022-03233-w>. Cited 5 times in pages 40, 44, 60, 61, and 86.

MOSCATELLI, E.; ANDREASEN, C. S.; AAGE, N.; PICELLI, R.; SILVA, E. C. Topology optimization of labyrinth seals using interface identification techniques. **Computer Methods in Applied Mechanics and Engineering**, Elsevier BV, v. 420, p. 116716, fev. 2024. ISSN 0045-7825. Available from Internet: <https://doi.org/10.1016/j.cma.2023.116716>. Cited 7 times in pages 40, 60, 63, 86, 101, 104, and 135.

MOSCATELLI, E.; SÁ, L. F. N. de; RANJBARZADEH, S.; PICELLI, R.; GIORIA, R. dos S.; SILVA, E. C. N. Hybrid geometry trimming algorithm based on integer linear programming for fluid flow topology optimization. **Computers & Fluids**, Elsevier BV, v. 244, p. 105561, ago. 2022. Available from Internet: <https://doi.org/10.1016/j.compfluid.2022.105561>. Cited 4 times in pages 40, 59, 78, and 149.

MOSCATELLI, E.; Sá, L. F.; EMMENDOERFER, H.; SILVA, E. C. Pure-displacement formulation and bulk modulus propagation for topology optimization with pressure loads. **Computer Methods in Applied Mechanics and Engineering**, Elsevier BV, v. 411, p. 116058, jun. 2023. ISSN 0045-7825. Available from Internet: <http://dx.doi.org/10.1016/j.cma.2023.116058>. Cited 2 times in pages 40 and 57.

OTHMER, C. A continuous adjoint formulation for the computation of topological and surface sensitivities of ducted flows. **International Journal for Numerical Methods in Fluids**, Wiley, v. 58, n. 8, p. 861–877, nov. 2008. Available from Internet: <https://doi.org/10.1002/fld.1770>. Cited in page 32.

PAPOUTSIS-KIACHAGIAS, E. M.; GIANNAKOGLOU, K. C. Continuous adjoint methods for turbulent flows, applied to shape and topology optimization: Industrial applications. **Archives of Computational Methods in Engineering**, Springer Science

and Business Media LLC, v. 23, n. 2, p. 255–299, dez. 2014. Available from Internet: <https://doi.org/10.1007/s11831-014-9141-9>. Cited in page 33.

PEDERSEN, C. B. W.; BUHL, T.; SIGMUND, O. Topology synthesis of large-displacement compliant mechanisms. **International Journal for Numerical Methods in Engineering**, Wiley, v. 50, n. 12, p. 2683–2705, 2001. Available from Internet: <https://doi.org/10.1002/nme.148>. Cited 3 times in pages 34, 70, and 134.

PICELLI, R.; MOSCATELLI, E.; YAMABE, P. V. M.; ALONSO, D. H.; RANJBARZADEH, S.; GIORIA, R. dos S.; MENEGHINI, J. R.; SILVA, E. C. N. Topology optimization of turbulent fluid flow via the TOBS method and a geometry trimming procedure. **Structural and Multidisciplinary Optimization**, Springer Science and Business Media LLC, v. 65, n. 1, jan. 2022. Available from Internet: <https://doi.org/10.1007/s00158-021-03118-4>. Cited 6 times in pages 33, 40, 59, 133, 151, and 163.

PICELLI, R.; SIVAPURAM, R.; XIE, Y. M. A 101-line MATLAB code for topology optimization using binary variables and integer programming. **Structural and Multidisciplinary Optimization**, Springer Science and Business Media LLC, v. 63, n. 2, p. 935–954, set. 2020. Available from Internet: <https://doi.org/10.1007/s00158-020-02719-9>. Cited in page 81.

PICELLI, R.; VICENTE, W.; PAVANELLO, R. Bi-directional evolutionary structural optimization for design-dependent fluid pressure loading problems. **Engineering Optimization**, Informa UK Limited, v. 47, n. 10, p. 1324–1342, 2015. ISSN 1029-0273. Available from Internet: <http://dx.doi.org/10.1080/0305215X.2014.963069>. Cited in page 37.

PICELLI, R.; VICENTE, W.; PAVANELLO, R. Evolutionary topology optimization for structural compliance minimization considering design-dependent fsi loads. **Finite Elements in Analysis and Design**, Elsevier BV, v. 135, p. 44–55, nov. 2017. ISSN 0168-874X. Available from Internet: <http://dx.doi.org/10.1016/j.finel.2017.07.005>. Cited in page 37.

POPE, S. B. **Turbulent Flows**. 1. ed. [S.l.]: Cambridge University Press, 2000. ISBN 978-0-521-59886-6. Cited 3 times in pages 44, 45, and 46.

SÁ, L. F.; YAMABE, P. V.; SOUZA, B. C.; SILVA, E. C. Topology optimization of turbulent rotating flows using spalart–allmaras model. **Computer Methods in Applied Mechanics and Engineering**, Elsevier BV, v. 373, p. 113551, jan. 2021. Available from Internet: <https://doi.org/10.1016/j.cma.2020.113551>. Cited in page 33.

SÁ, L. F. N.; OKUBO, C. M.; SÁ, A. N.; SILVA, E. C. N. Continuous boundary condition propagation model for topology optimization. **Structural and Multidisciplinary Optimization**, Springer Science and Business Media LLC, v. 65, n. 1, dez. 2021. Available from Internet: <https://doi.org/10.1007/s00158-021-03148-y>. Cited 3 times in pages 28, 41, and 59.

SCHäFER, M.; TUREK, S.; DURST, F.; KRAUSE, E.; RANNACHER, R. Benchmark computations of laminar flow around a cylinder. In: **Notes on Numerical Fluid Mechanics (NNFM)**. Vieweg+Teubner Verlag, 1996. p. 547–566. Available from Internet: <https://doi.org/10.1007/978-3-322-89849-4_39>. Cited 4 times in pages 14, 151, 153, and 154.

SCHRAMM, V.; DENECKE, J.; KIM, S.; WITTIG, S. Shape optimization of a labyrinth seal applying the simulated annealing method. **International Journal of Rotating Machinery**, Hindawi Limited, v. 10, n. 5, p. 365–371, 2004. ISSN 1023-621X. Available from Internet: <http://dx.doi.org/10.1155/S1023621X04000375>. Cited in page 27.

SIGMUND, O. Morphology-based black and white filters for topology optimization. **Structural and Multidisciplinary Optimization**, Springer Science and Business Media LLC, v. 33, n. 4-5, p. 401–424, jan. 2007. Cited in page 63.

SIGMUND, O. On the usefulness of non-gradient approaches in topology optimization. **Structural and Multidisciplinary Optimization**, Springer Science and Business Media LLC, v. 43, n. 5, p. 589–596, mar. 2011. Available from Internet: <https://doi.org/10.1007/s00158-011-0638-7>. Cited in page 77.

SIGMUND, O.; CLAUSEN, P. Topology optimization using a mixed formulation: An alternative way to solve pressure load problems. **Computer Methods in Applied Mechanics and Engineering**, Elsevier BV, v. 196, n. 13–16, p. 1874–1889, mar. 2007. ISSN 0045-7825. Available from Internet: <http://dx.doi.org/10.1016/j.cma.2006.09.021>. Cited 2 times in pages 57 and 124.

SIGMUND, O.; MAUTE, K. Topology optimization approaches. **Structural and Multidisciplinary Optimization**, Springer Science and Business Media LLC, v. 48, n. 6, p. 1031–1055, ago. 2013. Available from Internet: <https://doi.org/10.1007/s00158-013-0978-6>. Cited in page 78.

SILVA, A. L. F. d.; SALAS, R. A.; SILVA, E. C. N.; REDDY, J. Topology optimization of fibers orientation in hyperelastic composite material. **Composite Structures**, Elsevier BV, v. 231, p. 111488, jan. 2020. ISSN 0263-8223. Available from Internet: <http://dx.doi.org/10.1016/j.compstruct.2019.111488>. Cited in page 36.

SILVA, G. A. da; BECK, A. T.; SIGMUND, O. Topology optimization of compliant mechanisms considering stress constraints, manufacturing uncertainty and geometric nonlinearity. **Computer Methods in Applied Mechanics and Engineering**, Elsevier BV, v. 365, p. 112972, jun. 2020. Available from Internet: <https://doi.org/10.1016/j.cma.2020.112972>. Cited in page 36.

SILVA, K. E. S.; SIVAPURAM, R.; RANJBARZADEH, S.; GIORIA, R. S.; SILVA, E. C. N.; PICELLI, R. Topology optimization of stationary fluid–structure interaction problems including large displacements via the tobs-gt method. **Structural and Multidisciplinary Optimization**, Springer Science and Business Media LLC, v. 65, n. 11, nov. 2022. ISSN 1615-1488. Available from Internet: <http://dx.doi.org/10.1007/s00158-022-03442-3>. Cited in page 38.

SIVAPURAM, R.; PICELLI, R. Topology optimization of binary structures using integer linear programming. **Finite Elements in Analysis and Design**, Elsevier BV, v. 139, p. 49–61, fev. 2018. Available from Internet: <https://doi.org/10.1016/j.finel.2017.10.006>. Cited 2 times in pages 32 and 53.

SNECK, H. J. Labyrinth seal literature survey. **Journal of Lubrication Technology**, ASME International, v. 96, n. 4, p. 579–581, out. 1974. Available from Internet: <https://doi.org/10.1115/1.3452498>. Cited 4 times in pages 26, 28, 94, and 97.

SOUZA, B. C.; YAMABE, P. V. M.; SÁ, L. F. N.; RANJBARZADEH, S.; PICELLI, R.; SILVA, E. C. N. Topology optimization of fluid flow by using integer linear programming. **Structural and Multidisciplinary Optimization**, Springer Science and Business Media LLC, v. 64, n. 3, p. 1221–1240, maio 2021. Available from Internet: <https://doi.org/10.1007/s00158-021-02910-6>. Cited 6 times in pages 32, 40, 53, 55, 86, and 134.

SOUZA, B. C. de. **Topology optimization of fluid diodes based on integer linear programming.** Tese (Doutorado) — University of Sao Paulo, 2020. Available from Internet: <https://doi.org/10.11606/t.3.2021.tde-18052021-134145>. Cited 5 times in pages 28, 30, 40, 59, and 66.

SPALART, P.; ALLMARAS, S. A one-equation turbulence model for aerodynamic flows. In: **30th Aerospace Sciences Meeting and Exhibit**. American Institute of Aeronautics and Astronautics, 1992. Available from Internet: <https://doi.org/10.2514/6.1992-439>. Cited in page 46.

STEVEN, G. P.; LI, Q.; XIE, Y. M. Evolutionary topology and shape design for general physical field problems. **Computational Mechanics**, Springer Science and Business Media LLC, v. 26, n. 2, p. 129–139, ago. 2000. Available from Internet: <https://doi.org/10.1007/s004660000160>. Cited in page 32.

STOCKER, H. L. Advanced labyrinth seal design performance for high pressure ratio gas turbines. In: **ASME 1975 Winter Annual Meeting: GT Papers**. American Society of Mechanical Engineers, 1975. (WA1975-GTPapers). Available from Internet: <http://dx.doi.org/10.1115/75-wa/gt-22>. Cited in page 27.

TAYLOR, C.; HOOD, P. A numerical solution of the navier-stokes equations using the finite element technique. **Computers & Fluids**, Elsevier BV, v. 1, n. 1, p. 73–100, jan. 1973. ISSN 0045-7930. Available from Internet: <http://dx.doi.org/10.1016/0045-7930(73)90027-3>. Cited in page 73.

TYACKE, J.; DAI, Y.; WATSON, R.; TUCKER, P. Design optimisation of labyrinth seals using les. **Mathematical Modelling of Natural Phenomena**, EDP Sciences, v. 16, p. 2, 2021. ISSN 1760-6101. Available from Internet: <http://dx.doi.org/10.1051/mmnp/2020056>. Cited in page 28.

WANG, F.; LAZAROV, B. S.; SIGMUND, O. On projection methods, convergence and robust formulations in topology optimization. **Structural and Multidisciplinary Optimization**, Springer Science and Business Media LLC, v. 43, n. 6, p. 767–784, dez. 2010. Available from Internet: <https://doi.org/10.1007/s00158-010-0602-y>. Cited 3 times in pages 55, 63, and 80.

WANG, F.; LAZAROV, B. S.; SIGMUND, O.; JENSEN, J. S. Interpolation scheme for fictitious domain techniques and topology optimization of finite strain elastic problems. **Computer Methods in Applied Mechanics and Engineering**, Elsevier BV, v. 276, p. 453–472, jul. 2014. Available from Internet: <https://doi.org/10.1016/j.cma.2014.03.021>. Cited 4 times in pages 35, 57, 58, and 125.

WANG, M. Y.; WANG, X.; GUO, D. A level set method for structural topology optimization. **Computer Methods in Applied Mechanics and Engineering**, Elsevier BV, v. 192, n. 1-2, p. 227–246, jan. 2003. Available from Internet: <https://doi.org/10.1016/s0045-7825(02)00559-5>. Cited in page 31.

WEIN, L.; KLUGE, T.; SEUME, J. R.; HAIN, R.; FUCHS, T.; KäHLER, C.; SCHMIERER, R.; HERBST, F. Validation of RANS turbulence models for labyrinth seal flows by means of particle image velocimetry. In: **Volume 10A: Structures and Dynamics**. American Society of Mechanical Engineers, 2020. Available from Internet: <https://doi.org/10.1115/gt2020-14885>. Cited 2 times in pages 28 and 135.

WHALEN, J. K.; ALLEN, J.; CARDELL, J. D.; DUGAS, J. R. Polymer seal use in centrifugal compressors – two users' experiences over 15 years. **Proceedings of the Second Middle East Turbomachinery Symposium**, Turbomachinery Laboratory, Texas A&M University, mar. 2013. Available from Internet: <https://turbolab.tamu.edu/wp-content/uploads/2018/08/METS2Lecture6.pdf>. Cited in page 28.

WHITE, F. M. **Fluid Mechanics**. [S.l.]: McGraw-Hill, 2011. Cited in page 59.

XIE, Y.; STEVEN, G. A simple evolutionary procedure for structural optimization. **Computers & Structures**, Elsevier BV, v. 49, n. 5, p. 885–896, dez. 1993. Available from Internet: <https://doi.org/10.1016/0045-7949(93)90035-c>. Cited in page 32.

YOON, G. H. Topology optimization for stationary fluid-structure interaction problems using a new monolithic formulation. **International Journal for Numerical Methods in Engineering**, Wiley, v. 82, n. 5, p. 591–616, abr. 2010. Available from Internet: <https://doi.org/10.1002/nme.2777>. Cited 6 times in pages 37, 38, 51, 52, 66, and 134.

YOON, G. H. Stress-based topology optimization method for steady-state fluid–structure interaction problems. **Computer Methods in Applied Mechanics and Engineering**, Elsevier BV, v. 278, p. 499–523, ago. 2014. Available from Internet: <https://doi.org/10.1016/j.cma.2014.05.021>. Cited in page 37.

YOON, G. H. Topology optimization for turbulent flow with spalart–allmaras model. **Computer Methods in Applied Mechanics and Engineering**, Elsevier BV, v. 303, p. 288–311, maio 2016. Available from Internet: <https://doi.org/10.1016/j.cma.2016.01.014>. Cited 4 times in pages 33, 46, 47, and 151.

YOON, G. H. Topology optimization method with finite elements based on the k-ϵ turbulence model. **Computer Methods in Applied Mechanics and Engineering**, Elsevier BV, v. 361, p. 112784, abr. 2020. Available from Internet: <https://doi.org/10.1016/j.cma.2019.112784>. Cited in page 33.

YOON, G. H. A new monolithic design approach for topology optimization for transient fluid–structure interaction system. **Computer Methods in Applied Mechanics and Engineering**, Elsevier BV, v. 403, p. 115729, jan. 2023. ISSN 0045-7825. Available from Internet: <http://dx.doi.org/10.1016/j.cma.2022.115729>. Cited in page 38.

YOON, G. H.; KIM, Y. Y. Element connectivity parameterization for topology optimization of geometrically nonlinear structures. **International Journal of Solids and Structures**, Elsevier BV, v. 42, n. 7, p. 1983–2009, abr. 2005. Available from Internet: <https://doi.org/10.1016/j.ijsolstr.2004.09.005>. Cited in page 35.

YOON, S.-J.; LEE, J.-H.; LEE, S.-M.; TAK, N.-i.; KIM, M.-H.; KIM, K.-Y.; PARK, G.-C. Numerical and experimental investigation on labyrinth seal mechanism for bypass flow reduction in prismatic vhtr core. **Nuclear Engineering and Design**,

Elsevier BV, v. 262, p. 525–534, set. 2013. ISSN 0029-5493. Available from Internet: <http://dx.doi.org/10.1016/j.nucengdes.2013.05.028>. Cited in page 27.

ZHANG, X. S.; CHI, H.; ZHAO, Z. Topology optimization of hyperelastic structures with anisotropic fiber reinforcement under large deformations. **Computer Methods in Applied Mechanics and Engineering**, Elsevier BV, v. 378, p. 113496, maio 2021. Available from Internet: <https://doi.org/10.1016/j.cma.2020.113496>. Cited in page 36.

ZHAO, Y.; WANG, C. Shape optimization of labyrinth seals to improve sealing performance. **Aerospace**, MDPI AG, v. 8, n. 4, p. 92, abr. 2021. ISSN 2226-4310. Available from Internet: <http://dx.doi.org/10.3390/aerospace8040092>. Cited in page 28.

ZHOU, M.; LAZAROV, B. S.; WANG, F.; SIGMUND, O. Minimum length scale in topology optimization by geometric constraints. **Computer Methods in Applied Mechanics and Engineering**, Elsevier BV, v. 293, p. 266–282, ago. 2015. ISSN 0045-7825. Available from Internet: <http://dx.doi.org/10.1016/j.cma.2015.05.003>. Cited in page 135.

ZYMARIS, A.; PAPADIMITRIOU, D.; GIANNAKOGLOU, K.; OTHMER, C. Continuous adjoint approach to the spalart–allmaras turbulence model for incompressible flows. **Computers & Fluids**, Elsevier BV, v. 38, n. 8, p. 1528–1538, set. 2009. Available from Internet: <https://doi.org/10.1016/j.compfluid.2008.12.006>. Cited in page 33.

APPENDIX A – DIODICITY OBJECTIVE FUNCTION

This section presents the main findings of Moscatelli et al. (2022) regarding the design of fluidic diodes with geometry trimming. This contribution is not part of the main text because the author decided to follow other approaches that are less computational expensive than running two fluid flow simulations to compute the diodicity at each optimization iteration. Fluidic diodes are devices that allow the fluid flow in one direction and prevent the flow in the opposite direction. Their performance may be measured by the diodicity function (LIN et al., 2015), which is given by the ratio of the total energy dissipation in the opposite (reverse) direction by the total energy dissipation in the forward direction as follows

$$\mathrm{Di} = \frac{\int_{0\Omega} \frac{\nu}{2} \left(\nabla \boldsymbol{v}_{\mathrm{rev}} + \nabla \boldsymbol{v}_{\mathrm{rev}}{}^{T}\right) : \left(\nabla \boldsymbol{v}_{\mathrm{rev}} + \nabla \boldsymbol{v}_{\mathrm{rev}}{}^{T}\right) \mathrm{d}\Omega + \int_{0\Omega} \kappa\left(m\right) \boldsymbol{v}_{\mathrm{rev}} \cdot \boldsymbol{v}_{\mathrm{rev}} \, \mathrm{d}\Omega}{\int_{0\Omega} \frac{\nu}{2} \left(\nabla \boldsymbol{v}_{\mathrm{fwd}} + \nabla \boldsymbol{v}_{\mathrm{fwd}}{}^{T}\right) : \left(\nabla \boldsymbol{v}_{\mathrm{fwd}} + \nabla \boldsymbol{v}_{\mathrm{fwd}}{}^{T}\right) \mathrm{d}\Omega + \int_{0\Omega} \kappa\left(m\right) \boldsymbol{v}_{\mathrm{fwd}} \cdot \boldsymbol{v}_{\mathrm{fwd}} \, \mathrm{d}\Omega} \tag{A.1}$$

where the subscripts "fwd" and "rev" indicate the forward and reverse direction, respectively. If the diodicity is high, the fluidic diode allows the fluid to flow in the forward direction while presenting an obstacle for the flow in the reverse direction. According to Lin et al. (2015), the topology optimization of fluidic diodes also requires penalizing the porous dissipation in the reverse direction. Then, the objective function is given by

$$F_{\mathrm{Di}} = \frac{1}{\mathrm{Di}} + \underbrace{\frac{w_{\mathrm{rev}}}{L_{\mathrm{C}}} \int_{0\Omega} \frac{\kappa\left(m\right) \boldsymbol{v}_{\mathrm{rev}} \cdot \boldsymbol{v}_{\mathrm{rev}}}{\kappa_{\max} {V_{\mathrm{C}}}^2} \, \mathrm{d}\Omega}_{\text{penalization}} \tag{A.2}$$

with w_{rev} indicating the weight of the penalization factor.

The analysis and design domains for the topology optimization of fluidic diodes is presented in Fig. A.1. The symmetry of the problem about the centerline of the diode permits considering only the upper part of the domain during analysis and optimization, reducing the overall computational cost. For the forward flow problem, the fluid enters at the left edge and leaves at the right edge. For the reverse flow problem, the inlet and outlet edges are switched.

Figure A.2 illustrates the effect of the penalization weight in the design of fluidic diodes. It is seen that low values of w_{rev} make the objective function oscillatory. However, the results for low values of w_{rev} also present higher diodicity values, indicating superior performance. When the value of w_{rev} is high, the optimizer does not place solid elements

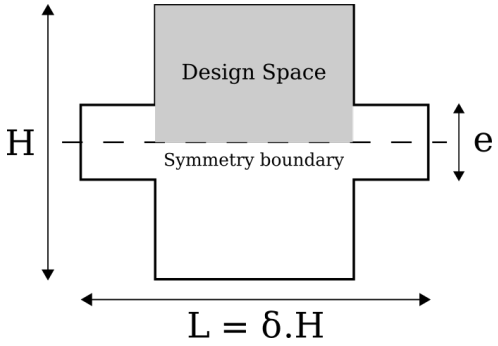

(a) Design domain

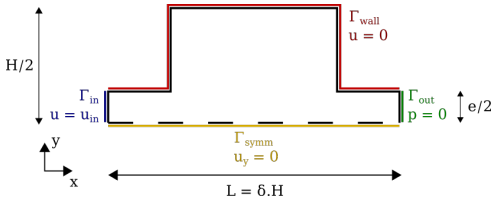

(b) Forward problem

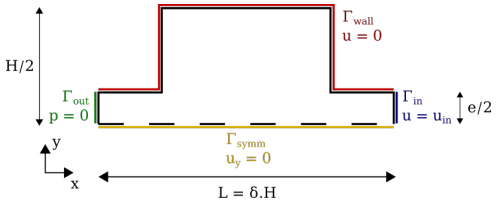

(c) Reverse problem

Figure A.1 – Description of the fluidic diode problem.

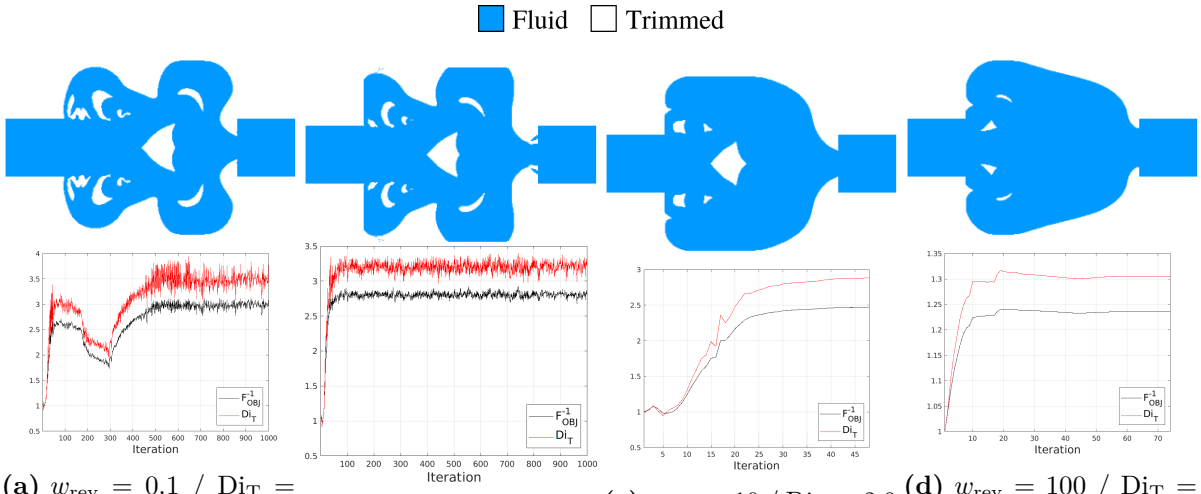

(a) $w_{\text{rev}} = 0.1$ / $\text{Di}_\text{T} = 3.4$ **(b)** $w_{\text{rev}} = 1$ / $\text{Di}_\text{T} = 3.2$ **(c)** $w_{\text{rev}} = 10$ / $\text{Di}_\text{T} = 2.9$ **(d)** $w_{\text{rev}} = 100$ / $\text{Di}_\text{T} = 1.3$

Figure A.2 – Penalization factor (w_{rev}) effect on obtained result illustrated for Re = 100. As the penalization factor is increased, results with lower diodicity are obtained. Therefore, it is important to use low w_{rev} values.

at the centerline of the fluidic diode, reducing the capacity of the device to deviate the flow. The calibration of w_{rev} is necessary due to the multi-objective nature of the diodicity functional. The multi-objective function nature complicates the convergence of the objective function and increases the computational cost, as two flow analysis are required. Therefore, alternative objective functions and topology optimization formulation have been explored in this work.

APPENDIX B – FENICS TOPOPT FOAM FORMULATION

This work attempted to use "FEniCS TopOpt FOAM" for turbulent flow topology optimization. However, as seen in Sections 4.1.5 and 4.1.6, the convergence history was oscillatory. This appendix presents an in-depth investigation concerning these oscillations. First, a discussion regarding the projection from FVM to FEM is presented. An alternative projection is proposed in an attempt to avoid numerical artifacts introduced by the projection, such as the numerical seepage in solid domain. Then, the calculation of some parameters is validated by solving the flow around a cylinder benchmark (SCHäFER et al., 1996). Finally, the highly-studied pipe bend problem (BORRVALL; PETERSSON, 2003; YOON, 2016; ALONSO; RODRIGUEZ; SILVA, 2021; PICELLI et al., 2022) is solved following different solution procedures for the forward problem. It is shown that the projection from FVM to FEM limits the choice of the objective function and introduces oscillations even for a properly chosen objective function. The alternative projection proposed in this section reduces seepage; however, it deviates the fluid flow from the physical solution. Therefore, the alternative projection does not work and it is not used in results section. It is described here for future reference.

B.1 Other Parameters

The viscous energy dissipation E_d and the porous dissipation P_o are commonly used for fluid flow topology optimization to compute the total energy dissipation. Therefore, evaluating their behavior when interfacing OpenFoam and FEniCS is important. These functionals are calculated as follows

$$E_\mathrm{d}\left(\nu,\, \boldsymbol{v}\right) = \int_{0_\Omega} \frac{\nu}{2} \left(\nabla \boldsymbol{v} + \nabla \boldsymbol{v}^T\right) : \left(\nabla \boldsymbol{v} + \nabla \boldsymbol{v}^T\right) \mathrm{d}\Omega \tag{B.1}$$

$$P_\mathrm{o}\left(m,\, \boldsymbol{v}\right) = \int_{0_\Omega} \kappa\left(m\right) \boldsymbol{v} \cdot \boldsymbol{v} \,\mathrm{d}\Omega \tag{B.2}$$

It is important to note that the porous dissipation P_o is also a measure of the fluid seepage in the solid domain. In general, high values of P_o indicate that the material model is not modeling the no-slip condition appropriately.

B.1.1 Projection from FVM to FEM

The $\mathcal{L}_2$-projection of a function $\boldsymbol{u}_0 \in \mathcal{V}_0 \subset [\mathcal{L}_2]^{n_d}$ to another function space $\mathcal{V} \subset [\mathcal{L}_2]^{n_d}$ is the function $\boldsymbol{u}$ that minimizes the quadratic difference ($[\mathcal{L}_2]^{n_d}$ norm) of the functions. The $\mathcal{L}_2$-projection may be stated as the following minimization problem

$$\min_{\boldsymbol{u}\in\mathcal{V}} \quad A(\boldsymbol{u}) \coloneqq \frac{1}{2}\|\boldsymbol{u}-\boldsymbol{u}_0\|^2_{\mathcal{L}_2} \tag{B.3}$$

As the functional A is convex, the solution of the problem B.3 is unique and can be found by solving the optimality condition

$$DA(\boldsymbol{u})[\boldsymbol{v}] = 0 \qquad \forall \boldsymbol{v} \in \mathcal{V} \tag{B.4}$$

Then, the solution $\boldsymbol{u}$ is found by calculating the Fréchet's derivative of A as follows

$$DA(\boldsymbol{u})[\boldsymbol{v}] = \int_\Omega (\boldsymbol{u}-\boldsymbol{u}_0)\cdot\boldsymbol{v}\,\mathrm{d}\Omega = 0 \qquad \forall \boldsymbol{v} \in \mathcal{V} \tag{B.5}$$

$$\int_\Omega \boldsymbol{u}\cdot\boldsymbol{v}\,\mathrm{d}\Omega = \int_\Omega \boldsymbol{u}_0\cdot\boldsymbol{v}\,\mathrm{d}\Omega \qquad \forall \boldsymbol{v} \in \mathcal{V} \tag{B.6}$$

In fluid flow topology optimization with density-based methods, it is important that the velocity in the solid phase is zero to guarantee that the simulated flow is an accurate representation of the physical flow. This condition is satisfied by using a sufficiently large value of $\kappa_{\max}$. However, an artificial velocity is introduced when projecting the cell-centered velocity calculated by the FVM to a higher-order function space required by FEM. This artificial velocity is illustrated in Fig. B.1, in which a cell-centered scalar function is projected to a first-order finite element function space.

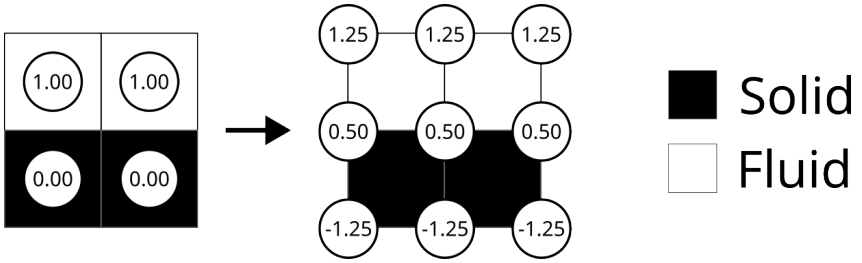

Figure B.1 – $\mathcal{L}_2$-projection of a scalar function from a cell-centered to a nodal function space.

This work proposes alleviating this phenomenon with a modified projection that also minimizes the porosity functional

$$\min_{\boldsymbol{u}\in\mathcal{V}} \quad A(\boldsymbol{u}) + P_\mathrm{o}(m,\,\boldsymbol{u}) \tag{B.7}$$

The Fréchet's derivative of P_o is given by

$$DP_\mathrm{o}(m,\, \boldsymbol{u})[\boldsymbol{v}] = \int_\Omega \kappa(m)\boldsymbol{u}\cdot\boldsymbol{v}\,\mathrm{d}\Omega \tag{B.8}$$

Then, the modified projection is given by the solution of the following linear problem

$$\int_\Omega (1+\kappa(m))\boldsymbol{u}\cdot\boldsymbol{v}\,\mathrm{d}\Omega = \int_\Omega \boldsymbol{u}_0\cdot\boldsymbol{v}\,\mathrm{d}\Omega \qquad \forall \boldsymbol{v}\in\mathcal{V} \tag{B.9}$$

Another way of interpreting the modified projection given by Eq. B.9 is as the solution of $\boldsymbol{u}=\boldsymbol{u}_0$ on Ω with a weak imposition of zero velocity on solid elements. Figure B.2 illustrates the application of the modified projection to the same case of Fig. B.1. It is possible to observe that the modified projection avoids seepage of the function value to solid elements as desired.

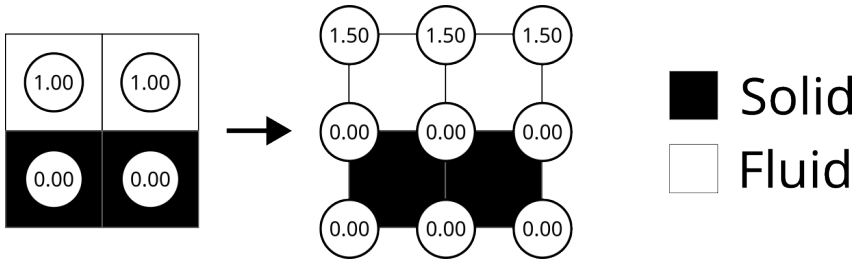

Figure B.2 – Modified projection of a scalar function from a cell-centered to a nodal function space.

B.2 Flow Around a Cylinder Benchmark

The first validation for the solvers used in this work was to run the flow around a cylinder benchmark (SCHäFER et al., 1996), which provides reference data (computed with high-order spectral methods) for the drag coefficient C_D, the lift coefficient C_L, and the pressure difference Δp over the cylinder, which is $p\,(0.15, 0.2) - p\,(0.25, 0.2)$. The expected values are presented in Table B.1 and the errors obtained for each formulation are presented in Table B.2. The drag and lift coefficients are calculated as follows

$$C_\mathrm{D} = \frac{1}{V_\mathrm{C} L_\mathrm{C}} \int_{\Gamma_o} \boldsymbol{\sigma}_\mathrm{f}\boldsymbol{n}\cdot\boldsymbol{l}_\mathrm{D}\,\mathrm{d}\Gamma \tag{B.10}$$

$$C_\mathrm{L} = \frac{1}{V_\mathrm{C} L_\mathrm{C}} \int_{\Gamma_o} \boldsymbol{\sigma}_\mathrm{f}\boldsymbol{n}\cdot\boldsymbol{l}_\mathrm{L}\,\mathrm{d}\Gamma \tag{B.11}$$

where Γ_o is the cylinder surface, $\boldsymbol{l}_\mathrm{D}$ is the direction (-1, 0), and $\boldsymbol{l}_\mathrm{L}$ is the direction (0, -1). The characteristic length L_C is the cylinder diameter, and the characteristic velocity V_C is the mean velocity of the parabolic profile (2/3 of the maximum velocity).

According to Table B.2, the parameters obtained within FEniCS are closer to the

Table B.1 – Reference data for the flow around a cylinder benchmark (SCHäFER et al., 1996).

Parameter	Symbol	Expected value
Drag coefficient	C_D	5.57953523384
Lift coefficient	C_L	0.010618948146
Pressure difference	Δp	0.11752016697

reference data (Table B.1) than the parameters obtained by calculating the velocity and pressure in OpenFoam and projecting these fields to FEniCS. This indicates that the projection step may introduce high errors in the evaluation of the parameters.

Table B.2 – Validation of the fluid flow solvers developed for this work by solving the flow around a cylinder benchmark from (SCHäFER et al., 1996).

Case	Forward	Adjoint	ϵ_{C_D} (%)	ϵ_{C_L} (%)	$\epsilon_{\Delta p}$ (%)
1	FEniCS	CG P2/P1	0.81	12.45	1.01
2	FEniCS	MINI	0.86	50.75	15.20
3	FEniCS	DG P2/P1	0.78	12.23	0.94
4	OpenFoam	CG P2/P1	44.49	231.38	0.26
5	OpenFoam	MINI	32.15	1076.11	0.26
6	OpenFoam	DG P2/P1	26.91	855.90	8.28

It is also important to visualize the effect of the projection from OpenFoam to FEniCS in the velocity and pressure fields. According to Figs. B.3a and B.3c, the differences in the velocity fields are concentrated at the inlet. However, an inspection of the actual velocity difference field (Fig. B.3e) shows that there are discrepancies of the order of the maximum velocity close to the cylinder. For the pressure fields, the differences are even more visible when comparing the fields of Figs. B.3b and B.3d. The maximum pressure value close to the cylinder wall is higher when the OpenFoam variables are projected to FEniCS. Also, the pressure field past the cylinder presents some numerical artifacts.

The high errors observed in Table B.2 for the projection from OpenFoam to FEniCS, despite the visual similarity of the velocity and pressure fields in Fig. B.3, are due to the localized differences in the velocity and pressure fields around the cylinder walls (according to Figs. B.3e and B.3f). As the parameters from Table B.1 are calculated over the cylinder walls, these localized differences may impact C_D, C_L, and Δp more than parameters calculated over other regions of the domain. For example, the viscous energy dissipation E_d and the head loss J are parameters that may suffer less from the discrepancies in velocity and pressure, so they were calculated and the results are summarized in Table B.3. As there is no reference data for E_d and J in (SCHäFER et al., 1996), the "errors" are arbitrarily calculated with respect to the FEniCS CG P2/P1 formulation.

According to Table B.3, the parameters E_d and J, which are commonly used in topology optimization, suffer less from the errors introduced in the projection from OpenFoam to FEniCS. Therefore, it is still important to evaluate the behavior of the projection

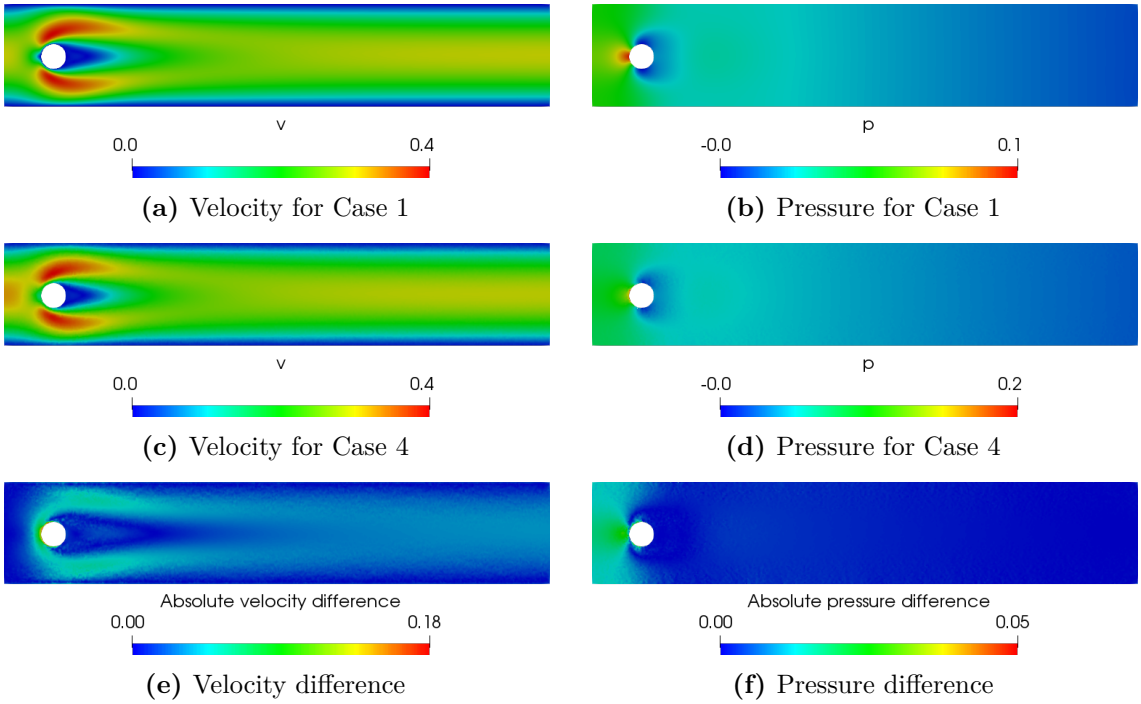

(a) Velocity for Case 1 **(b)** Pressure for Case 1

(c) Velocity for Case 4 **(d)** Pressure for Case 4

(e) Velocity difference **(f)** Pressure difference

Figure B.3 – Comparison of velocity and pressure fields obtained with FEniCS and OpenFoam projected to FEniCS.

Table B.3 – Comparison of viscous energy dissipation E_d and head loss J for the solution of the flow around a cylinder with different numerical approaches. The "errors" are arbitrarily calculated with respect to the FEniCS CG P2/P1 formulation.

Case	Forward	Adjoint	E_d $(\times 10^3)$	J $(\times 10^3)$	ϵ_{E_d} (%)	ϵ_J (%)
1	FEniCS	CG P2/P1	5.883	7.329	-	-
2	FEniCS	MINI	5.894	7.344	0.18	0.20
3	FEniCS	DG P2/P1	6.091	7.346	3.53	0.23
4	OpenFoam	CG P2/P1	6.154	7.496	4.61	2.27
5	OpenFoam	MINI	7.530	7.497	28.0	2.29
6	OpenFoam	DG P2/P1	0	7.496	100	2.27

from OpenFoam to FEniCS in topology optimization problems because in density-based topology optimization the solid walls are represented by a fictitious porous material, and also because the objective function is not necessarily a parameter calculated over solid walls.

B.3 Topology Optimization for Laminar Flow

The highly-studied pipe bend design is selected to benchmark the code developed in FEniCS and OpenFoam. Two centerline inlet velocities and two objective functions are tested for laminar flow, resulting in four testing scenarios. For each test, six cases combining different forward and adjoint solvers are presented. The first case is to use FEniCS for forward and adjoint analysis with the CG formulation with P2/P1 elements.

The second case uses FEniCS for forward and adjoint analysis and the DG formulation with P2/P1 elements. The other cases use the FVM implementation from OpenFoam for forward analysis and FEniCS for adjoint analysis with: CG P2/P1 elements for the third case, CG MINI elements for the fourth case, CG P2/P1 elements and the modified projection (Section B.1.1) for the fifth case, and DG P2/P1 elements for the sixth case. For all studies conducted in this section, a Darcy number of 10^{-9} is used to obtain almost zero seepage in the solid domain.

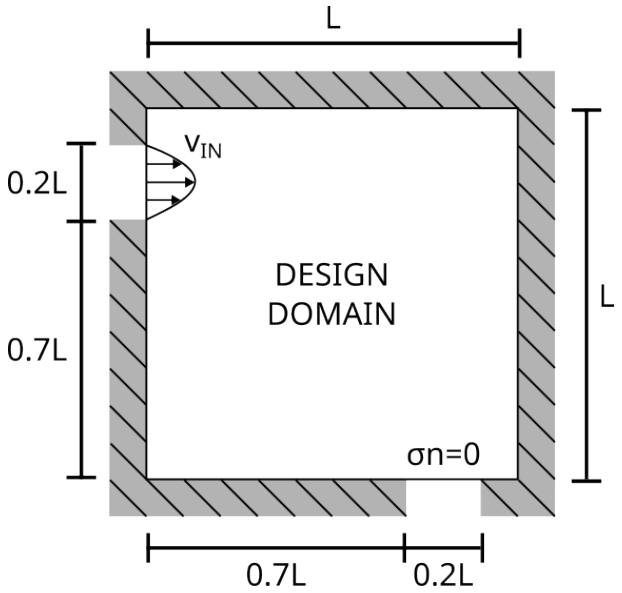

Figure B.4 – Pipe bend design domain.

The first test considers a parabolic inlet with a centerline velocity of $v_{\text{in}} = 0.45$ mm/s (Re = 1) and the power dissipation $E_{\text{t}} = E_{\text{d}} + P_{\text{o}}$ as the objective function. The results are presented in Table B.4 and Fig. B.5. The first and second rows of Table B.4 show that the results obtained with a pure FEniCS implementation with CG and DG have similar functional values. Also, the designs of Figs. B.5a and B.5b are almost identical. The third row of Table B.4 shows that the porosity functional obtained after projecting the flow variables from OpenFoam to FEniCS is inaccurate, becoming even higher than the viscous energy dissipation. This makes the P_{o} part of the objective function dictate the optimization and the result from Fig. B.5c is different from Figs. B.5a and B.5b. The fourth row also shows an inaccurate P_{o} value. Additionally, the optimization result of Fig B.5d presents a non-optimal narrow channel, showing that the inaccuracies compromised the optimization convergence.

The fifth case represents an attempt to eliminate artificial seepage introduced in the projection from OpenFoam to FEniCS by also minimizing the P_{o} functional during the projection (Eq. B.9). In the fifth row of Table B.4, it is seen that the viscous energy dissipation has the same order of magnitude as Cases 1 and 2; however, the porous energy dissipation is lower. Also, the topology optimization result from Fig. B.5e is different from Figs. B.5a and B.5b, indicating that the modified projection deteriorates the fluid flow

simulation result.

The sixth row of Table B.4 also shows an attempt to eliminate the seepage introduced in the projection by using a DG formulation for adjoint analysis. Although the P_o value becomes more accurate, the E_d cannot be calculated with Eq. B.1 because the finite volume velocities are first mapped to a DG0 function space and then projected to the DG2 function space. As DG0 $\subset$ DG2, all velocity degrees of freedom of each element become equal and there is no velocity gradient inside the elements. Therefore, the viscous energy dissipation is zero for the sixth case, which is completely inaccurate. It would be necessary to derive a DG0 equation for E_d.

Table B.4 – Pipe bend topology optimization for Re = 1 and total dissipation ($E_t = E_d + P_o$) as objective function. The symbol † indicates the use of the modified projection (Eq. B.2).

Case	Forward	Adjoint	Figure	E_t (mW)	E_d (mW)	P_o (mW)
1	FEniCS	CG P2/P1	B.5a	2.94×10^{-8}	2.94×10^{-8}	2.14×10^{-14}
2	FEniCS	DG P2/P1	B.5b	2.96×10^{-8}	2.96×10^{-8}	2.17×10^{-14}
3	OpenFoam	CG P2/P1	B.5c	1.94×10^{-4}	4.40×10^{-8}	1.94×10^{-4}
4	OpenFoam	CG MINI	B.5d	1.18×10^{-1}	2.28×10^{-5}	1.18×10^{-1}
5	OpenFoam	CG P2/P1†	B.5e	3.36×10^{-8}	3.36×10^{-8}	1.99×10^{-18}
6	OpenFoam	DG P1/P1	B.5f	1.24×10^{-14}	6.66×10^{-36}	1.24×10^{-14}

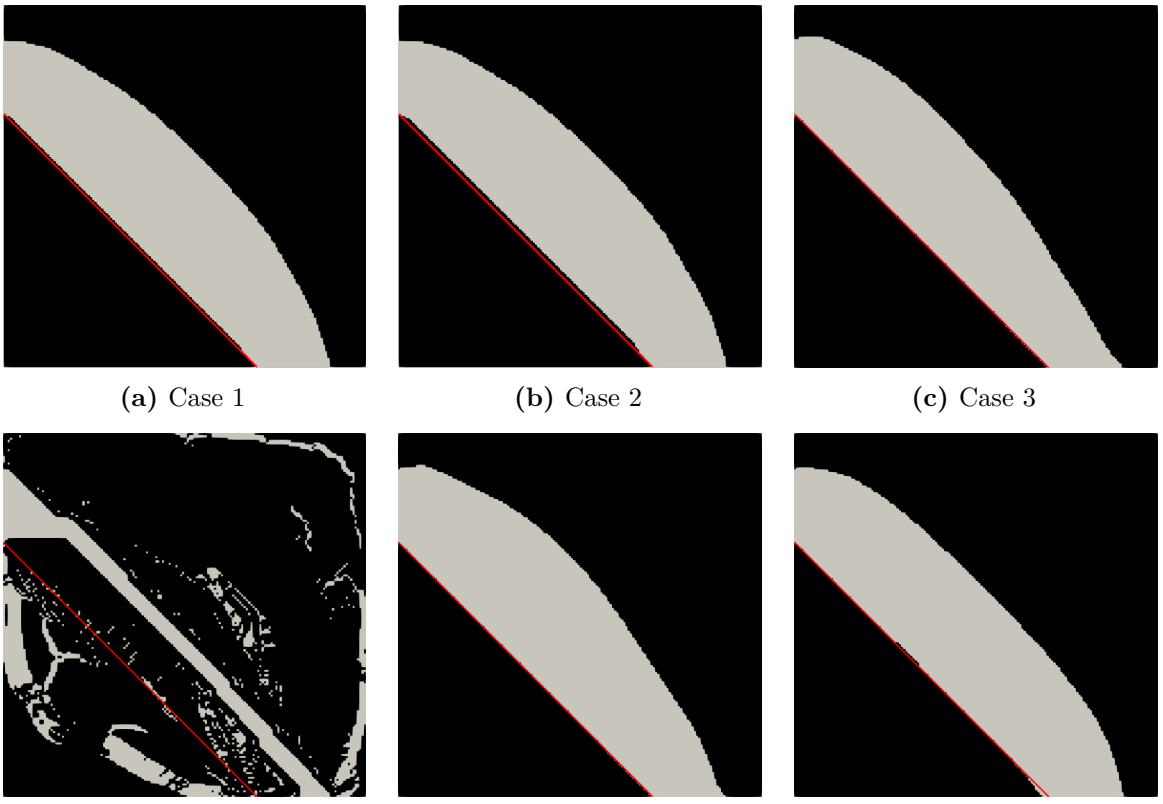

(a) Case 1 **(b)** Case 2 **(c)** Case 3

(d) Case 4 **(e)** Case 5 **(f)** Case 6

Figure B.5 – Pipe bend topology optimization for Re = 1 and total dissipation ($E_t = E_d + P_o$) as objective function.

The same analysis is repeated for an inlet centerline velocity of $v_{in} = 89.3$ mm/s (Re

= 200). The idea is to check if the same behavior is observed for higher velocities. The results of this analysis are presented in Table B.5 and Fig. B.6. Again, the results of Cases 1 and 2 match, the fourth case presents bad convergence, and the sixth case has zero viscous energy dissipation. The novelty here is the bad convergence of Case 3. For higher velocities, the artificial seepage is even larger and the optimization produces a bad design.

Table B.5 – Pipe bend topology optimization for Re = 200 and total dissipation ($E_t = E_d + P_o$) as objective function. The symbol † indicates the use of the modified projection (Eq. B.2).

Case	Forward	Adjoint	Figure	E_t (mW)	E_d (mW)	P_o (mW)
1	FEniCS	CG P2/P1	B.6a	1.71×10^{-3}	1.71×10^{-3}	6.95×10^{-10}
2	FEniCS	DG P2/P1	B.6b	1.70×10^{-3}	1.70×10^{-3}	6.94×10^{-10}
3	OpenFoam	CG P2/P1	B.6c	$9.89 \times 10^{+1}$	9.31×10^{-3}	$9.89 \times 10^{+1}$
4	OpenFoam	CG MINI	B.6d	$6.66 \times 10^{+1}$	1.21×10^{-2}	$6.66 \times 10^{+1}$
5	OpenFoam	CG P2/P1†	B.6e	1.81×10^{-3}	1.81×10^{-3}	9.47×10^{-14}
6	OpenFoam	DG P2/P1	B.6f	4.78×10^{-10}	6.88×10^{-29}	4.78×10^{-10}

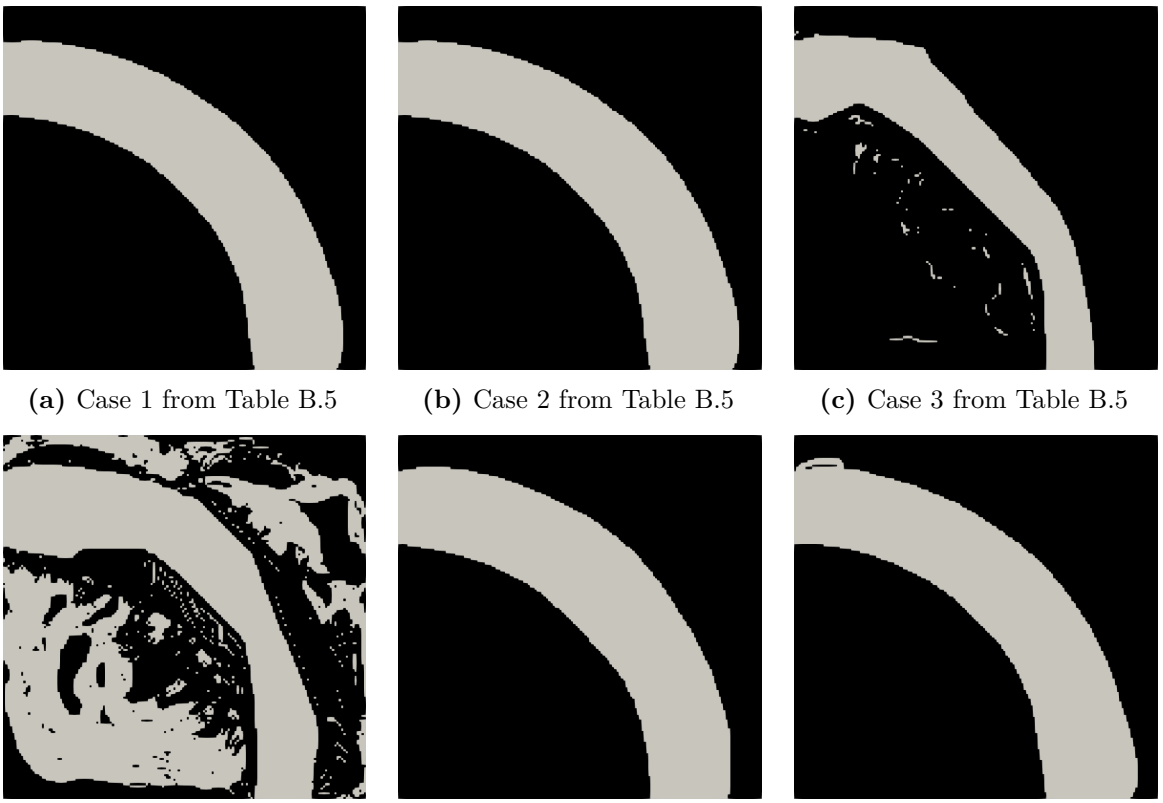

(a) Case 1 from Table B.5 **(b)** Case 2 from Table B.5 **(c)** Case 3 from Table B.5

(d) Case 4 from Table B.5 **(e)** Case 5 from Table B.5 **(f)** Case 6 from Table B.5

Figure B.6 – Pipe bend topology optimization for Re = 200 and total dissipation ($E_t = E_d + P_o$) as objective function.

The convergence problems observed in previous tests are related to the inaccuracy of velocity and pressure fields inside the design domain. Therefore, it is interesting to test the behavior of other objective functions that are defined over the boundaries. One candidate that is directly related to the total energy dissipation is the head loss J. The pipe bend problem is solved again for $v_{in} = 0.45$ mm/s (Re = 1) and the results are presented in

Table B.6 and Fig. B.7. Although the values of E_d and P_o differ significantly for certain cases, all J values have the same order of magnitude. Also, the optimization results of Fig. B.7 are sufficiently close to each other to argue that the new objective function avoids the artificial seepage problem for the Re = 1 situation.

Table B.6 – Pipe bend topology optimization for Re = 1 and head loss J objective function. The symbol † indicates the use of the modified projection (Eq. B.2).

Case	Forward	Adjoint	Figure	J (mm)	E_d (mW)	P_o (mW)
1	FEniCS	CG P2/P1	B.7a	2.55×10^{-4}	2.94×10^{-8}	2.07×10^{-14}
2	FEniCS	DG P2/P1	B.7b	2.54×10^{-4}	2.93×10^{-8}	2.07×10^{-14}
3	OpenFoam	CG P2/P1	B.7c	3.16×10^{-4}	3.32×10^{-8}	1.36×10^{-4}
4	OpenFoam	CG MINI	B.7d	3.20×10^{-4}	4.35×10^{-8}	1.10×10^{-4}
5	OpenFoam	CG P2/P1†	B.7e	3.16×10^{-4}	3.15×10^{-8}	1.68×10^{-18}
6	OpenFoam	DG P1/P1	B.7f	3.16×10^{-4}	1.18×10^{-33}	1.25×10^{-14}

(a) Case 1 from Table B.6 **(b)** Case 2 from Table B.6 **(c)** Case 3 from Table B.6

(d) Case 4 from Table B.6 **(e)** Case 5 from Table B.6 **(f)** Case 6 from Table B.6

Figure B.7 – Pipe bend topology optimization for Re = 1 and head loss J objective function.

The advantages of changing the objective function are also evident by repeating the scenario of v_{in} = 89.3 mm/s (Re = 200) for the minimization of the head loss (Table B.7 and Fig. B.8): the optimization results and J are close despite the divergences in E_d and P_o. Therefore, in this work, minimization/maximization of J is favored over the minimization/maximization of $E_d + P_o$ to obtain better behavior when using FEniCS TopOpt FOAM.

Table B.7 – Pipe bend topology optimization for Re = 200 and head loss J objective function. The symbol † indicates the use of the modified projection (Eq. B.2).

Case	Forward	Adjoint	Figure	J (mm)	E_d (mW)	P_o (mW)
1	FEniCS	CG P2/P1	B.8a	7.05×10^{-2}	1.66×10^{-3}	8.71×10^{-10}
2	FEniCS	DG P2/P1	B.8b	7.05×10^{-2}	1.66×10^{-3}	8.70×10^{-10}
3	OpenFoam	CG P2/P1	B.8c	8.20×10^{-2}	1.84×10^{-3}	$7.06 \times 10^{+0}$
4	OpenFoam	CG MINI	B.8d	8.39×10^{-2}	2.24×10^{-3}	$6.08 \times 10^{+0}$
5	OpenFoam	CG P2/P1†	B.8e	8.13×10^{-2}	1.69×10^{-3}	5.78×10^{-14}
6	OpenFoam	DG P2/P1	B.8f	7.82×10^{-2}	6.77×10^{-29}	4.05×10^{-10}

(a) Case 1 from Table B.7 **(b)** Case 2 from Table B.7 **(c)** Case 3 from Table B.7

(d) Case 4 from Table B.7 **(e)** Case 5 from Table B.7 **(f)** Case 6 from Table B.7

Figure B.8 – Pipe bend topology optimization for Re = 200 and head loss J as objective function.

Another important point to evaluate a topology optimization implementation is to check the objective function history. Figure B.9 presents the evolution of J for the results of Table B.7. The objective function curves for the pure FEniCS implementations (Cases 1 and 2) are smooth, while the curves for the FEniCS TopOpt Foam implementations oscillate (Cases 3 to 6). The most smooth behavior in FEniCS TopOpt Foam is obtained with the DG formulation. However, this formulation cannot be used directly with RANS equations in the context of FEniCS TopOpt Foam because all turbulence models depend on some sort of magnitude of the velocity gradient (for example, the magnitude of the deformation gradient tensor or magnitude of the spin tensor), which becomes zero for DG after projecting from OpenFoam to FEniCS. It would be necessary to devise a DG0 formulation accounting for the gradients between the elements. Therefore, in this work,

the CG P2/P1 formulation will be used for turbulent flow topology optimization with FEniCS TopOpt Foam.

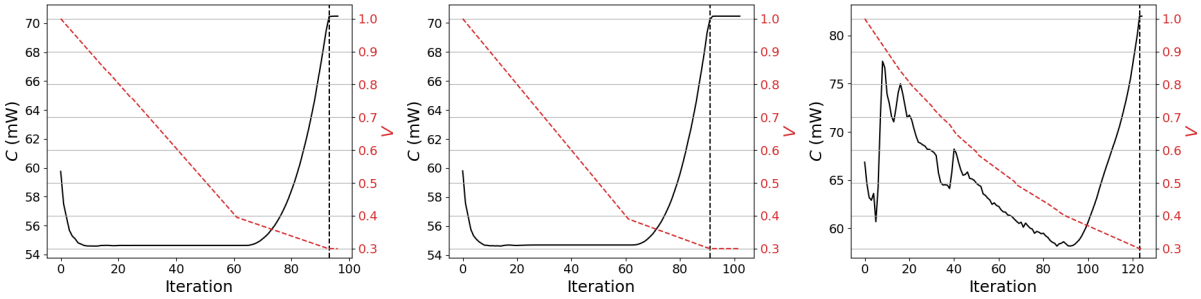

(a) Case 1 from Table B.7 **(b)** Case 2 from Table B.7 **(c)** Case 3 from Table B.7

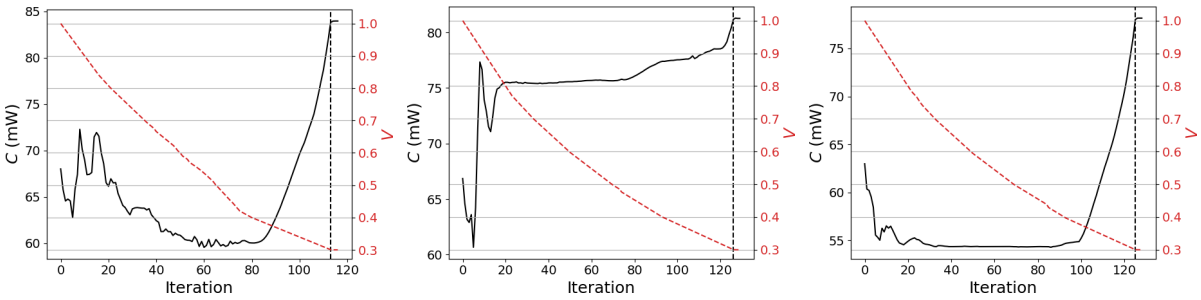

(d) Case 4 from Table B.7 **(e)** Case 5 from Table B.7 **(f)** Case 6 from Table B.7

Figure B.9 – Convergence history for the pipe bend topology optimization for Re = 200 and head loss J objective function.

The summary of the conclusions regarding the selection of the formulation to use with FEniCS TopOpt FOAM is:

- The head loss J and total energy dissipation $E_\mathrm{d}+P_\mathrm{o}$ are equivalent objective functions according to the comparison of Figs. B.5a and B.7a or Figs. B.6a and B.8a, for example;
- The head loss is a better choice of objective function than the total power dissipation when combining OpenFOAM and FEniCS/dolfin-adjoint according to Tables B.4, B.5, B.6, and B.7;
- The modified projection eliminates the artificial seepage introduced by the projection from OpenFoam variables to FEniCS variables. However, the modified projection reduces the accuracy of P_o (according to Tables B.5, B.6, B.7, and B.8);
- The use of Discontinuous Galerkin formulations also eliminates the artificial seepage introduced by the projection from OpenFoam variables to FEniCS variables. However, the projected fields have zero gradient inside the element (according to Tables B.5, B.6, B.7, and B.8), so it is not possible to calculate E_d without devising a new equation for E_d based on the gradient between elements. Also, the velocity gradient is necessary for RANS turbulence closure models, so new equations would also be necessary for the turbulence models;

- The CG P2/P1 formulation with J objective function is the best candidate for turbulent flow topology optimization using the FEniCS TopOpt FOAM approach.

B.4 Topology Optimization for Turbulent Flow

The pipe bend problem is also solved for an inlet Reynolds number of 1000 and $\tilde{\nu}_{\text{in}} = 10^{-4}$ by using the RANS equations and the Spalart-Allmaras turbulence model. For these boundary conditions, the flow inside the pipe bend is turbulent, as observed in Fig. B.10, where it is possible to see recirculation zones with high turbulent kinematic viscosity compared to the molecular kinematic viscosity of water $\nu = 8.9 \times 10^{-6}$ m^2/s. The optimization is run with $\beta_{\text{fl}} = 0.5\%$ and $\epsilon_V = 0.5\%$ to assert that the linerization errors are small and are not responsible for oscillations. Table B.8 summarizes some results obtained by varying the Darcy number and the coefficient $\lambda_{\tilde{\nu}}$.

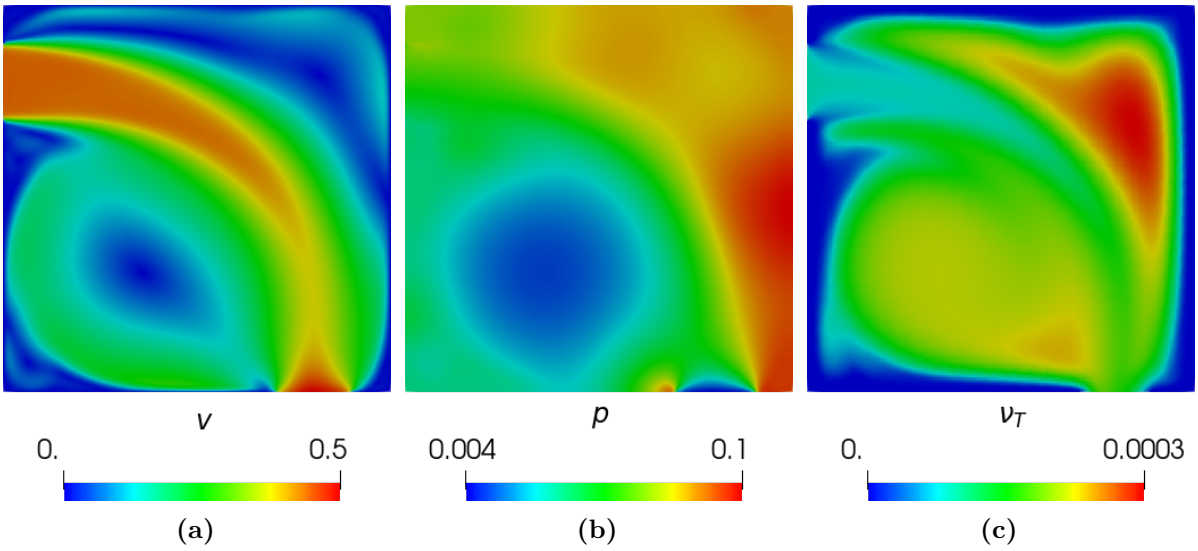

Figure B.10 – Pipe bend velocity, pressure, and turbulent kinematic viscosity for Re = 1000.

Table B.8 – Pipe bend topology optimization for Re = 1000 and head loss J objective function.

Case	Da	$\lambda_{\tilde{\nu}}$	Fig.	J (mm)	E_{d} (mW)	P_{o} (mW)	Iter.	Δt (h)
1	10^{-3}	1	B.11a	$3.74 \times 10^{+0}$	4.05×10^{-1}	2.71×10^{-1}	400	96
2	10^{-4}	1	B.11b	$4.03 \times 10^{+0}$	6.26×10^{-1}	1.62×10^{-1}	310	75
3	10^{-5}	1	B.11c	$7.73 \times 10^{+1}$	$1.18 \times 10^{+1}$	$1.37 \times 10^{+1}$	395	85
4	10^{-5}	0.1	B.12a	$5.02 \times 10^{+0}$	7.61×10^{-1}	5.13×10^{-1}	400	98
5	10^{-5}	0.01	B.12b	$4.54 \times 10^{+0}$	6.94×10^{-1}	4.06×10^{-1}	400	98

From Fig. B.11, it is possible to see that the optimization is sensitive to the inverse permeability parameter and completely wrong results, such as the multiple narrow channels of Fig. B.11c, may be obtained by an improper selection of the Darcy number. The artificial seepage introduced by the projection from OpenFoam to FEniCS is more critical in turbulent regimes due to the higher velocities. Also, the artificial dispersion of fluid

parameters to the solid phase happens for the $\tilde{\nu}$ variable, introducing additional deviations from the physical behavior.

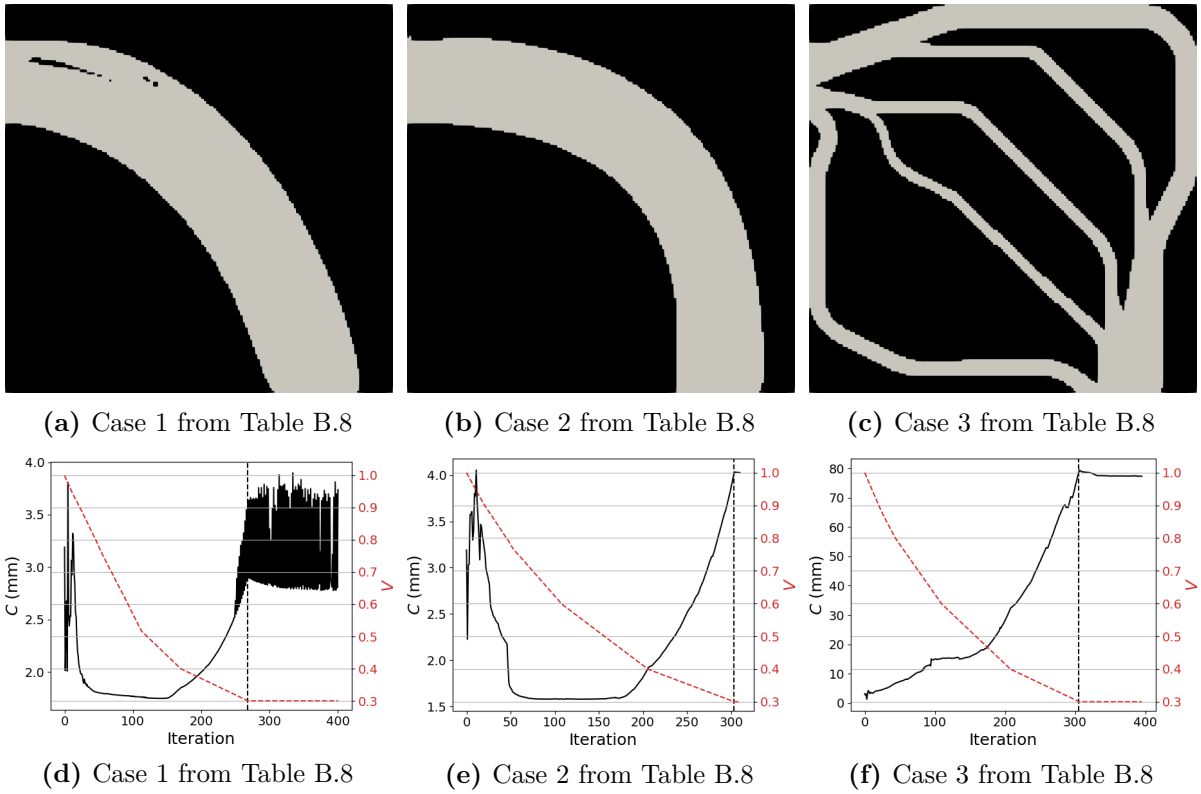

(a) Case 1 from Table B.8 **(b)** Case 2 from Table B.8 **(c)** Case 3 from Table B.8

(d) Case 1 from Table B.8 **(e)** Case 2 from Table B.8 **(f)** Case 3 from Table B.8

Figure B.11 – Pipe bend topology optimization for Re = 1000 and head loss J objective function.

One attempt to avoid the convergence problems observed in Fig. B.11c is to select different inverse permeability values for the $\tilde{\nu}$ transport equation by adjusting the parameter $\lambda_{\tilde{\nu}}$. This attempt is illustrated in Cases 4 and 5 of Table B.8 and Fig. B.12, which shows that the reduction of $\lambda_{\tilde{\nu}}$ eliminates the problem of multiple channels observed in Fig. B.11c. However, the issue of solid islands being added and removed close to the inlet is reintroduced.

It is also instructive to analyze the evolution of the design variable field along the optimization. Therefore, the design history of Case 2 is selected for analysis (as this is the case with better convergence), and evenly spaced iterations of Case 2 are presented in Fig. B.13. Initially, the optimizer places solid elements to suppress the turbulent dissipation at the upper right and lower left regions. Then, it places more solid until the volume constraint is reached. This convergence history is not in accordance with the literature (see Picelli et al. (2022), for example) because a solid island is expected in the lower left part of the design domain in the first iterations.

(a) Case 4 from Table B.8

(b) Case 5 from Table B.8

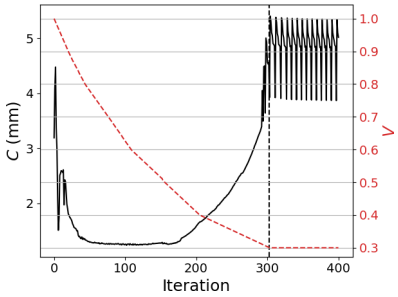

(c) Case 4 from Table B.8

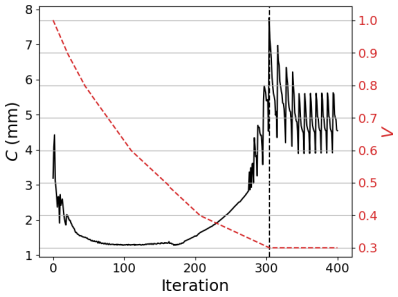

(d) Case 5 from Table B.8

Figure B.12 – Pipe bend topology optimization for Re = 1000, Da = 10^{-5} and head loss J objective function. Different values of $\lambda_{\tilde{\nu}}$ are used.

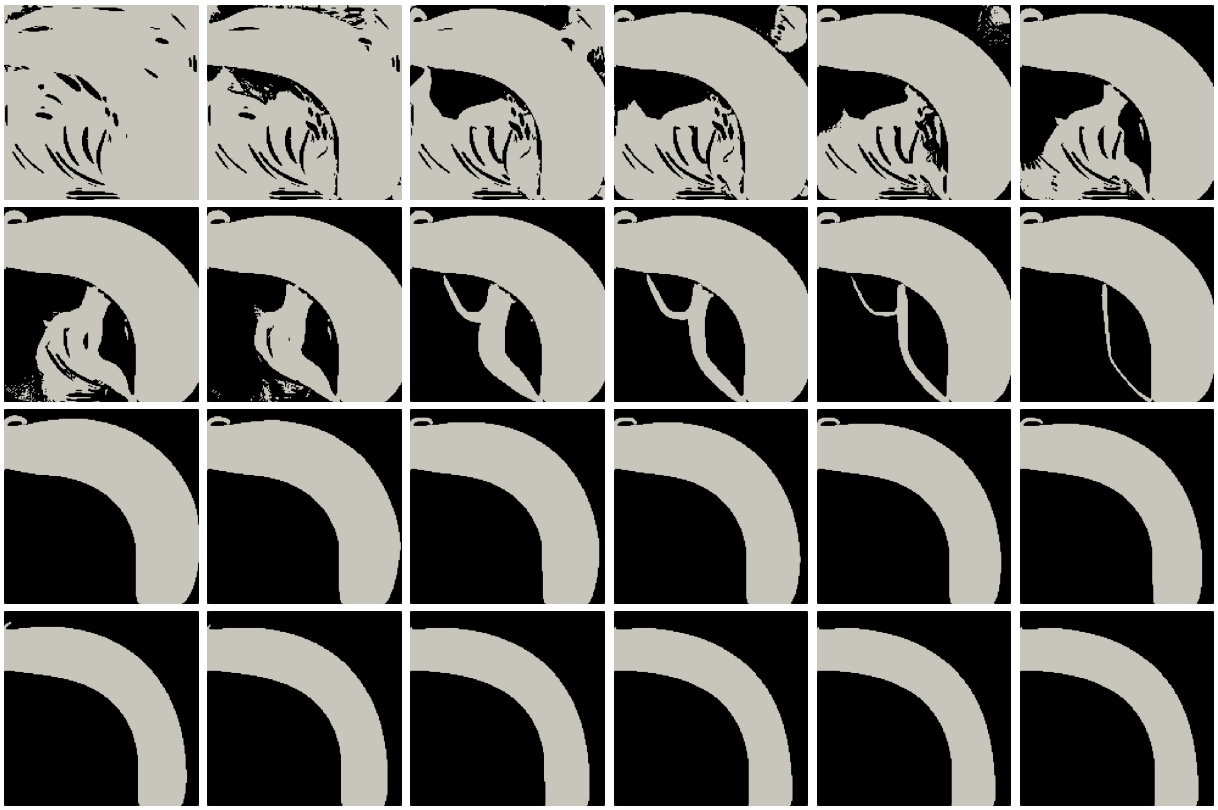

Figure B.13 – Pipe bend topology optimization history for Case 2 of Table B.8.

APPENDIX C – DISCONTINUOUS PDE DENSITY FILTER

This appendix presents a discretization of the PDE density filter (Eq. 2.46) with discontinuous Galerkin finite elements of order 0 (DG0). The objective of exploring this discretization was to test the PDE filter with element-wise degrees of freedom, which were found to be more robust for topology optimization with nonlinear solid mechanics. For simplicity, the deduction considers a version of Eq. 2.46 with Neumann boundary conditions only. Then, the strong form of the filtering problem is given by

$$\begin{aligned} -{R_\mathrm{f}}^2\nabla^2 m_\mathrm{f} + m_\mathrm{f} &= m \quad \text{on } \Omega^\mathrm{m} \\ \nabla m_\mathrm{f}\cdot\boldsymbol{n} &= 0 \quad \text{in } \Gamma^\mathrm{m} \end{aligned} \tag{C.1}$$

and the weak form for an element K is

$${R_\mathrm{f}}^2\int_K \nabla m_\mathrm{f}\cdot\nabla w_m \,\mathrm{d}\Omega - {R_\mathrm{f}}^2\int_{\partial K}(\nabla m_\mathrm{f}\cdot\boldsymbol{n})\, w_m \,\mathrm{d}\Gamma + \int_K m_\mathrm{f}\, w_m \,\mathrm{d}\Omega = \int_K m\, w_m \,\mathrm{d}\Omega \tag{C.2}$$

where w_m is a test function. By calling two elements that share an internal edge as K^+ and K^-, the sum of the contributions of all the elements of the mesh is given by

$$\begin{aligned} {R_\mathrm{f}}^2\int_{\Omega^\mathrm{m}} \underbrace{\nabla m_\mathrm{f}}_{\substack{0 \text{ in } \Omega^\mathrm{m} \\ \text{for DG0}}}\cdot\nabla w_m \,\mathrm{d}\Omega - {R_\mathrm{f}}^2\int_{\Omega^\mathrm{m}} \underbrace{(\nabla m_\mathrm{f}\cdot\boldsymbol{n})}_{0 \text{ on } \Gamma^\mathrm{m}} w_m \,\mathrm{d}\Gamma \\ - {R_\mathrm{f}}^2\int_{{}^0\Gamma_\mathrm{i}} \left((\nabla m_\mathrm{f}\cdot\boldsymbol{n})\, w_m\right)^+ + \left((\nabla m_\mathrm{f}\cdot\boldsymbol{n})\, w_m\right)^- \,\mathrm{d}\Gamma \\ + \int_{\Omega^\mathrm{m}} m_\mathrm{f}\, w_m \,\mathrm{d}\Omega = \int_{\Omega^\mathrm{m}} m\, w_m \,\mathrm{d}\Omega \end{aligned} \tag{C.3}$$

where ${}^0\Gamma_\mathrm{i}$ denotes the internal edges of the mesh and $(\cdot)^+$ and $(\cdot)^-$ denote the quantity for K^+ and K^-, respectively. The gradient is not defined on ${}^0\Gamma_\mathrm{i}$ due to the discontinuity of m_f on ${}^0\Gamma_\mathrm{i}$. Still, it is possible to define discontinuous Galerkin formulations by choosing consistent definitions for the derivative term. In this work, the gradient of the filtered field projected in the normal direction is approximated as follows

$$\begin{aligned} (\nabla m_\mathrm{f}\cdot\boldsymbol{n})^+ &= \frac{{m_\mathrm{f}}^- - {m_\mathrm{f}}^+}{h^+} \\ (\nabla m_\mathrm{f}\cdot\boldsymbol{n})^- &= \frac{{m_\mathrm{f}}^+ - {m_\mathrm{f}}^-}{h^-} \end{aligned} \tag{C.4}$$

where h is the element size. The substitution of the gradient definition in the weak equation

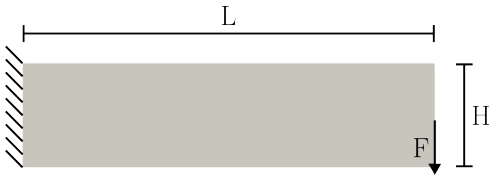

(a) Cantilever problem

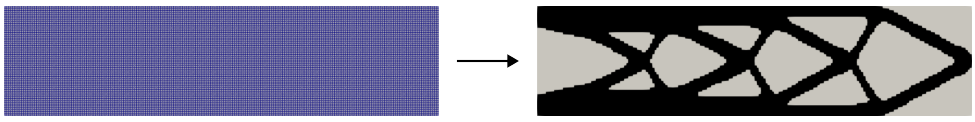

(b) Structured mesh result

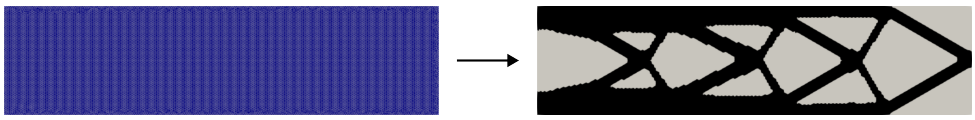

(c) Unstructured mesh result

Figure C.1 – Application of the discontinuous density filter (Eq. C.7) to the topology optimization of a cantilever beam with structured and unstructured meshes.

gives

$$\int_{\Omega^{\mathrm{m}}} m_{\mathrm{f}}\, w_m \,\mathrm{d}\Omega - {R_{\mathrm{f}}}^2 \int_{{}^{0}\Gamma_{\mathrm{i}}} \left(\frac{{m_{\mathrm{f}}}^{+} - {m_{\mathrm{f}}}^{-}}{h^{-}} \right) {w_m}^{-} + \left(\frac{{m_{\mathrm{f}}}^{-} - {m_{\mathrm{f}}}^{+}}{h^{+}} \right) {w_m}^{+} \,\mathrm{d}\Gamma = \int_{\Omega^{\mathrm{m}}} m\, w_m \,\mathrm{d}\Omega \tag{C.5}$$

The term inside the integral over the internal edges may be rearranged as follows

$$\begin{aligned} \left(\frac{{m_{\mathrm{f}}}^{+} - {m_{\mathrm{f}}}^{-}}{h^{-}} \right) {w_m}^{-} + \left(\frac{{m_{\mathrm{f}}}^{-} - {m_{\mathrm{f}}}^{+}}{h^{+}} \right) {w_m}^{+} &= {m_{\mathrm{f}}}^{+} \left(\frac{{w_m}^{-}}{h^{-}} - \frac{{w_m}^{+}}{h^{+}} \right) + {m_{\mathrm{f}}}^{-} \left(\frac{{w_m}^{+}}{h^{+}} - \frac{{w_m}^{-}}{h^{-}} \right) \\ &= \left({m_{\mathrm{f}}}^{-} - {m_{\mathrm{f}}}^{+} \right) \left(\frac{{w_m}^{+}}{h^{+}} - \frac{{w_m}^{-}}{h^{-}} \right) \end{aligned} \tag{C.6}$$

Then, the PDE-filter equation for DG0 finite elements is given by

$$\int_{\Omega^{\mathrm{m}}} m_{\mathrm{f}}\, w_m \,\mathrm{d}\Omega + {R_{\mathrm{f}}}^2 \int_{{}^{0}\Gamma_{\mathrm{i}}} \left({m_{\mathrm{f}}}^{+} - {m_{\mathrm{f}}}^{-} \right) \left(\frac{{w_m}^{+}}{h^{+}} - \frac{{w_m}^{-}}{h^{-}} \right) \mathrm{d}\Gamma = \int_{\Omega^{\mathrm{m}}} m\, w_m \,\mathrm{d}\Omega \tag{C.7}$$

Figure C.1 shows the ability of the discontinuous density filter given by Eq. C.7 to regularize the topology optimization of a cantilever beam with structured and unstructured meshes. The design domain measures $L = 1$ m by $H = 0.25$ m and is composed of nylon with Young's modulus of 3 GPa and Poisson's ratio of 0.4. The magnitude of the applied load is $F = 1$ kN and the analysis is linear. The physical filter radius is $r_{\min} = H/8$ (with $R_{\mathrm{f}} = r_{\min} / \left(2\sqrt{3}\right)$) and the element size is 0.005. The structured mesh is composed of quadrilateral elements, while the unstructured mesh is formed by triangular elements, also showing the generality of the discretization with respect to the element geometry.

The discontinuous version of the PDE density filter (Eq. C.7) is also less stable for

performing topology optimization in nonlinear solid mechanics than the discrete matrix filter given by Eq. 2.48. Therefore, the reduced stability is not associated with nodal design variables, as the PDE filter with cell-centered design variables is also less stable. After further investigation, the problem is associated with the support of the filtering operation. The discrete filter (Eq. C.7) may be written as a matrix multiplication as follows

$$m_{\mathrm{f}} = (\boldsymbol{H}_{\mathrm{m}} m) \oslash \boldsymbol{h}_{\mathrm{s}} \tag{C.8}$$

where the matrix $\boldsymbol{H}_{\mathrm{m}}$ is composed of the products $w_{\mathrm{e}}(\boldsymbol{x}_i) V_i$, and the vector $\boldsymbol{h}_{\mathrm{s}}$ is the sum of the rows of $\boldsymbol{H}_{\mathrm{m}}$. The symbol $\oslash$ denotes the point-wise division. As the matrix $\boldsymbol{H}_{\mathrm{m}}$ is sparse, each design variable only affects the elements inside the filter radius, giving compact support for the discrete filtering operation. The PDE filter (in continuous or discontinuous version) may be rewritten as follows

$$\boldsymbol{K}_{\mathrm{f}} \boldsymbol{m}_{\mathrm{f}} = \boldsymbol{L}_{\mathrm{f}} \boldsymbol{m} \Rightarrow \boldsymbol{m}_{\mathrm{f}} = \left(\boldsymbol{K}_{\mathrm{f}}^{-1} \boldsymbol{L}_{\mathrm{f}} \right) \boldsymbol{m} \tag{C.9}$$

Although the matrix $\boldsymbol{K}_{\mathrm{f}}$ is sparse, its inverse is not. Then, the product $\left(\boldsymbol{K}_{\mathrm{f}}^{-1} \boldsymbol{L}_{\mathrm{f}} \right)$ is dense, and the PDE filter has no compact support. This feature may be viewed through a numerical example that considers a square domain of size 3, a mesh of 3x3 elements, and a physical filter radius of 1.2, as shown in Fig. C.2. The matrix $\boldsymbol{K}_{\mathrm{f}}$ is presented in Eq. C.10, and its inverse in Eq. C.11. The matrix $\boldsymbol{L}_{\mathrm{f}}$ is the identity matrix for DG0 elements. Therefore, the PDE filter operation has not compact support because $\boldsymbol{K}_{\mathrm{f}}^{-1}$ is dense. On the other hand, the discrete filter has compact support because $\boldsymbol{H}_{\mathrm{m}}$ is sparse (Eq. C.12). Therefore, the discrete filter introduces fewer small values in the filtered field than the PDE filter.

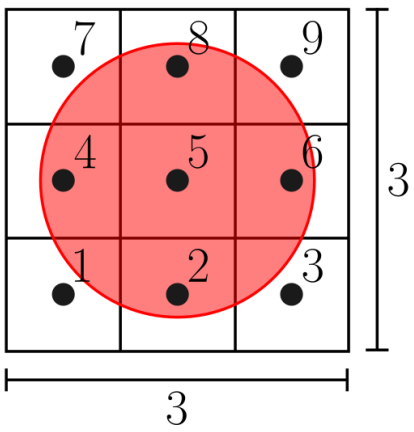

Figure C.2 – Mesh for evaluating the support of the density filters. The black dots are the degrees of freedom and the red circle indicate the filter radius.

$$\boldsymbol{K}_{\mathrm{f}} = \begin{bmatrix} 1.170 & -0.085 & 0 & -0.085 & 0 & 0 & 0 & 0 & 0 \\ -0.085 & 1.255 & -0.085 & 0 & -0.085 & 0 & 0 & 0 & 0 \\ 0 & -0.085 & 1.170 & 0 & 0 & -0.085 & 0 & 0 & 0 \\ -0.085 & 0 & 0 & 1.255 & -0.085 & 0 & -0.085 & 0 & 0 \\ 0 & -0.085 & 0 & -0.085 & 1.339 & -0.085 & 0 & -0.085 & 0 \\ 0 & 0 & -0.085 & 0 & -0.085 & 1.255 & 0 & 0 & -0.085 \\ 0 & 0 & 0 & -0.085 & 0 & 0 & 1.170 & -0.085 & 0 \\ 0 & 0 & 0 & 0 & -0.085 & 0 & -0.085 & 1.255 & -0.085 \\ 0 & 0 & 0 & 0 & 0 & -0.085 & 0 & -0.085 & 1.170 \end{bmatrix} \tag{C.10}$$

$$\boldsymbol{K}_{\mathrm{f}}{}^{-1} = \begin{bmatrix} 0.8635 & 0.0592 & 0.0044 & 0.0592 & 0.0076 & 0.0008 & 0.0044 & 0.0008 & 0.0001 \\ 0.0592 & 0.8086 & 0.0592 & 0.0076 & 0.0524 & 0.0076 & 0.0008 & 0.0037 & 0.0008 \\ 0.0044 & 0.0592 & 0.8635 & 0.0008 & 0.0076 & 0.0592 & 0.0001 & 0.0008 & 0.0044 \\ 0.0592 & 0.0076 & 0.0008 & 0.8086 & 0.0524 & 0.0037 & 0.0592 & 0.0076 & 0.0008 \\ 0.0076 & 0.0524 & 0.0076 & 0.0524 & 0.7599 & 0.0524 & 0.0076 & 0.0524 & 0.0076 \\ 0.0008 & 0.0076 & 0.0592 & 0.0037 & 0.0524 & 0.8086 & 0.0008 & 0.0076 & 0.0592 \\ 0.0044 & 0.0008 & 0.0001 & 0.0592 & 0.0076 & 0.0008 & 0.8635 & 0.0592 & 0.0044 \\ 0.0008 & 0.0037 & 0.0008 & 0.0076 & 0.0524 & 0.0076 & 0.0592 & 0.8086 & 0.0592 \\ 0.0001 & 0.0008 & 0.0044 & 0.0008 & 0.0076 & 0.0592 & 0.0044 & 0.0592 & 0.8635 \end{bmatrix} \tag{C.11}$$

$$\boldsymbol{H}_{\mathrm{m}} = \begin{bmatrix} 1.2 & 0.2 & 0 & 0.2 & 0 & 0 & 0 & 0 & 0 \\ 0.2 & 1.2 & 0.2 & 0 & 0.2 & 0 & 0 & 0 & 0 \\ 0 & 0.2 & 1.2 & 0 & 0 & 0.2 & 0 & 0 & 0 \\ 0.2 & 0 & 0 & 1.2 & 0.2 & 0 & 0.2 & 0 & 0 \\ 0 & 0.2 & 0 & 0.2 & 1.2 & 0.2 & 0 & 0.2 & 0 \\ 0 & 0 & 0.2 & 0 & 0.2 & 1.2 & 0 & 0 & 0.2 \\ 0 & 0 & 0 & 0.2 & 0 & 0 & 1.2 & 0.2 & 0 \\ 0 & 0 & 0 & 0 & 0.2 & 0 & 0.2 & 1.2 & 0.2 \\ 0 & 0 & 0 & 0 & 0 & 0.2 & 0 & 0.2 & 1.2 \end{bmatrix} \tag{C.12}$$

$$\boldsymbol{h}_{\mathrm{s}} = \begin{bmatrix} 1.6 & 1.8 & 1.6 & 1.8 & 2 & 1.8 & 1.6 & 1.8 & 1.6 \end{bmatrix} \tag{C.13}$$